DIRECT INJECTION DIESEL ENGINE COMBUSTION DIAGNOSTICS

by

Zainal Ambri Abdul-Karim

A Doctoral Thesis

Submitted in partial fulfillment of the requirements
for the award of
Doctor of Philosophy of Loughborough University

June 2004

ACKNOWLEDGEMENT

I wish to express my debt of gratitude to Universiti Teknologi PETRONAS for giving the opportunity and providing the financial support to undertake the research work at Loughborough University.

I wish to express my heartiest appreciation and thankfulness to my wife, Faridah, and my five children for their constant support, patience and encouragement, both emotionally and spiritually, during the course of my research.

I am thankful to both my supervisors, Dr Graham Wigley and Dr Andrew Clarke, for the helpful discussions, suggestions and constructive feedbacks during the entire research period. I've gained considerable experience and knowledge while under their supervision.

Special thanks to the department technicians, Adrian Broster, Steve Taylor and Graham Smith for their support in ensuring that the equipment in the engine test cell are in proper operating conditions. To my research colleague, Jill Patterson, who often extended her invaluable assistance and advice on many occasions during the experimental work.

For the spray imaging experimental work, I wish to thank and acknowledge Ron Bickinton and Tony Wells, both at Lister Petter R&D Department, in Dousley, for facilitating me during the experiments and the use of test equipments at the research laboratory.

ABSTRACT

The demand for the protection of the environment from air pollution and reduction of carbon dioxide has resulted in worldwide exhaust emissions regulations imposed on the diesel engines. Fortunately, diesel engine offers the best fuel economy and low emissions of carbon dioxide of most engines currently available. However, the engine's inherent drawbacks are that the engine is heavy, noisy, and expensive, in addition to producing significant level of particulates and nitrogen oxides emissions.

The present research attempts to understand the combustion characteristics and emissions trade-off by experimental investigations of the diesel engine using a production Lister Petter 2.97 litres, four-cylinder, high-speed, direct injection diesel engine. The investigation involved the analysis of the in-cylinder pressure data, heat release rate calculation and exhaust gas measurements of various injectors having different nozzle geometry. The engine experiments cover both the investigation of the fuel injection and the engine operating parameters such as injection rate, nozzle geometry, the engine load and speed. The effects of each parameter on ignition delay, heat release rate, nitrogen oxides emissions, smoke density, and total hydrocarbon levels were investigated. Two complementary diagnostic techniques were employed in order to assist in understanding the injection characteristics. The first technique involved the imaging of the fuel sprays from the different injectors in a constant volume spray chamber using a CCD camera. The images were than process using a dedicated image processing software. The second technique involved the measurements of the fuel injection rates from the injectors using the Bosch Tube meter.

A three-zone model was developed to determine the heat release rate of combustion. The cylinder pressure data was used to validate the model written in Matlab computer programme. The model is based on the principles of the First Law of Thermodynamics applied to the three zones, formed due to the fuel injection into the combustion chamber. The heat release rate profiles produced by the model were used to analyse the formation of pollutants that were measured in the exhaust gas.

The results showed that injectors with large nozzle hole diameters produced high smoke levels, especially at high engine load conditions with small increase in NOx. These injectors also caused the sprays to impinged on the combustion chamber walls at high load conditions. On the other hand, injectors having small nozzle hole diameters produced high levels of NOx while the smoke emission levels were low. The effect of nozzle geometry has little significant on the emissions of THC.

TABLE OF CONTENTS

LIST OF FIGURES

LIST OF TABLES

NOMENCLATURE, SYMBOLS AND UNITS

A_{comb}	Combustion surface area	(m^2)
A_{cyl}	Cylinder head surface area	(m^2)
A_p	Piston crown surface area	(m^2)
A_t	Flow area of tubing	(mm^2)
B	Cylinder bore	(m)
C_a	Area contraction coefficient	N/D
C_h	Nozzle discharge coefficient	N/D
C_s	Needle seat discharge coefficient	N/D
C_v	Velocity coefficient	N/D
F/A	Fuel-air ratio	N/D
H	Enthalpy	(kJ)
I_λ	Intensity of radiation	(W/m^2sr nm)
K	Absorption coefficient	N/D
L	Flame thickness	(mm)
L_s	Stroke	(m)
M	Molecular weight	(kg/kmol)
N	Engine speed/Pump speed	(rpm)
Nu	Nusselt number	N/D
P	Pressure	(kN/m^2)
Pr	Prandtl number	N/D
Q	Heat	(kJ)
Q_{comb}	Heat of Combustion	(kJ)
Q_{wall}	Heat loss to wall	(kJ)
R	Gas constant	(kJ/kgK)
Re	Reynolds number	N/D
R_o	Universal gas constant	(kJ/kmolK)
S	Spray penetration length	(m)
T	Temperature	(K)
U	Internal energy	(kJ)
	Flow velocity	(m/s)
V	Volume	(m^3)
Vc	Clearance volume	(m^3)
V_{inj}	Velocity of injected fuel	(m/s)
W	Work	(kJ)

a	Convective heat transfer constant	N/D
	Crank radius	(m)
	Number of carbon atom	N/D
	Velocity of sound in fluid	(m/s)
b	Index relating (Nu) to (Re)	N/D
	Number of hydrogen atom	N/D
c	Radiant heat transfer constant	N/D
c_1	Planck's first radiation constant	N/D
c_2	Planck's second radiation constant	N/D
c_a	Coefficient for area of contraction	N/D
c_p	Specific heat at constant pressure	(kJ/kgK)
c_v	Specific heat at constant volume	(kJ/kgK)
d_o	Nozzle orifice diameter	(m)
h	Specific enthalpy,	(kJ/kg)
	Heat transfer coefficient	(W/m^2K)
k	Gas thermal conductivity	(W/mK)
l	Connecting rod length	(m)
l_n	Nozzle orifice length	(m)
m	Mass	(kg)
m_{cyl}	Mass of mixture in combustion chamber	(kg)
m_{fb}	Mass of burned fuel	(kg)
m_{fi}	Mass of injected fuel	(kg)
m_{RP}	Mass of mixture - burned or unburned	(kg/kmol O_2)
m_{trap}	Mass of trapped air in combustion chamber	(kg)
n	Number of moles	N/D
	Polytropic index	N/D
q	Fuel quantity	(mm^3)
s	Distance between crank axis and piston axis	(m)
t	Time	(s)
t_b	Drop breakup time	(s)
u	Specific internal energy	(kJ/kg)
v_p	Mean piston speed	(m/s)
x	Mass fraction	N/D
	Characteristic length	(m)
x_b	Residual mass fraction	N/D
x_{uO2}	Mass fraction of oxygen in unburned zone	N/D
y	Molar H/C ratio of fuel	N/D

GREEK SYMBOLS

α	Stoichiometric air-fuel ratio	N/D
	spectral range constant	N/D
ε	Stoichiometric fuel-air ratio	N/D
ε_λ	Monochromatic emissivity	N/D
γ	Specific heat ratio c_p/c_v	N/D
λ	Wavelength	(nm)
μ	Gas dynamic viscosity	(kg/ms)
θ	Crank angle	(degree)
θ_s	Spray angle	(degree)
ϕ	Fuel-air equivalence ratio	N/D
ψ	Molar N/O ratio	N/D
ρ	Density	(kg/m^3)
ρ_d	Density of diesel fuel	(kg/m^3)

SUBSCRIPT

1	Zone 1
2	Zone 2
a	Air
atm	Atmosphere
b	Burned
d	Diesel
f	Fuel
g	Gas
i	Species
l	Liquid
s	Stoichiometric
u	Unburned
v	Vapour

ABBREVIATION

BMEP	Brake Mean Effective Pressure
BSFC	Brake Specific Fuel Consumption
CA	Crank Angle
CCD	Charged-Coupled Device
CDM	Crank Degree Marker
CID	Charged-Injection Device
CO	Carbon Monoxide
CO_2	Carbon Dioxide
CR	Common Rail
DI	Direct Injection
EGR	Exhaust Gas Recirculation
EUI	Electronic Unit Injector
FID	Flame Ionisation Detector
FIE	Fuel Injection Equipment
FSN	Filter Smoke Number
H_2O	Water
HC	Hydrocarbon
HSDI	High Speed Direct Injection
IDI	Indirect Injection
LDA	Laser Doppler Anemometry
LDV	Laser Doppler Velocimetry
LIF	Laser Induced Fluorescence
LII	Laser Induced Incandescence
NDIR	Non-Dispersive Infrared Detector
NO	Nitric Oxide
NO_2	Nitrogen Dioxide
NOx	Nitrogen Oxides
NOP	Nozzle Opening Pressure
O_2	Oxygen
O_3	Ozone
PDA	Phase Doppler Anemometry
PM	Particulate Matter
PIV	Particle Image Velocimetry
rpm	revolution per minute
SOC	Start of Combustion

SOI	Start of Injection
TDC	Top Dead Centre
THC	Total Hydrocarbon
VCO	Valve Covered Orifice
VOC	Volatile Organic Compounds

CHAPTER 1: INTRODUCTION

1.1 MOTIVATION

Growing concerns about environmental preservation and cleaner air have created a demand for a lower pollution or environment friendly automotive diesel engine. As a result, regulation covering diesel engine emissions such as nitrogen oxides, particulate matter, carbon monoxide, carbon dioxide and unburned hydrocarbon have been formulated in many countries and become increasingly strict in some. Nitrogen oxides, or NOx, is a collective term referring to two species of oxides of nitrogen, i.e. nitric oxide (NO) and nitrogen dioxide (NO_2). In the atmosphere, NOx mixes with water vapour to produce nitric acid which is later deposited as acid rain. Particulate matter, or PM, is the term used for fine solid particles found in the air including dust, soot, smoke and dirt. PM is commonly associated with health problems, especially to humans with heart and lung diseases.

Diesel engine manufacturers have to address the emissions from the engine exhaust gases in order to meet the current and future worldwide exhaust emission regulations which limit the emission of pollutants especially nitrogen oxides (NOx) and particulate matter (PM) from diesel engine while at the same time maintaining a fuel economy and quiet engine to satisfy the customers. Fortunately, diesel engines are known to have the highest thermal efficiency and offer superior fuel economy among engines of an equivalent capacity which leads to lower fuel costs, as shown in Figure 1.1. The figure shows the comparison of current fuel consumption between gasoline and diesel passenger cars in Europe. From the figure, the fuel consumption of direct injection (DI) diesel engine passenger cars are significantly lower than both that of gasoline and indirect injection (IDI) diesel engine. This is in part due to their high compression ratios, and that the air-fuel mixture is always weak of stoichiometric. Increase in maximum brake mean effective pressure (BMEP) with the advancement of turbocharging and new generation of high-pressure fuel injection systems have enabled a reduction in engine size and weight per power output. This has made the modern diesel engine comparable to the gasoline engine, as shown in Figure 1.2.

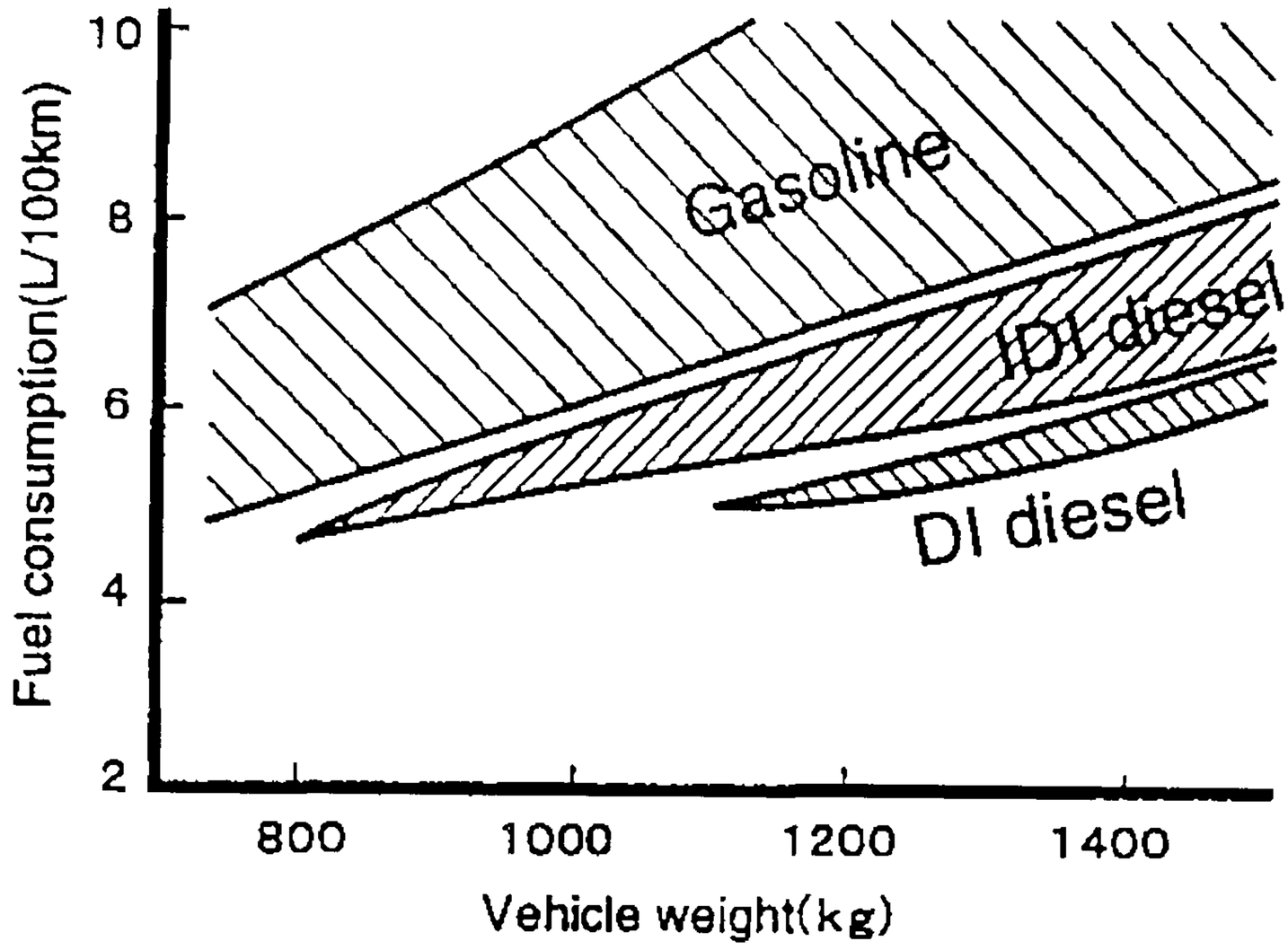

Figure 1.1: Fuel consumption comparison between gasoline and diesel engine passenger cars in Europe Source from (Hikosaka, 1997)

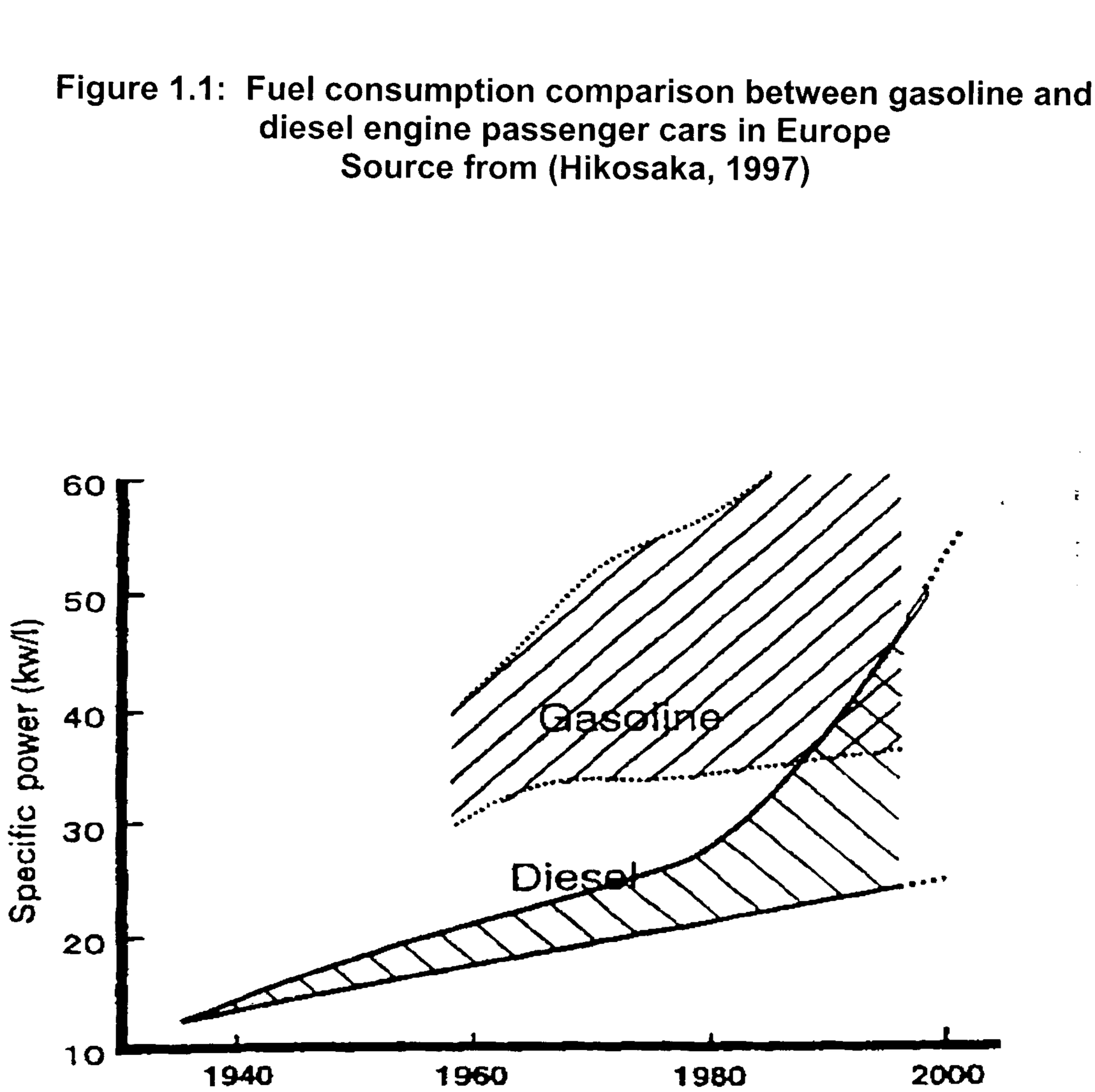

Figure 1.2: Trend of specific power development of diesel engine passenger cars as compared to gasoline engine in Europe Source from (Hikosaka, 1997)

Over the last few years, significant increase in diesel engine passenger cars production over gasoline engine has been attributed to the high fuel efficiency, reliability and robustness of the engine as well as providing longer service life. Recently, Ricardo Consulting Engineers (Ricardo, 2002) estimated that the diesel passenger car sales would exceed 50 per cent by year 2005. Figure 1.3 shows the car production forecast up to year 2006 in Europe. From the figure, passenger cars powered by diesel engine represent 40 per cent of the total passenger car production in the Europe market and 98 per cent of these diesel engines are of direct injection diesel engines. In addition, diesel engines are widely available in all sizes and speed, covering a large range of application, while maintaining the traditional role as power plants of heavy-duty vehicles.

Unlike gasoline engines, Schindler (Schindler, 2000) reported that diesel engines do not emit evaporative volatile organic compounds (VOCs) which contribute to the production of ozone in the atmosphere and their low carbon dioxide (CO_2) emissions help to reduce the green house effect. Despite the fuel economy and low CO_2 emissions advantages of the diesel engine as compared to the gasoline engine, diesel engine has relatively high exhaust levels of NOx and PM emissions. The engine's inherent high compression ratio produces noise and high maximum gas temperatures in the combustion chamber that directly cause higher diesel emissions. The global concerns of the effects of these pollutants on the quality of air are growing as a result from increase in volume of diesel engine. Thus, stringent emissions regulations are being imposed on the emissions of not only the above two pollutants but also of hydrocarbon (HC) and carbon monoxide (CO).

The development of emissions standard for high-speed direct injection (HSDI) diesel engine in Europe from year 1992 to the expected limits in year 2005 is shown in Table 1.1. It must be realised that there is a trend of continual tightening of emissions legislation imposed on the diesel engines in the past and inevitable will still continue in the future. The fact that the maximum emission levels for around 2008 are already currently being set proves this. In the past, significant improvements have been achieved in controlling the exhaust gaseous emissions, as shown in Figure 1.4. According to the figure, the reduction of NOx and particulate matter from Euro I to Euro III are already 42 per cent and 64 per cent respectively. However, the challenge is a further emission reduction of not less than 45 per cent for both pollutants are required to meet the forthcoming Euro IV in the attempt to move towards zero emissions regulations.

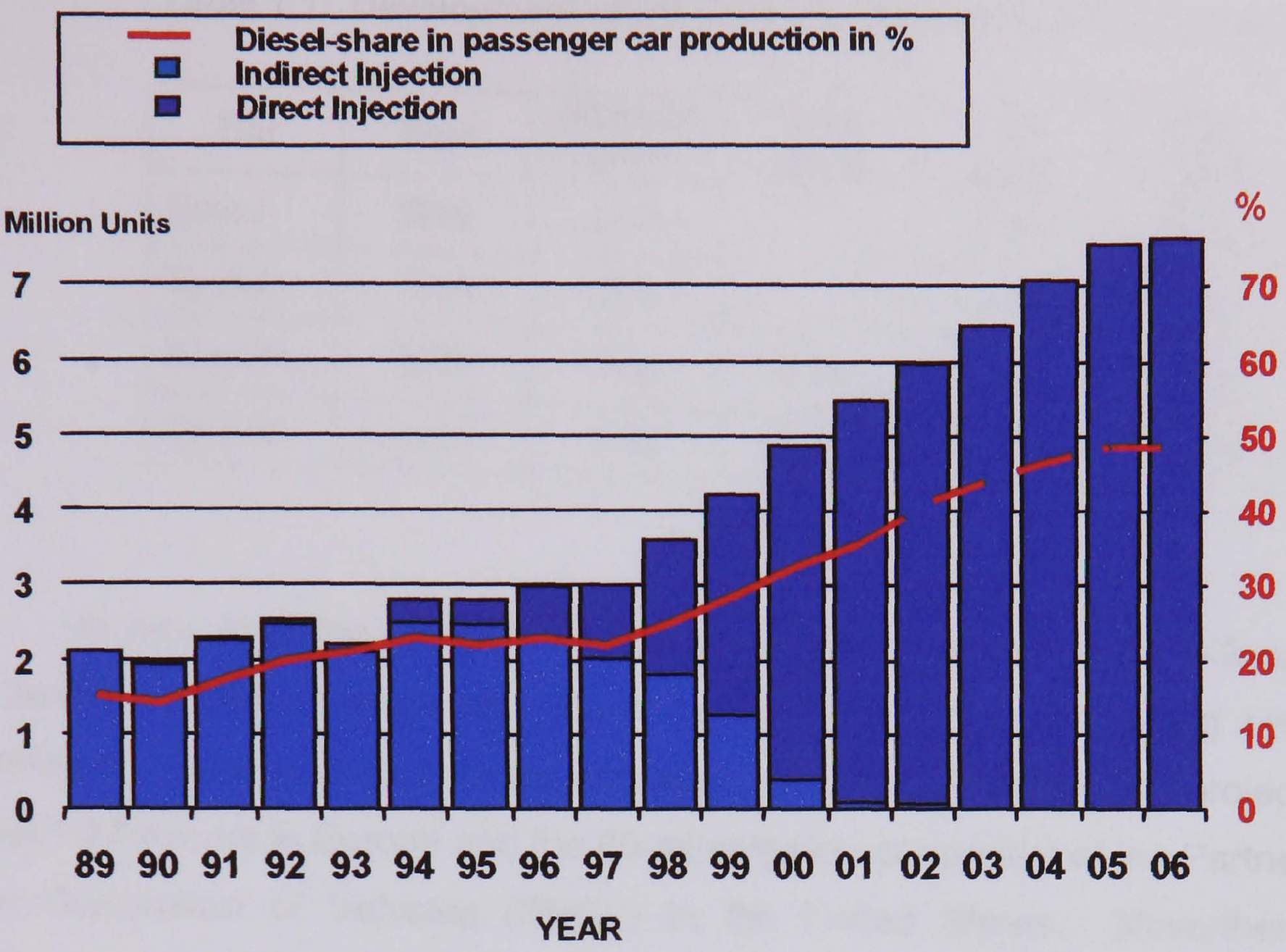

Figure 1.3: Diesel engine passenger car production forecast in Europe
Source from (Weissbeck, 2002)

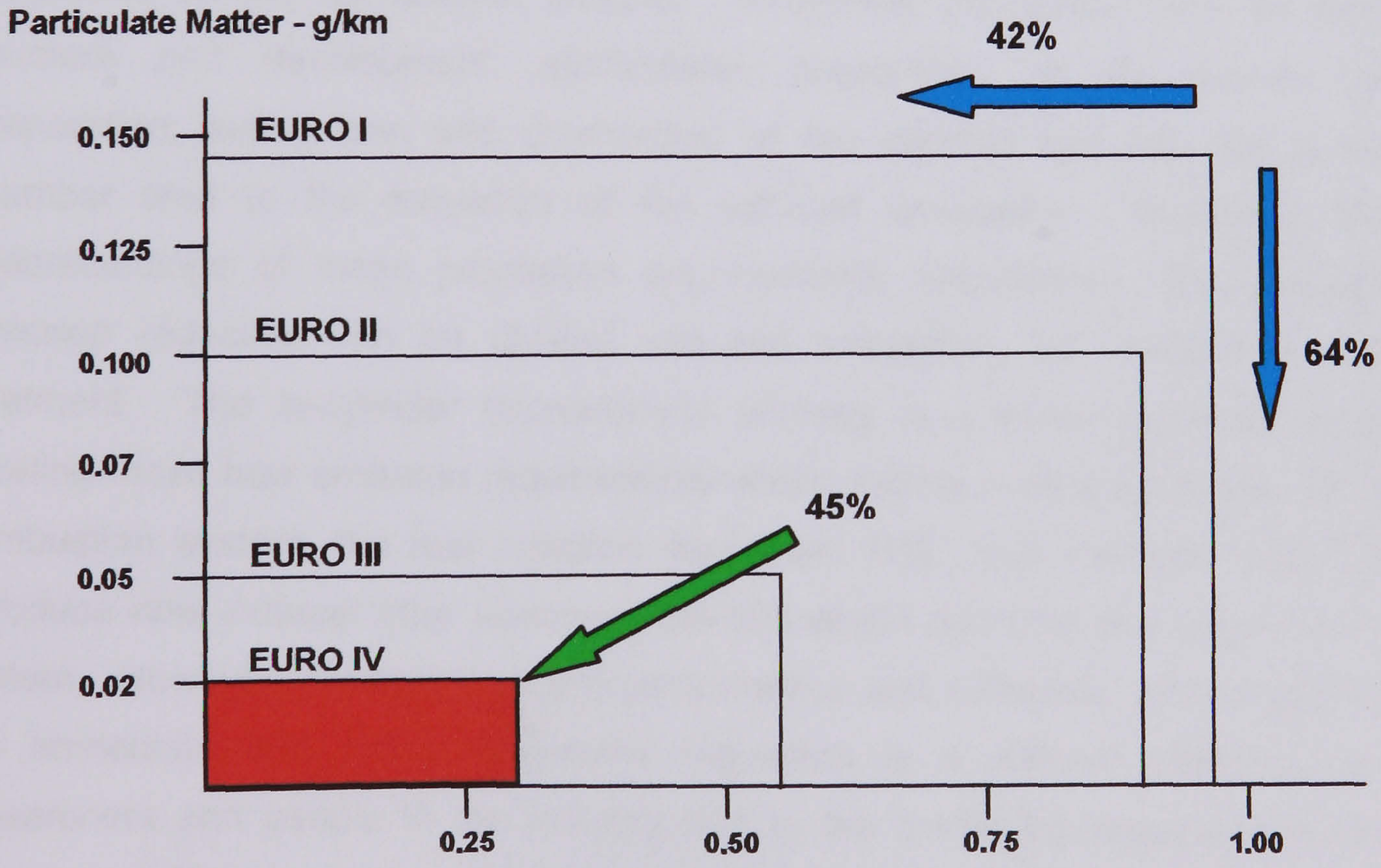

Figure 1.4: Emission legislation trends for HSDI diesel engine in Europe

Table 1.1: Development of EU emission standards for diesel cars

Tier	Year	HC+NOx g/km	NOx g/km	CO g/km	PM g/km
Euro I	1992	0.97	-	2.72	0.14
Euro II	1999	0.9	-	1.0	0.10
Euro III	2000	0.56	0.50	0.64	0.05
Euro IV	2005	0.30	0.25	0.50	0.025

In view of all the above factors, diesel engine has attracted significant attention for research and development efforts in terms of further improving performance, developing fuel-economy and low-emission vehicles. Among such projects are the 3-liter/100km cars in Europe and the 80-miles/gallon car project of the Partnership for a New Generation of Vehicles (PNGV) in the United States. Nevertheless, more complete data and analyses are required to understand the fundamental processes involved in a direct injection diesel engine performance. Diesel engine, therefore, will remain an important power source in automotive applications.

It was found that the production of NOx and PM in diesel engine are highly dependant on the combustion process. In-cylinder processes such as fuel spray structure and development, atomisation, preparation of the fuel-air mixture, evaporation, autoignition and combustion of the injected fuel into the combustion chamber lead to the formation of the exhaust emissions. Therefore, thorough understandings of these processes are inevitably necessary. The strategies for emission reduction can be divided into two categories, i.e. in-cylinder and after treatment. The in-cylinder improvement strategy is a more preferred means for meeting these new emission requirements which include improving further the engine combustion system, the fuel injection equipment (FIE) and the fuel, rather than to introduce new exhaust after treatment devices which add cost and complexity to the system. However, improving engine performance and efficiency while trying to meet the immediate and future emissions regulation is a difficult challenge to both researchers and people in the industry due to the conflicting requirement that they possess. For example, lowering the maximum temperature reached during combustion is known to reduce the NOx emissions. Lower in-cylinder temperature can be achieved by several methods such as cooling the intake air or increasing the EGR ratio. However, low in-cylinder temperature limits the complete oxidation of soot,

thereby increasing particulate emission. On the other hand, increasing the fuel injection pressure improves fuel atomisation and mixture preparation. This enhances the oxidation of soot, thus reducing formation of particulate matter but with a penalty in NOx. The above phenomenon is known as the NOx-PM trade-off and is shown graphically in Figure 1.5. The NOx-PM trade-off and other trade-offs will be discussed further in Chapter 2 of this thesis. Another conflicting aspect of the diesel engine with regards to optimising engine performance and emissions requirement is that, changing the engine parameters may affect fuel economy, combustion noise and also the engine overall performance. The combined effects of injection pressure and timing, gas flow characteristics and combustion chamber design on combustion and emissions of high-speed direct injection diesel engine are further complicated by air utilisation, mixture preparation and heat transfer within the confined space and reduced time. Therefore, the strategies for the optimisation of NOx, PM and HC which are targeted to achieve the best trade-off with regards to fuel consumption and combustion noise are limited to the specific application only. In addition, the development of high pressure fuel injection system and the design of the combustion chamber require extensive research in order to evaluate their effects on the overall engine performance.

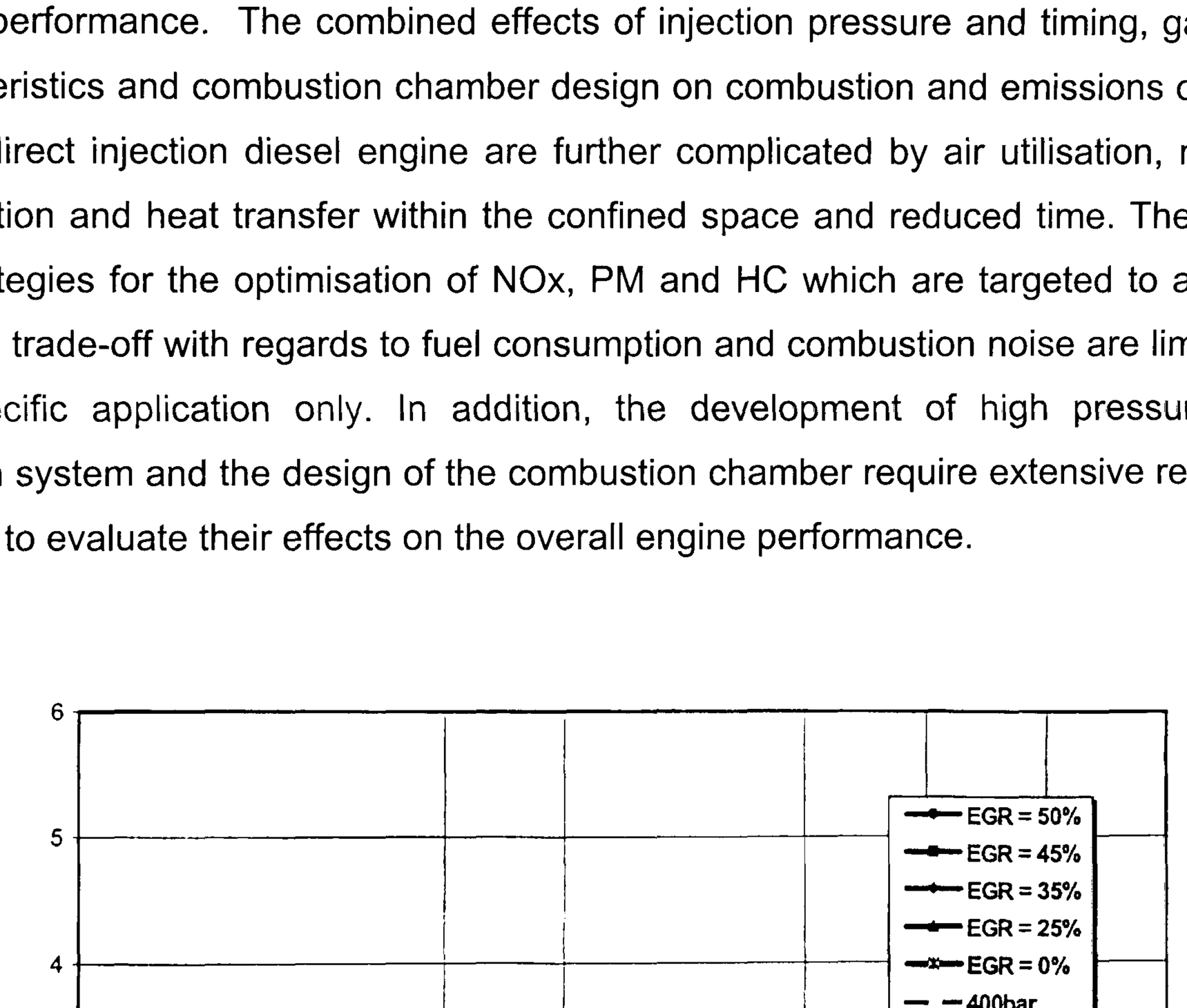

Figure 1.5: Emission trade-off between NOx and PM at different EGR ratio and fuel injection pressure Source from (Henein et al., 2001)

The first step in understanding the mechanisms of pollutant formation are to analyse the atomisation, self-ignition and combustion of the injected fuel. For the purpose of understanding the effects of various parameters on engine performance and exhaust emissions, an extensive investigation was performed on the combustion phenomena in a production multi-cylinder, high-speed, direct injection (HSDI) diesel engine. Direct measurement of exhaust gas composition provides information on the emissions trade-off while data of the pressure with respect to crank angle histories were used to develop the heat release rate curves which provide information of the combustion characteristics. The main difference between the current study and those in the literature survey is primarily in the use of an actual production direct injection diesel engine as opposed to single cylinder research engine, in gathering data on diesel fuel spray combustion and emissions. The engine offers more realistic flow and geometric conditions since the intake and exhaust gas dynamics as well as the combustion chamber geometry, are virtually unaffected.

1.2 OBJECTIVES

The overall goal of the research project is to determine the effects of varying certain parameters on the fuel spray structure, combustion characteristics and the formation of pollutants in direct injection (DI) diesel engine which are necessary for development and testing of numerical models. Consequently, in pursuing the research goal, detailed experiments will be carried out to meet the following specific objectives:

1.2.1 To develop an imaging system for fuel spray development which employs an optical system.

1.2.2 To understand the relationship between diesel fuel spray combustion phenomena and exhaust emissions by combustion analysis and quantitative measurement of exhaust gas composition.

1.2.3 To explain combustion phenomena such as start of injection, ignition delay period, and combustion of the injected spray by analysing the in-cylinder pressure histories and heat release rate profiles.

1.2.4 To develop a programme for a three-zone model as a tool for determining the in-cylinder temperatures and heat release rate of combustion.

1.3 RESEARCH METHODOLOGY

In order to achieve the research objectives, the research undertook the following investigations:

1.3.1 Imaging of non-evaporative fuel sprays of three different types of injectors in a constant volume combustion bomb using a CCD camera.

1.3.2 Measurement of the fuel injection rates from three different types of injectors using the Bosch Tube meter.

1.3.3 Determination of engine baseline operating conditions and exhaust gas emissions measurements.

1.3.4 Investigation of engine performances at various operating conditions and analysis of the exhaust gas composition.

1.3.5 Analysis of the rate of heat release and validation of the three-zone heat release rate model.

1.4 OUTLINE OF THESIS

The thesis is divided into seven chapters. Chapter 1 serves as an introduction to the thesis which discusses the motivation for performing the research. The chapter also provides a list of aims that the present work is trying to achieve and the investigation methodology undertook in order to complete the research.

Chapter 2 provides a brief literature review on diesel engine research to date as regards research on spray characteristics, cavitation phenomena, the fuel-air mixture preparation and combustion of the diesel fuel spray. The chapter also reviews some of the strategies developed in order to reduce the exhaust emissions from diesel engine.

Chapter 3 describes and discusses the results from two experimental works performed in characterising the fuel injection. The first experiments involved the visualisation of the fuel sprays from various injectors having different nozzle hole diameters in a constant volume spray chamber. The second experiment involved the measurement of the rate of injection of the above injectors using the Bosch Tube meter.

Chapter 4 provides details of the engine facilities for the current research work and the investigation performed on the Lister Petter X90, four-cylinder, high-speed, direct injection diesel engine. This is followed by Chapter 5, which presents the results obtained from the engine investigations and exhaust gas emissions measurements. Discussion of the results as well as the validation of heat release rate model are presented.

Chapter 6 describes the heat release model developed, in an attempt to understand the combustion process in an engine from the readily available cylinder pressure data. The heat release rate calculation is the rate that fuel and air would need to react to equilibrium combustion product to give the observed cylinder pressure curve. The model described is a three-zone model based on the First Law of Thermodynamics and ideal gases equations. The model is implemented using the Matlab computer programme.

Finally, Chapter 7 gives a conclusion remarks on the findings of the research, and outlines some suggestions for future work.

A list of references from which information were taken for this thesis is included in the last few pages of the thesis. Other information in relation to the thesis is given in the Appendices.

CHAPTER 2: LITERATURE REVIEW

2.1 FUEL SPRAY RESEARCH

Diesel fuel sprays have been systematically studied by many researchers with different approaches, various measurement techniques and under different engine conditions using 'engines' which allow wide optical access into the combustion chamber and conducted under well control operating conditions. However, the conditions of which the research is being investigated are very far from that of the real engine conditions. This is either because the geometry of the combustion chamber was highly modified, the operation was not non-steady process or because the atmosphere in which the fuel was injected was very different from the actual engine. Researchers such as Araneo et al. (Araneo et al., 1999), Gong et al. (Gong et al., 1992), and Kuniyoshi et al. (Kuniyoshi et al., 1980), have used various constant volume vessels to simulate the in-cylinder conditions of diesel engine for fuel spray research, both for non-evaporating and evaporating spray studies. Kosaka et al. (Kosaka et al., 1992) extensively used a rapid compression machine with combustion chamber to study the structure of diesel sprays. While, high pressure spray chamber was used to look at specific characteristics of the spray such as spray penetration, spray angle, drop size distribution and velocity by researchers such as Hiroyasu and Arai (Hiroyasu and Arai, 1990), Kozma and Farrell (Kozma and Farrell, 1997), Naber and Siebers (Naber and Siebers, 1996), Rajalingam and Farrell (Rajalingam and Farrell, 1999), and Siebers (Siebers, 1998). Although some of these studies were performed at elevated temperature and pressure, simulation of the conditions in the actual diesel engine that include the shape of the combustion chamber and the flow of the gases are very difficult. Therefore, many research labs used an operating single cylinder diesel engine, either based on a heavy-duty production engine or a dedicated research engine to study the diesel spray phenomena.

Optical access through the combustion chamber of the above 'engine' at various location is made possible by having quartz or sapphire windows on the sides of the combustion chamber in the cylinder head of the engine, using an elongated piston with transparent crown or by using an engine that allows optical access with a combination of the above. Another type of access to the combustion chamber is the

endoscope-based optical system which offers minimal modification of the original engine geometry while providing a reasonable large field of view of the combustion chamber. A cross-sectional area of each research engine mentioned above is shown in Figure 2.1.

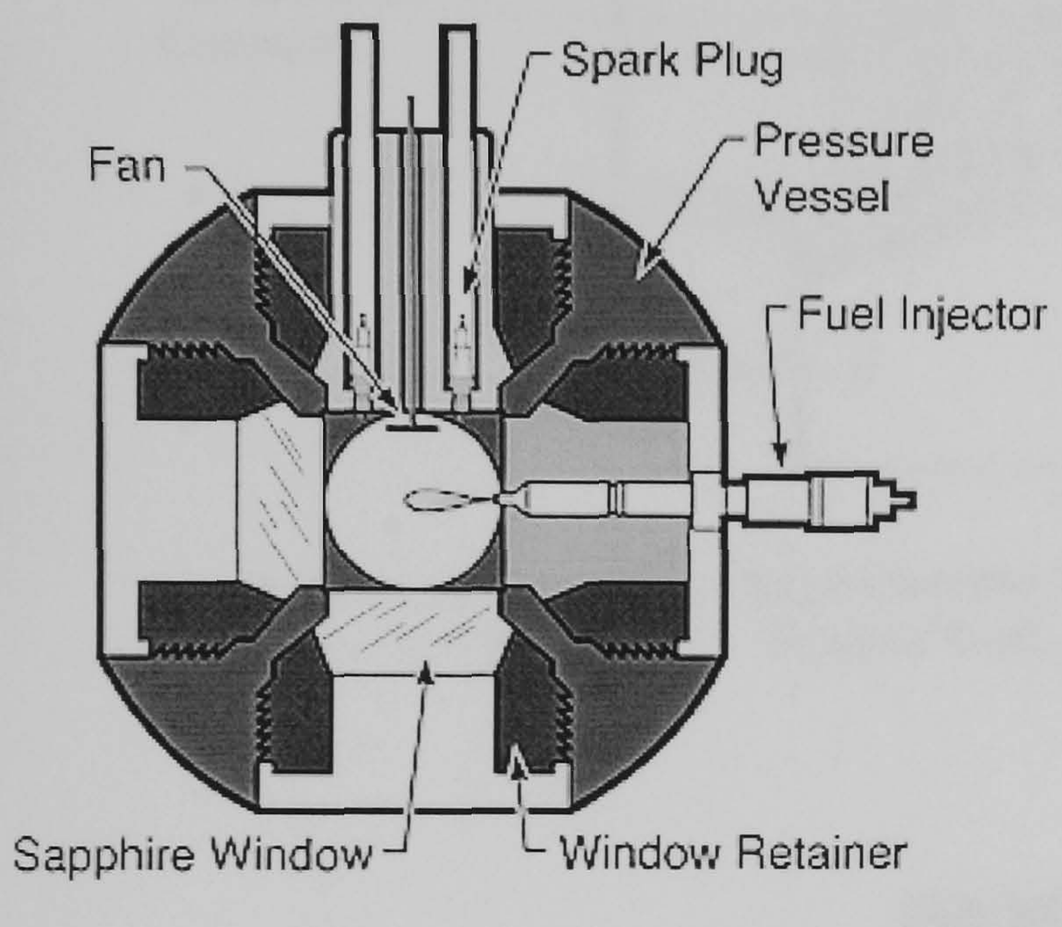

(a) Constant volume chamber
Source from (Edwards et al., 1992)

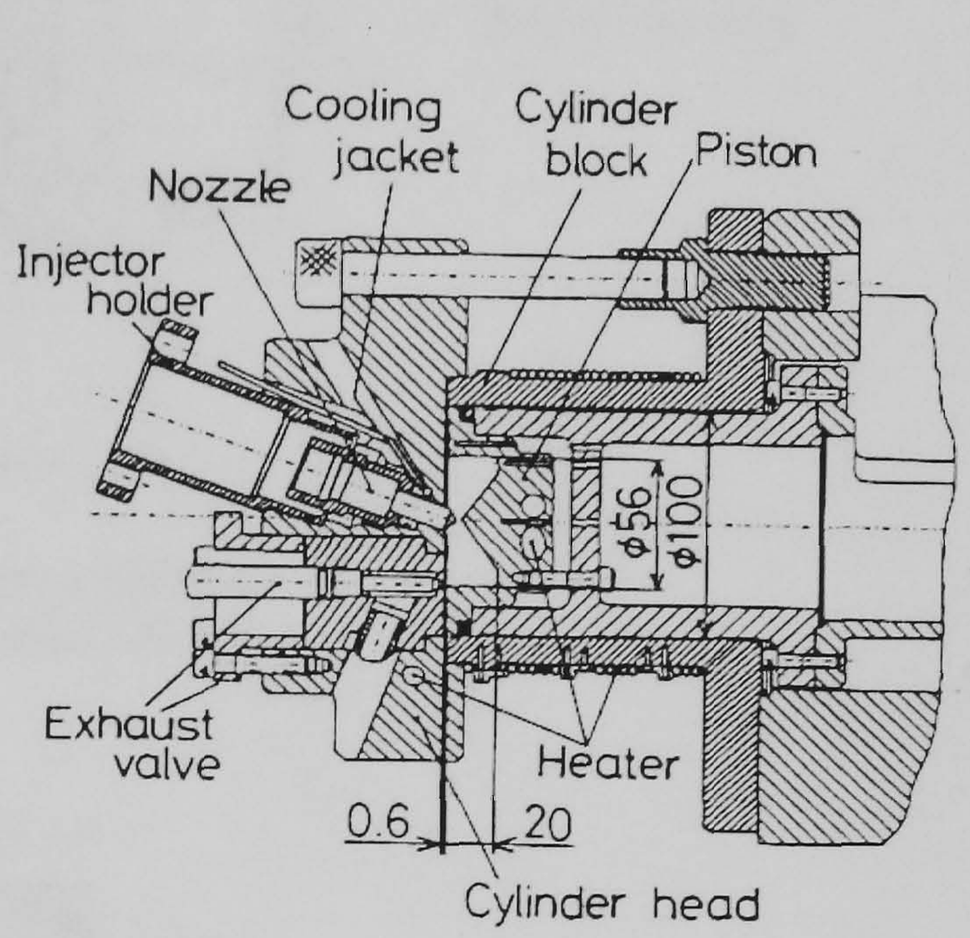

(b) Rapid compression machine
Source from (Kosaka et al., 1992)

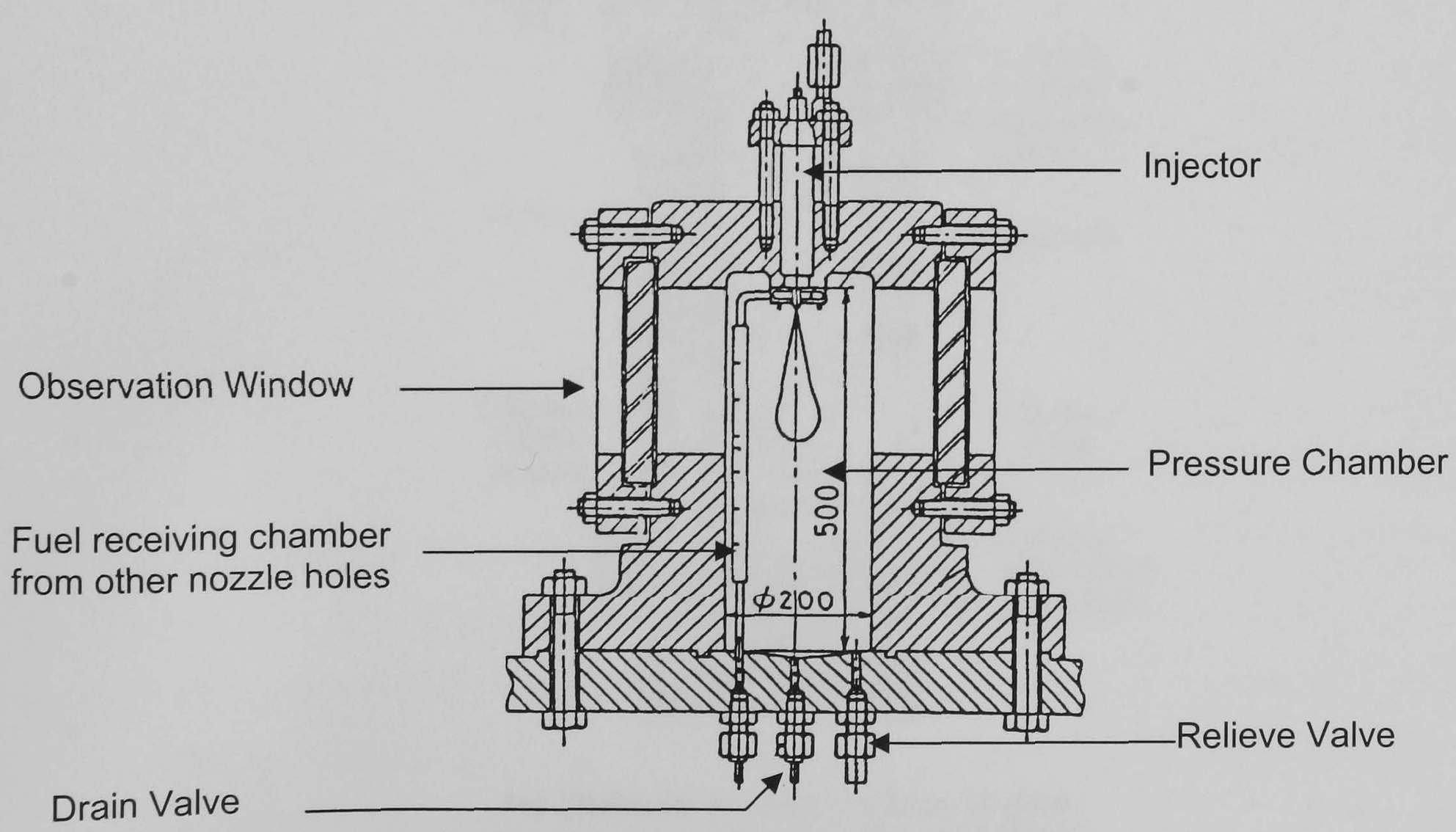

(c) High pressure chamber
Source from (Kuniyoshi et al., 1980)

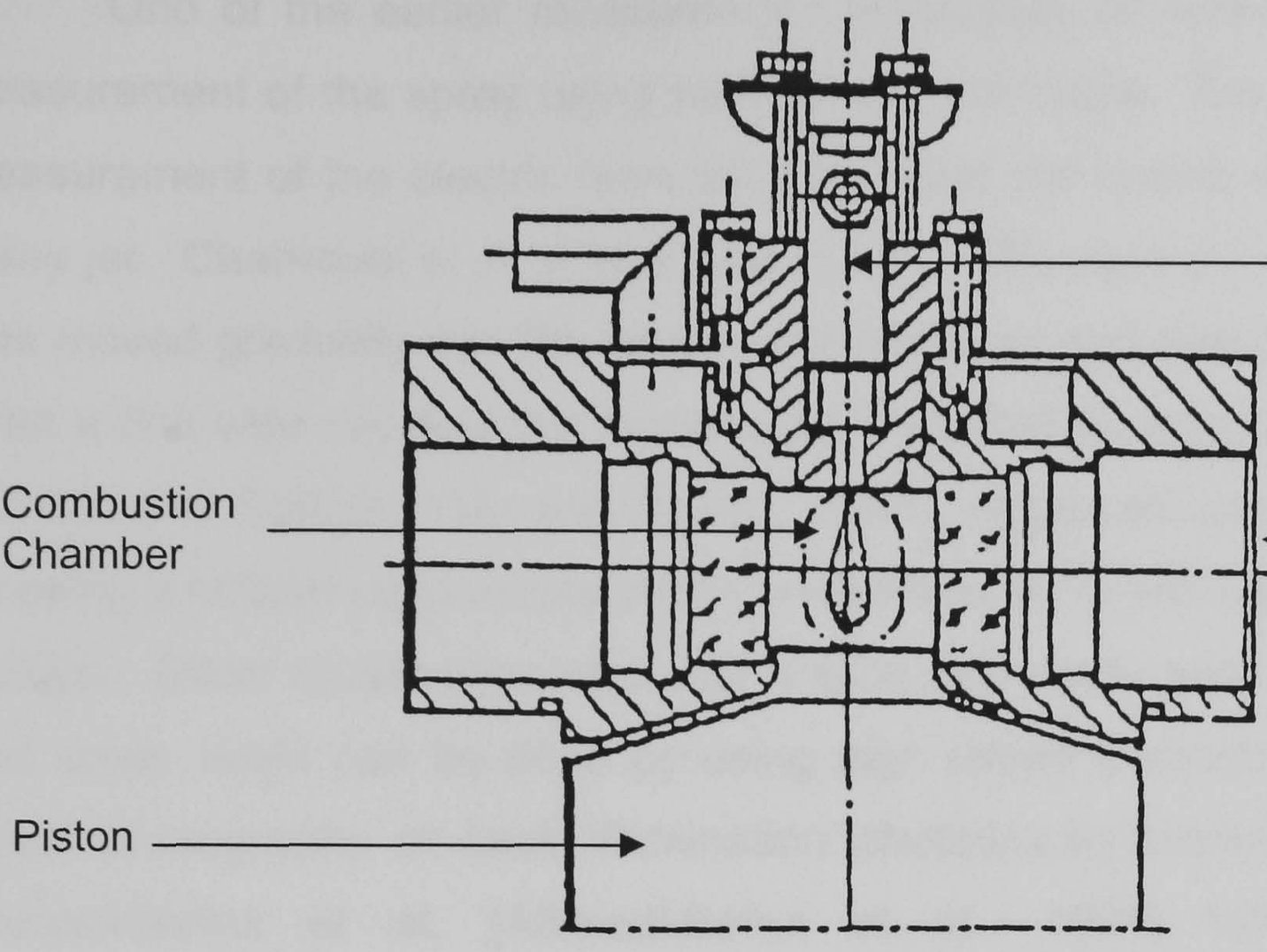

(d) Extended combustion chamber
Source from (Bürgler et al., 1992)

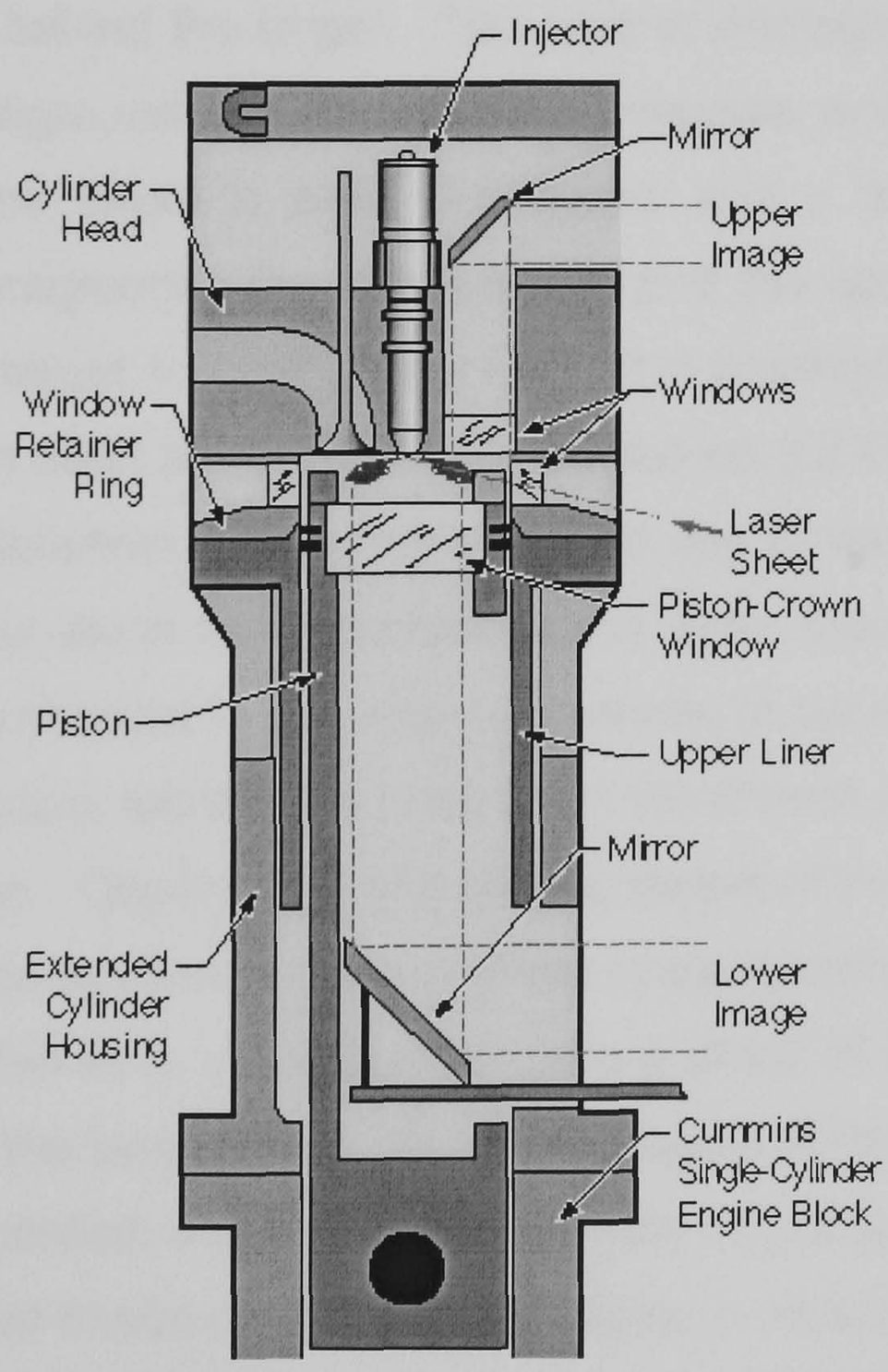

(e) Multiple access optical engine
Source from (Dec and Espey, 1995)

Figure 2.1: Various optical access research engines

One of the earlier measurement techniques of spray structure was by direct measurement of the spray using conductivity technique. Conductivity is based on the measurement of the electric resistance between the nozzle and a metal placed in the spray jet. Chehroudi et al. (Chehroudi et al., 1985) used a 1 mm diameter needle that was moved gradually into the spray while Hiroyasu and Arai (Hiroyasu and Arai, 1990) used a fine wire net detector to measure the spray resistance. Recent measurement by Yule and Salters (Yule and Salters, 1995), employed an intrusive probe technique by using a refined conductivity probe to measure the break-up length of transient diesel sprays. Other observation of diesel engine fuel spray such as spray tip penetration and spray angle can be done by using high speed photography techniques such as direct photography or back illumination photography technique, i.e. shadowgraphy. Ahmadi-Befrui et al. (Ahmadi-Befrui et al., 1991) indicated that high-speed photography technique allows investigation of the spatial and time variation of the spray properties. Direct photography is the least complicated technique but only liquid fuel and flame can be recorded. Back illumination photography uses a diffused light source which is located behind the target. This type of photography produces a dark object with a bright background. Shadowgraphy produces similar output as a back photography whereby the target is back illuminated and a dark object shadow is recorded on a bright background. The difference is that the light is focused onto the target and causing the target to cast a shadow. The photographs are captured by using an imaging system such as charged-coupled device (CCD) or charged-injection device (CID) camera. Schlieren photography can be use to record translucent target such as fuel spray vapour since the technique works when there are variations in the refractive index or phase contrast in the subject gradients or boundaries.

Many laser diagnostic techniques have been developed recently and applied to diesel fuel spray research. Observation and measurement of the optically dense inner spray structure is possible by means of laser sheet imaging technique as employed by Hentschel et al. (Hentschel et al., 1994), which uses a sheet of laser light to illuminate the spray. The plane of the laser defines the cross section of the spray that is imaged. The images are then recorded, enabling detail analysis of the spray structures. Laser sheet imaging can also be based on an optical principle in which light is scattered from small particles or droplets. This technique is known as Mie scattering and can be used to identify mixture formation such as evaporation, phase-to-phase interaction, and air entrainment features of the fuel spray. Gülder et al. (Gülder et al., 1992) and Smallwood et al. (Smallwood et al., 1994) used 2-D Mie scattering to visualise the

inner structure of a transient dense diesel spray. The laser sheet technique was also used by Espey and Dec (Espey and Dec, 1995) by elastic scattering imaging to measure the liquid core length of an evaporating fuel jet. Luminosity imaging such as Laser Induced Incandescence (LII) can be used to provide information on soot concentration and particle size distribution. In another investigation, Dec and Espey (Dec and Espey, 1995) used the LII method to study the early soot development in the combustion chamber of a direct injection diesel engine. Other technique includes the Laser Induced Fluorescence (LIF) which utilises the laser radiation absorption principle to excite molecules to higher energy levels.

Point measuring techniques such as Laser Doppler Velocimetry (LDV) measures the target speed by comparing the scattered light and reflective wave off a target with the original light as used by Coghe (Coghe and Cossali, 1994; Coghe, 2000) and Araneo et al. (Araneo et al., 1999). Baritaud et al. (Baritaud et al., 1994) used the LDV techniques to measure the field velocity of the air in an optical model engine. Particle Image Velocimetry (PIV) records the images obtained from illuminated particle by a double-pulsed sheet of light and analysis by a spatial autocorrelation of small regions of the image. Kozma and Farrell (Kozma and Farrell, 1997) used the PIV method to study the air entrainment into transient diesel spray while in a separate study, Rajalingam and Farrell (Rajalingam and Farrell, 1999) used PIV to investigate the effect of injection pressure on the air entrainment in the diesel spray. Laser Doppler Anemometry (LDA) and Phase Doppler Anemometry (PDA) used a photomultiplier to detect light scattered by the particle to measure their sizes. Pitcher and Wigley (Pitcher and Wigley, 1994) used two-component PDA system to determine the axial and radial velocity components as well as drop size of evaporating diesel sprays. Other researchers such as Payri et al. (Payri et al., 1996), and Yoda and Tsuda (Yoda and Tsuda, 1997) used PDA method to measure the droplet sizes at different sections of non-evaporating fuel sprays.

In direct injection (DI) diesel engines, the performance of the engine is influenced significantly by the 'quality' of the fuel sprays and the preparation of the spray with the compressed air charge due to the propagation and distribution of the fuel in the combustion chamber. Improvement of the fuel characteristic such as spray penetration, spray dispersion, drop size distribution and velocity in turn determine the diesel combustion process and the associated formation of pollutants. Hence, a fundamental understanding of the fuel spray structure and spray combustion in diesel engine are essential and are the main focus goal for diesel engine improvements.

2.2 FUEL SPRAY STRUCTURE

The liquid fuel is injected by the fuel injection system at high pressure through one or more nozzles in the injector tip towards the end of the compression stroke. As the liquid fuel jet leaves the nozzle, the high-speed jet flow becomes turbulent, causing the jet to spread out forming stream wise vortices that entrain and mix with the surrounding air. The shape of this spray and how it evolves with time is characterised by its penetration and cone angle. Researchers such as Heywood (Heywood, 1988), Hiroyasu and Arai (Hiroyasu and Arai, 1990), Pitcher and Wigley (Pitcher and Wigley, 1994), and Yule and Salters (Yule and Salters, 1995) have suggested that close to the nozzle, there is a finite length of a narrow liquid column which is known as the break-up length. Other researchers such as Gülder et al. (Gülder et al., 1992) and Arcoumanis et al. (Arcoumanis et al., 1999) argued that the spray is fully atomised at the exit of the nozzle. A conceptual model of a diesel fuel spray is shown in Figure 2.2. Assumptions of the fuel spray initial conditions at the nozzle exit and the spray development thereafter, based on a spray model concept, are essential in spray modelling.

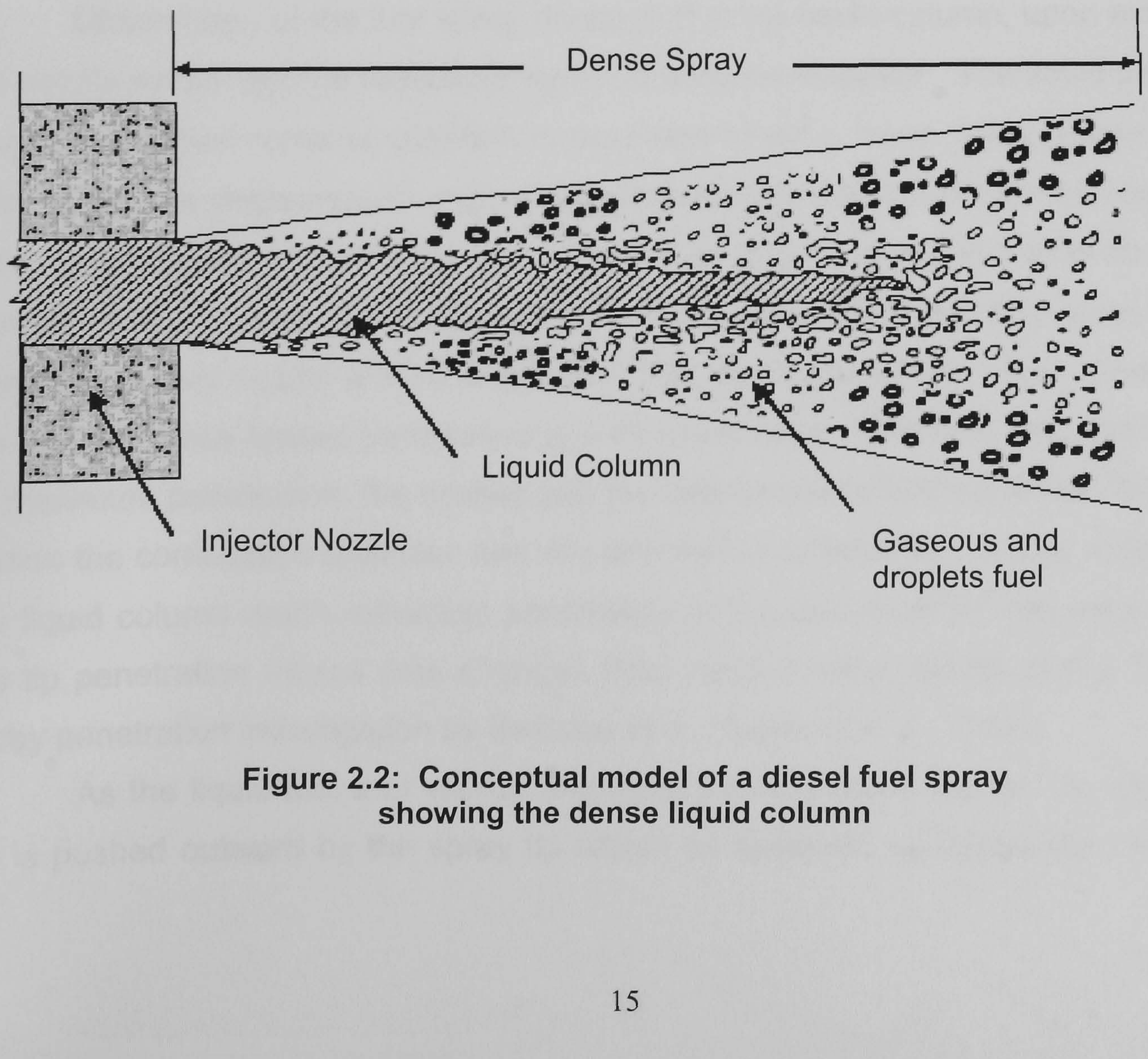

Figure 2.2: Conceptual model of a diesel fuel spray showing the dense liquid column

Determination by experiments of the exact length of this liquid column is extremely difficult since the surrounding spray near the injector nozzle is optically dense. In addition, the type of injection system employed and the injection condition, i.e. transient or steady conditions, may produce significant differences between the two cases. However, investigation using the conductivity probe technique by Yule and Salters (Yule and Salters, 1995) had detected the existence of a break-up length of the order of 100 or more nozzle diameters. The investigation involved the use of two different single hole injectors for liquid of different viscosity and density injecting into engine condition gas density. Their results showed that the break-up length increases with increase in liquid viscosity and reduces with increase in gas density. Similarly, laser diagnostic technique such as two-component PDA system by Pitcher and Wigley (Pitcher and Wigley, 1994) was employed to measure the velocity and drop size from a single hole sac type nozzle in a single cylinder research diesel engine. Their results also showed the presence of non-contiguous liquid column composed of several ligament structures close to the nozzle exit. The existence of a dense liquid column region may favour higher soot formation rates due to rich mixtures and minimal air penetration. In addition, the structure of the liquid column length and liquid phase geometries close to the injector nozzle is important in determining the major dynamic mechanisms responsible for the liquid core disintegration and the subsequent atomisation of the liquid jet as indicated by Lee and Mitrovic (Lee and Mitrovic, 1996).

Observation of the fuel spray revealed that the liquid column, upon exiting from the nozzle would reach a maximum liquid penetration distance. The liquid penetration length would then remains constant or oscillates about a mean value before cease to exist about one degree crank angle (^{o} CA) towards the end of injection as observed by Ricart and co-workers (Ricart et al., 1997). This phenomenon was also observed by Kosaka et al. (Kosaka et al., 1992) in their investigation of diesel fuel spray structure using single hole nozzle and by Espey and Dec (Espey and Dec, 1995). Even though the liquid fuel has limited penetration into the combustion chamber, and after reaching its maximum penetration, the droplet and the vapour phase fuel continues to penetrate across the combustion chamber and mix with the in-cylinder air. It was observed that the liquid column reach maximum penetration in the gas at about the same time that the tip penetration versus time changes from rapid to slow, similar to the findings of spray penetration investigation by Baritaud et al. (Baritaud et al., 1994).

As the liquid fuel and vapour propagates axially along the jet, the surrounding air is pushed outward by the spray tip region as observed by Rajalingam and Farrell

(Rajalingam and Farrell, 1999). Araneo et al. (Araneo et al., 1999) and Coghe (Coghe, 2000) observed that the air behind the tip is then recirculated and entrained into the spray side, almost perpendicular to the axis of the spray as shown by the flow field around the spray from PIV measurement in Figure 2.3. The outer surface of the jet breaks up into drops of different sizes due to droplet spreading and the formation of vortex structures in the spray periphery. The drops rapidly mix with the in-cylinder air as they move away from the nozzle, resulting in the mass of air within the spray to increase, causing the spray to become progressively wider as it moves downstream, thus forming a cone-shaped spray. Kozma and Farrell (Kozma and Farrell, 1997) found that air entrainment was responsible for the first stage of the mixture formation and the completeness of the fuel-air mixing affects the spray combustion during the early and main diffusion periods which in turn determines the combustion heat release rate and, formation of nitrogen oxides and soot in the exhaust gas.

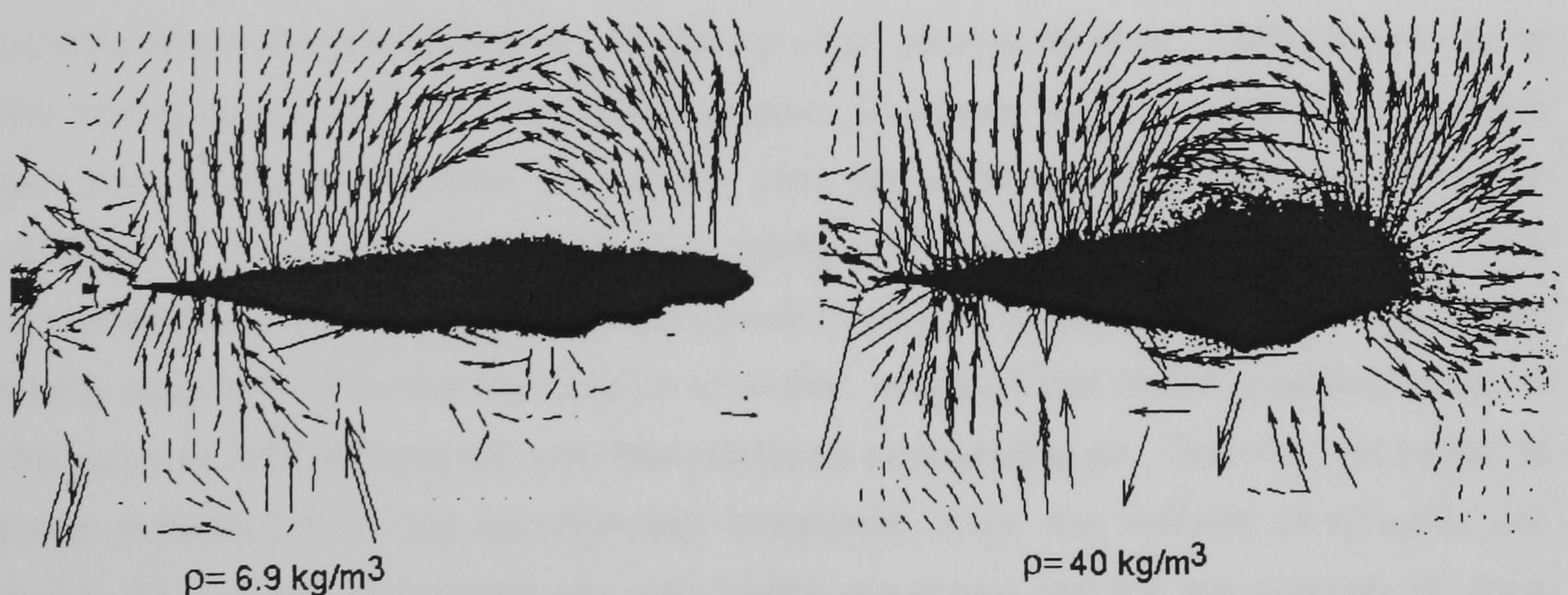

Figure 2.3: PIV flow field for two different gas density showing air being entrained into the spray behind the spray tip
Source from (Araneo et al., 1999)

2.3 FUEL JET ATOMISATION

As the liquid fuel jet penetrates into the combustion chamber, the jet disintegrates into large number of small droplets. Due to further droplet break-up, the size decreases rapidly within a short distance from the nozzle and then gradually increases. Gong et al. (Gong et al., 1992) observed this phenomenon during the investigation of droplet size distribution in a heated constant volume bomb. Reitz and Diwakar (Reitz and Diwakar, 1987) also proved this phenomenon by computations of their spray break-up model. However, investigation into the drop size distribution in the fuel spray by DiGiorgio et al. (DiGiorgio et al., 1995) had showed the existence of an internal zone inside the spray which is made of droplets of smaller diameter. In this zone, the droplet diameter tends to increase with downstream distance on the spray axis and decreases with radial distance as reported by Arcoumanis et al. (Arcoumanis et al., 1997). This phenomenon occurs because the fuel droplets in the mixing regions have different behaviour than those in the main jet region due to different aerodynamic interactions with the surrounding gas. The mixing region is the region around the spray periphery whereas the main jet lies inside the spray. Payri et al. (Payri et al., 1996) found that fuel injection conditions and gas density are the controlling parameters to the phenomenon. Kuniyoshi et al. (Kuniyoshi et al., 1980) found that in the mixing region, the velocities of the droplets are slower and the numbers of droplets per unit volume are smaller than in the main jet region. Similar findings were also obtained by Araneo et al. (Araneo et al., 1999). DiGiorgio et al. (DiGiorgio et al., 1995) reasoned that the leading droplets are decelerated due to the aerodynamic drag of the nearly stagnant air in the combustion chamber, whereas the droplets behind those in the spray tip interact and mix with the entrained surrounding air. The main jet region is more protected from the aerodynamic resistance, thus, the velocity of droplets are faster, the number of droplets per unit volume are larger and the surrounding air does not readily entrain as much as in the droplets around the main liquid region. As a result, the droplets in the wake of the preceding region propagate to the leading edge at higher velocities as observed by Ahmadi-Befrui et al. (Ahmadi-Befrui et al., 1991) and Winklhofer et al. (Winklhofer et al., 1993). Chang and Farrell (Chang and Farrell, 1997) reported that the fuel concentration of the leading edge of the spray increases when moving away axially from the injector when bigger droplets are formed due to the coalescence.

2.4 FUEL BREAK-UP MECHANISMS

There are several reasons which could be the cause for the liquid fuel jet to break up. However, the break-up of liquid is not only caused by a single factor such as the aerodynamic unstable wave growth theory but could also be due to a combination of other factors such as liquid cavitation and turbulence induced in the nozzle hole. One of the main reasons for the injected fuel jet to break-up is due to the aerodynamic interaction between the ambient gas and the fast moving liquid drop that leads to the rapid growth of unstable waves on the surface of the liquid jet as observed by Reitz et al. (Reitz and Bracco, 1982; Reitz and Diwakar, 1987) and reported also by Lee and Mitrovic (Lee and Mitrovic, 1996). This is known as the Kelvin-Helmholtz instability which is a result from velocity shear between the interfaces of two fluids moving with different speeds causing wrinkle or waves to be formed on the liquid surface. Another reason could be due to the liquid jet turbulence within the nozzle itself caused by the variations of the injection velocity, or by the radial component of velocity in the turbulent flow which can also contribute to the immediate disruption of the jet at the nozzle exit. Studies on the flow structure in the nozzle hole by Arcoumanis et al. (Arcoumanis et al., 1999; 2000), Dan et al. (Dan et al., 1997b), Gülder et al. (Gülder et al., 1992) and Soteriou et al. (Soteriou et al., 1995) revealed that the flow in multi-hole injectors is a cavitating two-phase flow and this cavitation phenomenon affects the atomisation process. Initiation of cavitation in the nozzle could also be due to the geometry of the nozzle such as imperfection of manufactured nozzle inlet, or a sharp corner of the nozzle inlet as observed by Spikes and Pennington (Spikes and Pennington, 1959).

The process of atomisation has always been a debatable issue in diesel engine fuel spray studies. Faeth (Faeth, 1990) suggested that, in steady pressure-atomised diesel sprays, the dense spray region may consists of an intact liquid core that is surrounded by a multiphase mixing layer that begins at the injector exit. The atomisation progresses by primary break-up at the liquid surface forming droplets through stripping from boundary layers on the rippled liquid core surface, followed by a secondary break-up of ligaments and large drops. Whereas, in the unsteady diesel spray, the fuel spray is a transient jet that does not behave like the steady spray and is different to the steady jet in many aspects. Gülder et al. (Gülder et al., 1992) believed that the highly transient nature of the diesel spray ensures rapid and complete atomisation of the fuel at the nozzle exit, and this effect could be more significant with

very high flow rates as in new modern fuel injection system. The most acceptable mechanisms for liquid core disintegration that are found in the literature have been ascribed to three of the followings, all of which contribute to the atomisation of the liquid fuel, aerodynamic-induced atomisation, liquid jet turbulence-induced atomisation and the cavitation-induced atomisation.

2.4.1 Aerodynamic-Induced Atomisation

The aerodynamic break-up is initiated by primary break-up of the liquid jet, caused by forces such as the development of aerodynamically-induced waves on the liquid surface of the jet. These waves, generated by the relative motion between the in-cylinder gas and the injected fuel, produce instability, known as Kelvin-Helmholtz instability, on the liquid surface. Bayvel and Orzechowski (Bayvel and Orzechowski, 1993) found that this instability increases in amplitude downstream from the nozzle. The stripping of the boundary layers from the liquid core surface during the primary break-up is accompanied by secondary break-up of sheets or ligaments, and finally into smaller drops as described by Lefebvre (Lefebvre, 1989). The aerodynamic break-up theory predicts an intact length of liquid jet extended far downstream of the nozzle, based on the assumption that the unstable waves need a certain time to grow in amplitude until they reach the critical amplitude necessary for droplet formation. Bayvel and Orzechowski (Bayvel and Orzechowski, 1993) and Bergwerk (Bergwerk, 1959) concluded that injection pressure, injection velocity, the liquid properties and the in-cylinder charge conditions are the factors determining the aerodynamic-induced atomisation process.

2.4.2 Turbulence-Induced Atomisation

Liquid turbulence is a possible contributor to the disintegration and atomisation process of the diesel sprays. The kinematic viscosity ratio between the fuel and the ambient gas determine the shearing phenomena to the turbulent liquid jet. The initial perturbations on the liquid jet surface are induced by the jet internal turbulence that originates from the strong shear stress along the nozzle wall and the growth of these perturbations with time leads to liquid atomisation. Lefebvre (Lefebvre, 1989)

suggested that the turbulence in the liquid is also due to the radial velocity component of the jet flow which break the surface of the jet at the nozzle exit when the surface tension forces restraining them no longer exist. However, Faeth (Faeth, 1990) suggested that turbulence-induced atomisation is probably not a major feature of most practical dense spray.

2.4.3 Cavitation-Induced Atomisation

Another view of the break-up process is the liquid disintegration due to cavitation inside the nozzle of the fuel injector. Several mechanism of liquid disintegration due to cavitation can be found in the literature. The study of cavitation in the nozzle hole of a diesel injector goes back as early as Bergwerk (Bergwerk, 1959), and Spikes and Pennington (Spikes and Pennington, 1959), whose results are used as the basis for hypothesis on nozzle cavitation by later researchers. Bergwerk (Bergwerk, 1959) investigated the flow in spray holes particularly the effects of flow contraction from the sac volume into injection hole using transparent scaled-up model. He argued that the turbulent velocity component within the jet that was attributed to the spontaneous break-up are not of sufficient magnitude in the relevant Reynolds number range of interest to explain the atomisation phenomena. Through his observation, he found that large amplitude pressure disturbances in the flow created by liquid cavitation inside the nozzle could lead to the atomisation of the liquid jet as it emerges from the nozzle hole. For high discharge velocities, Bayvel and Orzechowski (Bayvel and Orzechowski, 1993) observed that the pressure of the liquid inside the nozzle orifice drops to the value of the liquid vapour pressure causing vapour bubbles to form in the nozzle. These bubbles are carried with the liquid to the nozzle exit, and upon exiting the orifice, the cavitation bubbles collapse in the liquid, generating pressure waves that cause initial perturbation of the liquid jet. Spikes and Pennington (Spikes and Pennington, 1959) found that cavitation is associated with sharp corners of the orifice that cause high velocities in the moving liquid stream. These high velocities produce a local region of low static pressure at the inlet region of the orifice. Dissolved air will be released from the liquid or vapour bubbles will be formed when the static pressure is sufficiently low and this will in turn cause changes in the density and viscosity of the flow which may produce variations in the flow rate and influence the jet break-up process.

In the investigation done by Reitz and Bracco (Reitz and Bracco, 1982), they found that cavitation is present in all those cases in which jet atomisation was found to occur close to the nozzle. They hypothesised that the collapse of cavitation bubbles within the nozzle would produce large velocity fluctuations which then on exit from the nozzle cause the initial perturbation of the liquid jet. However, they concluded that cavitation could not be the only mechanism of liquid jet atomisation.

Hiroyasu and Arai (Hiroyasu and Arai, 1990) in their summary of previous reported experiments results, defined the disintegration of a liquid column that is broken up into a fine spray which appeared immediately as the liquid was injected from the nozzle, as a complete spray. They reasoned that the liquid column disintegration was initiated directly by an internal turbulence in the nozzle hole caused by cavitation and subsequently after the nozzle exit by a shear force due to high relative velocity between the liquid and the surrounding air.

Cavaliere et al. (Cavaliere et al., 1989) however, commented that different atomisation regimes have to be considered in order to justify the wide spectrum of two-dimensional scattering patterns of the sprays recorded very close to the nozzle hole. Their analysis of the unsteady diesel spray was made possible by employing two-dimensional laser light scattering diagnostics and imaging intensification systems. They suggested that the atomisation process could be represented by several serial atomisation processes which occur at different distance from the nozzle. The atomisation of the fuel just after the nozzle exit at the beginning of the needle lift could be the result of micro explosion due to expansion undergone by the two-phase flow through the nozzle hole. When the needle has completely lifted, the atomisation is due to the greater instability of the accelerating liquid column, while a significant increase of cavitation due to the narrowing of the liquid passages as the needle goes down is attributed for the continuous atomisation of the liquid fuel.

The same results were also observed by Kosaka et al. (Kosaka et al., 1992) during their investigation of the dense spray structure using two-dimensional imaging techniques. They found that the disintegration of the liquid occurs in the vicinity of the nozzle orifice. They concluded that aerodynamic interaction between the liquid and gas phase is not the only caused of liquid atomisation but also by other factors such as cavitation of liquid in the nozzle orifice and instability of the liquid flows.

Further investigations into the dense internal spray structure of the transient diesel sprays were carried out by Gülder et al. (Gülder et al., 1992) and Smallwood et al. (Smallwood et al., 1994) using laser diffraction and laser sheet illumination

techniques. Their results showed that the spray is completely atomised at the nozzle outlet without evidence of an intact liquid core for the range of the peak injection pressure studied. Gülder et al. (Gülder et al., 1992) reasoned that the first out flowing material of the nozzle is already a two phase medium and readily atomised as it exits from the nozzle hole. When the sac chamber is completely filled with liquid fuel, the liquid column exiting from the nozzle hole quickly atomises in front of the nozzle tip due to the very strong disturbances originating from the highly transient pressure dynamics of the diesel injector and the aerodynamic shear forces.

Soteriou et al. (Soteriou et al., 1995) found that cavitation in diesel fuel injection equipment is caused by two different mechanisms which they referred to as dynamically induced cavitation and geometry induced cavitation. Their observation are based on results obtained from experiments using real sized nozzle and also scaled up acrylic models of 20 times normal size. Dynamically induced cavitation is said to arise when the sudden decrease in pressure, due to pressure wave activity or valve movement, falls below vapour pressure in certain locations in the nozzle. This will cause small bubbles of vaporised fuel and undissolved air to form and under more severe situation, some of the bubbles will coalesce to form voids or pockets of gas. Whereas, geometry induced cavitation is said to be initiated by high velocity fluid flow created by sudden changes in flow path geometry which resulted in significantly large reduction in local pressure along the region, thus, forming vapour bubbles in these critically low pressure regions.

The investigation using transparent glass nozzle of the same size as in diesel injectors by Chaves et al. (Chaves et al., 1995) agrees in many aspects with the results from Soteriou et al. (Soteriou et al., 1995) investigations. They observed that diesel sprays atomised directly at the nozzle exit due to cavitation in the nozzle hole. The onset of cavitation at the inlet corner of the nozzle is caused by small imperfections of the nozzle inlet and with increasing injection pressure, the cavitation reaches the nozzle exit.

The cavitation phenomena was also confirmed to occur in the nozzle of transparent models as reported by Dan et al. (Dan et al., 1997b) during their direct observation of the fuel flow inside the acrylic models. They proposed that a twin vortex of fuel flow produces a main flow in the sac chamber and the main flow is contracted in the centre region of the sac chamber. This main flow is sheared with the vortex flow, which then generates turbulence in the sac region. At large pressure differences between the injection pressure and the ambient pressure, the separation due to the

shearing would occur at the edge of the hole inlet. At larger pressure differences, cavitation bubbles are initiated at the needle valve seat region which would dominate the sac chamber at further increase in pressure differences.

During Lai et al. (Lai et al., 1998) investigation of the high pressure spray characteristics of valve covered orifice (VCO), they found that the spray angle does not correlate very well with injection pressure. They hypothesised that the behaviour could be due to oscillation of cavitation bubble inside the injector. Later, their observation of the microscopic photographs taken, showed fine fuel mist at the nozzle exit, confirming cavitation-enhanced break up mechanism.

Arcoumanis et al. (Arcoumanis et al., 1999; 2000) and Afzal et al. (Afzal et al., 1999) performed extensive comparison between computational and experimental results for the temporal and spatial variation of the spray characteristics. Their observation of flow characteristics in the nozzle of an enlarged transparent model of a multi-hole sac type nozzle and VCO nozzle, and on real size optical nozzle revealed that there exist cavitation film regimes in the nozzle which was initiated at the entrance of the nozzle hole. They also observed a more complex flow structure, the formation of cavitation strings connecting adjacent hole in their investigation on both the enlarge nozzle models and the real size nozzle. The interaction of these cavitation strings and the cavitation films in the nozzle hole enhances the flow turbulence in the liquid. They concluded that hole cavitation, injection velocity and droplet deformation are the dominant parameters influencing diesel spray development and fuel-air mixing.

Therefore, the dense core of the diesel fuel spray close to the nozzle hole tip of a modern diesel engine, which was regarded as a liquid column having certain penetration length was now found to be a fully atomised spray. The spray is made of two phase medium consisting of, part vaporised fuel and air mixture and part liquid fuel droplets. The findings were further proven recently, by a research team from Argonne Research Laboratory in collaboration with Wayne State University and Robert Bosch GmbH using high-brilliance Advance Photon Source (APS) x-rays. The data obtained on the structure and behaviour of high pressure diesel sprays as close as 3 nozzle diameter from the nozzle revealed that there is no intact liquid column near the nozzle, as was reported by Sekar (Sekar, 2000) and Powell et al. (Powell et al., 2001). It is believed that cavitation mechanism could be the major cause of liquid fuel atomisation in modern, multi-hole, high pressure fuel injection system.

2.5 FUEL SPRAY PENETRATION

The extent to which the spray tip penetrates is directly dependent upon the pressure differential across the nozzle orifice, the density ratio between the liquid fuel and the gas surrounding the spray, the gas temperature and the nozzle orifice diameter. Experimental measurement of liquid spray penetration in the laboratory at condition close to the combustion chamber condition in diesel engine was observed to be short. Espey and Dec (Espey and Dec, 1995) investigation using a multi-hole injector in a single cylinder, DI optical engine found that the maximum penetration length of the liquid fuel varies between 13 to 30 mm depending on the ambient gas density and gas temperature condition in the chamber. They concluded that the penetration length decreases with increase in temperature and also increase in the charge density. Similar results were also observed by Ricart et al. (Ricart et al., 1997), when using a multi-hole injector in a single cylinder, DI engine equipped with endoscope imaging system. These values give close agreement with calculated values using the correlation available in literature.

Several correlations have been suggested to determine the spray penetration distant, S. An early formula developed by Dent (Dent, 1971) based on coaxial gas jets theory is given by;

$$S = 3.07\left[\left(\frac{\Delta P}{\rho_g}\right)^{0.5} \cdot t\, d_o\right]^{0.5}\left(\frac{294}{T_g}\right)^{0.25} \quad \text{(m)} \qquad (2.1)$$

Where S is the spray tip penetration (m), ΔP is the pressure drop across the nozzle (Pa), t is the time after start of injection (s), d_o is the nozzle diameter (m), ρ_g is the charge gas density (kg/m^3), and T_g is the charge gas temperature (K).

Chiu et al. (Chiu et al., 1976) in their spray mixing model, proposed a spray tip penetration correlation by assuming that the spray behaves as a turbulent gaseous jet. This correlation is written as;

$$S = \left[\frac{450 \cdot {d_o}^{0.5}\left(\rho_f / \rho_d\right)^{0.4}}{\left(1+\rho_g/\rho_{atm}\right)^{0.8}} \cdot \left(\frac{\rho_g}{\rho_{atm}}\right)^{0.5}\left(\Delta P\right)^{0.25}\right] \cdot t^{0.6} \quad \text{(in)} \qquad (2.2)$$

Where ρ_f, ρ_d, ρ_{atm} are the reference fuel density, the diesel fuel density and the atmospheric air density (lbm/in^2) respectively. Note also the unit for d_o is inches and ΔP is lbf/in^2.

Hiroyasu and Arai (Hiroyasu and Arai, 1990) found that initial spray penetration is proportional to time with no dependency on gas density whereas at later stages, the spray penetration distance is proportional to the square root of time and proposed their correlation for spray penetration as follows;

$$0 < t < t_b \qquad S = 0.39\left(\frac{2\Delta P}{\rho_l}\right)^{0.5} \cdot t \qquad \text{(m)} \qquad \text{(2.3a)}$$

$$t > t_b \qquad S = 2.95\left(\frac{\Delta P}{\rho_g}\right)^{0.25} \cdot (t d_o)^{0.5} \quad \text{(m)} \qquad \text{(2.3b)}$$

where ρ_l is the injected liquid density (kg/m^3) and t_b is break-up time (s) given by ;

$$t_b = \frac{28.65\,\rho_l d_o}{(\rho_g \Delta P)^{0.5}} \quad \text{(s)}$$

All three correlations agree to the spray tip penetration dependence on the injection pressure of 1/4th power. As for the gas density, correlation (2.2) provided a different value while correlation (2.3a) shows no dependence on gas density prior to break-up. Naber and Siebers (Naber and Siebers, 1996) found that higher gas density has an effect on the spray tip penetration as a result of increase in spray dispersion due to increase in air entrainment in the spray. They derived theoretical penetration correlations for non-evaporating spray using characteristic penetration time and length scales to account for the effects of spray penetration through dispersion. Close agreement between the experimental results on the effects of gas density on non-evaporating spray and the proposed correlation were also found by Araneo et al. (Araneo et al., 1999). They also derived a time scale and a length scale which are

very similar to the ones derived by Naber and Siebers (Naber and Siebers, 1996) to better fit the results. The correlation by Naber and Siebers (Naber and Siebers, 1996) given in equation (2.4) also took into account that the initial spray penetration period will also be affected by the injector tip design through the velocity coefficient, C_v and the injector opening time.

$$S = \left[\frac{C_v (2C_a)^{0.5}}{a\,\boldsymbol{tan}(\theta/2)}\right]^{0.5} \left(\frac{\Delta P}{\rho_g}\right)^{0.25} \cdot (t\,d_0)^{0.5} \quad \text{(m)} \tag{2.4}$$

Where $\boldsymbol{tan}(\theta/2)$ is the tangent of the spray dispersion half angle, C_v is the velocity coefficient, C_a is the area contraction coefficient, and a is the arbitrary constant.

In general, research has shown that the fuel spray tip penetration was strongly affected by the ambient gas temperature and density. Increasing any one or a combination of these effects, will cause a decrease in the spray penetration. Increasing gas temperature in the combustion chamber leads to a decrease in spray penetration mainly due to increase in the evaporation rate of the fuel as found by Espey and Dec (Espey and Dec, 1995), Zhang et al. (Zhang et al., 1997) and Larsson (Larsson, 1999). Increasing air density causes an increase of the drag forces which in turn reduces the penetration velocity and thus penetration length of the spray. Naber and Siebers (Naber and Siebers, 1996) found that the spray dispersion increases with increase in air density due to air entrainment into the spray. Similarly, Espey and Dec (Espey and Dec, 1995) found that increase in air density also increases the fuel and air mixing rates.

While increasing ambient pressure enhances atomisation of the fuel causing shorter penetration length as observed by Larsson (Larsson, 1999) and Zhang et al. (Zhang et al., 1997), extensive investigation on the effects of these parameters on the liquid phase of the fuel by Siebers (Siebers, 1998) also showed remarkably similar trends. Gong et al. (Gong et al., 1992) results of smaller droplet diameter at higher injection pressure, is another indication of improved atomisation. Verhoeven et al. (Verhoeven et al., 1998) found that the spray dispersion decreased strongly as the injection pressure was increased, particularly at high gas density. However, they found

that injection pressure has minor effect on spray penetration. Similar results were also observed by Zhang et al. (Zhang et al., 1997).

As for the effects of nozzle geometry on spray penetration, researchers such as Yoda and Tsuda (Yoda and Tsuda, 1997), Zhang et al. (Zhang et al., 1997) and Verhoeven et al. (Verhoeven et al., 1998) found that, reducing nozzle orifice diameter effectively reduces the spray penetration due to improvement in atomisation. In addition, Ishikawa and Zhang (Ishikawa and Zhang, 1999) found that air entrainment into the fuel spray increases with smaller nozzle orifice.

2.6 FUEL SPRAY DISPERSION AND EVAPORATION

Dispersion of the liquid fuel is a direct result of atomisation and has an influence on the spray penetration length and later to the evaporation of the liquid fuel droplets. The dispersion of the liquid fuel is normally measured by the spray cone angle, θ_s. Ambient gas and fuel properties are indisputable parameters that strongly affect the fuel spray cone angle. The spray cone angle was found to increase as the ambient gas density increases as observed by Naber and Siebers (Naber and Siebers, 1996), and by Espey and Dec (Espey and Dec, 1995) as a result of better atomisation due to the increase in drag forces. Similar results were also shown by Dan et al. (Dan et al., 1997a), Hiroyasu and Arai (Hiroyasu and Arai, 1990), and Kosaka et al. (Kosaka et al., 1992). The overall spray cone angle is wider as ambient gas temperature increases due to increase in hot air being entrained into the spray causing faster evaporation, whereas the liquid part of the spray was found to decrease with increase in ambient gas temperature as observed by Verhoeven et al. (Verhoeven et al., 1998). In general, an increase in fuel spray dispersion causes a corresponding reduction in spray penetration length. Nozzle parameters such as smaller orifice diameter (d_o), larger ratio of orifice length to diameter (l_o/d_o) and nozzle configuration are other contributing factors that increase the spray cone angle as investigated by Dan et al. (Dan et al., 1997b). On the effects of increasing the nozzle aspect ratio (l_o/d_o), Tsunemoto et al. (Tsunemoto et al., 1999) showed that there is an increase in spray penetration with a decrease in spray cone angle due to the increase in exit velocity. Nozzle inlet conditions such as nozzle orifice having sharp or round inlet was found to have an

influence on the spray characteristics or break-up process due to the flow characteristics in the nozzle. Chang and Farrell (Chang and Farrell, 1997) observed that, a nozzle having an orifice with sharp inlet was found to produce longer penetration in the initial part of the injection and a wider spray cone angle as compared to rounded inlet nozzle. The flow characteristics such as liquid velocity at exit of the nozzle orifice, the velocity distribution and the level of turbulence in the nozzle also have an effect on the spray cone angle as reported by Arcoumanis et al. (Arcoumanis et al., 1997). However, Payri et al. (Payri et al., 1996) found that the spray cone angle of a complete atomised spray showed little dependence on injection parameters. A summary of the effects of changing certain parameters on the spray characteristics are shown in Table 2.1.

Table 2.1 The effects of several parameters on diesel spray characteristics
(*The results show the affects on spray characteristics when increase in the attributes)

PARAMETER	ATTRIBUTE	SPRAY CONE ANGLE	SPRAY PENETRATION	DROP SIZE	DROP VELOCITY
Charge Gas Conditions	Temperature	increase	decrease	decrease	decrease
	Density	increase	decrease	decrease	decease
	Pressure	increase	decrease	decrease	decrease
Nozzle Geometry	Diameter	decrease	increase	increase	increase
	Ratio, l_o/d_o	decreases	increase	decrease	increase
	Inlet Profile (Sharpness)	increase	decease	decrease	decrease
Fuel Properties	Injection Pressure	decrease	increase	decrease	increase
	Viscosity	decrease	decrease	increase	decrease
	Density	decease	increase	increase	decrease

Evaporation of the droplets takes place when heat from the surrounding hot air is absorbed through the surface of the droplets. Espey and Dec (Espey and Dec, 1995) found that the hot air entrained into the spray was the primary source of energy

for the evaporation and not the energy from the combustion. The time required for the fuel to absorb the heat to ignition creates a delay period. Since ignition temperature is higher than the evaporation temperature, a further delay takes place before combustion begins. Thus, the smaller the droplets, the shorter the time for evaporation to be completed. The ignition delay was also shorter with increase in the ambient gas temperature as observed by Espey and Dec (Espey and Dec, 1995). The overall rate of evaporation depends on the pressure, temperature and density of the air; the temperature, volatility and diameter of the droplets in the spray, and the flow characteristics in the combustion chamber. Increasing the ambient density for instance, increases the mass of air entrained per mass of fuel injected causing rapid evaporation of the fuel as reported by Ishikawa and Zhang (Ishikawa and Zhang, 1999). The droplets on the outer edge of the spray will evaporate first, creating a fuel vapour-air mixture sheath around the liquid fuel. This evaporation and air-entrainment process gives rise to rapid lateral spray expansion and as the spray width increases, the leading region of the fuel spray consist of completely vaporised fuel and at the same time uniformly mixed with the air throughout the cross section. Local pockets of these vapour fuel and air mixtures along the edge of the spray later developed into ignition sites. Auto-ignition occurs at multiple sites across the regions of higher evaporation rates of the leading spray. Higher rates of injection at higher pressure produce more auto-ignition sites as well, thus enhancing the start of combustion.

2.7 AUTO-IGNITION

One important step in understanding pollutant formation in diesel combustion is through analysing the in-cylinder processes that lead to auto-ignition of the fuel-air mixture in the combustion chamber. The auto-ignition mechanism in a diesel spray is known to be one of the most complex processes of the diesel combustion stages. The engine conditions at which this auto-ignition occurs are important in determining the spatial and temporal distribution of the autoigniton in the combustion chamber. Edwards et al. (Edwards et al., 1992) visualised the combustion processes and auto-ignition in an optical access constant-volume vessel. Combustion luminosity was measured using photodiodes while photographic data were obtained using the

schlieren method. Baritaud et al. (Baritaud et al., 1994) investigated the spray and auto-ignition phenomena using laser induced exciplex fluorescence and Mie scattering techniques through an optical access single-cylinder engine having a pancake combustion chamber. While Dec and Espey (Dec and Espey, 1995) studied the ignition and early combustion of the optical single-cylinder, DI diesel engine having an elongated piston by imaging the natural chemiluminescence using a calibrated intensified video camera.

Ignition is governed by the local formation of fuel vapour, caused by the heat transfer from the in-cylinder air into the spray region and by its propagation during the delay period. The appearance of luminous emissions or chemiluminescence from the burning gases is an indication of chemical activity in the combustion chamber which can serve as a marker of the auto-ignition sites as suggested by Edwards (Edwards et al., 1992), Baritaud et al. (Baritaud et al., 1994), and Dec and Espey (Dec and Espey, 1995). During the initial injection of the liquid fuel, the fluid mechanics of the fuel jet is considered to be not affected by chemical reaction. As the fuel is injected out of the nozzle, the liquid phase of the fuel penetrates across the combustion chamber. Dec (Dec, 1997) concluded that there is strong evidence that fuel vapour regions already begin to develop along the sides of this liquid fuel distribution a short distance after the start of the liquid phase penetration. Mixing structures of these fuel vapours with air due to air entrainment into the spray, begin to form along the sides of the liquid fuel and the edges of the spray jet. Downstream of the liquid fuel region, the vapour fuel and air become well mixed to a relatively uniform fuel-air mixture, which provide a favourable environment to chemical reaction. It is in these mixing structures, that the initial sites of auto-ignition occur, as reported by Ricart and Reitz (Ricart and Reitz, 1996) and this was observed to coincide with the initial rapid rise in the apparent heat release rate.

Hentschel (Hentschel, 1996) found that the first self-luminescence is observed to occur about 0.5 – 1.0° CA prior to the start of heat release rate calculated from the in-cylinder pressure trace. The locations of the first auto-ignition sites occur far downstream of the injector along the spray as reported by several authors such as Ricart and Reitz (Ricart and Reitz, 1996) and Winklhofer et al. (Winklhofer et al., 1993). On the other hand, Edwards et al. (Edwards et al., 1992) and Baritaud et al. (Baritaud et al., 1994) have reported that the location of the first auto-ignition sites are close to the liquid phase tip, around the centre of the chamber in a region of high mean shear, and often close to the nozzle. Verhoeven et al. (Verhoeven et al., 1998) found that the

ignition delay period has an effect on the location of ignition being closer to the injector tip for shorter ignition delays. These discrepancies could be due to several reasons such as the differences in the injection system used, the variation in parameter conditions at which the investigation were conducted or due to the differences in engine geometry. However, authors such as Baritaud et al. (Baritaud et al., 1994), Dec and Espey (Dec and Espey, 1995), and Ricart and Reitz (Ricart and Reitz, 1996) agreed that auto-ignition occurs almost simultaneously at multiple sites across the downstream region of the fuel jet and also randomly along the length of the spray. The ignition sites further from the injector then developed into combustion regions. The flame propagates rapidly towards the bowl of the piston, along the spray axis and spreads out radially as it reaches the bottom of the piston bowl. The auto-ignition sites were observed not to occur at the same location due to cycle-to-cycle variations, differences in the swirl ratio and amount of fuel injected. With increasing amount of fuel injected, the occurrences of multiple ignition sites increases.

In-cylinder temperature does not have a large effect on the vapour phase penetration but has significant effect on the liquid phase fuel. The liquid phase penetration is reduced with increased charge gas temperature, indicating a faster vaporisation rate. This means that the auto-ignition sites will occur closer to the injector at an earlier crank angle degree. At low temperature, the fuel jet impinges on the piston bowl wall and the auto-ignition process is influenced by the deflection of the fuel jet off the wall as observed by Winterbone et al. (Winterbone et al., 1994). Raising the fuel injection pressure causes the sprays to propagate faster and the fuel-air mixture are formed further downstream, thus ignition sites tend to shift downstream of the spray as visualised by Yamaguchi et al. (Yamaguchi et al., 1990). In addition, higher injection rates at higher pressures produce more auto-ignition sites, thus enhancing the start of combustion as reported by Henein et al. (Henein et al., 2001).

Longer ignition delays cause larger cycle-to-cycle variations for the auto-ignition sites within the mixture. Longer ignition delays also will cause more fuel impingement on the piston bowl wall, which will influence the auto-ignition process. When ignition delay is due to retarding the fuel injection timing, the location of the auto-ignition sites is shifted closer to the injector, due to the late start of injection.

Air swirl in the piston bowl due to the motion of the piston, and inward velocity flow (squish) into the bowl has significant influence on the air mixture and on the local ignition and flame propagation. Winklhofer et al. (Winklhofer et al., 1993) observed that the flow field dominates the mixing of vapour fuel and air and the further transport

of the mixture. Hentschel et al. (Hentschel, 1996) reported that the fuel vapour is shifted by the swirl flow and ignites on the leeward side of the sprays. Hentschel et al. (Hentschel et al., 1994) also observed that the auto-ignition areas grow together and finally the sprays burn completely along the shifted spray axis. Arnold et al. (Arnold et al., 1990) investigations on the effect of swirling and non-swirling flow field on the fuel spray made the following conclusions. Without swirl, the first ignition site appeared around the vapour fuel regions and then several other sites regions appear at various locations in the combustion chamber. With swirl, the first visible light appeared between the vapour fuel regions near the injector tip and continued to be concentrated in the centre of the chamber until eventually the flame spread and engulfed the sprays.

Werlberger and Cartellieri (Werlberger and Cartellieri, 1987) found that air swirl in the combustion chamber has only a minor influence on the fuel jet development at full load. They explained that at full load, the high injection pressure produces a narrow fuel jet which remains relatively unaffected by the air swirl in the combustion chamber. With increasing engine load, the injected fuel, the injection pressure and thus the amount of fuel which hits the chamber wall increase and this influences the locations for the occurrence of auto-ignition as reported by Hentschel et al. (Hentschel et al., 1994). Engine component temperature also rises with increase in engine load which affect the vaporisation rate of the fuel. Under low load conditions and with swirl, auto-ignition starts near the centre of the piston bowl, close to the nozzle. At part load, the locations are located along the spray axis from the nozzle to the combustion chamber wall. Without swirl, at low load, ignition delay is longer and ignition sites occur at location further downstream of the sprays. On the other hand, at higher load and without swirl, auto-ignition occurs earlier and the ignition sites are concentrated in a smaller region as observed by Baritaud et al. (Baritaud et al., 1994).

Arcoumanis et al. (Arcoumanis et al., 1995b) investigated the effect of EGR on auto-ignition in an optical, 1.9L, DI four-cylinder diesel engine. Their findings showed that for 0% EGR at idling speed, auto-ignition site locations are observed to be closer to the injector. Their spatial variation is also reduced and they seem to be located downstream of the sprays. With increasing EGR, the spread and sites of auto-ignition increases, which is attributed to the increase inhomogeneity of the intake charge at higher level of EGR.

2.8 COMBUSTION

Combustion of the fuel in a diesel engine is a complex process due to the irreversible and non-adiabatic cyclic processes involved. It is very difficult to explain the combustion processes to a well defined sequence of events but generally they can be ascribed to proceeds in four stages, as shown in Figure 2.4.

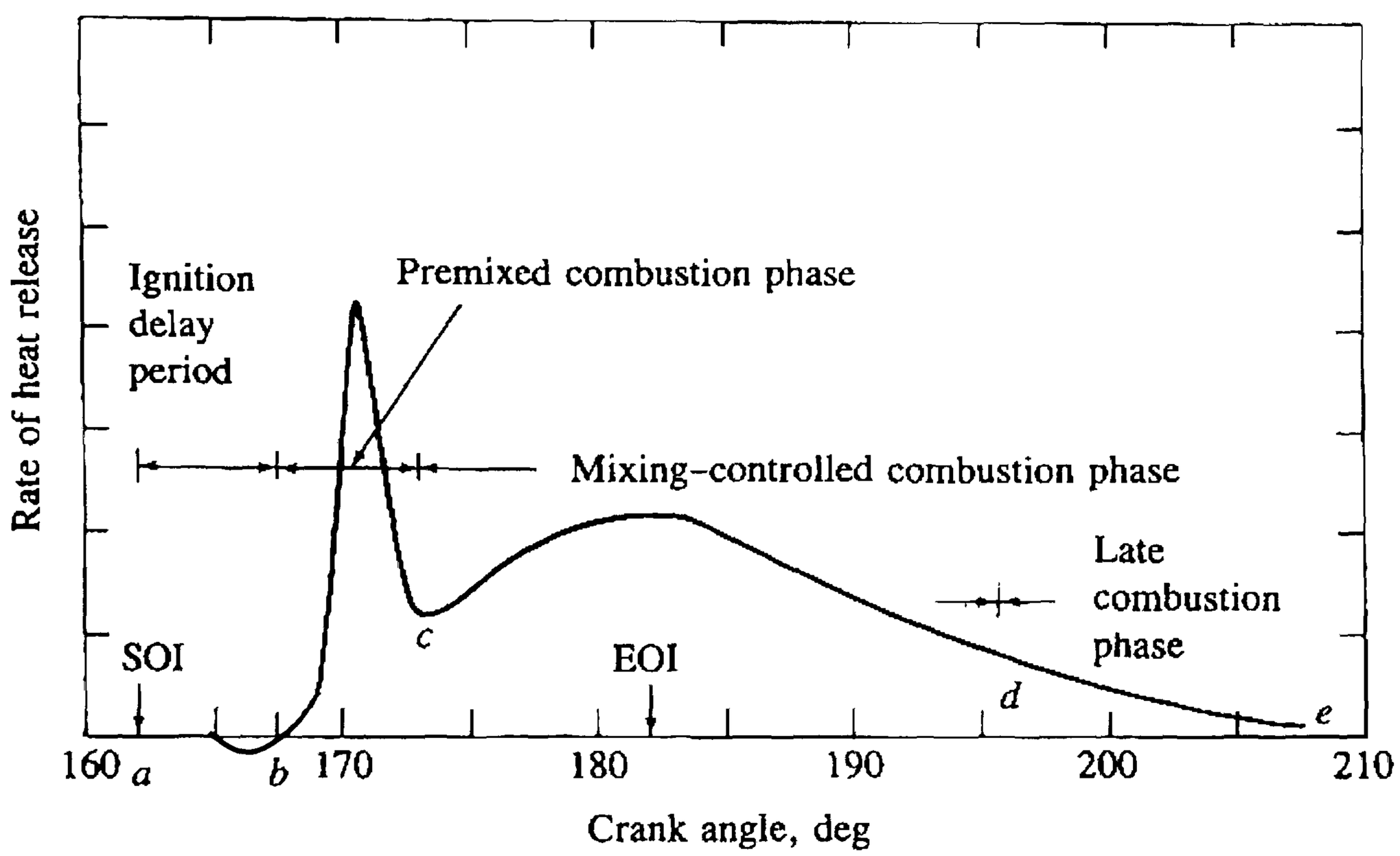

Figure 2.4: Typical combustion phases in diesel engine
Source from (Heywood, 1988)

Combustion starts after the fuel initially injected into the combustion chamber undergoes a short delay period, known as ignition delay, during which the fuel evaporates, entrains and mixes with the hot in-cylinder charge and then autoignites at numerous locations in the combustion chamber. The heat release rate curve, which is marked 'b' in Figure 2.4, first goes negative just after the start of injection (SOI) because of heat loss due to the vaporisation of the initial liquid fuel. The ignition delay

is defined as the time period between the start of fuel injection and the start of combustion (SOC). Ignition delay is an important variable in diesel combustion because it has a strong correlation to the details of the fuel preparation process, the distribution and the mixing of fuel with the air. Challen and Baranescu (Challen and Baranecsu, 1999) reported that ignition delay determine the amount of fuel that is burned in the premixed combustion phase. Longer ignition delays allow more fuel to be mixed with the air causing high heat release rate. Karimi (Karimi, 1989) acknowledged that the ignition delay is responsible for this initial combustion stage as is evident from the rate of heat release diagram. Tanin et al. (Tanin et al., 1999) observed that the subsequent large premixed charge causes a high in-cylinder burned gas temperature, resulting in higher NOx emissions.

The initial burning of the fuel and air mixture after this delay period is called the premixed combustion phase. Immediately upon auto-ignition, the mixture burns rapidly and this is characterised by a rapid heat release and a corresponding rise in pressure. The initial premixed combustion phase can be represented by the crank angle (CA) at the start of injection to approximately a few degrees CA beyond the peak heat release rate. Shundoh et al. (Shundoh et al., 1992) found that the premixed combustion proceeds very quickly and is confined to a turbulent layer on the spray periphery and was found not to exist in the fuel rich parts along the spray centre. Fuel droplet evaporation is now also influenced by the heat already released during the premixed combustion which enhances further combustible mixture formation. It is well recognised that the period prior to auto-ignition determines the amount of prepared mixture as mentioned earlier.

This is followed by a slower heat release, the diffusion combustion phase during which the burning rate is controlled by the atomisation, vaporisation and amount of fuel-air mixture being made available. Diffusion flame propagation now also occurs upstream of the ignition regime and away from the flame. Just after the end of injection with breakdown of the spray and the slower motion of droplets due to the ever decreasing injection pressure level, a combustible mixture is now also formed and burnt near the nozzle. Further motion of the flame is largely governed by the air swirl in the combustion chamber. Foster (Foster, 1985) reported that the initial and the diffusion combustion phases represent the main heat release period during which 80 percent of the total energy release are being released.

Finally there is the late combustion phase, where more complete combustion of the fuel is promoted well after the end of injection and throughout the expansion stroke.

During later stages of this combustion, the temperature in the combustion chamber has decreased to such an extent that combustion is no longer possible due to the expansion of the cylinder contents, i.e. the combustion is quenched.

Due to the heterogeneous fuel-air distribution in the combustion chamber, some fuel is pyrolysed or partly burnt during the premixed combustion and soot (carbon particles) is formed while over-mixed fuel and air in low-temperature zones produces unburned hydrocarbons. Takeda and Niimura (Takeda and Niimura, 1995), and Zhang et al. (Zhang et al., 1993) found that the oxides of nitrogen (NOx) are also formed in the local high temperature regions during this premixed combustion stage where the fuel-air mixture is near stoichiometric. On the other hand, Nehmer and Reitz (Nehmer and Reitz, 1994) found that most of the particulate matter (PM) is formed during the rich burning of the early stage of the diffusion combustion, due to a lack of available oxygen. However, most of the soot in the particulate matter is oxidised during the later diffusion combustion stage due to the heat release that continues but at a lower rate. The balance between the initial combustion stage and the following diffusion combustion stage with respect to degree of vaporisation and temperature field, is considered as a key to controlling combustion and formation of NOx and particulates. An ideal combustion curve for simultaneous reduction of NOx and particulate is shown in Figure 2.5.

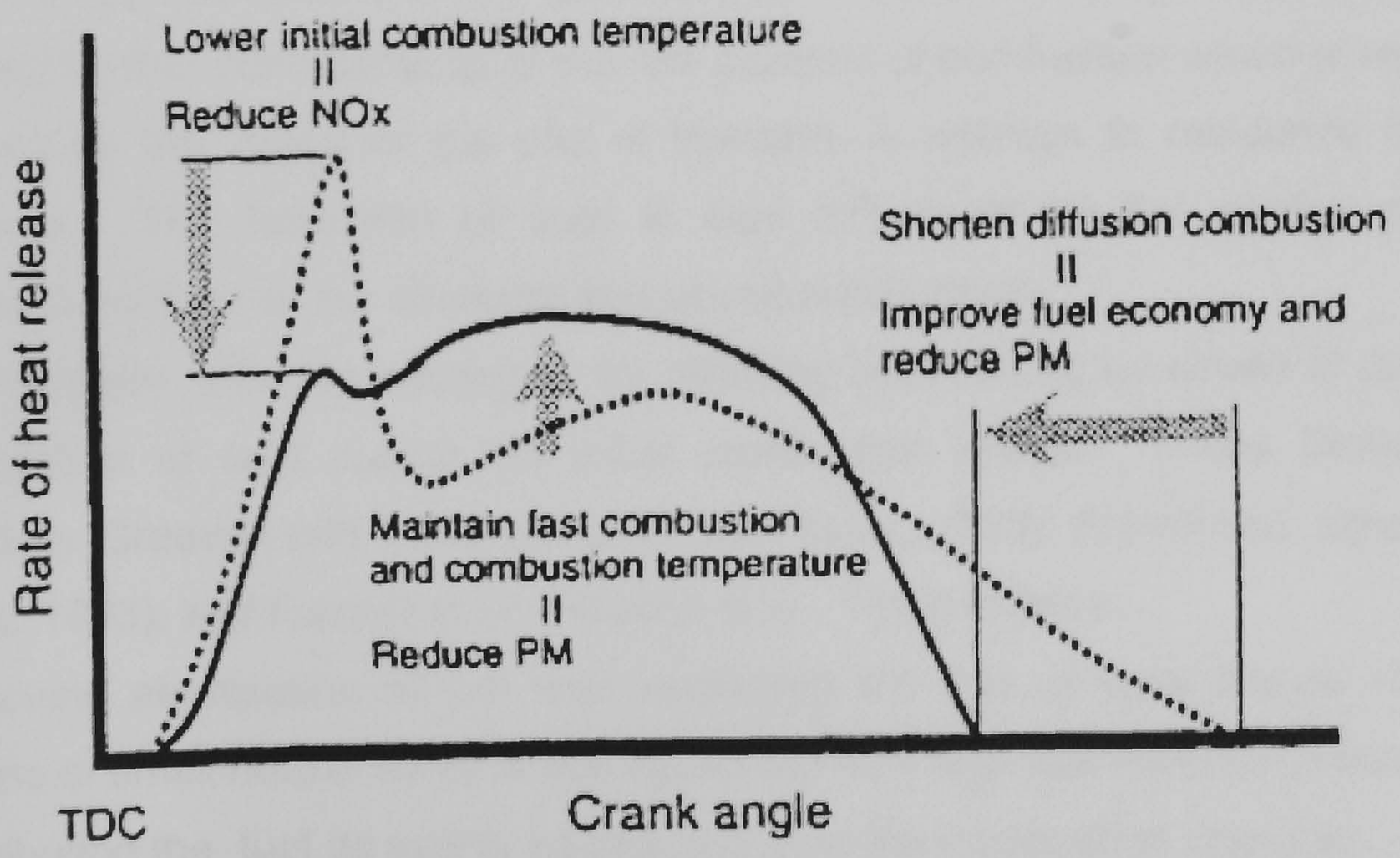

Figure 2.5: Ideal rate of heat release curve for simultaneous reduction in NOx and PM Source from (Hikosaka, 1997)

2.9 EXHAUST EMISSIONS

Soot (particulates) and nitrogen oxides are the two pollutants of most concerned about in diesel engine exhaust gas emissions due to the negative environmental and human health impact they possess. Unburned hydrocarbons and carbon monoxide on the other hand, are already low which do not create any major problem except at light loads.

2.9.1 Formation of Soot

Soot or carbon particles generated from the combustion process, ash particles from the lubricating oils, sulphates and organic soluble components from fuel and lubrication oil contribute to the total particulate mass emission in the diesel exhaust. Soot is formed early in the premixed combustion stage when the locally fuel rich mixtures are subjected to high in-cylinder temperatures. Zelenka et al. (Zelenka et al., 1990) found that, in-cylinder soot formation during combustion predominates over in-cylinder soot oxidation during the later part of the combustion. Soot produced in the early stage of the premixed combustion was very rapidly oxidised mainly due to the high temperature environment. When the temperature decreased in the expansion stroke, the oxidation of soot ceased and soot exits with the exhaust gases. Johnson (Johnson, 2000) reported that the concentration of soot in the exhaust seems to be determined by the characteristics of the late portions of combustion which is very much determined by the timing of the end of injection, in addition to residence time and temperature. The formation of soot is also influenced by the engine operating conditions in addition to the chemical and physical properties.

Therefore, effective strategies for reducing soot should be aimed at prohibiting the generation of soot during the initial combustion phase. These strategies as proposed by Greeves and Tullis (Greeves and Tullis, 1993), Karimi and Jane (Karimi and Jane, 1993), and Russell et al. (Russell et al., 1989) include:

- Improving atomisation of fuel and increasing the rate of local fuel-air mixing by means of small nozzle spray orifice combined with high fuel injection pressure.
- Distributing the fuel as evenly as possible over the combustion chamber.
- Intensive mixing of the fuel and air throughout the entire injection period.
- Avoiding excessive wall impingement of the fuel.

2.9.2 Formation of Hydrocarbons

The presence of hydrocarbons (HC) in the diesel exhaust due to incomplete combustion of the fuel-air mixture, originates from several sources in the diesel engine. It can be due to over-lean mixtures due to poor distribution of the fuel at light loads, evaporation of the liquid fuel impingement on the combustion chamber walls and bowl, fuel trapped in the crevice volumes inside the cylinder, fuel emptying from the nozzle sac volume, from flame quenching due to liquid fuel impingement on walls and from the system lubricating oil. The control mechanisms for these hydrocarbons as suggested by Greeves and Tullis (Greeves and Tullis, 1993), Heywood (Heywood, 1988) and Russell et al. (Russell et al., 1989) include:

- Complete combustion of the injected fuel.
- Suitable injection timing schedule.
- Smaller nozzle sac volume.
- Reduce lubricating oil consumption.

2.9.3 Formation of Oxides of Nitrogen

Oxides of nitrogen (NOx) refer to the mixture of nitric oxide (NO) and nitrogen dioxide (NO_2). NO is the most significant contributor to the total NOx production and Stone (Stone, 1999) reported that over 90 per cent of the NOx from the engine is NO. NOx is formed during the initial rapid combustion phase and in the main diffusion zone of combustion and is influenced by the amount of fuel injected during ignition delay, duration of the ignition delay and the peak burned gas temperature in the combustion chamber. There are three types of NOx that are formed during the combustion of fuel in a diesel engine. These are typically known as thermal, prompt and fuel NOx, and are described below.

(a) Thermal NOx

Thermal NOx is formed with the other combustion products in the high temperature regions, generating both nitrogen and oxygen atoms from the air through dissociation. The formation mechanism is given by the extended Zel'dovich mechanism which consists of the following principal reactions;

$$O + N_2 \Leftrightarrow NO + N \quad (2.1)$$

$$N + O_2 \Leftrightarrow NO + O \quad (2.2)$$

$$N + OH \Leftrightarrow NO + H \quad (2.3)$$

The NO formation rate is only significant at high temperatures (greater than 1800 K) and significant residence time. This is due to fixation of the nitrogen requires the breaking of the strong nitrogen triple bond, making it the rate-limiting step of the extended Zel'dovich mechanism.

(b) Prompt NOx

Prompt NOx is formed in the flame front where there are fuel rich layers of the premixed combustion. This rapid chemical reaction in low concentration oxygen decomposes the nitrogen molecules under the influence of hydrocarbon radicals. Borman and Ragland (Borman and Ragland, 1998) reported that prompt NOx contribution to the total NOx is very small and not significant in the diesel engine. The formation process can be described as;

$$CH + N_2 \Leftrightarrow HCN + N \quad (2.4)$$

$$C + N_2 \Leftrightarrow CN + N \quad (2.5)$$

(c) Fuel NOx

Fuel NOx originates from the oxidation of the nitrogen compounds or chemically-bound nitrogen found in the fuel and is formed during the combustion process at relatively low temperatures. The contribution of fuel NOx depends on the type of fuel used and is estimated to be small in diesel engines.

The most effective means to reduce NOx formation as suggested by Russell et al. (Russell et al., 1989), Karimi and Jane (Karimi and Jane, 1993), and Tullis and Greeves (Tullis and Greeves, 1996) include:

- Reducing the local peak flame temperature by using air charge cooling.
- Reducing the ignition delay by retarding the injection timing.
- Controlling the peak and duration of heat release by fuel injection rate shaping and air motion in the combustion chamber.
- Reducing the premixed combustion fraction by reducing the mass of fuel injected during the ignition delay period.

2.10 EMISSIONS REDUCTION STRATEGIES

Strategies for future direct injection (DI) diesel engines will need to look into new elements of diesel technology in order to meet the stringent future emissions limits. The engine should be turbocharged with intercooling, having a cylinder head with four valves, centrally located vertical injector, a re-entrant axisymmetric combustion chamber, a high pressure fuel injection system capable of rate shaping, exhaust gas recirculation (EGR) and fitted with an effective after treatment system. Researchers such as Bazari and French (Bazari and French, 1993), Hentschel (Hentschel, 1996), Herzog et al. (Herzog et al., 1992) Hikosaka (Hikosaka, 1997), Mori (Mori, 1997), and Murayama (Murayama, 1994) have suggested the incorporation of major or key technology areas that can be considered in the strategies for simultaneous reduction in exhaust emission and at the same time improve fuel economy. These key technologies include:

- Improvements of the engine intake system such as turbocharging, charge cooling, swirl and turbulence.
- Electronically controlled high pressure fuel injection system including multiple injection schemes, injection rate control and smaller nozzle orifice.
- Controlled exhaust gas recirculation (EGR).
- Reformulation of fuel and lubrication oil.
- Development of exhaust gas after-treatment system.

2.10.1 Intake System

Intake air temperature and pressure are parameters that influence mixture formation and combustion in the combustion chamber. Cooling of the intake air reduces both NOx and particulates. The effects of cooling the intake air are to reduce the evaporation rate of the fuel and the flame temperature which in turn reduces NOx formation while the oxidation of the soot increases due to the availability of more oxygen in the combustion chamber as reported by Bazari and French (Bazari and French, 1993), and Hentschel (Hentschel, 1996). Reduction in both NOx and soot were also found by Venkatesan and Abraham (Venkatesan and Abraham, 2000) with decreasing intake air temperatures. The effects of increasing the inlet air temperature have two opposing results with respect to NOx emissions. When the effect of increasing the air temperature is to reduce to ignition delay period, then less NOx is formed due to the lower amount of premixed burning fraction. However, when the overall in-cylinder temperature increases due to an increase in inlet air temperature, then the formation of NOx increases as well. Increasing intake air temperature could also reduce the intake air density which would increase the fuel-air ratio. This would affect the fuel economy and increase the diffusion combustion fraction which would increase the particulates.

When the intake air pressure increased, NOx formation initially showed an increase at low ranges of pressure but a decrease as pressure increased further, whereas the soot showed the opposite trend. By increasing the intake air pressure, the density of charge gas in the combustion chamber increases. This increases the availability of oxygen and nitrogen which increases the NOx production as observed by Bazari and French (Bazari and French, 1993), and Herzog et al. (Herzog et al., 1992) and at the same time enhances the oxidation of the soot as observed by Hentschel (Hentschel, 1996). On the other hand, Tanin et al. (Tanin et al., 1999) found that further increases in air pressure (increase air mass) reduce the in-cylinder temperature due to the dilution effect that provides a leaner air-fuel ratio, thus reducing both NOx and particulates production. Bazari and French (Bazari and French, 1993) observed a trend of increasing NOx and fuel consumption (BSFC) with increases in boost pressure, developed by turbocharging. Increasing the intake air boost pressure reduces the spray tip penetration and produces a wider cone angle due to the enhanced air entrainment at higher in-cylinder gas densities. The effect of increasing air density also increases the drag forces on the fuel spray leading to better

atomisation. Soot emission is reduced due to improved mixing, while NOx is reduced due to a shorter ignition delay which thereby reduces the premixed combustion fraction as found by Cho (Cho, 1999). With turbocharging however, the inlet charge temperature also increases along with the pressure which will encourage the formation of NOx. Thus, turbocharging and cooling the intake charge temperature have the advantages of reducing both NOx and particulate matter.

Also of importance are the air flow characteristics which are determined by the inlet port geometry, valve configuration and chamber shape. Air swirl in the combustion chamber enhances the fuel-air mixing process and therefore increases the transport of unburned mixture into the burning spray regions. The increase in fuel-air mixture generated causes a higher flame temperature, resulting in higher NOx levels while soot and PM are reduced but at the expense of fuel consumption. On the other hand, Miles (Miles, 2000) found that increasing swirl ratio decreases the ignition delay, the initial premixed burn and the peak rates of heat release, thus reducing formation of NOx. However, too much swirl increases heat loss to the combustion walls and promotes extremely lean fuel-air regions in the combustion chamber. Winterbone et al. (Winterbone et al., 1994) found that the former leads to longer ignition delay periods, causing higher NOx formation, while the latter cause more unburned hydrocarbons to be formed. Therefore, simultaneous reduction in NOx and PM are possible by introducing low swirl in the early stages of combustion which allows a fuel rich initial combustion, and then higher swirl in the later stages to enhance mixing and to reignite the PM during the diffusion combustion.

Mori (Mori, 1997) and Needham and Whelan (Needham and Whelan, 1994) suggested that controlling the swirl and turbulence in the combustion chamber can be made possible through multivalve cylinder head which reduces pumping losses and increases the quantity of air due to increased valve area, in the combustion chamber. Shiozaki et al. (Shiozaki et al., 1998) found that four valve engines could provide a more uniform combustion without promoting local hot spots of flames, thus prohibiting the promotion of NOx production in the combustion chamber. Further improvement of the in-cylinder gas flow characteristics are realised by employment of re-entrant type combustion chamber or optimised bowl shape piston that produced a fast initial combustion while maintain adequate swirl intensity during the expansion stroke as found by Hikosaka (Hikosaka, 1997). The intense recirculation of the in-bowl flow structure of a re-entrant type bowl in the regions of spray expansion is beneficial for promoting oxidation of soot. The combination of controlled high air motion along with

controlled high pressure fuel injection which has driven the trend towards small holes has enable the modern high speed low emissions diesel.

2.10.2 Combustion System

The combustion characteristics in diesel engines are greatly influenced by the mixture preparation process, i.e. the distribution and the mixing of the fuel with the compressed air charge. Control of the in-cylinder fluid mechanics is benefited when the fuel-air mixture is made rich at the initial combustion phase to prevent the formation of NOx and diluting it with more air at the later phase of combustion to promote the oxidation of soot. Alternatively, NOx and PM production can be reduced by having a low intensity turbulence in the combustion chamber at the initial phase of combustion and strong in the later phases to enhance mixing of fuel and air as mentioned above.

Both of the above strategies were investigated by Konno et al. (Konno et al., 1992), and Chikahisa and Araki (Chikahisa and Araki, 1996), using an auxiliary injector having a chamber called "Combustion Chamber for Disturbance (CCD)" in conjunction with the main injector. A cross section of the engine cylinder head with the CCD system is shown in Figure 2.6. The strong turbulence generated during the combustion process was accomplished by injecting a small amount of fuel, from a separate fuel injection pump, into the CCD during the main combustion. The burned gas from the CCD enters the main combustion chamber as high momentum jets, creating strong turbulence in the cylinder. The results of Konno et al. (Konno et al., 1992) experiments showed that CCD effectively reduces smoke at all engine speeds (800-1200 rpm) and load conditions without increasing NOx as shown in Figure 2.7. The effect of the CCD system when combined with EGR was also investigated. The results showed that at low loads, smoke was reduced substantially while some reduction in NOx was observed. However, slight increases in smoke with large reductions in NOx were found when the CCD system was combined with water injection into the intake manifold.

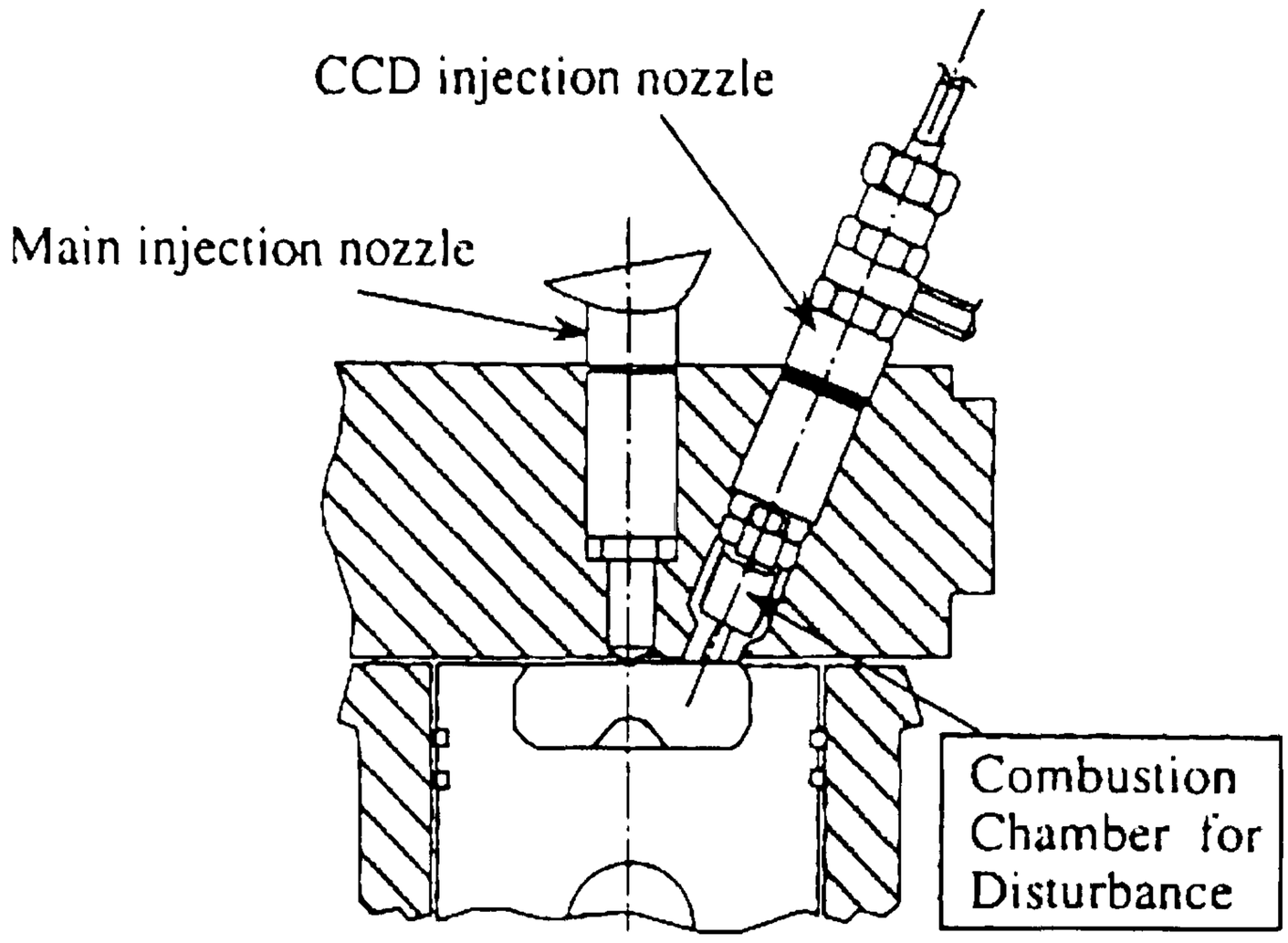

Figure 2.6: Cross-section of a CCD system
Source from (Konno et al., 1992)

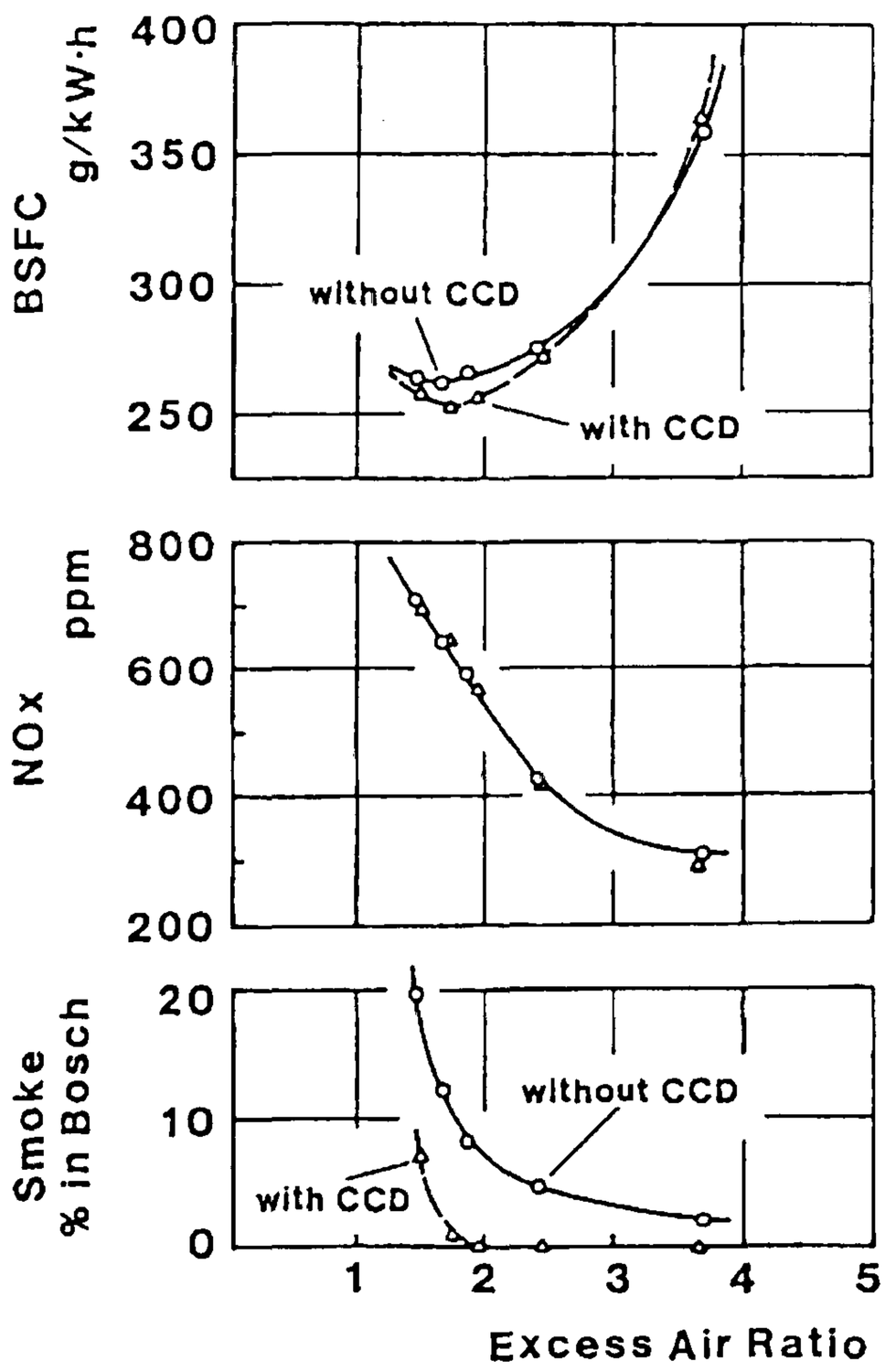

Figure 2.7: Emissions measurement results from a CCD system
Source from (Konno et al., 1992)

Another attempt to reduce NOx emission especially at high loads was by employing multiple stage combustion, introduced by Hashizume et al. (Hashizume et al., 1998). The concept of Multiple Stage Diesel Combustion (MULDIC) was to reduce the volume of the stoichiometric region in order to prevent NOx production and to make combustion occurs under fuel rich conditions by two separate combustion events. In the first stage combustion, fuel was injected extremely early (up to 150° BTDC) and combustion only occurs just before TDC. Homogeneous premixed lean mixture was formed and prevented the production of NOx due to the uniform temperature distribution in the combustion chamber. The second combustion occurs under high temperature but NOx production was suppressed due to low oxygen (O_2) concentration. Further reduction in NOx emission is possible when injection timing is retarded.

Simultaneous reduction in NOx and particulates is also possible when the sprays from two or more injectors are designed to make them collide into one another, as investigated by Chehroudi (Chehroudi et al., 1996) and by Takeda and Niimura (Takeda and Niimura, 1995). The colliding or interacting sprays create disturbance in these regions which weakened the penetration and improved air utilisation and consequently promoted oxidation of the soot. Improvement in both PM and fuel consumption while maintaining low NOx can be achieved when fuel quantities in the injectors, separation time between injections and angle at which the sprays collide were optimised.

Kato et al. (Kato et al., 1992) studied the fuel mixture formation process when the fuel jet from the nozzle was made to impinge against an obstruction installed in front of the nozzle. They observed that the fuel spray diffused symmetrically in a disk shape and has shorter penetration. There was more uniform fuel distribution in the combustion chamber and the flame progressed at a faster rate. Their results showed improvement in smoke, NOx and total hydrocarbons (THC) emissions and at the same time better specific fuel consumption.

2.10.3 Fuel Injection System

Advanced fuel injection technology can help reduce NOx and particulates emissions. More precise control of the injection pressure, rate and timing, while using

a high-pressure injection system, not only permits simultaneous reductions in NOx and particulates formation during combustion, but can also reduce engine noise.

The characteristics of fuel injection system in DI diesel engine such as start of injection (SOI), shape of the rate of injection and injection spray characteristics are among the most important factors that influence the emissions and performance of the engine. In order to reduce the emissions while maintaining the engine performance, the fuel injection system need to satisfy the following requirements, as suggested by Ashley et al. (Ashley et al., 1995), Boehner and Hummel (Boehner and Hummel, 1997), Bürgler et al. (Bürgler et al., 1992) and Takaishi et al. (Takaishi et al., 1989):

- High injection pressure capability (>1200 bar)
- Optimisation of injection rate or pilot injection for low fuel consumption and reduction of combustion noise
- Precise control of injection quantity
- Flexible control on injection timing
- Adaptation to load, engine speed and temperature
- Stable and durable
- Favourable distribution of the fuel into the air of the combustion chamber
- Lowest possible spray orifice area.

Fuel injection system featuring high injection pressure and flexible control of injection timing as a function of engine speed, load and temperature requires the employment of electronic control fuel injection system. Electronics fuel system control allows the freedom to minimise the various trade-offs (HC-NOx-PM-BSFC) in steady state and transient operation. Microprocessor control on the other hand has enable precise measurement of fuel to be introduced at predetermined crank angle position into the combustion chamber at a very high pressure. Several established diesel FIE manufacturers such as Bosch, Lucas Diesel and Nippon Denso have introduced into the market new and innovative products. Table 2.2 summarised some of the functional characteristics of the fuel injection systems currently available for HSDI diesel engine such as cam driven unit injector system with hydraulically actuated nozzle needle (EUI), hydraulically intensified low pressure common rail system (HEUI), and high pressure common rail system (CR).

Table 2.2 : High pressure fuel injection systems for HSDI diesel engines Reproduced from (Herzog, 1998)

	Electronic Unit Injector (EUI)	Intensifier (HEUI)	Common Rail (CR)
Current Max. Pressure (bar)	1800	1500	1350
Potential Max. Nozzle Pressure (bar)	2200	1800	1650
Injection Rate Control	Mechanically: TSI, Storage Element Electronically: Pilot	Mechanically: PRIME Electronically: Pilot	Mechanically: Delta, Boot Electronically: Pilot
Injector Package Size	Dia.: 17/21 mm	Dia.: 17/25 mm	Dia.: 17 mm

(a) Raising Mean Injection Pressure

The overall effect of increasing the fuel injection pressure is to produce more NOx and less soot. Henein et al. (Henein et al., 2001) found that, increasing the mean injection pressure provide fast transport of fuel into the combustion chamber which promotes better fuel atomisation, thus reducing ignition delay. Raising the mean injection pressure also increase air entrainment and improves fuel-air mixing due to increase in turbulence intensity and enhances vaporisation as observed by Araneo (Araneo et al., 1999), and Pierpont and Reitz (Pierpont and Reitz, 1995a). Lapuerta et al. (Lapuerta et al., 1999) found that the peak pressure and temperature was also higher, causing higher NOx formation while at the same time promotes both soot formation and oxidation. Yamaguchi et al. (Yamaguchi et al., 1990) observed an increased of turbulence intensity at the early stage of diffusion combustion with increasing injection pressure. As a result, air entrainment into the spray increases and a nearly homogeneous lean fuel-air mixture in the combustion chamber is formed which ensure lower soot and particulates emissions. The effect of increasing injection pressure can also be obtained by reducing the spray orifice diameter. However, the disadvantage of too high mean injection pressure is the increase in combustion noise

in particular at part load and with low charge density. Bürgler et al. (Bürgler et al., 1992) and Takaishi et al. (Takaishi et al., 1989) found that higher injection pressure levels caused a shorter duration of injection and higher peak value of rate of injection. This in turn caused an increase in combustion noise and NOx emission while causing a decrease in smoke and HC emissions. Reducing the initial injection quantity, i.e., the amount of fuel injected during the ignition delay period and increasing the number of injection orifice or by using pilot injection schemes can be used as a countermeasure strategy as investigated by Kato et al. (Kato et al., 1998). Increasing the injection pressure to reduce particulates emissions is an effective mean, however there are constrains as to how high injection pressure can be reliably increased due to limitations on material strength, increase in parasitic losses and fuel system cost as reported by Tow et al. (Tow et al., 1994).

(b) Control of Fuel Injection Rate

In a fuel injection system with injection rate modulation device, the injection events are tailored by varying the fuel flow during the injection period. The fuel injected quantity during the ignition delay is kept to a minimum by reducing the initial fuel injection rate in order to minimise the fuel burning and rate of pressure rise in the premixed combustion phase which reduces NOx formation and combustion noise as investigated by Hwang et al. (Hwang et al., 1999) and Russell and Lee (Russell and Lee, 1995). The initial fuel propagates at lower spray speeds, resulting in ignition and combustion located closer to the nozzle. This is followed by a moderate increase in injection rate in order to avoid creating a high heat release rate. Borman (Borman and Ragland, 1998) reported that, terminating the fuel end rapidly during the final phase of combustion reduces smoke, hydrocarbons and particulates emission, and also avoids the increase in fuel consumption as observed by Erlach et al. (Erlach et al., 1995). This practice of tailoring the injection events is known as fuel injection rate shaping. One example of injection rate shaping is pilot injection, in which a very small amount of fuel is injected early, as the initiator of combustion of the main injection event. Ikegami et al. (Ikegami et al., 1997) found that pilot injection decreases the ignition delay of the main injection and hence the main injection can be retarded. Post injection is another type of rate shaping in which a small quantity of fuel is injected very late in the

expansion stroke after completion of the main injection. Multiple or split fuel injection on the other hand refers to splitting, more or less evenly, the main injection into two or more separate injections.

Yamaguchi et al. (Yamaguchi et al., 1990) found that substantial improvement in the particulates-NOx trade-off is also achieved by reducing the initial injection quantity and at the same time increasing the injection period by using a smaller nozzle orifice diameter. The result is to reduce the amount of premixed combustion which in turn reduces the emissions of NOx and improvement of smoke as observed by Kato et al. (Kato et al., 1998). Experimental results by Erlach et al. (Erlach et al., 1995) using injection rate shaping strategy showed that simultaneous reduction of 9% NOx and 7% fuel consumption while keeping soot emission low can be achieved. Ikegami et al. (Ikegami et al., 1997) also found that the combination of pilot injection and high pressure injection suppress the rapid initial combustion as the quantity of fuel in the first injection is reduced and decrease the ignition delay of the main ignition, thus reduces the NOx production while the main injection can be retarded. The subsequent injected fuel into the combustion chamber burns rapidly but does not contribute significantly to soot production. Reduction of NOx by 35% and smoke by 60-80% without worsening the fuel consumption was also found by Shundoh et al. (Shundoh et al., 1992) using this strategy. In experiments by Minami et al. (Minami et al., 1995), 5% improvement in fuel consumption and 40% reduction in HC emission were obtained with pilot injection and retarded injection timing especially at low load.

(c) Control of Fuel Injection Timing

The requirement for low fuel consumption is to advance the injection timing especially in the high-speed region while retarding the injection timing in the low-speed region reduces NOx and combustion noise as suggested by Takaishi et al. (Takaishi et al., 1989). The injection timing can be advance by using a smaller nozzle orifice diameter while maintaining the same NOx level. The smaller nozzle orifice diameter cause a reduction in initial injected quantity, thus fuel consumption decreases at low and middle loads as found by Kato et al. (Kato et al., 1998). Advancing the injection while injecting more fuel during ignition delay produces rapid mixing of the remaining fuel and oxygen at the end of the diffusion combustion phase. This ensures complete

burning of the injected fuel and as a result reducing particulate matter as observed by Zhang et al. (Zhang et al., 1993).

Retarded injection and a low initial rate of injection, on the other hand can assist in reducing the lean mixture developed during injection at a relatively higher rate during the early part of injection. Thus reducing unburned hydrocarbons formation. Russell et al. (Russell et al., 1989) found that the NOx is also reduced due to lower peak cylinder pressure which is associated with local peak temperature during combustion. Injection timing retard can be effective in reducing NOx emission but this usually results in increase of particulates, deterioration of fuel economy and increase of CO_2 emissions. In addition, there is a restriction on retard of injection timing beyond which NOx emission cannot be further reduced as reported by Shundoh et al. (Shundoh et al., 1992) and Tullis and Greeves (Tullis and Greeves, 1996). Henein et al. (Henein et al., 2001) found that retarding injection timing beyond TDC would increase ignition delay period which cause significant increase in the premixed burn fraction leading to higher NOx level. Therefore, there are some conflicts in the reduction strategies whereby retarding the injection timing is very effective in minimising the ignition delay and hence reduction of NOx and combustion noise, but on the other hand, smoke and particulates are likely to rise to unacceptable levels. Conversely, increases mean rate of injection, which is often introduced to reduce smoke and particulates, can give rise to high levels of combustion noise and unburned hydrocarbons at certain engine conditions.

(d) Multiple Injections

Experiment results had showed that simultaneous reduction in NOx and particulates is possible with high pressure, multi injection fuel system in which the initial injection rate is reduced to lower NOx concentration and the average injection rate is increased to reduce smoke. Takeda and Niimura (Takeda and Niimura, 1995) fitted three fuel injectors onto a single cylinder DI diesel engine in order to control the fuel injection quantity and injection timing from each injector. In addition, independent control of the fuel injection pressure of the injectors was also possible. They found that improvement in both PM and fuel consumption while maintaining low NOx was possible under the optimum condition of the set-up. However, the effects of fitting six

injectors showed no increase in particulates and NOx but significantly increase in fuel consumption. Nehmer and Reitz (Nehmer and Reitz, 1994) investigation of several ratios of pilot injection with different dwell time indicated that the quantity of fuel in the first injection has significant effect on the rate of pressure rise in the combustion chamber. As the quantity of fuel in the first injection is increased, NOx tends to increase while particulates emissions decreased.

Another experimental study by Tow et al. (Tow et al., 1994) using the same engine as Nehmer and Reitz (Nehmer and Reitz, 1994) were carried out to evaluate double and triple injection schemes at load conditions of 25% and 75% of maximum torque. Their findings showed that at high loads, particulates could be reduced by a factor of three using a double injection with relatively long delay between injections. For triple injections, particulates and NOx were reduced by 50% and 30% respectively at 25% load. 10 degree crank angle (^{0}CA) was found to be the optimum dwell time between first and second injection for the double injections and between second and third injection for the triple injections.

All of the above results suggest that multiple injections provide the flexibility in controlling the combustion process while allowing injection timing to be retarded which is required for simultaneous reductions in particulates and NOx. At low loads, a small dwell is required to counter the long ignition delay in reducing premix burn fraction. This resulted in reduced average combustion gas temperature due to a restriction on premixed combustion, thus reducing NOx. While the late injections in both double and triple injections promotes particulates oxidation later in the cycle due to a slower combustion during the diffusion stage. In addition, the high fuel injection pressure assists in improving atomisation and fuel-air mixing, hence reducing particulates and smoke emissions.

(e) Other Fuel Injection System Strategies

Another FIE parameters of importance which can be controlled in order to optimised combustion and emissions are the nozzle orifice diameters, number of orifice and orifice geometry. With small orifice area, the quantity of fuel injected during the ignition delay is reduced and this is the primary reason for lower temperature in the initial (premixed) combustion stage, thus reducing NOx formation. The initial injection

fuel quantity also produces a fuel rich initial combustion which assists further in reducing NOx. However, fuel consumption and soot level increases due to longer injection period especially at high loads. Kato et al. (Kato et al., 1992) found that the initial fuel injection can be effectively reduced by decreasing the nozzle orifice diameter. Their results showed that NOx was reduced significantly with increase in fuel consumption, but this can be overcome by advancing the injection timing. Contrary to the findings, Kobori et al. (Kobori et al., 1996), found that extremely small nozzle orifice (micro-hole nozzle) increases air utilisation significantly promoting lean combustion which contributed to increase in NOx emission. Yoda and Tsuda (Yoda and Tsuda, 1997) improved the NOx and particulates trade-off by enlarging the spray orifice inlet chamfer which increases the fuel flow velocity. They found that reduction of both particulates and smoke emissions especially at high loads was the attribute of atomisation improvement. Pierpont and Reitz (Pierpont and Reitz, 1995a) on the other hand investigated the effects of sharp and rounded edged nozzles on the NOx and particulates trade-off at 25% and 75% loads. Their results showed that sharp edged nozzle reduced particulates significantly and gave low BSFC as compared to rounded edged nozzles. However, at high injection pressures, rounded edged nozzles gave better BSFC. Chang and Farrell (Chang and Farrell, 1997) results showed similar relationship. They found that sharp inlet nozzle generated smaller droplet size gave a wider spray angle than rounded inlet nozzle.

Other strategy includes the prevention of secondary injection at low pressure after main injection. Dribbling of small fuel quantities from the sac volume causes incomplete combustion of the fuel during the final combustion phase. This causes an increase in smoke and particulates emission. Additionally, fluctuations of fuel injection at every cycle cause torque fluctuation which results in increase in combustion noise and instability in engine governing.

2.10.4 Exhaust Gas Recirculation

Exhaust gas recirculation (EGR) returns a faction of the exhaust gas back to the combustion chamber by mixing the gas with fresh air in the intake manifold. The effects of EGR to combustion are that it reduces the concentration of oxygen in the intake air, increases the intake gas temperature and also the concentration of carbon

dioxide and water vapour. These lead to a richer mixture and increase in thermal capacity of the intake gas (both CO_2 and H_2O absorb heat in the cylinder), resulting in lower NOx formation. However, EGR caused an increase in soot and fuel consumption especially at higher load conditions due to larger amount of EGR and prolong diffusion burning period.

Researchers have found that EGR is effective in reducing the emission of NOx. Shimazaki et al. (Shimazaki et al., 1996) used an in-cylinder electromagnetic gas-sampling valve to directly sample the combustion products in the combustion chamber to investigate the effects of EGR in pollutant production. Their results showed that as residual gas concentration increases, the combustion rate was slower and NOx decreases due to reduction in initial oxygen concentration.

Uchida et al. (Uchida et al., 1993) studied the effect of EGR in combination with increased intake boost pressure by supercharging and high fuel injection pressure. They also used a reentrant combustion chamber which assists in improving combustion. They observed that NOx emission can be reduced almost in proportion to the EGR ratio. Increase in both the intake boost pressure and EGR ratio caused in-cylinder temperature to deceased due to a higher excess air and inert gas concentration resulting in lower NOx production. They also found that diffusion combustion is affected by supercharging which enhanced air-fuel mixing rather than EGR, thus reducing smoke and total hydrocarbons (THC). Similar studies by Arcoumanis et al. (Arcoumanis et al., 1998), performed using a single-cylinder Ricardo Hydra engine showed that both NOx and soot emissions increase with increase in EGR rate while increasing boost pressure by supercharging have a significant reduction on smoke levels.

Konno et al. (Konno et al., 1992), however suggested that EGR should not be used at high loads which caused higher fuel consumption due to low volumetric efficiency. However, reduction of NOx is much more required at high loads due to the fact that 60% of all NOx emissions came from the high load working range as observed by Baert et al. (Baert et al., 1999). Tullis and Greeves (Tullis and Greeves, 1996) found that when EGR is used at advanced injection timings, more favourable NOx versus break specific fuel consumption (BSFC) can be obtained.

Pierpont et al. (Pierpont et al., 1995b) investigated the combined effect of using multiple injections and EGR to achieve simultaneous reduction of NOx and particulates emissions while improving on fuel consumption. Since the particulates reducing effects of multiple injections has been attributed to enhance mixing, the mixing

characteristic of different nozzle spray angles was also investigated. They found that a 125 degree spray angle nozzle benefit at lowering particulates due to significant spray impingement on the piston bowl wall as compared to 140 degree spray angle nozzle which spray angle is parallel to the piston bowl wall. Their overall results showed that by using a 125 degree spray angle, optimal triple injection (48-6-36-6-16) and 6% EGR rate, NOx was reduced to 2.2 g/bhp-hr and particulates to 0.07 g/bhp-hr without significant increase in BSFC at 75% peak torque.

Montgomery and Reitz (Montgomery and Reitz, 1996) extended further the study made by Pierpont et al. (Pierpont et al., 1995b) using optimised quadruple injection in combination with EGR. They found that the lowest emission was with 10% EGR rate. They concluded that further simultaneous reduction in NOx and particulates can be achieved when other parameters such as higher injection pressure and smaller nozzle orifice diameter are used.

A summary of the researches performed to reduce the exhaust gas emissions from the diesel engines are shown in Table 2.3.

Table 2.3 Summary of diesel engine research

Researcher & Institution	Investigated Parameter	Method	Engine Used
Werlberger and Cartellieri (1987). AVL-List GmbH	Effect of wall temperature, split injection, wall jet and swirl on combustion.	Endoscopic high speed photography.	Single cylinder HSDI, 2-valve, diesel engine,
Karimi, E. R. (1989) Perkins Technology	Investigation of fuel spray and combustion events.	Endoscopic high speed photography	Perkins four-cylinder, 4.4 L, optical diesel engine.
Arnold et al. (1990) Pennsylvania State University	Effects of non-swirling and swirling flow fields on sprays.	Measurement of flow field using Laser Doppler Velocimetry High-speed photography of fuel spray and combustion.	Single-cylinder with extended piston, optical research engine.
Yamaguchi et al. (1990) Advanced Combustion Engineering Institute Co. Ltd and Japan Automobile Research Institute, Inc.	Effect of high pressure fuel injection on combustion.	High-speed shadowgraphy technique. Using different type of fuel injection system.	Single-cylinder, optical, DI diesel engine.
Shundoh et al. (1992). Advanced Combustion Engineering Institute Co. Ltd and Japan Automobile Research Institute, Inc.	Effect of heat insulation, glow-assist, pilot injection and injection timing	Measurement of exhaust gas emission sand calculation of heat release rate.	Single-cylinder DI diesel engine with variable compression ratio using different piston.
Konno et al. (1992). Hokkaido University	Effect of turbulence, EGR, water injection for simultaneous reduction in smoke and NOx.	Combustion Chamber for Disturbance (CCD) Injector. In-cylinder gas sampling method.	Single-cylinder, DI diesel engine.
Kato et al. (1992). Nippon Clean Engine Lab. Co. and Kanazawa Institute of Technology	Effect of fuel impingement on emissions.	OSKA-DH cylinder head	Single-cylinder, optical DI diesel engine.
Uchida et al (1993). Hino Motors, Ltd., Waseda University and Nippon Oil Co. Ltd.	Effect of EGR and supercharging on emissions.	Using re-entrant combustion chamber. Measurement of exhaust gas emissions	Single-cylinder DI diesel engine
Bazari* and French** (1993). *Lloyd's Register **Ford Motor Co.	Effect of EGR, injection system, swirl and valve timing on engine performance and emissions trade-offs.	Exhaust gas emissions measurement. Combustion-emissions model simulation.	Four-cylinder HSDI, turbocharged diesel engine.
Karimi and Jane (1993) Perkins Technology Ltd.	Effect of turbulent combustion chamber on combustion.	Laser Doppler Anemometry measurement of in-cylinder velocity.	Optical single-cylinder with variable swirl inlet port. Six-cylinder, turbo-charged diesel engine.

Researcher & Institution	Investigated Parameter	Method	Engine Used
Zhang et al. (1993) Isuzu Advanced Engineering Centre, Ltd.	Effect of pumping rate, nozzle hole size and injection timing on flame motion and temperature.	Cross-correlation method for flame motion measurement. Two-colour method for flame temperature measurement.	Optical single-cylinder, 4 valves, DI diesel engine.
Pitcher and Wigley (1994). AVL List	Axial and radial velocity components, dropsize and sample number.	Two-component PDA system.	Optical single-cylinder research diesel engine.
Baritaud et al (1994). Institut Français du Pétrole	Determination of spray structure, penetration length and auto-ignition. Effect of intake air temperature, air density, injected quantity and engine speed.	Visualising liquid and gas fuel of the spray with planar laser induced exciplex fluorescence. Imaging of liquid and gas fuel using video CCD camera.	Optical single-cylinder model engine.
Arcoumanis et al. (1994) Arcoumanis et al. (1995b). Imperial College of Science, Technology & Medicine and Volkswagen AG	Observation of spray-to-spray variations, cycle-to-cycle variations on spray development and combustion. Effect of EGR on spray development, combustion and emissions	Spray and flame imaging using intensified CCD camera. Sequence of spray and combustion images using high-speed camera. High-speed cinematography. Emission measurements.	Four-cylinder, 1.9L, optical, HSDI diesel engine (Volkswagen).
Takeda and Niimura (1995). New ACE Institute Co. Ltd.	Effect of multiple injections, injection timing and direction, injection quantity on emissions trade-offs.	Multi-injectors system – three injectors per cylinder.	Single-cylinder, DI diesel engine.
Espey* and Dec** (1995) *Daimler-Benz AG **Sandia National Laboratories	Effect of TDC temperature and density on liquid fuel penetration length.	Laser elastic-scatter imaging.	Cummins-N series heavy-duty, DI single-cylinder, optical diesel engine.
Dec* and Espey** (1995) *Sandia National Laboratories **Pennsylvania State University	Investigation of soot formation in DI diesel engine.	Low-sooting fuel Imaging of natural chemiluminescence by Laser-Induced Incandescence (LII). Elastic scattering technique	Cummins-N series heavy-duty, DI single-cylinder, optical diesel engine.
Tow et al. (1994) Nehmer and Reitz (1994) Pierpont and Reitz (1995a) Pierpont, Montgomery and Reitz (1995b) Montgomery and Reitz (1996) University of Wisconsin-Madison.	Effect of multiple injection strategies on emissions. Effect of injection rate and split injections on emissions. Effect of injection pressure and nozzle geometry on emissions Effect of multiple injection and EGR on particulate and NOx trade-off. Effect of multiple injection and EGR on particulate and NOx trade-off on six-mode cycle.	Simulated turbocharging strategies using compressed air. Multiple injection strategies. Measurement of exhaust gas emissions.	Single-cylinder (Caterpillar 4306), heavy-duty diesel engine.

Researcher & Institution	Investigated Parameter	Method	Engine Used
Minami et al. (1995). Isuzu Advance Engineering Center, Ltd.	Effect of pilot injection on combustion	Pseudo high-speed image photographic system.	Six-cylinder, turbocharged DI diesel engine.
Chikahisa and Araki (1996). Hokkaido University.	Effect of different combustion chamber and EGR on emissions.	Two-stage combustion method.	Single-cylinder, DI diesel engine.
Greeves and Tullis (1993) Tullis and Greeves (1996) Lucas Diesel Systems	Effect of nozzle hole diameter and injection pressure on particulate-NOx trade-off. Effect of EGR and pilot injection using EUI on NOx-BSFC trade-off.	EUI 200 injection system. Simulation of FTP 8 steady state modes Measurement of exhaust gas emissions	Ricardo Proteus single-cylinder, 4-valve research engine.
Shimazaki et al. (1996). Isuzu Advanced Engineering Centre, Ltd.	Effect of high-pressure fuel injection and EGR on emissions.	In-cylinder gas sampling method. Visualisation of combustion process	Single-cylinder, optical, 2-stroke DI diesel engine.
Dec (1997) Sandia National Laboratories	Development of diesel combustion conceptual model.	Laser sheet imaging. Three types of fuel with different sooting characteristics.	Cummins-N series heavy-duty, DI single-cylinder, optical diesel engine
Ricart and Reitz (1996) University of Wisconsin-Madison.	Effect of pilot injections on combustion.	Endoscopic combustion visualisation. KIVA-II for ignition and combustion models validation.	Caterpillar heavy-duty DI single-cylinder oil test engine (SCOTE).
Ricart et al. (1997) University of Winconsin-Madison	Effect of engine load, fuel amount and injection timing on liquid fuel penetration length.	Endoscopic spray imaging. KIVA-II for spray penetration calculations	Caterpillar heavy-duty DI single-cylinder oil test engine (SCOTE).
Zhang et al. (1997) Isuzu Advanced Engineering Center Ltd	Effect of injection pressure, nozzle geometry, intake air pressure and temperature on liquid phase penetration.	Laser beam elastic-scattering and shadowgraphy imaging of spray.	Optical single-cylinder, 4 valves, DI diesel engine.
Zhang et al. (1998) Isuzu Advanced Engineering Center Ltd	Effect of combustion chamber geometry and nozzle geometry on combustion.	Visualisation of combustion phenomena. KIVA-II combustion model simulation	Optical HSDI diesel engine with common rail fuel injection system.
Kato et al. (1998). Mitsubishi Motors Corp.	Effect of reducing initial fuel injection quantity on emissions.	Injector s with 3-way and two way valve.	Six-cylinder DI diesel engine with common rail system.
Arcoumanis et al. (1998) Imperial College, London	Effect of engine speed, load, EGR and air swirl on sprays, combustion and emission. Effect of boost pressure	Laser diagnostic and imaging of fuel sprays. Emission measurements.	Single-cylinder, HSDI Ricardo Hydra
Hashizume et al. (1998). New ACE Institute Co. Ltd.	Effect of colliding fuel sprays and injection timing on emissions. Effect of fuel Cetane number.	Multiple Stage Diesel Combustion (MULDIC). Multiple injector system. Laser shadowgraphy for combustion visualisation	Single-cylinder, DI diesel engine.

Researcher & Institution	Investigated Parameter	Method	Engine Used
Larsson, A. (1999) Scania CV AB	Effect of injection timing, inlet air temperature and pressure, engine load, and nozzle hole diameter on flame temperature and soot distribution.	Endoscopic spray imaging and combustion visualisation. Two-colour method. Measurement of exhaust gas emissions.	Single-cylinder with optical access, DI diesel engine.
Tsunemoto et al. (1999) Kitami Institute of Technology	Effects of injection parameter and nozzle specification on nozzle sac pressure.	Measurement of nozzle sac pressure using strain gauge. Measurement of HC emissions.	Six-cylinder DI diesel engine
Tanin, K.V. et al. (1999) University of Wisconsin-Madison	Emission characteristics of six-mode cycle. Effect of boost pressure on combustion.	Six-mode cycle simulation of the EPA Federal Transient Test Procedures. KIVA-II combustion model simulation.	Caterpillar heavy-duty DI single-cylinder oil test engine (SCOTE).
Venkatesan and Abraham (2000) Purdue University	Effect of increasing intake air temperature	Combustion analysis Local Characteristic Time Model (LECT)	Cummins N-14 single-cylinder DI diesel engine
Miles P. C. (2000) Sandia national Laboratories	Effect of swirl on combustion.	Imaging of natural combustion luminosity.	Four-valve, optical HSDI research engine.
Henein, N.A. et al. (2001) Wayne State University	Effect of Injection pressure, EGR, swirl ratio effects on emissions	Measurement of exhaust gas emissions.	Single cylinder HSDI, 4-valve DI diesel engine, vertical injector, multihole VCO nozzle, common rail system

2.11 IN-CYLINDER FLAME TEMPERATURE

Flame temperature in the combustion chamber of a diesel engine has a direct influence on the NOx formation and soot oxidation. Understanding the flame temperature characteristics is therefore essential in order to predict the formation of both NOx and soot, and eventually to control their emissions. The well-known two-colour method is one of the means that can provide information about the in-cylinder temperature and soot concentration as reported by Ladommatos and Zhao (Ladommatos and Zhao, 1994a; 1994b). The method is based on measurement of the radiation intensity from incandescent soot particles in the combustion chamber at two different wavelengths using optical fibre bundle. The measured radiation intensities are then split into two, filtered by using band pass filters and processed using the two-colour method to calculate the flame temperature and soot concentration. The method however, requires optical access into the combustion chamber in order to measure, during combustion, the instantaneous values of the flame temperature and soot concentration.

The two-colour method was originally proposed by Hottel and Broughton (Hottel and Broughton, 1932) who used it to estimate the temperatures of furnaces using optical pyrometer. The method was later extensively used by Matsui et al. (Matsui et al., 1979; 1980; 1982) as the in-cylinder flame temperature measuring method in diesel engines. Matsui and co-workers used a spectroscopic arrangement consisting of a quartz window installed in the cylinder head of a single cylinder DI diesel engine. The light from the combustion process was led to the spectroscopic section through a light guide fibre after passing the aperture system. The light was split into three, where each light was passed through an interference filter having a centre wavelength of 529nm, 624nm and 738nm respectively. The intensity of the lights were detected and measured by a photomultiplier. These electrical signals were then used as inputs for the calculation of the flame temperature, T and the soot concentration, KL. They found that soot was promptly formed just after the start of diffusion combustion phase and peaks at around the end of injection, then the soot was oxidised rapidly, followed by the termination of oxidation when the flame temperature drops to 1800K. The maximum flame temperature was independent of injection amount but soot concentration increases with increase in injection amount. When injection timing was advanced, both maximum flame temperature and soot concentration increases and the

maximum flame temperature was reached earlier. However, the soot concentration reduces when injection timing was advanced further.

Yan and Borman (Yan and Borman, 1988) measured the in-cylinder flame temperature and particulates concentration of a Cummins single cylinder diesel engine by means of an optical radiation probe. The radiation probe consists of a specially designed trifurcated fibre optical bundle and a sapphire rod window. The radiation signals were collimated by the condensing lenses and filtered by the band pass filters before reaching the silicon photovoltaic detectors. The three interference filters have a wavelength of 550nm, 700nm, and 850nm respectively with bandwidth of 0.025 μm each. The radiation signals were amplified by a two-stage amplifier and all the experimental data were collected by using a data acquisition system. The results showed that flame temperature was found to be higher with increase in intake air pressure, whereas soot concentration in the exhaust is lower due to earlier and faster oxidation as a result of higher flame temperature. They also found that increasing the coolant temperature will cause more late burning to occur which resulted in higher soot production. Increasing inlet air temperature however, has little effect on the in-cylinder soot production due to the increase in flame temperature is too small to have any influenced on the soot production.

The effects of low coolant and suction air temperature on the flame temperature and soot concentration were investigated by Asou et al. (Asou et al., 1992) in a single cylinder DI diesel engine. In their two-colour method, the continuous radiant spectra from the flame pass through a sapphire optical window which was installed in the cylinder head and then the signal was guided to a bifurcating optical fibre. The light was led through two types of band pass filters, each having a wavelength of 653nm with half intensity width of 12nm and 503nm with a width of 9nm respectively. The radiant energy of each light was detected by the photomultiplier. The combustion phenomenon was taken using a 16-mm high-speed photography by a 3000 frames per second high-speed camera. Their results showed that both the flame temperature and the soot concentration reduce when the coolant and the intake air are decreased respectively.

Researchers such as Kobayashi et al. (Kobayashi et al., 1992), Zhang et al. (Zhang et al., 1993), Winterbone et al. (Winterbone et al., 1994) and Arcoumanis et al. (Arcoumanis et al., 1995a) observed the flame in the combustion chamber by using an optical accessible engine having a transparent bowl fitted with an extended piston. Kobayashi et al. (Kobayashi et al., 1992) investigated the effects of injection pressure

and nozzle hole diameter on flame temperature distribution in a single cylinder DI diesel engine by analysis of the flame images taken using high-speed photography. Photographs of the flame were first taken using a rotating prism type 16-mm high-speed camera having a framing speed of 6000 frames per second through the transparent piston bowl. The photographs of a halogen lamp were also simultaneously photographed as a calibration standard. The high-speed photographs were then processed by the image processor having a colour CCD camera. Digital images of two wavelengths (red and blue) were obtained for the flame and the standard lamp and by applying the two-colour method, the real temperature and the KL factor were obtained. They found that flame temperature is higher when injection pressure increases due to rapid compression of the burned gases. The KL factor which is an index of soot density was found to reduce due to higher oxidation rate of soot especially at late period of combustion as injection pressure increases. They also found that the effect of reducing nozzle orifice diameter also cause higher flame temperature due to increase in air entrainment into the spray.

Zhang et al. (Zhang et al., 1993) recorded the combustion phenomena of an optical single cylinder DI diesel engine by direct photography using a high-speed camera at the speed of 4000 frames per second. Effects of engine parameters such as pumping rate, injector nozzle hole diameter and injection timing on the flame motion and flame temperature were investigated. Measurement of the flame temperature by two-colour method was done by processing the high-speed photographs and measuring the film density for the red and blue colours. The wavelengths used were 460nm (blue) and 650nm (red). Their results also showed that flame temperature was higher when injection timing was advanced or when the injection rate was increased. As for the effects of reducing nozzle orifice diameter, they observed that the flame temperature was lower in the premixed combustion stage and higher in the diffusion combustion stage due to increase in flame motion at the later stage.

The effects of swirl on flame temperature distribution in the combustion chamber was investigated by Winterbone et al. (Winterbone et al., 1994) using a single cylinder Ricardo Hydra DI diesel engine. The combustion was recorded on high-speed film which was then captured by a monochrome CCD camera through two different band pass filters, 581nm and 631nm respectively. The images were then converted into a computer images and calibrated to obtain the temperature. The results showed that high swirl increases the ignition delay period which increases the NOx formation, while soot concentration reduces due to better mixing of the fuel and air.

Arcoumanis et al. (Arcoumanis et al., 1995a) investigated extensively the effect of various levels of EGR on the combustion characteristics using a four cylinder, optical VW DI diesel engine. Temperature and soot concentration information was obtained using two-colour method with interference filters centered at wavelengths of 450nm and 640nm. The optical set-up used only one monochromatic intensified single shot per cycle CCD camera. The image processing was performed using visual image processing programme on a silicon graphics workstation. The effects of increasing EGR were found to decrease the core flame temperature and reduce the overall formation of soot.

Li and Wallace (Li and Wallace, 1995) inserted three optical fibre probes that measured the temperature simultaneously at different location, either at the spray axis, on the spray edge or between two sprays. The measurements were performed inside the combustion chamber of an air-cooled Lister ST-1 single cylinder DI diesel engine under different load levels. The soot concentration predicted by the in-cylinder two-colour measurement results were compared with the exhaust soot concentrations measurement using the direct sampling method. In the experiment, the optical fibre which was connected to a three-way coupler splits the light signal into two equal parts. Each of these two light signals was filtered through filter lenses having wavelengths of 550nm and 700nm, with a bandwidth of 10nm. The light signals were detected by photomultiplier and each output was converted into a voltage and then amplified. A high-speed data acquisition system was employed to record and process the data. They observed that soot formation starts early in the premixed combustion stage and increases with engine load. The results also showed good correlation between the calculated soot concentration using the two-colour method and the measured concentration by direct sampling method.

Another method that allows in-cylinder temperature distribution to be measured by using the two-colour method is the endoscope-based measurement system as investigated by Shiozaki et al. (Shiozaki et al., 1996; 1998). They investigated the effects of fuel injection timing, engine load and EGR on flame temperature of a multi-cylinder production engine using the endoscope system and in another investigation, the influence of intake valve number and fuel injection rate was clarified. In both of the investigations, the flame light from the combustion chamber was divided into two colours by filters of wavelengths 470nm and 650nm. The images of combustion flame observed by the endoscope using the two wavelengths were recorded with a framing streak camera which includes two-colour optics, cooled CCD

camera, computer and a timing controller. The flame temperature and KL factor are immediately calculated by a computer using the two colour images from the CCD camera. The results showed that flame temperature reduces with increasing EGR and with retarded injection timing, whereas the flame temperature was higher with increasing engine load. As for the effects of intake valve number to flame temperature, they found that the maximum flame temperature of the two valves engine was higher than the four valves engine. This was due to the less uniformity of the two valves engine compared to the four valves engine causing higher maximum flame temperature. However, introducing pilot injection reduces the premixed combustion stage due to shorter ignition delay period which subsequently reduces the maximum flame temperature.

Hampson and Reitz (Hampson and Reitz, 1998) used multidimensional combustion and soot modelling to compare the in-cylinder temperature fields and soot concentration measurements obtained in conjunction with the images captured through the use of endoscope system. The effects of single and split injection strategies on soot concentration (KL factor) and temperature fields were investigated. The imaging system consists of the endoscope and optical linkage, relay optics (for image doubling, colour separation and focusing), a gated image intensifier, a CID camera and video monitor, a frame grabber, and a timer board to control time delay and gate width. The two interference filters used have a central wavelength of 550nm and 650nm. The engine used for the investigation was a turbocharged, single cylinder, heavy-duty, DI diesel engine. They found that split injection was beneficial to soot oxidation as compared to single injection due to several reasons. The temperature rise as a result of the immediate combustion of the second fuel pulse enhances soot oxidation and this continued into the expansion stroke due to overall higher temperatures which ensure continual burning of the remaining fuel.

Larsson (Larsson, 1999) optically studied the fuel injection and combustion of a single cylinder DI diesel engine using endoscope and a video system. In the optical measurement the influence of several parameters were investigated. The two-colour method was used to calculate the flame temperature and to get values of the soot concentration from the 24-bit RGB bitmaps images using CCD (Primary RGB colour filter) camera and image processing software. The colour information in the images was used to separate the liquid fuel spray image from the flame image and from these, liquid fuel spray penetration, flame lift-off and flame length were measured. From the two-colour method calculation, the flame temperature and NOx formation were found

to increase when the injection timing was advanced. However, exhaust smoke density was lower due to promotion of soot oxidation.

A summary of the investigation for in-cylinder temperature and soot concentration measurements using the two-colour method is given in Table 2.4. The principle of the two-colour method as described by Ladommatos and Zhao (Ladommatos and Zhao, 1994a), is provided in Appendix VII of the thesis.

Table 2.4: Summary of two-colour method investigations

INVESTIGATOR	EQUIPMENT/TECHNIQUE	PARAMETER STUDIED AND FINDINGS
Matsui et al. (1979). Tokyo Institute of Technology	Spectroscopic optical assembly and emission-absorption method for flame temperature and soot concentration measurements. Engine - Single cylinder, 4-stroke DI diesel engine. λ_1 529nm, λ_2 624nm, λ_3 738nm	• The standard tungsten lamp can be used as a simplified temperature calibration source. • Verification of the two-colour method to measure in-cylinder temperature and soot concentration was obtained by comparative measurement using emission-absorption method.
Matsui et al. (1980). Tokyo Institute of Technology	Spectroscopic optical assembly for simultaneous measurements of the visible & infrared wavelength regions. Engine - Single cylinder, 4-stroke DI diesel engine. Visible: λ_1 549nm, λ_2 750nm Infrared: λ_3 2300nm, λ_4 3980nm	• Flame temperature Both methods shows similar results during main combustion period but higher temperature values by infrared method at latter combustion period. • KL factor Value obtained from visible method is half the value obtained by infrared method. Reasons for differences could be due to: 1. spectral range constant, α, has a larger effect on the infrared region. 2. Selected wavelengths did not measure the characteristic of the temperature. 3. Effect of wall reflection was not taken into account.
Matsui et al. (1982). Tokyo Institute of Technology	Measurement of soot concentration by sampling of combustion gas using electromagnetic needle type sampling valve. Visible: λ_1 529nm, λ_2 738nm	• Injection amount. Maximum flame temperature is constant regardless of injection amount. Increasing injection amount, the KL factor becomes higher due to increase of soot formed in the cylinder. • Injection timing. Maximum flame temperature increases with injection timing advance. KL factor is maximum for injection timing -15^{0}ATDC and when injection timing is advance further, the maximum value of KL factor reduces due to: 1. Proportion of initial premixed combustion increases. 2. Flame temperature is too high to form soot. 3. Spray penetrates far ahead resulting in fuel to be accumulated in clearance part. Injection timing retard, KL factor decreases due to drop of flame temperature that suppress soot formation. • Nozzle opening pressure. Increasing injection pressure, provides faster combustion due to increase of spray momentum which promotes mixing process. Soot is oxidised faster and thus, yields low KL factor.

INVESTIGATOR	EQUIPMENT/TECHNIQUE	PARAMETER STUDIED AND FINDINGS
Yan and Borman. (1988). University of Wisconsin-Madison Engine Research Center	Measurement of radiation signal using an optical radiation probe. Engine: single cylinder heavy-duty diesel engine. λ_1 550nm, λ_2 700nm, λ_3 850nm	• Intake pressure. Increase intake air pressure, exhaust soot reduces. • Coolant temperature. Higher coolant temp., late portion of flame temp. increases, more soot production due to late burning which is due to delayed end of injection and lower injection rate. • Engine load. Soot production increases and maximum flame temperature increases with load. • Intake air temperature. Increasing inlet air temperature has no influence to the in-cylinder soot when flame temperature increase is too small to have any influence on soot production.
Ason et al. (1992). Shimazu Corp., Tonen Corp., Toyota Motor Corp. Doshisha University	High-speed photography of flame through optical window and borescope. Engine: single cylinder four-stroke horizontal water-cooled DI diesel engine. λ_1 653nm, λ_2 503nm	• Effects of low coolant temperature and low intake air temperature. Decrease coolant and intake air temp., maximum cylinder pressure, flame temperature and soot concentration reduce. Ignition delay is long and luminous small lump of flame appears in the visual field.
Kobayashi et al. (1992). Japan Automotive Research Institute and Advanced Combustion Engineering Institute Co. Ltd.	High-speed photography of flame through transparent piston bowl with extended piston. Engine: Single cylinder four-stroke DI diesel engine. λ_1 red, λ_2 blue	• Injection pressure. Increasing injection press., results in higher flame temperature due to rapid compression of burned gases. KL factor reduces due to higher oxidation rate of soot at late period of combustion. • Nozzle orifice diameter. Reducing nozzle orifice diameter, the entrained air into the spray increases and distribution of equivalence ratio in the flame is more spread, thus higher flame temp. • Combustion chamber geometry. Flame temperature is higher at the combustion chamber centre than on its periphery region. KL factor is larger at the tip of flame.
Zhang et al. (1993). Isuzu Advanced Engineering Center, Ltd.	High-speed photography of flame through transparent piston bowl and extended piston. Engine: Single cylinder four-stroke DI diesel engine. λ_1 650nm (red) λ_2 460nm (blue)	• Pumping rate. Increasing fuel pumping rate, flame motion is more active and produces higher flame temperature. • Nozzle hole diameter. Flame motion is more active with smaller injector orifice. • Injection timing. Flame temperature increases with advance injection timing.

INVESTIGATOR	EQUIPMENT/TECHNIQUE	PARAMETER STUDIED AND FINDINGS
Winterbone et al. (1994). University of Manchester Institute of Science and Technology.	High-speed photography of flame through transparent piston bowl with extended piston. Engine: Ricardo Hydra single cylinder DI diesel engine. λ_1 581nm, λ_2 631nm	• Swirl ratio. Too much swirl increases ignition delay period, NOx increases while soot decreases. • Fuel jet impingement on wall. Too much impingement increases soot formation. • Combustion chamber. Engine with symmetrical chamber have better utilisation of air available which would be equally mixed with all the fuel jets, giving more even distribution of temperature in the chamber, thus NOx and particulate reduce.
Arcoumanis et al. (1995a). Imperial College of Science, Technology and Medicine.	High-speed photography of flame through transparent piston bowl with extended piston. Engine: VW high-speed, 4 cylinder, 1.9L DI diesel engine. λ_1 450nm, λ_2 640nm	• EGR. The EGR effects on combustion increases with engine load and speed. Increasing EGR rates produces higher cyclic press. variations and lower high-temp. regions, and lower core flame temperature. Increasing EGR leads to increase in fragmentation of the temp and KL factor distribution, delay and reduce the overall formation of soot.
Li and Wallace. (1995). University of Toronto.	Measurement of light signals through optical fibre probes at various locations on the head of test engine. Engine: Single cylinder air-cooled DI diesel engine. λ_1 550nm, λ_2 700nm	• Different load levels. Soot formation is rapid and starts as soon as ignition occurs early in the premixed burning period. Amount of soot increases with engine load. Soot oxidation is relatively slow and dominates at the end of the mixing-controlled combustion period.
Shiozaki et al. (1996). Hino Motors Ltd.	Photography of combustion images through an endoscope and on-line image processing. Engine: Four cylinders DI diesel engine. λ_1 470nm, λ_2 650nm	• Fuel injection timing. Retarded injection timing, resulted in lower maximum value of mean flame temperature and lower NOx emissions, although ignition was delayed. • Engine load. Flame temperature higher with increasing engine load. • EGR. Increasing EGR, flame temperature reduces.
Shiozaki et al. (1998). Hino Motors Ltd.	Photography of combustion images through an endoscope and on-line image processing. Engine: Four and six cylinder DI diesel engine. High-speed photography of flame through transparent piston bowl with extended piston. Engine: Single cylinder DI diesel engine. λ_1 470nm, λ_2 650nm	• Intake valve number. Maximum temperature in 2 valve engine is higher than 4 valve engine. With the 2 valves engine, combustion are less uniform, producing higher max. flame temperature due to local stoichiometric combustion. This engine also achieved higher temp regions during combustion. • Fuel injection rate. Pilot injection reduces NOx emission due to shorter ignition delay and reduction of premixed burning. Pilot injection also reduces max flame temp.

INVESTIGATOR	EQUIPMENT/TECHNIQUE	PARAMETER STUDIED AND FINDINGS
Hampson and Reitz. (1998). University of Wisconsin-Madison	Spray and combustion imaging using endoscope optical system. Multidimensional modelling of soot concentration and flame temperature. Engine: Caterpillar, single cylinder, heavy-duty, DI turbocharged production engine. λ_1 550nm, λ_2 650nm	• Single and split injection. Split injection is beneficial due to; - time for soot oxidation increases at high temp - immediate and rapid combustion of the subsequent fuel injection pulses do not contribute significantly to further soot production - increase mixing and increase temp associated with rapid burning of high press spray from the subsequent injections.
Larsson. (1999). Scania CV AB.	Spray and combustion imaging using endoscope optical system and recording images on 24-bit RGB bitmaps format. Engine: Single cylinder DI turbocharged diesel engine. λ_1 red λ_2 blue	• Injection timing. Advancing injection timing increases average flame temp and NOx. Soot burn-off is also promoted leading to lower smoke density. • Inlet air temperature. Increasing inlet air temp, reduces ignition delay and diffusion combustion starts early. A lower heat release during premixed combustion is observed. However, inlet air temperature increase, produces larger regions with higher temp, thus higher NOx and lower smoke density.

CHAPTER 3: FUEL INJECTION CHARACTERISTICS

3.1 FUEL INJECTION SYSTEM

The reduction of emissions from the diesel exhaust requires the complete mixing of the injected fuel with the air and the complete combustion of the resulting mixture. The mixing process is governed by the injection characteristics, the air motion in the combustion chamber and the geometry of the piston bowl. Of these factors fuel injection is a very important parameter in the performance of a diesel engine. The fuel injection system is responsible for supplying the diesel engine with the fuel which must be injected at the precise time, with a metered amount and at high injection pressure. A pictorial diagram of a typical diesel fuel injection system (Paul-Trading-Corp, 2002) is shown in Figure 3.1. The pressure required for the fuel injection is generated by the system's fuel injection pump which forces the fuel through the injector which then sprays the fuel into the combustion chamber through small holes in the injector nozzle. The momentum and kinetic energy of the fuel spray provides the primary means for mixing the air and the fuel in the combustion chamber.

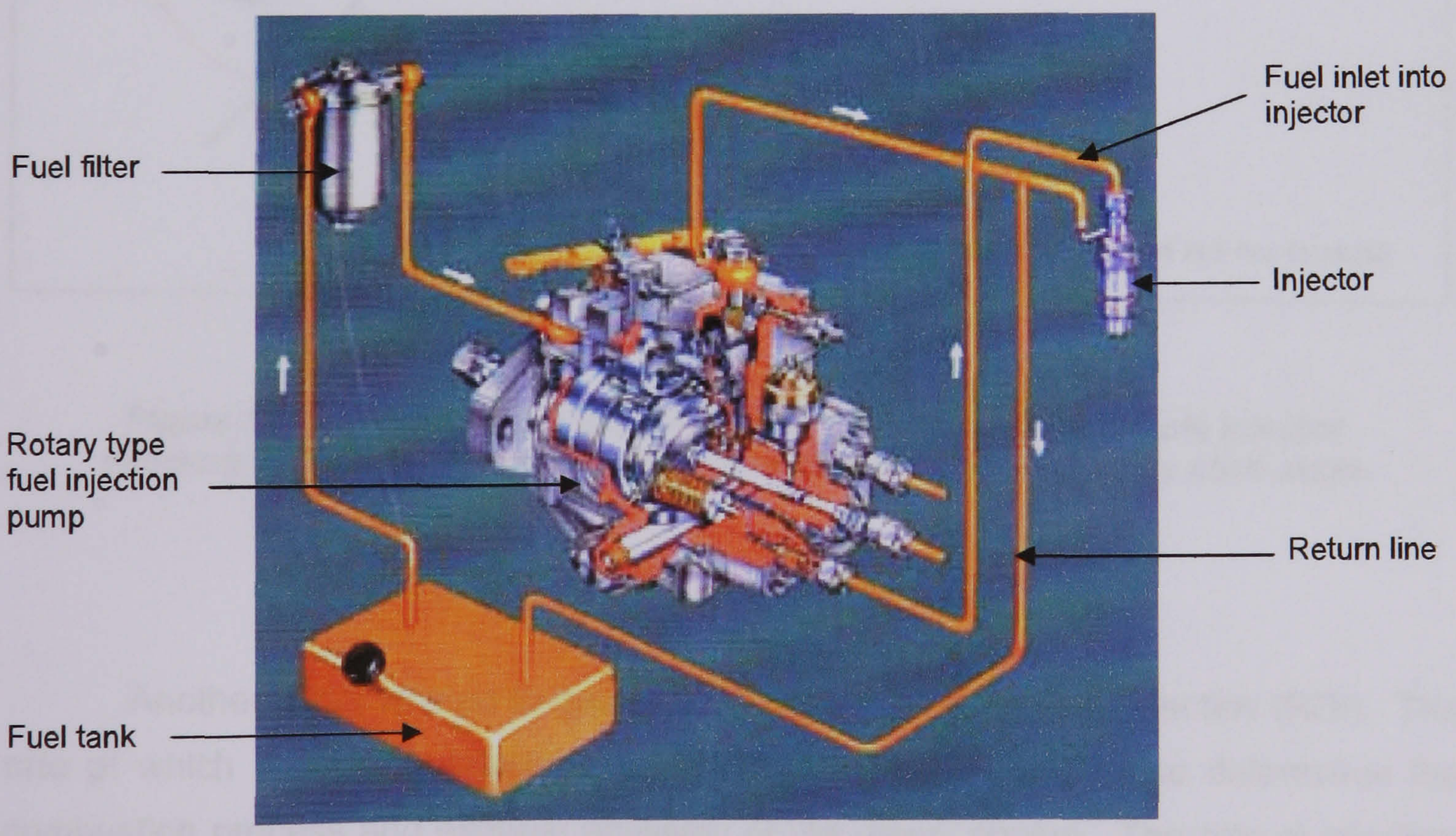

Figure 3.1: Diagram of a diesel fuel injection system (Paul-Trading-Corp, 2002)

The performance of the diesel engine also depends upon several other factors with respect to the injection system. The nature of the flow through the hole of the nozzle, i.e. whether the fuel is a single-phase flow or a cavitating two-phase flow upon exiting the nozzle hole, determines the quality of the injected fuel. This quality is characterised by the spray parameters such as the spray penetration length, the spray cone angle, the droplet size and distribution, and the spray pattern which define the diesel fuel spray structure. A typical structure of a diesel fuel spray from a multi-hole nozzle is shown in Figure 3.2.

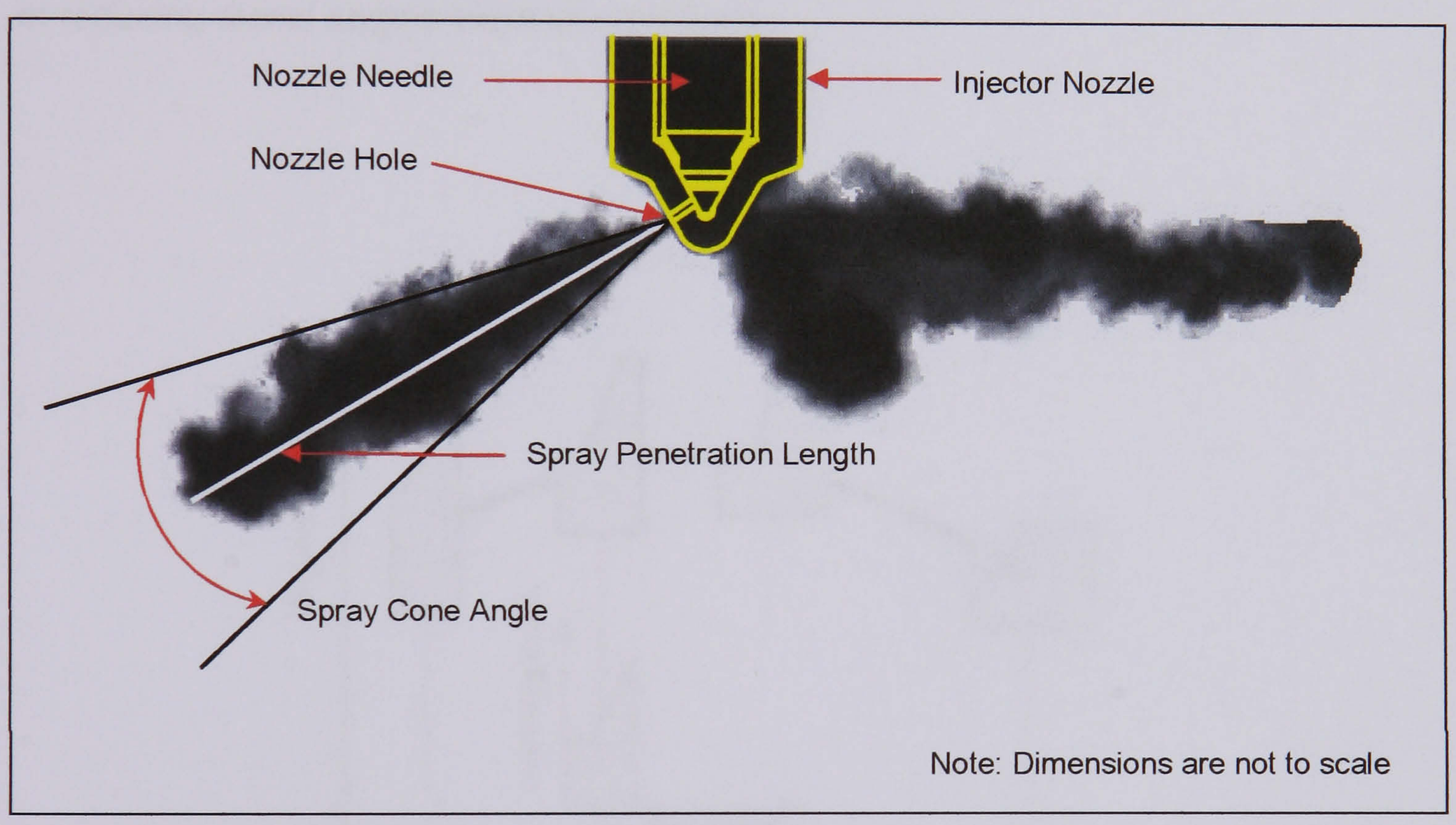

Figure 3.2: A schematic of the diesel fuel sprays from a multi-hole injector showing the nozzle tip details, spray penetration length and spray cone angle

Another factor related to the injection system is the rate of injection (ROI). The rate at which the fuel is injected into the combustion chamber also determines the combustion process and exhaust emission of the diesel engine. The rate of injection defines the fuel delivery quantity per stroke and the instantaneous mass flow rate

excessive fuel does not accumulate in the cylinder during the initial ignition delay i.e. before combustion begins. Injection should then proceed at such a rate that the rise in combustion pressure is not too great, yet the fuel is introduced as rapidly as possible to obtain complete combustion. The ability to change injection timing as a function of engine speed and load in addition to tailoring the injection rates according to the combustion events are therefore important strategies in reducing the exhaust emissions. Arcoumanis et al. (Arcoumanis et al., 1992) stated that, knowing the fuel spray characteristics and the fuel injection rate from a fuel injection system are thus paramount in determining the performance of a given engine. Examples of the rate of injection profiles as a function of engine speed and load are shown in Figure 3.3. These are the ideal injection rate strategies in order to employ the fuel injection system in reducing diesel engine exhaust emissions.

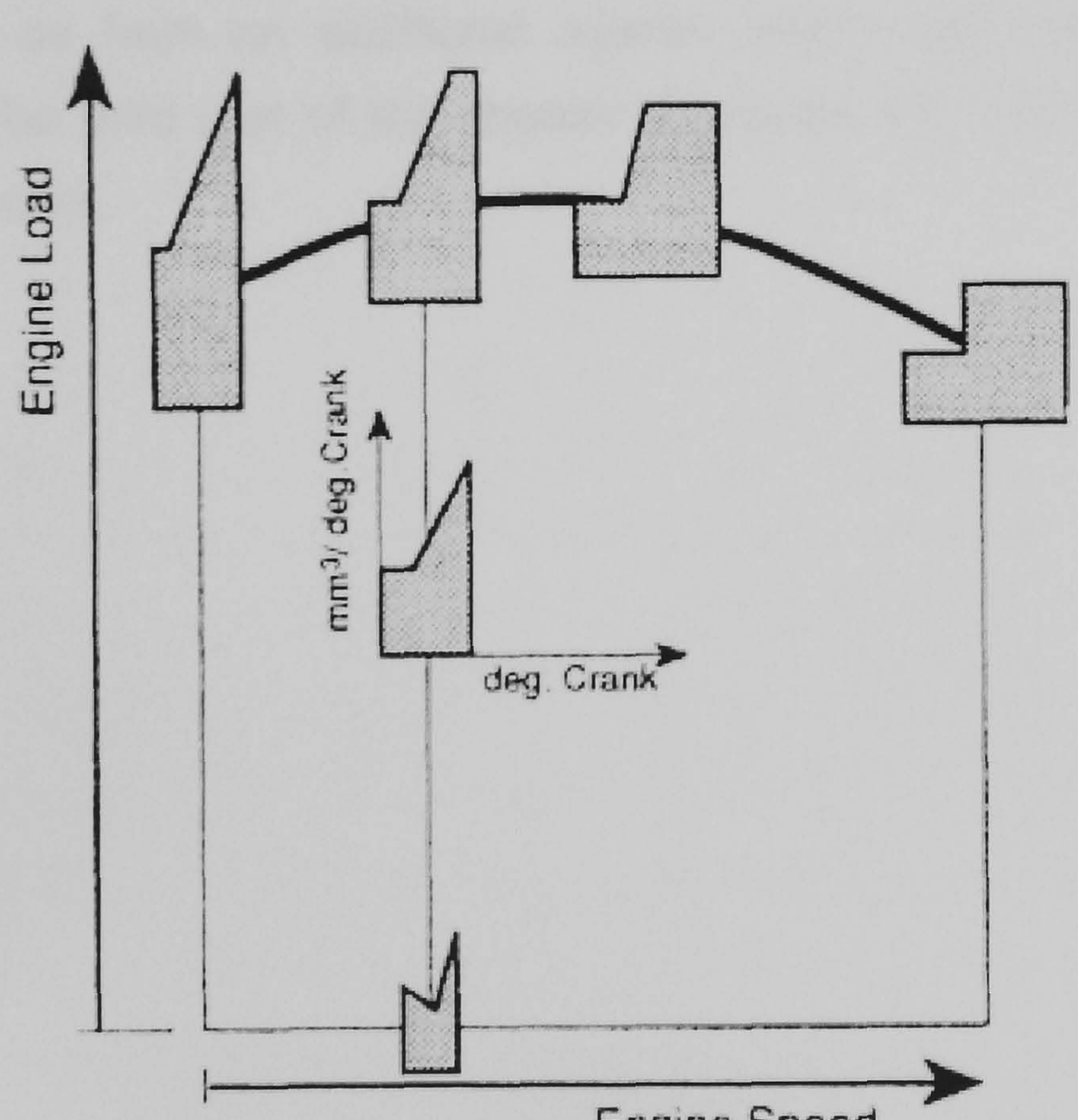

Figure 3.3: Ideal rate of injection characteristics
Source from (Bürgler et al., 1992)

This chapter is concerned with the fuel injection characteristics of various injectors and how they affect the spray structure and combustion process in the diesel engine. The main objectives of the current work are:

- To determine the spray pattern, penetration length and spray cone angle of various injectors by a visualisation technique.

- To measure the injection rate of the various injectors by using the 'Bosch Tube' injection rate meter.

The description of the work performed in order to achieve the above objectives is divided into three parts. The first part describes the experimental work to visualise the spray characteristics, i.e. the spray pattern, the spray penetration length and the spray cone angle of three different injectors. The second part describes the experimental work to measure the rate of injection (ROI) and calculation of the injection quantity per pump stroke from the same three injectors used in the spray visualisation work, as well as from an additional injector which was made available for this experiment. The third part of the chapter discusses the results obtained from both experimental works.

3.2 PART I: FUEL SPRAY CHARACTERISTICS

An investigation of the spray characteristics was performed to compare quantitatively the effects of changing engine speed and load (i.e. fuelling) on the spray pattern, the spray penetration length and the spray cone angle. Spray characteristics from three different injectors manufactured by Lucas-Delphi, having VCO nozzles of different hole diameters were investigated under atmospheric conditions at various injection pump speed and fuel lever position. The injection pump fuel lever position determines the amount of fuel delivery to the injector. The three injectors used in this investigation were obtained from the production Lister Petter diesel engine, from which two injectors are from the 4-cylinder engine series and one from the 3-cylinder engine series. The first set of injectors having five holes with each hole diameter of 0.194 mm were used in the standard 4-cylinder engine while the second set of injectors having five holes but of larger hole diameter of 0.225 mm were from the same engine series but with a turbocharger. Both injectors have a spray angle of 140°. The total flow area of the standard injector is 0.148 mm^2 with a flow rate of 950 cc/min. The injector for the turbocharged engine has a total flow area of 0.199mm^2 and a flow rate of 1300 cc/min. The third set of injectors had the same flow rate as the standard injector, i.e. 950 cc/min, but with six nozzle holes and a spray angle of 140° spacing. These injectors were used on the 3-cylinder engine series. Each hole diameter was 0.177 mm with a total flow area 0.148 mm^2. The standard injectors were used as the reference injectors in this investigation and were designated as L1, while the injectors for the engine with turbocharger were designated as L2 and the injectors with six-holes as L3. Specifications of the injectors are given in Table 3.1.

Images of the diesel sprays from all three injectors injected into a constant volume spray chamber filled with calibration fluid were taken using a back-lit technique. The reasons for this were that the constant volume spray chamber could only be used with compressed air up to a maximum pressure of 15 bar and visualisation of the sprays was hampered due to smearing of the chamber windows as a result of fuel impingement upon injection. Therefore, the strategy for injecting liquid into liquid was employed to assist the visualisation of the sprays. The strategy for injecting liquid into liquid was investigated by Way (Way, 1977) which reported that the behaviour of a fuel jet in air may be represented by a water jet in water when the compressibility effects are not considered. Way derived appropriate equivalence air jet to fuel jet ratios for the momentum, density, mass flow, combustion chamber dimensions, flow dynamic and

time scale with respect to the crank angle. The findings showed that the visualisation of the spray was simpler and similar flow dynamic could be obtained at lower velocities.

The images obtained from the experiments have provided information on (a) the spray plume shape and pattern, in addition to (b) the liquid spray penetration length and (c) the spray cone angle. This information will be matched with the heat release rate profile in the combustion chamber in conjunction with the measured in-cylinder pressure traces and the exhaust gas emissions measurements.

Table 3.1: Injector specifications for spray imaging.

Injector Type	L1	L2	L3
Engine use	Standard 4X90	Turbo 4X90	Standard 3X90
Injector Manufacturer	Lucas-Delphi	Lucas-Delphi	Lucas-Delphi
Nozzle Identification Number	LJBT 01601	LJBTX 01607	LJBT 01602
Injection Pressure (bar)	575	575	575
No. of Orifice	5	5	6
Orifice Diameter (mm)	0.194	0.225	0.177
Orifice l/d ratio	1/0.194	1/0.225	1/0.177
Spray Angle (degree)	140^{o}	140^{o}	140^{o}
Nozzle Opening Pressure (bar)	250	258	255
Flow Rate (cc/min)	950	1300	950
Total Flow Area (mm^2)	0.148	0.199	0.148

3.2.1 Spray Visualisation Experimental Set-Up

The experimental set-up for imaging the fuel sprays consisted of a constant volume spray chamber, the fuel injection system, an imaging and recording system, and an analysis system for the resulting images. The equipment arrangement for the experiment is shown in Figure 3.4. The injectors used were Lucas-Delphi diesel injectors, VCO type nozzle with single stage lift having an injector body diameter of 17 mm. Three injectors were used, each representative of the range of injectors supplied by Lister Petter, i.e. a standard injector, L1, which was used as the reference injector, a high flow rate injector, L2, and a high injection rate injector, L3. Figure 3.5 shows images of the injectors used in the experiment. Prior to commencing the experiment, the nozzle opening pressure (NOP) of all injectors was measured on a nozzle test rig, the Hartridge Nozzle Testmaster. This procedure also provided a chance for a visual inspection of the sprays from each nozzle holes in order to observe any hole blockages or spray pattern differences. The data from these measurements are recorded in Table 3.2.

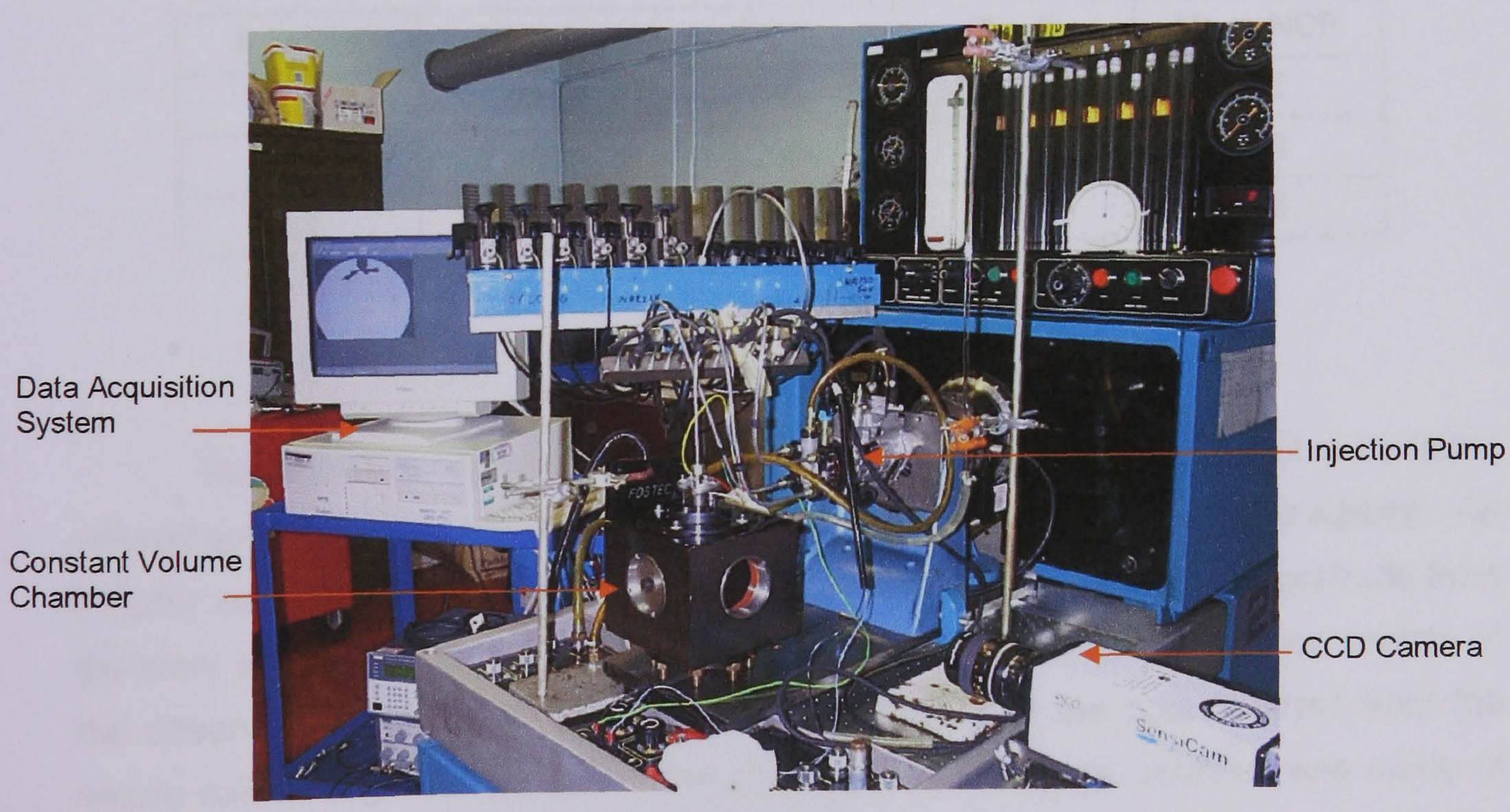

Figure 3.4: Equipment used for the spray visualisation experiment

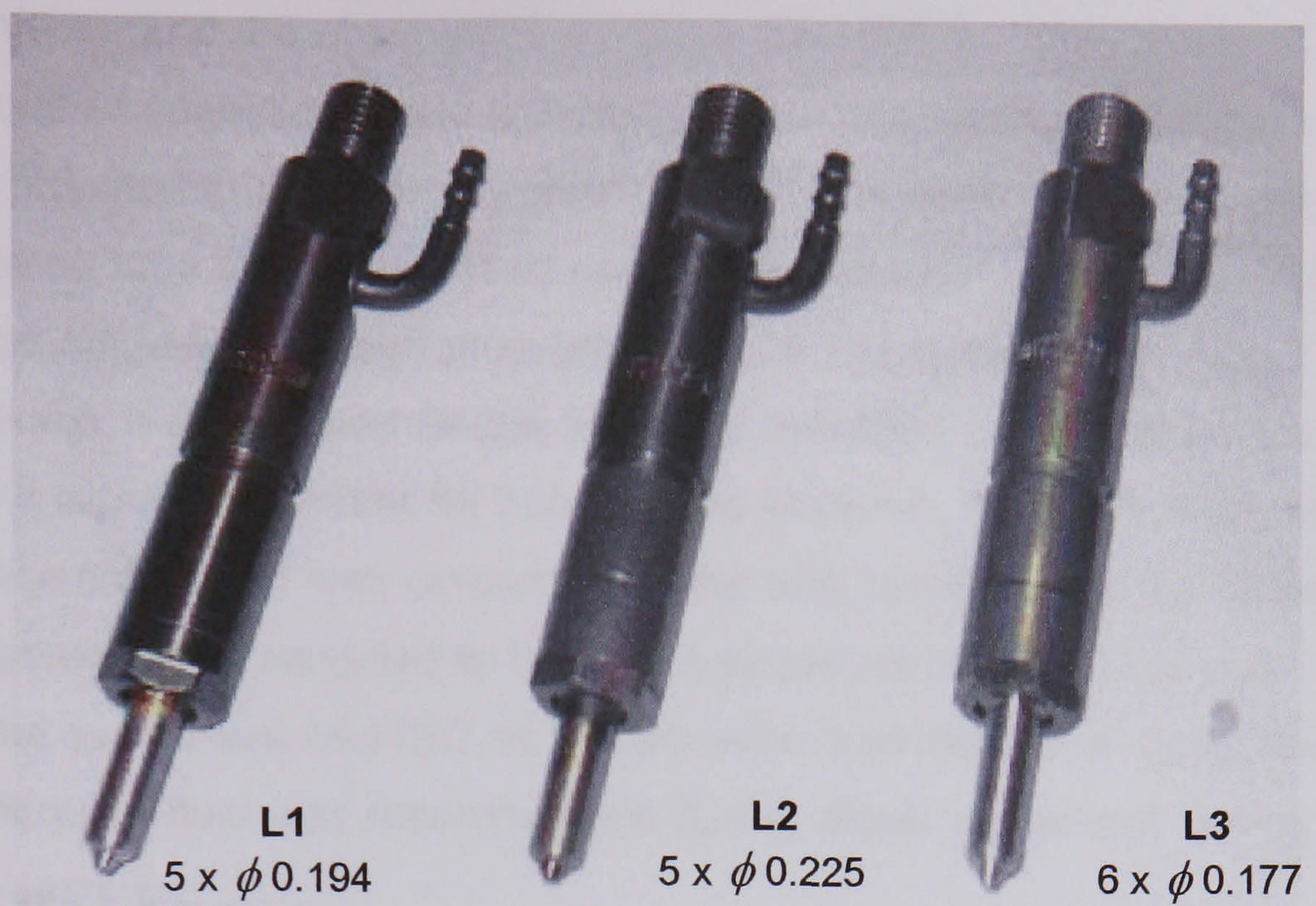

Figure 3.5: Image of the injectors used in the experiment

Table 3.2: Nozzle opening pressure measurements

Injector	Try 1	Try 2	Try 3	Mean NOP
L1	240	245	240	242
L2	258	255	255	256
L3	255	255	250	253

The injectors were mounted sequentially onto the upper face of a constant volume spray chamber which was used to visualise the fuel spray from the injector. An adaptor was fitted to the injector which allowed the tip of the injector to protrude from the inner top surface of the chamber such that the tip was visible in the top section of the observation windows. This enabled visualisation of the sprays direct from the nozzle exit through the window. The constant volume spray chamber was made of steel, having a total volume of 725 cm^3 and was capable of operating at chamber pressures up to 15 bar. It was designed to accept up to four 80 mm diameter windows, three on the sides and one at the bottom. Sectional and pictorial views of the chamber

with the injector and the observation windows mounted on it are shown in Figure 3.6. Inlet and outlet connections were provided on one of the side of the spray chamber. A hose was attached to the outlet connection as a drain outlet. The inlet was connected to a calibrated tube that was used to measure the amount of fuel being injected. The injector was supplied with high pressure fuel by a Delphi rotary pump type 1333. The injection pump was mounted on the Hartridge HA-2500 pump test bench which was fitted with a digital tachometer for pump speed read out. Only one high pressure pipe from the injection pump was connected to the test injector while the other three high pressure pipes were connected to the return system of the Hartridge unit. The test oil used for the experiment was ISO 4113 calibration fluid instead of diesel fuel. The use of the calibration fluid was recommended during diesel equipment testing due to the following reasons:

- Although it has similar characteristics to diesel fuel, the fluid viscosity and density characteristics are controlled within a very narrow limit to ensure accurate and repeatable results.
- It does not evaporate readily. Hence, it is much safer and more pleasant to work with.
- It has anti-corrosion additives, in addition to oxidation stability and anti-wear characteristics which are beneficial in protecting the fuel injection system.

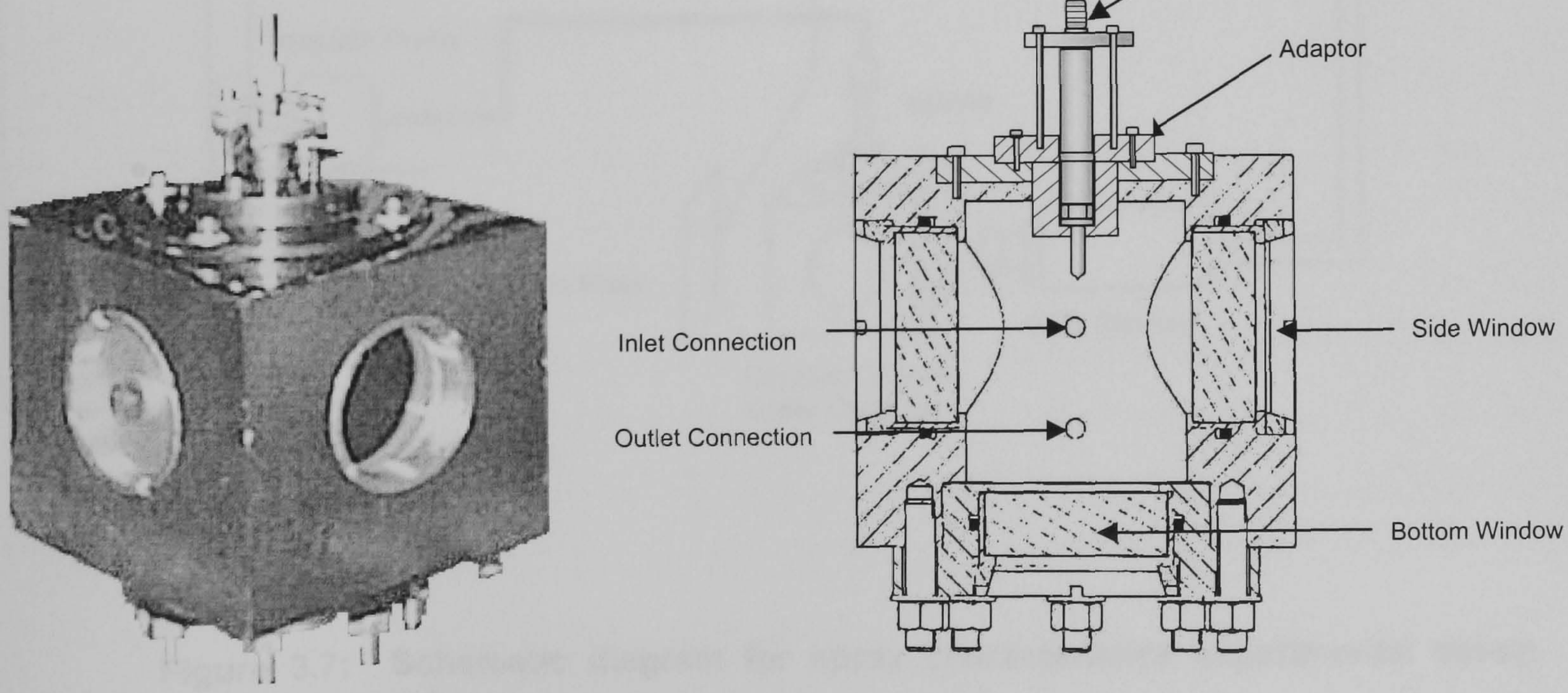

Figure 3.6: Constant volume spray chamber used in the spray visualisation experiment

3.2.2 Imaging System

Images of the spray in the constant volume chamber were captured using a high resolution CCD camera with a back-lit illumination scheme. The apparatus and experimental set-up for the spray visualisation is shown schematically in Figure 3.7. An EG&G MVS 7020 Xenon flash light coupled to a Fostec fibre optic panel was used to provide a uniform light intensity distribution against which the nozzle and the sprays were imaged. The strobe panel was placed in front of a window on one side of the chamber while the camera was positioned in front of a window on the opposite side.

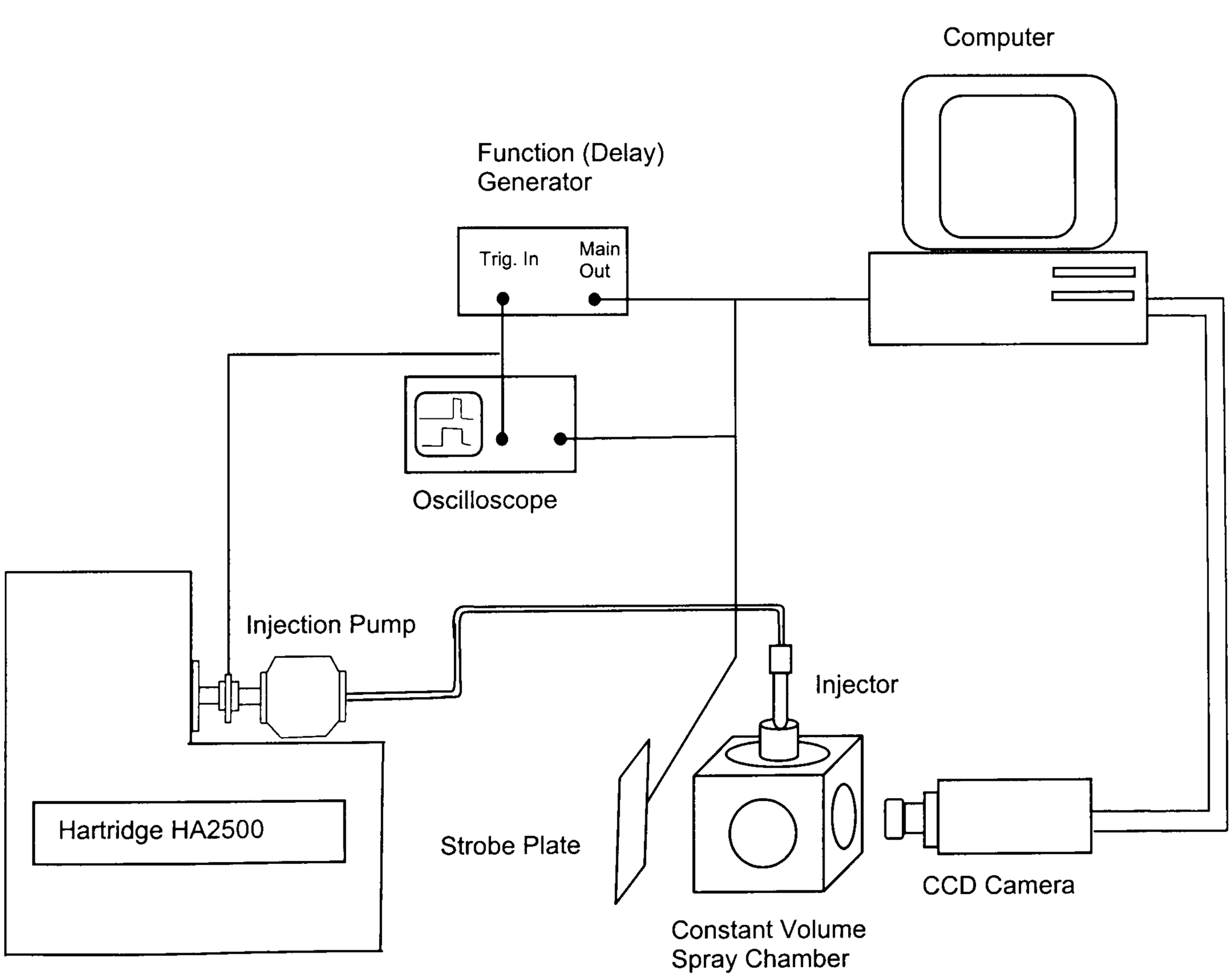

Figure 3.7: Schematic diagram for spray characteristics experimental set-up

The images were digitally recorded with a PCO Sensicam Fast Shutter CCD camera equipped with a Nikon 55 mm focal length macro lens. It provided an image size of 62.2 mm by 49.6 mm, represented by 1280 by 1024 pixels, a depth of field of approximately 3 mm with an intensity level resolution of 12-bits. The camera shutter speed was set to 5 micro-seconds with a maximum frame rate of 8 Hz at full pixel resolution. A magnetic pick-up generated an external trigger with every rotation of the shaft of the Hartridge unit. This provided an electronic signal, referenced to the start of injection, which, through a variable delay unit, controlled both the flash unit and camera. The Sensicam software enabled control of the camera delay period with respect to the trigger signal, exposure time and the number of images captured in addition to recording and previewing the images. An imaging processing software package, PCO Picture, purpose-build to handle the 12 bit images created by the PCO Sensicam Fast Shutter CCD camera was, used to analyse the captured images. This software also allowed the camera image format to be converted into standard Windows bitmaps format for further processing, the ability to scale the images and removal of image backgrounds.

3.2.3 Operating Conditions

The experiments to visualise the spray development were first performed with a fixed fuel lever position and a fixed injector pump speed for all three injectors. It must be realised that the injector pump speed was representative of one-half of the engine speed since the pump was used on a four-stroke diesel engine. The selected speed ranged from the minimum engine speed at maximum load, i.e. 1000 rpm, to the engine speed at maximum torque, i.e. 2000 rpm. Hence, pump speeds of 500 rpm and 1000 rpm respectively. The selected injector was first mounted onto the spray chamber. Then, the supply oil from the Hartridge unit to the injector pump was switched on before the motor was started. The injection pump speed was increased to the required speed. When the pump speed had stabilised, the camera was then set to capture 30 images in sequence with an exposure time of 1 micro-seconds and a delay of 5 micro-seconds after the trigger signal. This delay time between the time of the flash triggering and the image being captured ensured that the flash was at its maximum intensity when the exposure occurs. The fuel injection gross flow rate was determined by measuring the time to collect 6 ml of fuel. Real time images of the sprays were

displayed on the computer monitor while the exposure time with respect to the start of injection, was provided by the function generator unit and displayed on an oscilloscope. Upon completion, the injector was removed and replaced with another injector. This was done in order to obtain images from each of the different injectors without changing the lever position. The imaging procedures were repeated again in order to obtain a total of 30 images of the other injectors at the same lever position and pump speed setting. After imaging of all the sprays from the three injectors, the lever position was adjusted to a new position, and imaging of the spray at the previous pump speed was performed. This was again repeatedly done for all lever positions and pump speed. The experimental conditions are shown in Table 3.3.

Table 3.3: Experimental conditions for spray imaging

Pump Speed (RPM)	500, 700, 800, 900, 1000
Lever Position (%)	25, 75, 100
Injectors	L1, L2, L3
*** All images were taken at the time instant of 31 ms after the trigger signal for start of injection.**	

Upon completing the above set of experiments, a series of images were captured at the increment of 0.25ms using the standard 5 holes injector at 50% lever position and a constant pump speed of 900 RPM. At each setting, 10 images were captured upon which only one image which provide the best visual clarity was selected to be representative of the structure of the sprays at that instant. These images were then compiled to represent the sequence of spray propagation from the start of injector to the end of injection. An animation of these images was also produced with the intention to be used during slide presentations.

3.3 PART II: INJECTION RATE MEASUREMENT

Measurements of the rate of fuel injection from four nozzles were performed using an injection rate meter commonly known as the Bosch Tube meter. The instrument was specifically ordered from AVL Graz for measurement of injection characteristics for both gasoline and diesel injectors. Various adaptors were provided in order to enable measurement of a wide range of injectors. The design of the injection rate meter was based on a report by Wilhelm Bosch (Bosch, 1966) consisting of primarily a long high pressure tube of constant internal diameter. Details of the Bosch Tube meter used will be described in the next section of this chapter. The injection pressure traces against time (or crank angle) obtained from the Bosch Tube meter were then used for calculation of the injection rate.

The injection rate equation was derived from the pressure-velocity theory, which is only valid for a single pressure wave in an instationary flow, as reported by Arcoumanis et al. (Arcoumanis et al., 1992). The theory states that the pressure wave entering the control area is in equilibrium with the external force acting on the control surfaces, i.e. changes of pressure in the fluid are propagated at the velocity of sound, a, and produces a corresponding change in fluid flow velocity, i.e.

$$P = a\rho U \tag{3.1}$$

Where:

P Pressure, N/m^2

a Velocity of sound in fluid, m/s

ρ Density of fluid, kg/m^3

U Fluid flow velocity, m/s

When the fuel from the injector nozzle was discharged into the high pressure tubing, the continuity equation indicated that the instantaneous injection flowrate, dq/dt, injected from the nozzle into the measuring tube produced an equivalent liquid flow velocity, U, whose magnitude depended on the internal diameter of the tube. Hence;

$$\frac{dq}{dt} = A_t U \tag{3.2}$$

Where:

A_t Flow area of the tubing, mm^2

q Fuel quantity, mm^3

t Time, s

This flow gave rise to a pressure wave which was proportional to a pressure signal representative of the instantaneous injection flowrate, dq/dt. Thus, the injection rate based on the pressure trace was obtained by substituting equation (3.1) into (3.2), which yields:

As a function of time,
$$\frac{dq}{dt} = \frac{A_t}{a\rho} P \tag{3.3}$$

Or as a function of crank angle,
$$\frac{dq}{d\theta} = \frac{A_t}{6Na\rho} P \tag{3.4}$$

Where N is the pump speed in rpm.

The cumulative fuel quantity per pump stroke, Q_{stroke} was calculated by integration of equations (3.3) and (3.4) over the injection period;

$$Q_{stroke} = \int_{SOI}^{EOI} \frac{dq}{dt} dt = \frac{A_t}{a\rho} \int_{SOI}^{EOI} P dt \tag{3.5}$$

or

$$Q_{stroke} = \int_{SOI}^{EOI} \frac{dq}{d\theta} d\theta = \frac{A_t}{6Na\rho} \int_{SOI}^{EOI} P d\theta \tag{3.6}$$

3.3.1 Injection Rate Measurement Experimental Set-up

The test rig for measuring injection rate from the nozzle consisted of the Bosch Tube meter, an injection pump, a 30 kW constant torque motor, a shaft encoder and a data acquisition system. Four Lucas-Delphi diesel injectors were used in the experiment. Three of these injectors were the same set of injectors as used during the spray visualisation experiment. An additional set of injector was made available for the current experiments in order to make further comparisons. The fourth set of injector has a low flow characteristics of 700 cc/min, with the nozzle having 5 holes and a spray angle of 140°. Each hole has a diameter of 0.171 mm providing a total flow area of 0.115 mm^2. The same designations for the injectors were also used for this experiment, i.e. the standard injectors as L1, the turbo injectors as L2, the injectors with six holes as L3 and finally the fourth injectors as L4. Specifications of all four injectors used for the injection rate measurement are shown in Table 3.4.

These injectors were also tested on the Hartridge Nozzle Testmaster during which the nozzle opening pressure (NOP) of each sets of injectors were recorded and at the same time, visual inspections of the sprays were made. Results from these measurements are produced as a bar chart and shown in Figure 3.8

Table 3.4: Injector specifications for injection rate measurement

Injector Type	L1	L2	L3	L4
Engine use	Standard 4X90	Turbo 4X90	Standard 3X90	Not used
Injector Manufacturer	Lucas-Delphi	Lucas-Delphi	Lucas-Delphi	Lucas-Delphi
Nozzle Identification Number	LJBT 01601	LJBTX 01607	LJBT 01602	LJBTX 01603
Injection Pressure (bar)	575	575	575	575
No. of Orifice	5	5	6	5
Orifice Diameter (mm)	0.194	0.225	0.177	0.171
Orifice l/d ratio	1/0.194	1/0.225	1/0.177	1/0.171
Spray Angle (degree)	140°	140°	140°	140°
Nozzle Opening Pressure (bar)	235 ± 2	240 ± 2	240 ± 2	240 ± 2
Flow Rate (cc/min)	950	1300	950	700
Total Flow Area (mm^2)	0.148	0.199	0.148	0.115

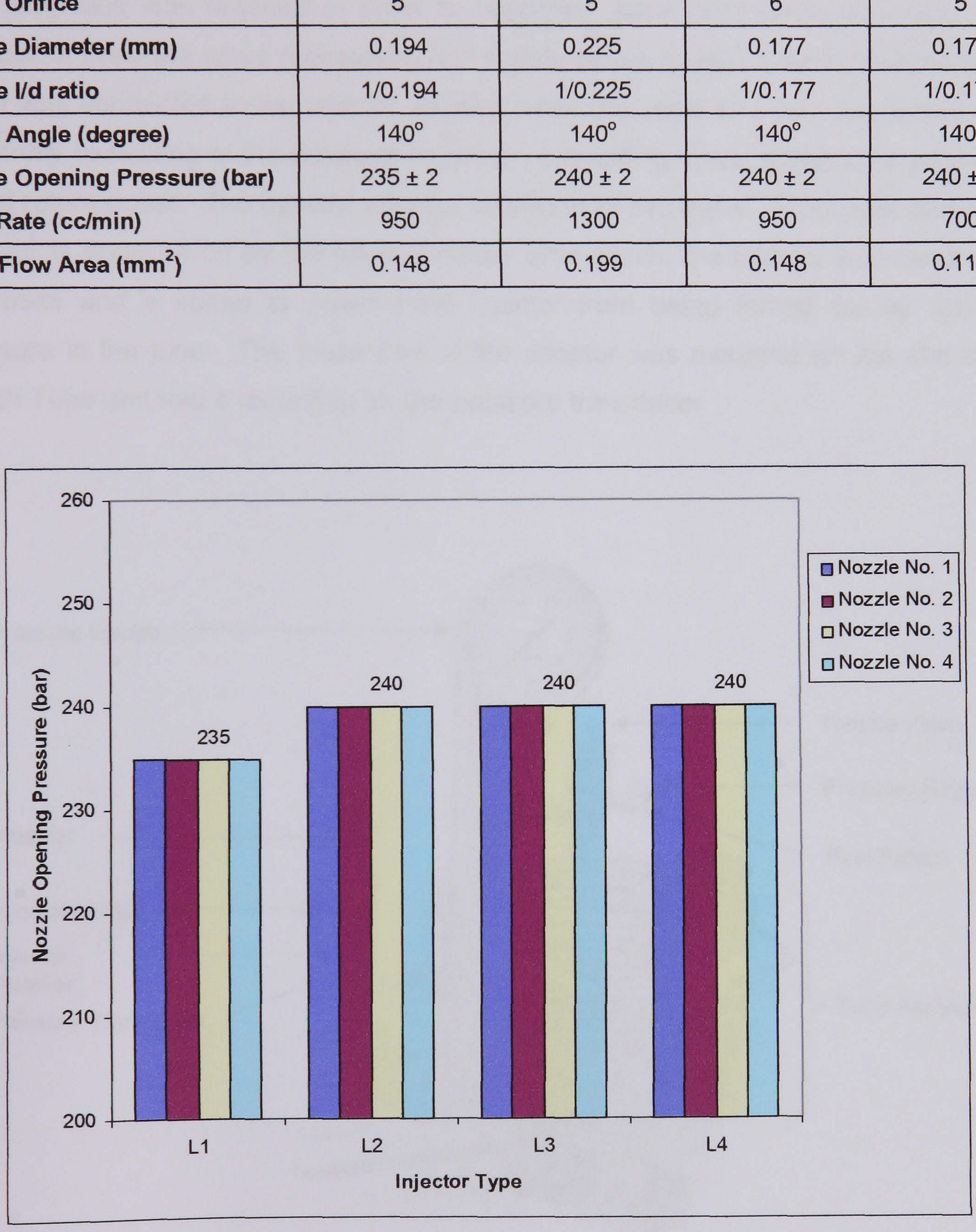

Figure 3.8: NOP measurements of all four sets of injectors

The Bosch Tube was made of a long length of high pressure tube of constant internal diameter. The tube is made of several sections of known tube length and volume which enables either diesel or gasoline applications. For the diesel injectors test, the total tube length measured 18,192 mm comprising of one 6,032 mm, one 6,017 mm, two 3,017 mm lengths, in addition to three 30 mm long connectors and a 19 mm injector adaptor. The fully assembled Bosch Tube meter is shown in Figure 3.9. The long tube was required in order to maximise wave attenuation and reduce the number of pressure wave reflections over a wide speed range. One end of the Bosch Tube was connected to the injector adaptor while the other end was connected to an assembly consisting of the pressure regulator, a throttling valve, a pressure gauge and a fuel return outlet. The injector adaptor consisted of two parts. The upper part of the adaptor is screwed on by the injector holder onto which, the injector was secured by two bolts and a clamp to prevent the injector from being forced out by the high pressure in the tube. The lower part of the adaptor was mounted on the end of the Bosch Tube and had a mounting for the pressure transducer.

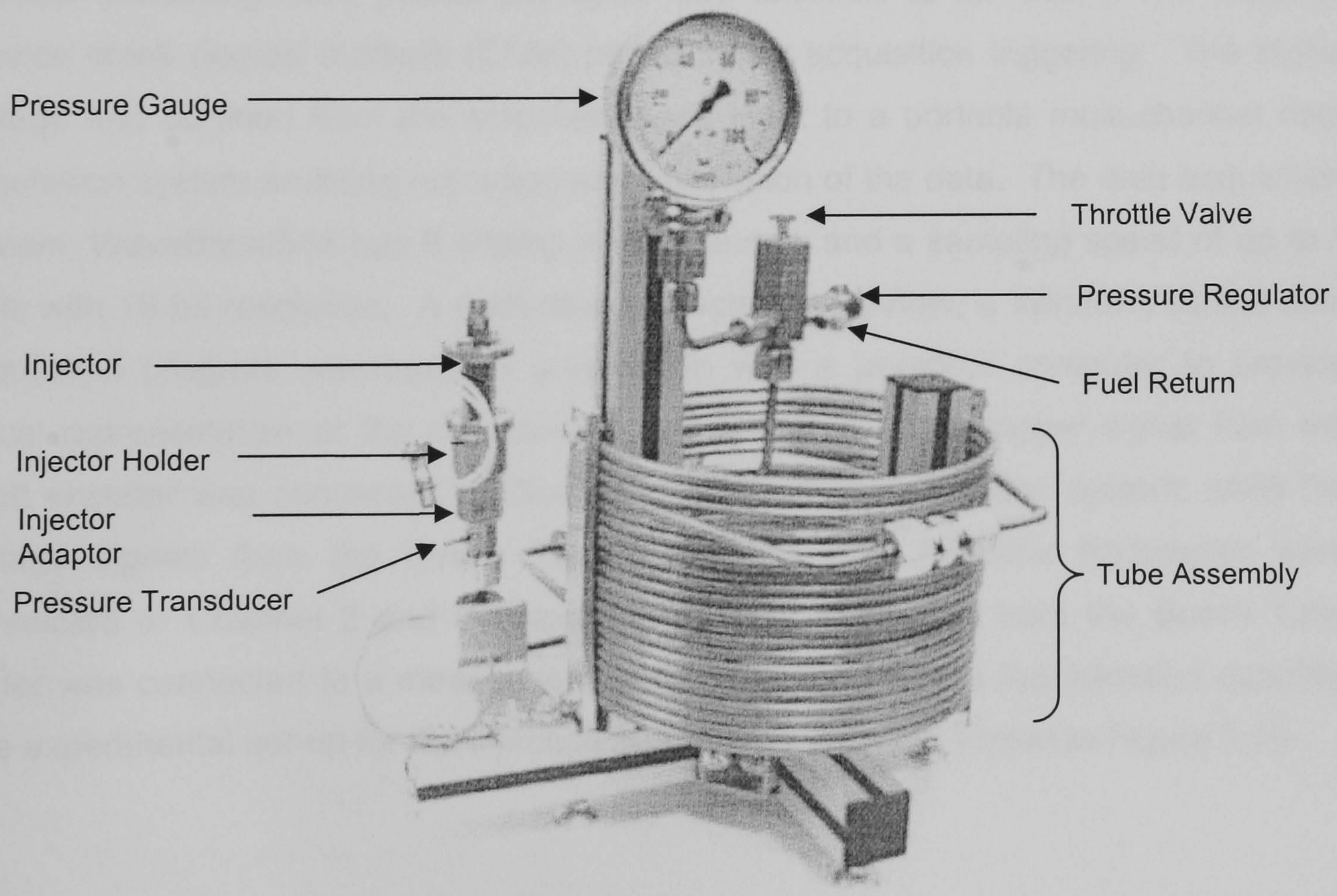

Figure 3.9: A completely assembled Bosch Tube

The injector was driven by a Delphi rotary pump type 1333, the same fuel injection pump used in the spray imaging experiment. However, in this experiment, the pump was coupled to a 30 kW constant torque motor which was mounted on a specially designed mobile injection test rig. A magnetic pick-up mounted on the rig provided electronic signals for pump speed measurement. Only one high pressure fuel line from the injection pump was connected to the test injector while the other three high fuel lines were connected to the fuel volume measuring system of the rig. The fuel line pressure was obtained by attaching a Kistler 4065 A1000 pressure transducer to the high pressure pipe at a location 80mm from the injector connector. A Kistler 4617 AD piezo-resistive amplifier was used to convert the pressure signal into a 0 to 10 volts analog output voltage. The pressure produced from the fuel injected into the measuring tube of the Bosch Tube meter was measured by an AVL GM12D pressure transducer. A Kistler Type 5011 B10 charge amplifier was used to amplify and convert the pressure signal from the transducer into a measurable voltage for all the measurements. Both the AVL GM12D and the Kistler 4065 A1000 pressure transducers were calibrated using a dead weight tester and the calibration curves for both pressure transducers are shown in Appendix I and II respectively. A shaft encoder producing 3600 pulses per cycle was attached to the end of the motor to provide crank degree markers (CDM) per cycle for acquisition triggering. The signal voltage and duration from the amplifiers were input to a portable multi-channel data acquisition system enabling recording and acquisition of the data. The data acquisition system, WaveBook/516 has 8 analog input channels and a sampling speed of up to 1 MHz with 16-bit resolution. A dedicated software, WaveView, a Windows-based data acquisition program was used in conjunction with a personal computer to provide visual representation of the collected data in real-time. The trigger signal from the shaft encoder was connected to Channel 1 of the data acquisition system, while the voltage signals from the Bosch Tube transducer and fuel line transducer were connected to Channel 2 and 3 respectively. The fuel return from the Bosch Tube meter was connected to a measuring cylinder to determine the fuel injection quantity. The experimental set-up for the injection rate measurement is shown in Figure 3.10.

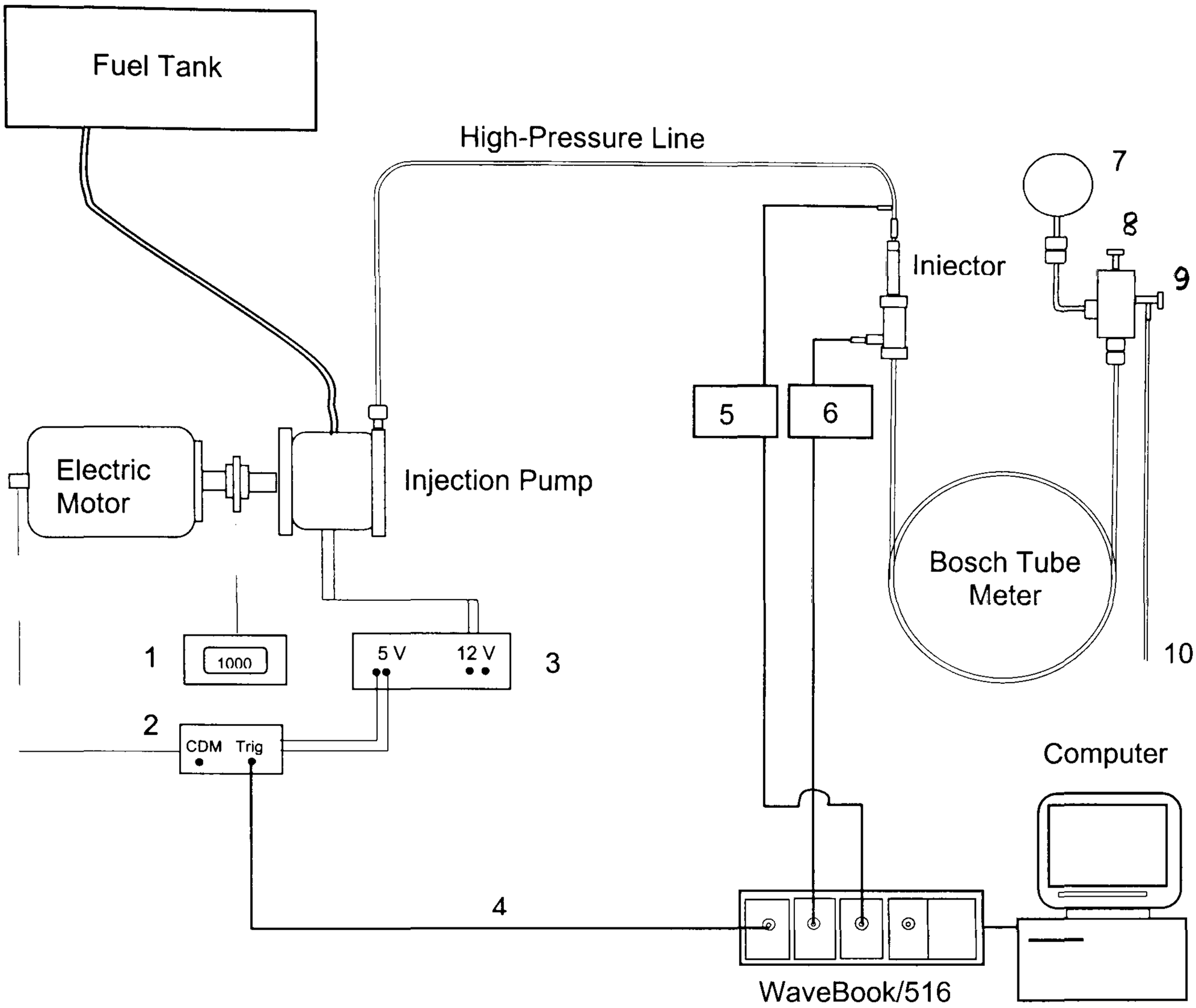

1	Pump Speed Reader	6	Injection Pressure Amplifier
2	Encoder Box	7	Pressure Gauge
3	Power Supply Box	8	Throttle Valve
4	Trigger Signal	9	Pressure Regulator
5	Fuel Line Pressure Amplifier	10	Fuel Return Line

Figure 3.10: Experimental set-up for injection rate measurement

3.3.2 Operating Conditions

The experiments to measure the rate of injection from all four injectors were performed at two constant pump speeds of 900 and 1000 rpm with five different fuel lever positions, i.e. variable fuel delivery. These speeds were chosen to represent the minimum full load engine operating speed (1800 rpm) and the normal engine operating

speed (2000 rpm) for stationary applications respectively. The lever positions are referred to as 0%, 25%, 50%, 75% and 100% representative of the amount of fuel delivery. The selected injector was first inserted into the injector holder and firmly placed into the injector adaptor with the clamps provided. One of the high pressure tubes from the injector pump was connected to the injector. The fuel supply valve from the fuel tank to the injector was then opened. The electric motor was started and the pump was brought to the required speed. The Bosch Tube assembly was first filled with test fluid through the long measuring tube into the throttling area. The test oil used throughout the experiment was the recommended ISO 4113 calibration fluid. The throttle valve on the Bosch Tube meter allowed adjustment for a variable flow out of the tube for the different flow conditions by varying the throttle area between 0 and 1.1 mm^2, as noted in the Bosch Tube meter operating manual (Gill, 2002). When the system was first started, the throttle valve was wide open to prevent the built up of excessive pressure. The pressure regulator provided a residual pressure in the tube while the system was in operation which approximated the engine combustion chamber compression pressure. Once the calibration fluid emerged from the return line, the back pressure was set to 50 bar for the diesel injector test by adjusting the pressure regulator. While running at the required speed and fuel delivery, the trace from the pressure transducer as well as the reflections of the injection pulse were observed on the computer monitor screen for a full cam revolution. The throttle area was then closed to reduce the flow area such that the best attenuation of the pressure waves in the system was obtained. Adjustment of the throttle valve was not required for other injection quantities or pump speeds as the pressure regulator would self-compensate for the reduced flow. The test conditions are shown in Table 3.5.

Table 3.5: Experimental conditions for injection rate measurement

Pump Speed (rpm)	900 1000
Lever Position (%)	0 25 50 75 100
Injectors	L1 L2 L3 L4

3.4 PART III: RESULTS AND DISCUSSION

The results and discussion for the spray imaging and fuel injection rate experiments are presented separately. The first section will discuss the results obtained from the spray imaging and the results from the rate of injection measurement will follow in the next section.

3.4.1 Results From Spray Visualisation Experiment

On the first attempt to visualise the spray emerging from the injector nozzle during the test run at a pump speed of 900 rpm, the sprays were seen to impinge on the chamber windows causing fuel misting and smearing on the glass which hindered visualisation of the sprays. The fuel that was collecting in the chamber started to foam due to agitation of the sprays in the chamber, making observation of the spray very difficult. Measurement of the fuel quantity in the tube was also difficult due to fluctuation of the fuel level in the tube. A decision was then made to fill the chamber with calibration fluid which was the same fluid used for the test. Upon doing this, the fluid in the chamber became steady and the sprays were able to be imaged without any of the above interference. This strategy of injection liquid into liquid was performed by Way (Way, 1977), as discussed in section 3.2 of this chapter.

The 12-bit, greyscale images of the sprays exiting from the nozzle captured by the CCD camera were edited using a specialised software, PCO Picture Viewer. This software was developed for imaging and analysing diesel sprays by Schneider (Schneider, 2002). The software stored the images into 16 bit BMP files. In order to be able to process the images using Windows platform, these images were saved to 8 bit BMP files which are a standard Windows bitmap format. This also significantly reduces the image file size from the original 2.5 MB to only 340 KB. Therefore, the resolution of all the images shown here were not exactly the same as when using the PCO Picture Viewer, especially when the contrast of the greyscales cannot be reproduced. Hence, one spray image from injector L1 and one spray image from injector L3 were selected to assist in visualising the different spray profile from each injector type. From these images, sketches of the spray structure were drawn in order to show the spray trajectory from each injector nozzle tip. A sketch of the image from the standard 5-hole injector, L1 is shown in Figure 3.11, while Figure 3.12 shows the sketch of an image from the 6-hole injector, L3. The spray profile from the turbo 5-hole

injector, L2, was not drawn since it has the same spray trajectory pattern as L1. The tip of the nozzle is shown at the top of each image which has a diameter of 7 mm. However, the sprays from the nozzle are not sketched to scale. The sprays moving away from the front window (and from the camera) are drawn with the dotted line. Each individual spray from the nozzle is assigned a number.

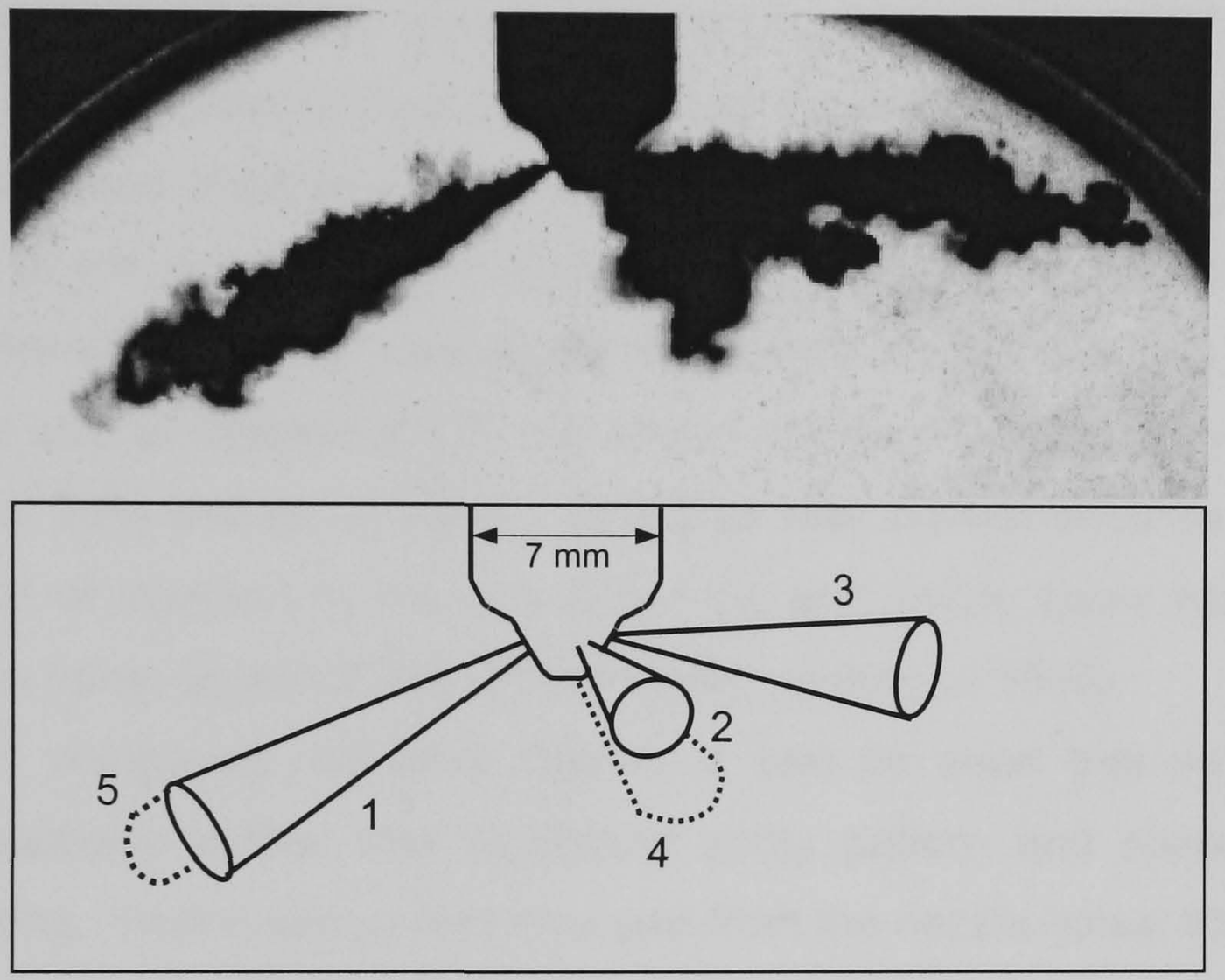

Figure 3.11: Sketch of the sprays from the image of injector L1 (N=800 rpm, t=31ms after SOI)

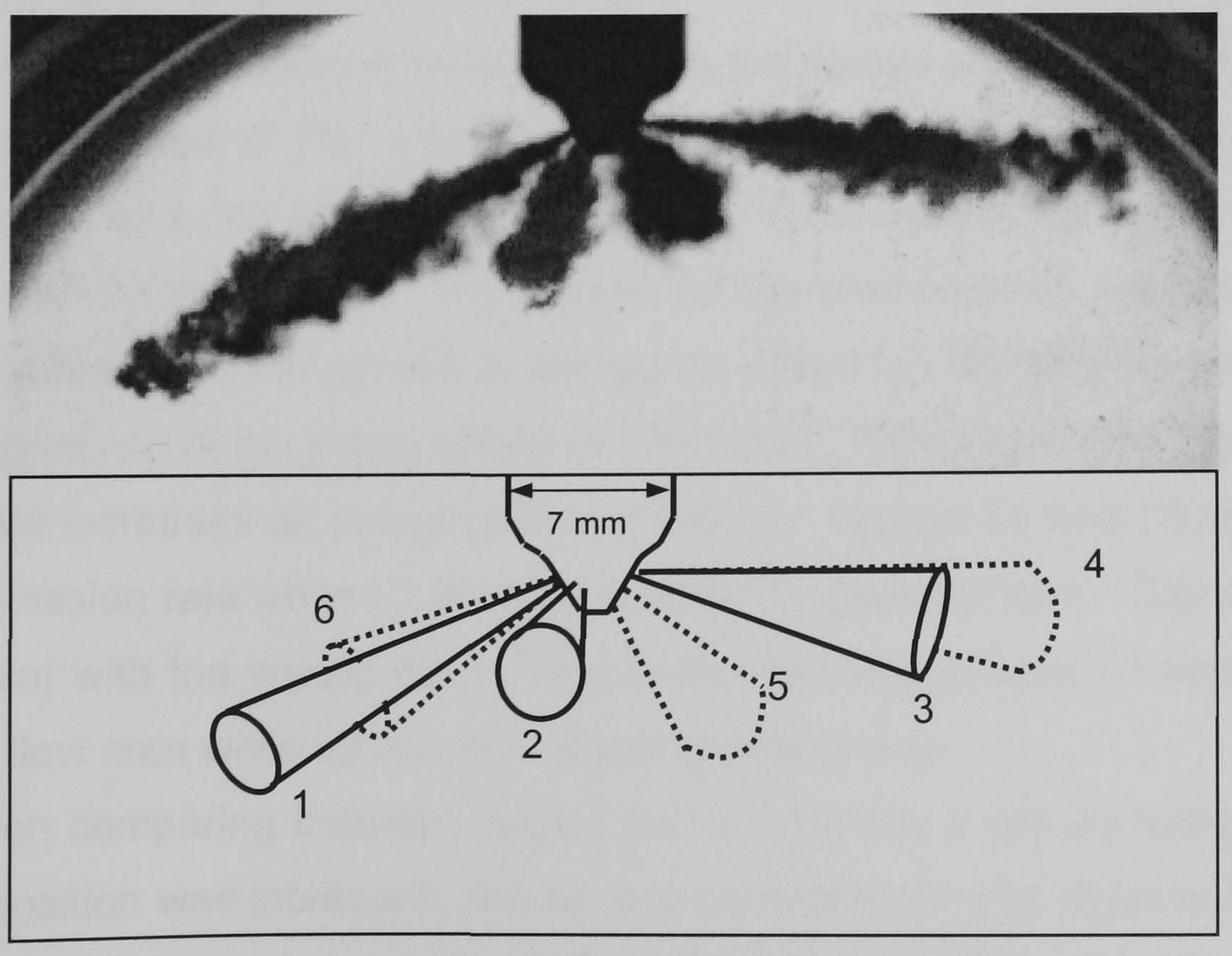

Figure 3.12: Sketch of the sprays from the image of the 6-hole injector L3 (N=800 rpm, t=31ms after SOI)

(a) Spray Pattern and Shape

Images of the sprays from all three injectors were taken at pump speeds of 500 to 1000 rpm with an increment of 100 rpm. The amount of fuel delivery was chosen at three fuel lever settings of the pump, referred to as 25%, 75% and 100%, to represent low, intermediate and high load conditions respectively. For each setting, 30 images of the sprays were captured and stored to the computer hard disk. Since the quality of the images was constant during the test, one image which showed a well-defined spray structure and trajectory from the nozzle holes was selected to represent the spray profile at the respected test conditions. The resulting spray images of all three injectors at the various pump speeds but at the time instant of 31 ms after the trigger signal for the start of injection (SOI), are shown in Figure 3.13(a) for fuel lever position at 25%, (b) at 75% and (c) at 100%. This time was chosen because it was the time from the start of injection to the time when the first visible spray emerged from the nozzle hole at pump speed of 700 rpm and lever position of 100%.

When comparing individual figures, it can be seen that all three injectors showed remarkably similar and consistent spray pattern and shape at each load (fuelling) setting. As the sprays first emerged from the nozzle holes, the shape of each spray initially took the shape of a wedge, consistent with the observation of Kuniyoshi et al. (Kuniyoshi et al., 1980), which later changed into a wavy, christmas tree like, shape as the spray progressed. The images also showed that the sprays at the pump speed of 700 rpm were denser as compared to the sprays at pump speed of 1000 rpm. Also, at pump speed of 700 rpm, the sprays were short and narrow, while at pump speed of 1000 rpm, the sprays can be seen to have developed into a 'diesel spray' during the same time instant. The reason to this phenomenon could be due to the slower progression of the sprays at the pump speed of 700 rpm as opposed to the sprays progression at the pump speed of 1000 rpm. This means that the rate of spray development increases as pump speed increases. Injector L1 and L3 showed similar spray progression rate while L2 showed a faster progression rate. This observation is in agreement with the nozzle details due to the fact that injector L1 and L3 have the same total flow area while L2 has the largest total flow area.

When comparing between figures (a), (b) and (c), it can be shown that as the fuel lever position was increased, the spray's development was observed to be slower as evident in the spray shape and density. The fuel from all three injectors at the fuel level position of 100% was still emerging from the nozzle hole while at the fuel level

position of 25%, fuel injection was completed during the same time period. This could be due to the increased fuel delivery in the nozzle at higher load setting causing a higher injection pressure. Increases in the injection pressure are shown to hasten the evolution of the fuel penetration.

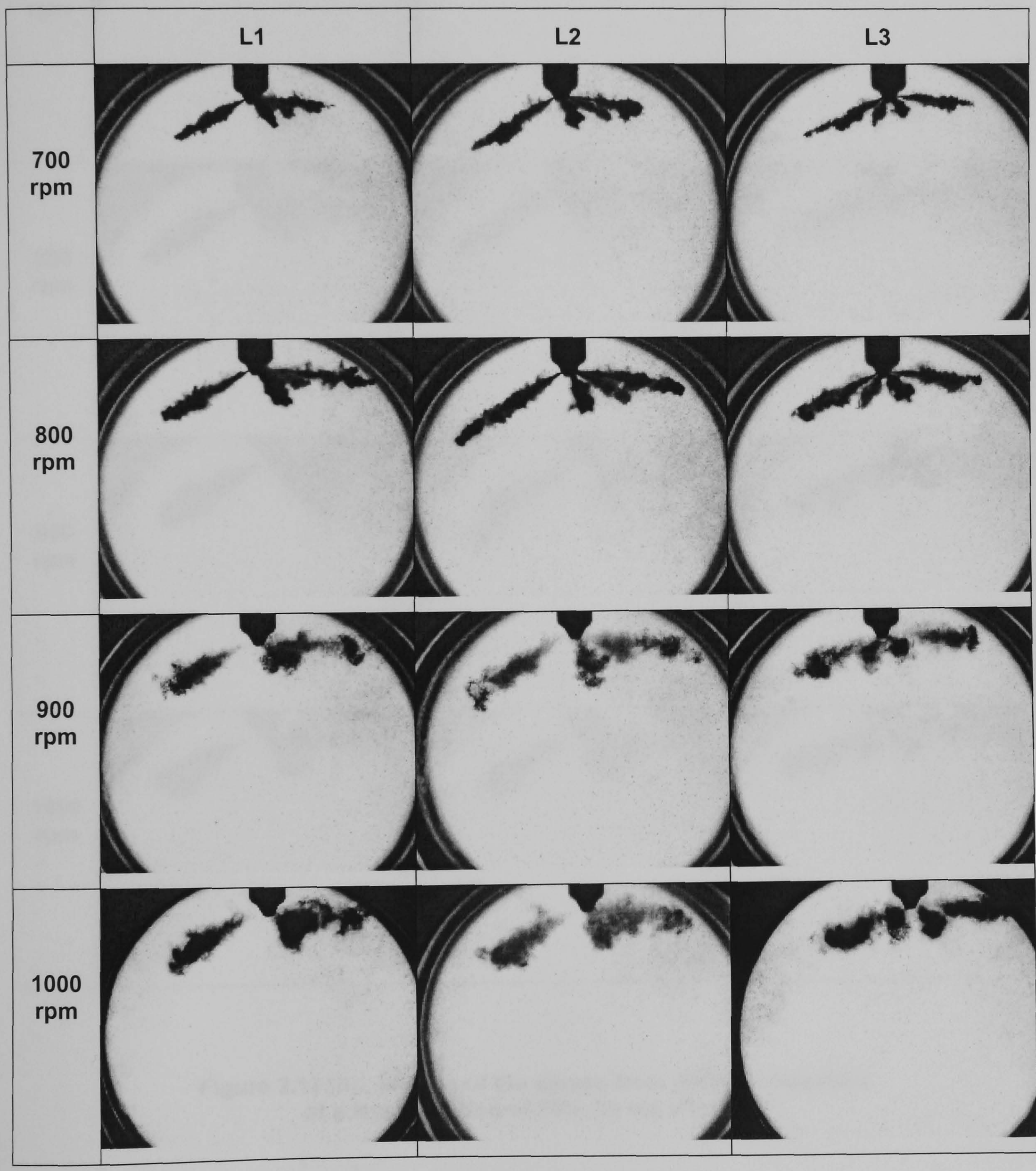

Figure 3.13 (a): Images of the sprays from different injectors at a lever position of 25%, 31 ms after SOI

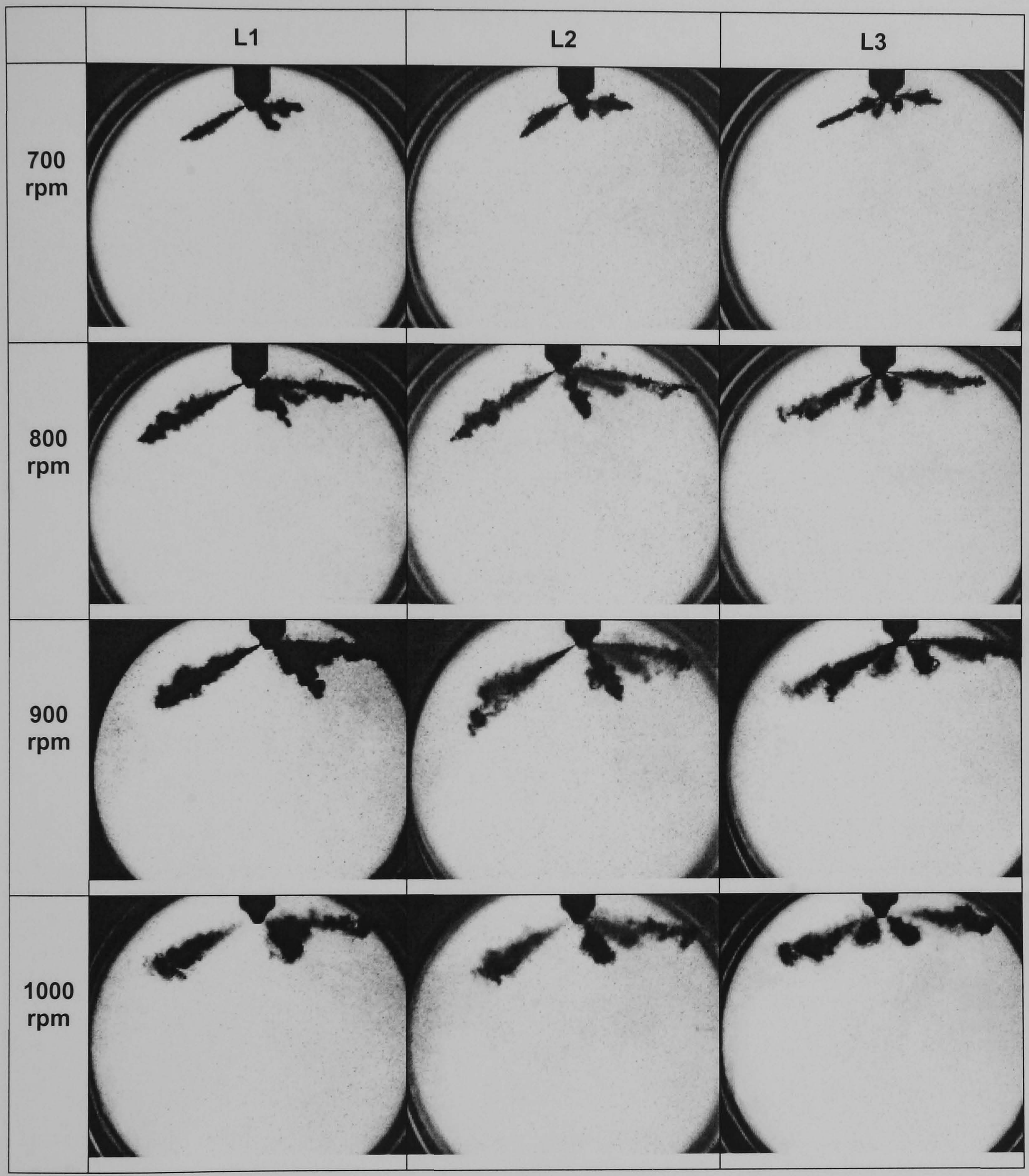

Figure 3.13 (b): Images of the sprays from different injectors at a lever position of 75%, 31 ms after SOI

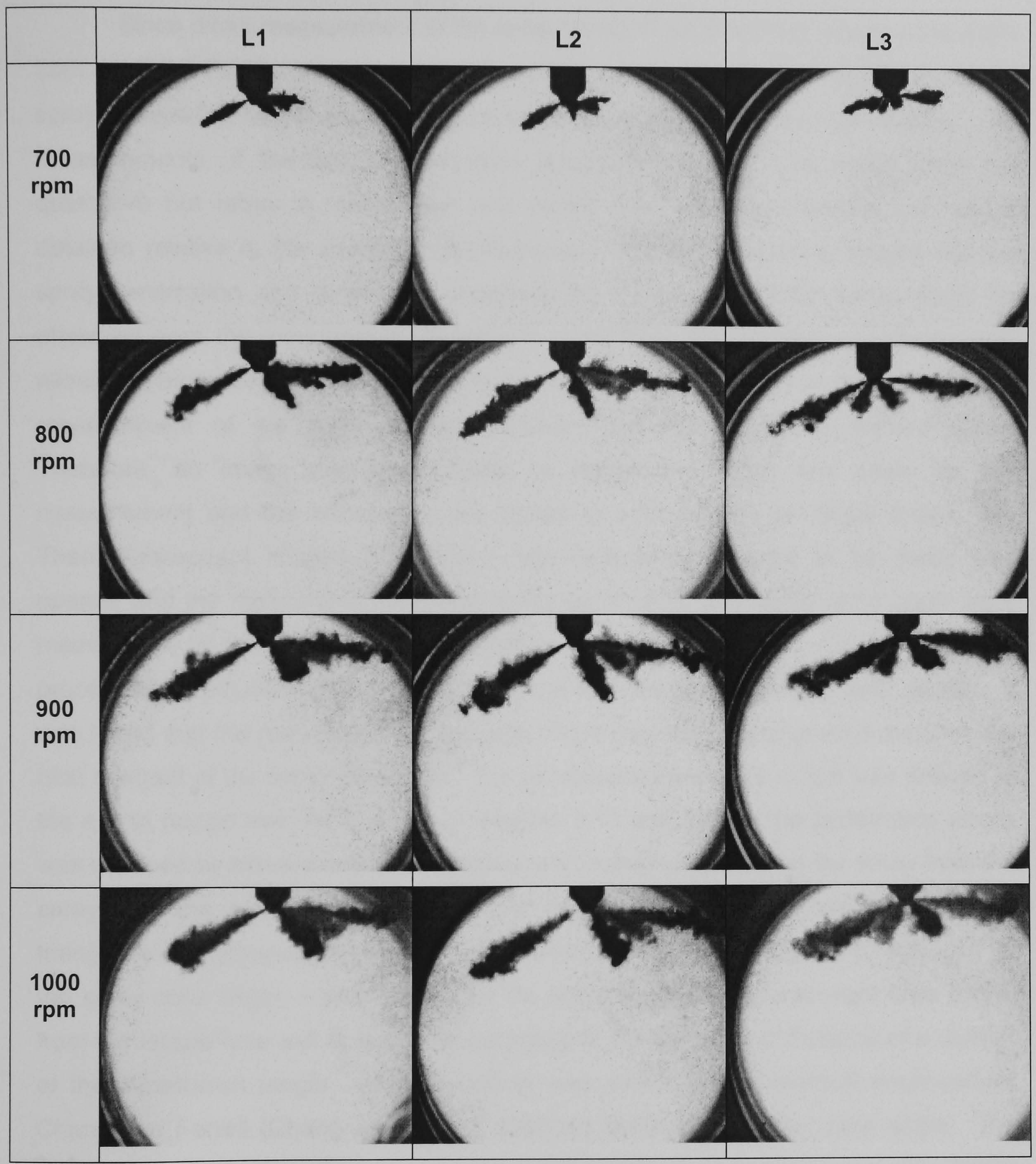

Figure 3.13(c): Images of the sprays from different injectors at a lever position of 100%, 31 ms after SOI

(b) Spray Penetration and Spray Cone Angle

Since direct measurement of the spray penetration length and spray cone angle from the PCO Picture Viewer software were not available, strategies to determine the spray penetration length and spray cone angle were performed from the images. The measurements of the spray penetration length and spray cone angle were not qualitative but rather a quantitative one which were used to compare the values obtained relative to the injectors specifications. This will provide an insight into the spray penetration and dispersion phenomenon if any established trends could be observed from the experiments carried out. The PCO Picture Viewer software only allowed measurement of the distance from the horizontal and vertical axes, and measurement of the angle formed between two points from a defined origin. Therefore, an image was first chosen to define the origin and scale for the measurement and the information are stored in a file known as 'Scale Image' file. Then, subsequent images from which the measurements were to be made was opened and the measurements for the spray penetration and spray cone angle were made based on the scales already defined in the 'Scale Image' file. The images were processed by adjusting between the minimum and maximum value of gray scales. It was found that the reduction of an average 15 percent of the background provides the best contrast of the spray structures. For all measurements, the origin was defined at the exit of nozzle hole No.1 shown in Figures 3.11 and 3.12. The penetration length was obtained by determining the horizontal and vertical distances of the spray from the spray tip to the exit of the nozzle hole and then by calculating the hypotenuse of the triangle using Pythagoras theorem. This procedure is shown in Figure 3.14(a). As for the spray cone angle, it was defined by the angle formed by two straight lines drawn from the nozzle hole exit to the outer boundary of the spray, at a distance of a quarter of the penetration length. This procedure was similar to the method employed by Chang and Farrell (Chang and Farrell, 1997) in defining the spray cone angle. The spray cone angle was then determined by the difference between the two angles formed with respect to the horizontal plane from the origin, as shown by the two lines in Figure 3.14(b). These measurements were made for all 30 images of each set of experiments and an average value were than calculated for both spray penetration length and spray cone angle. The resulting values were then plotted as shown in Figure 3.15 for the spray penetration length and in Figure 3.16 for the spray cone angle.

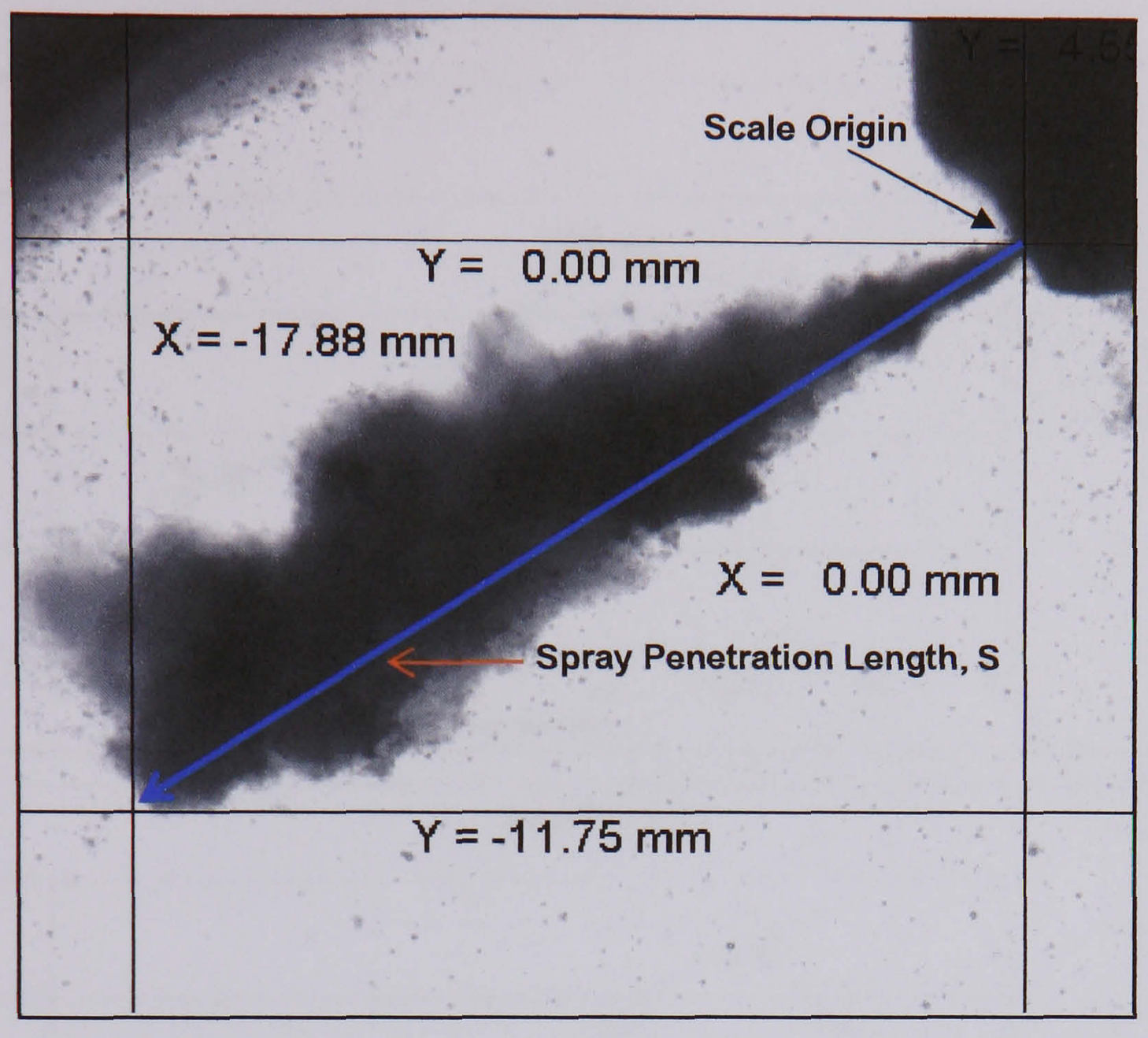

(a)

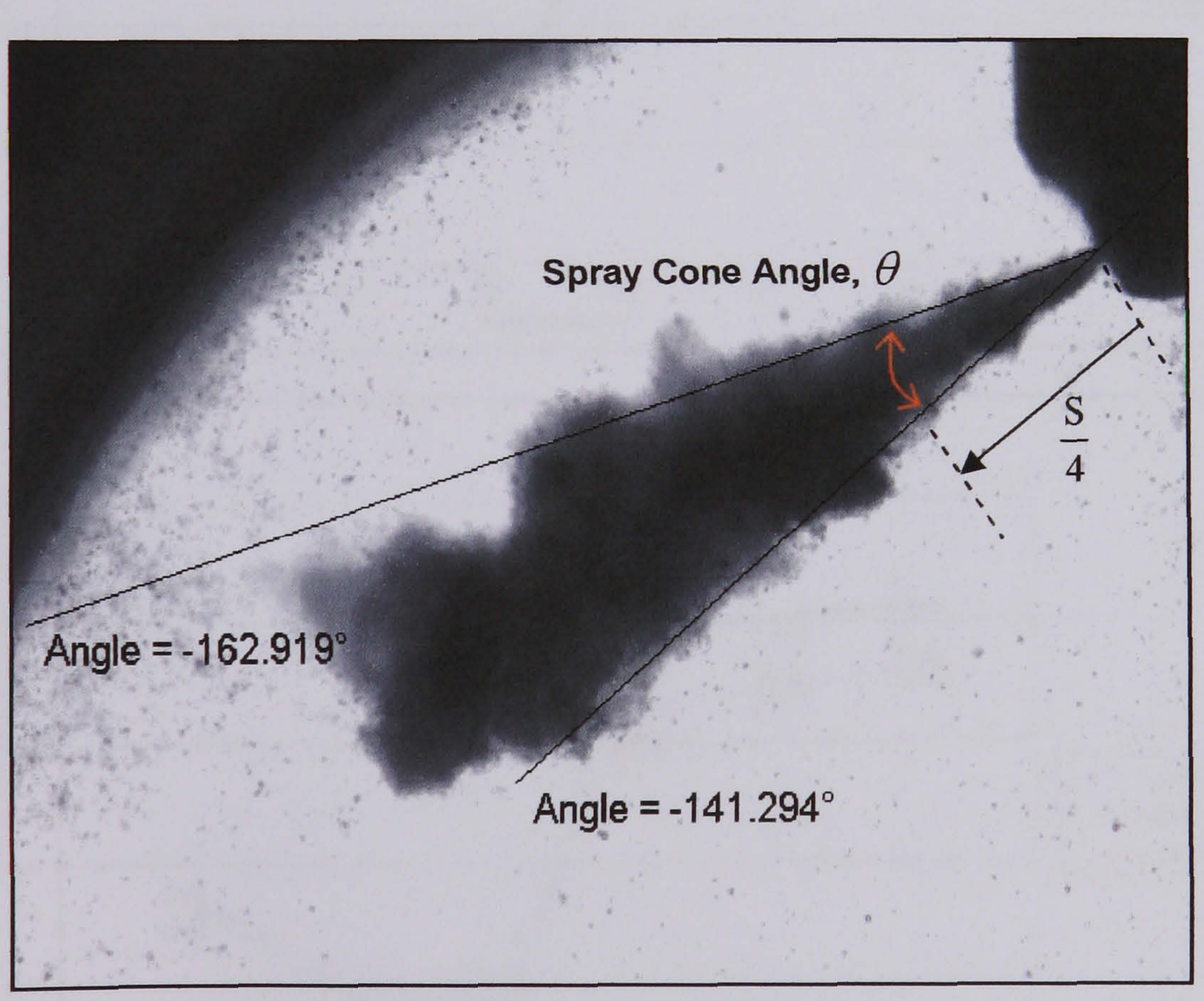

(b)

Figure 3.14: Images from PCO Picture software showing how (a) penetration length, *S* and (b) spray angle, θ were measured

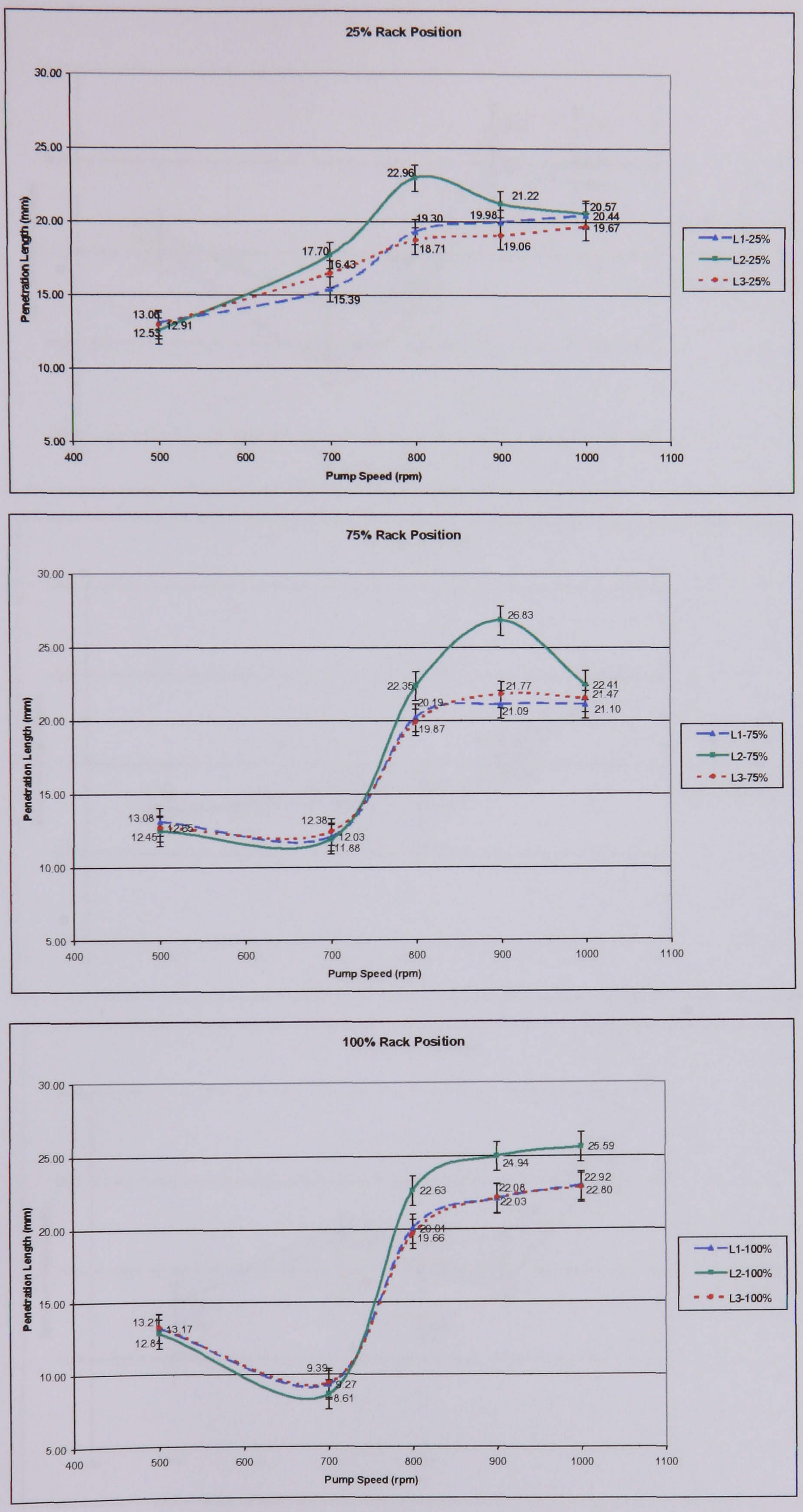

Figure 3.15: Spray penetration length of different injectors at a fixed lever position

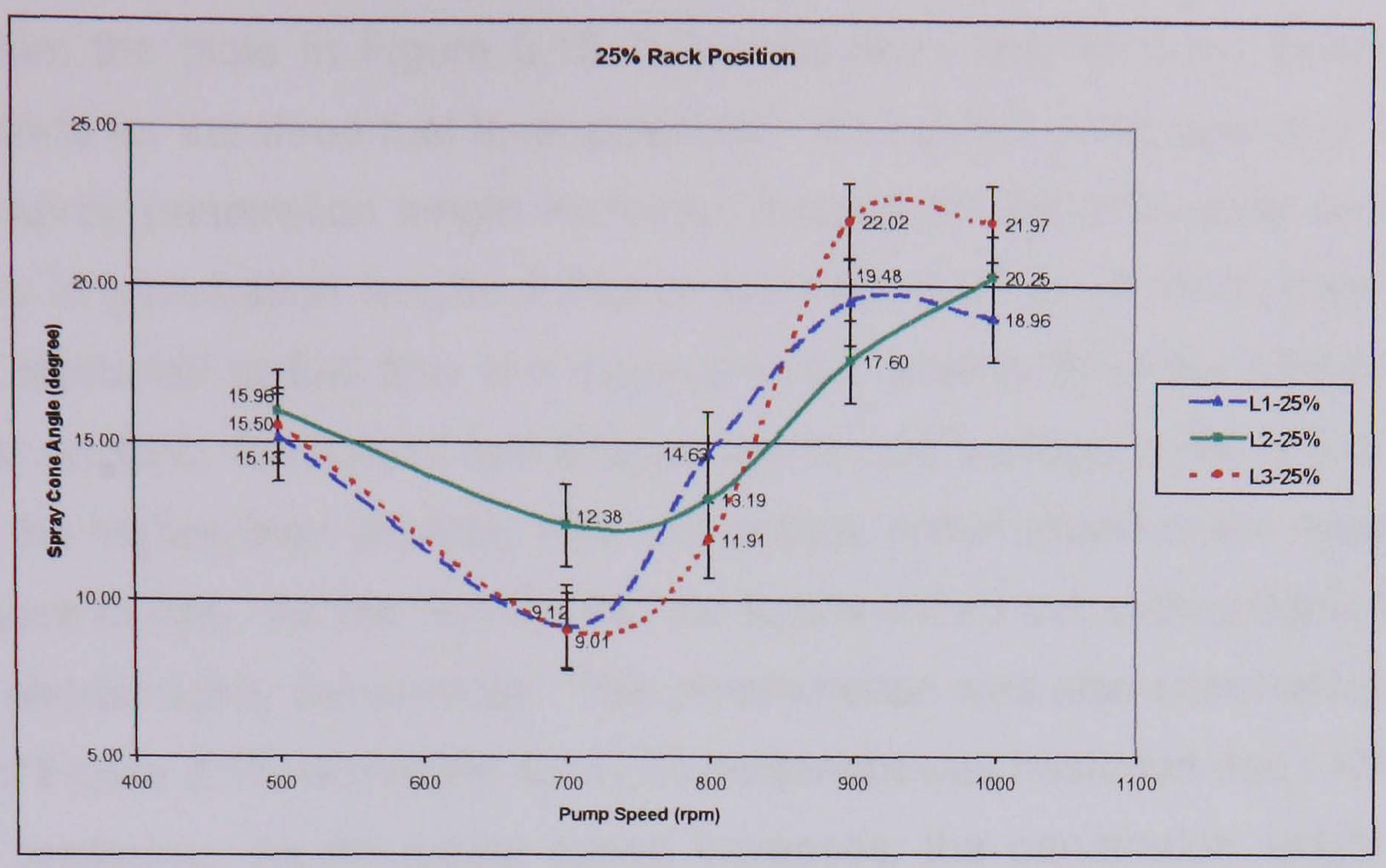

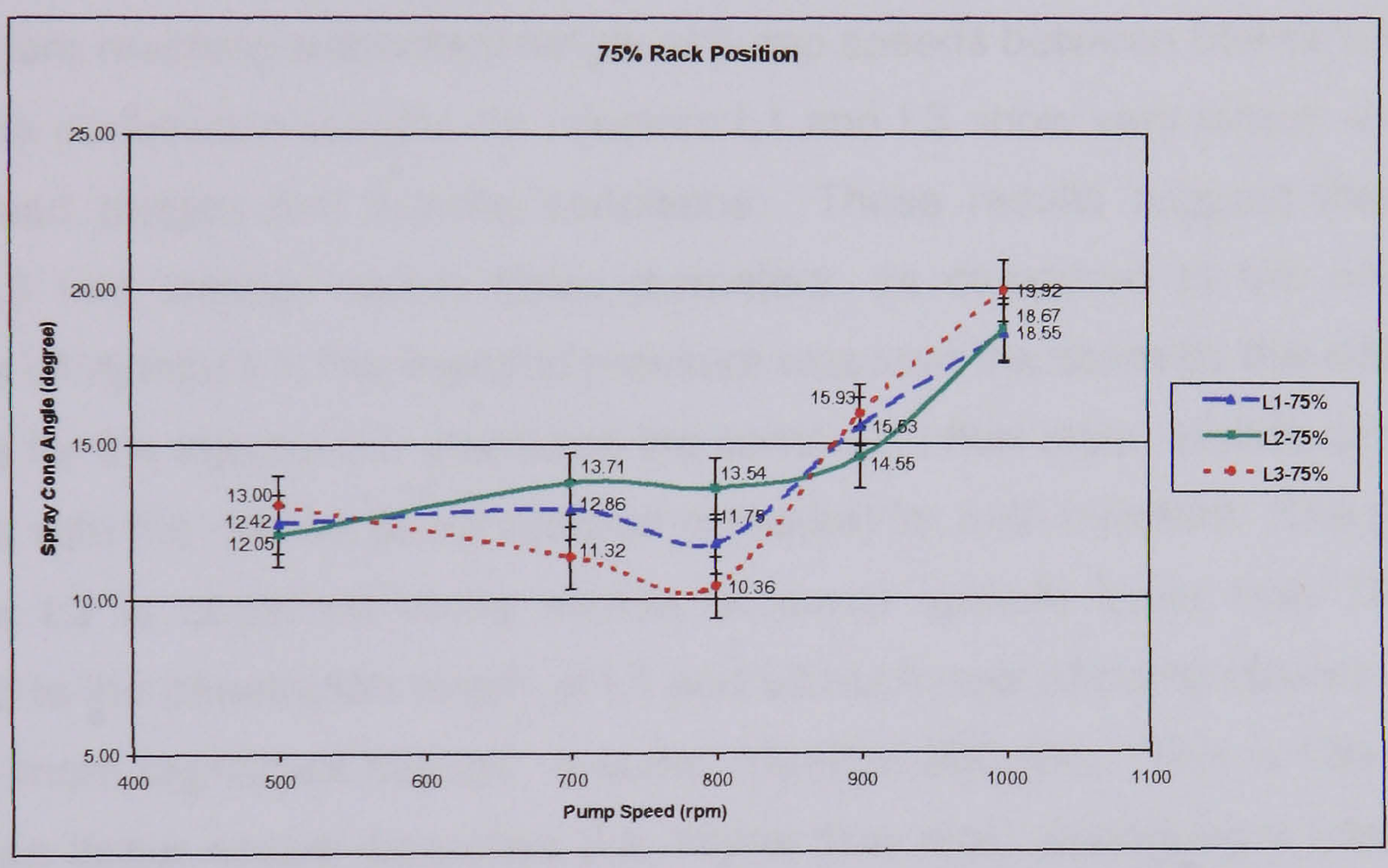

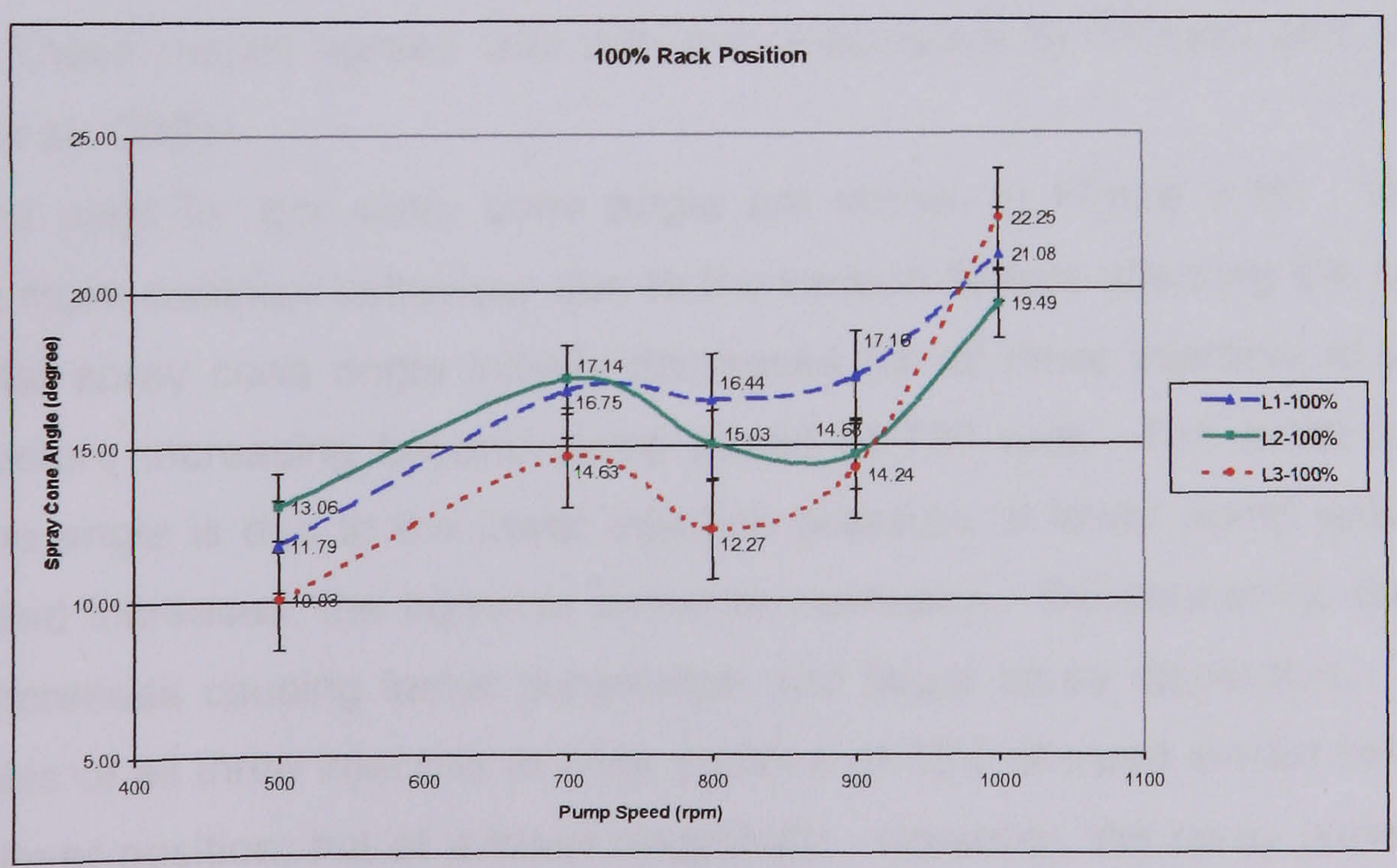

Figure 3.16: Spray cone angle of different injectors at a fixed lever position

From the plots in Figure 3.15, it can be seen that all three injectors exhibit similar trends for the three fuel lever positions. During the pump speed of 500 to 700 rpm, the spray penetration length increases linearly for the 25% lever position while decreases in penetration length at higher lever position for all three injectors. This could be attributed to fuel flow with respect to the needle lift of the injector. For the 25% lever position, the flow of fuel through the nozzle is proportional to the needle lift, while for the higher lever position, fuel had already accumulated in the nozzle causing the pressure to rise. As the needle lifts, the fuel is forced out, producing a finer spray, hence a shorter spray penetration. This phenomenon was also observed in the spray images of Figure 3.13, where the spray development was hastened due to increases in injection pressure. As the pump speed increases, the penetration length increases rapidly before reaching a constant length at pump speeds between 850 to 1000 rpm.

The penetration lengths for injectors L1 and L3 show very similar trends at all pump speed ranges and fuelling conditions. These results suggest that although injector L3 has smaller nozzle holes diameters, as compared to the nozzle holes diameters of injector L1, the injection pressure was kept the same by the addition of an extra hole for the injector L3, producing the same total flow area. Hence, providing the same flow rate (i.e. for the same injection pressure) for both injectors. The penetration length for L2 is observed to be shorter at pump speeds lower than 700 rpm as compared to the penetration length of L1 and L3 but longer at pump speeds above 700 rpm and, more significant beyond a pump speed of 800 rpm. This is due to the fact that L2 has larger nozzle diameters (i.e. higher flow rate), producing a lower injection velocity. These results agreed well with the observation by Morgan and co-workers (Morgan et al., 2001).

The plots for the spray cone angle are shown in Figure 3.16. The results showed a more complex behaviour due to the various factors affecting the spray cone angle. The spray cone angle initially decreases for all three injectors at 25% lever position before increasing beyond pump speed of 730 rpm. The initial decease in spray cone angle is due to the lower injection pressure at lower pump speed, but as pump speed increases, the injection pressure increases. Subsequently, the injection velocity increases causing faster penetration and larger spray dispersion. The spray cone angles of all three injectors at lever position of 75% showed similar behaviour as the 25% lever position, but of a lower magnitude. However, the spray cone angles of the 100% lever position showed an opposite behaviour. For this condition, the spray cone angles for all three injector increased linearly from the pump speed of 500 to 700

rpm. There was a reduction in spray cone angles between pump speeds of 700 to 800 rpm which is believed to be due to the increased injection velocity. The spray cone angle increased rapidly beyond 800 rpm during the steady state condition when the spray penetration length had reached the maximum length while the spray continued to disperse. The reason is due to the high fuel delivery in the injector which caused a higher injection pressure, thus increasing the fuel spray cone angle.

As with the penetration length, injectors L1 and L3 showed similar spray cone angle trends but with increasing differences in the values at higher fuelling conditions. This is due to the fact that both injectors have the same total flow area providing similar flow rate. However, the nozzle holes diameters of injector L3 are smaller than that of injector L1, thus producing narrow spray cone angle during the initial injection stage and progressively becomes wider, especially at higher pump speeds, as observed in Figure 3.16.

Finally, Figure 3.17 shows the spray sequence at every 0.25 ms for injector L1 progressing from the start of injection to the end of injection. The images were taken at a pump speed of 900 rpm and 50% lever position after a delay of 29 ms from the trigger signal. In the first 6 frames, the sprays can be seen to propagate rapidly during which the penetration length and spray cone angle was observed to increase with time. Upon this, the sprays penetration length seems to remain constant while the spray cone angle continues to grow as can be seen in frames 7 to 13. The sprays start to impinge on the chamber windows from frame 14 onwards and the density of the cloud appears to be reducing, suggesting that less fuel is being injected during this period of time. From frame 15 to frame 27, the spray structure remains the same, suggesting that the injection has reached a steady state condition before the end of injection.

Figure 3.17 (a): Spray sequence from frame 1 to 15

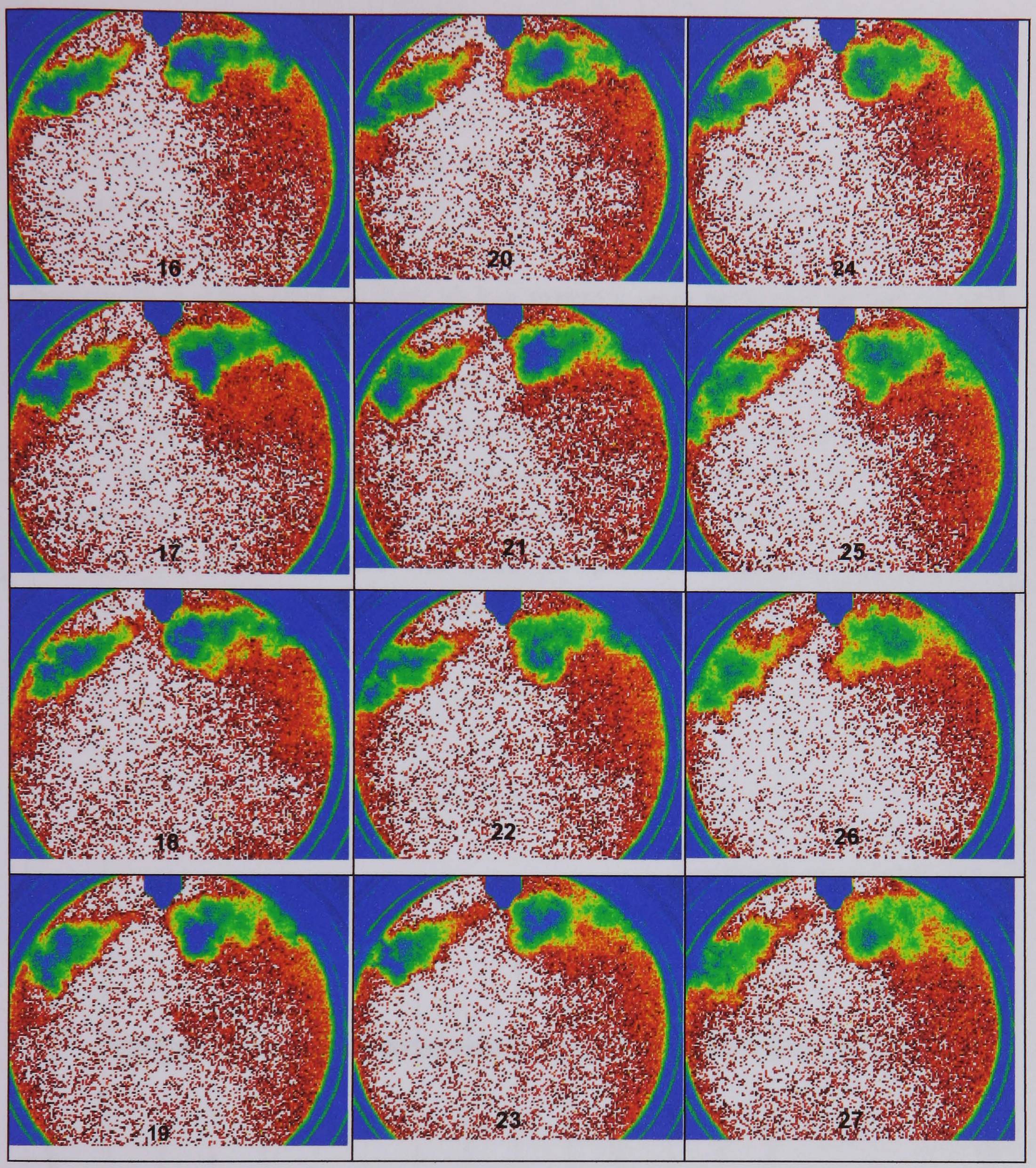

Figure 3.17 (b): Diesel fuel spray sequence from 29 ms after SOI. Images taken at every 0.25 ms at constant pump speed of 900 rpm and 50% lever position.

3.4.2 Results From the Injection Rate Measurements

The injection rates for the four different injectors were measured with the Bosch Tube meter. Recordings of the fuel line and injection pressure were carried out in conjunction with a portable multi-channel data acquisition system. The injection characteristics measurements from all four injectors were performed at two different pump speed settings, i.e. 900 rpm and 1000 rpm, representative of the engine speeds of 1800 and 2000 rpm respectively. Fuel delivery was varied at 5 different settings, i.e. 0%, 25%, 50%, 75% and 100%, representing conditions from low load to full load range. The acquired data from 32 consecutive injections were saved to the computer hard disk and than processed using Microsoft Excel. The ensemble average of these 32 consecutive injections were then used to represent the profile of the pressure curves at each of the respective conditions. An example of the signals' profile obtained from the experiments is shown in Figure 3.18

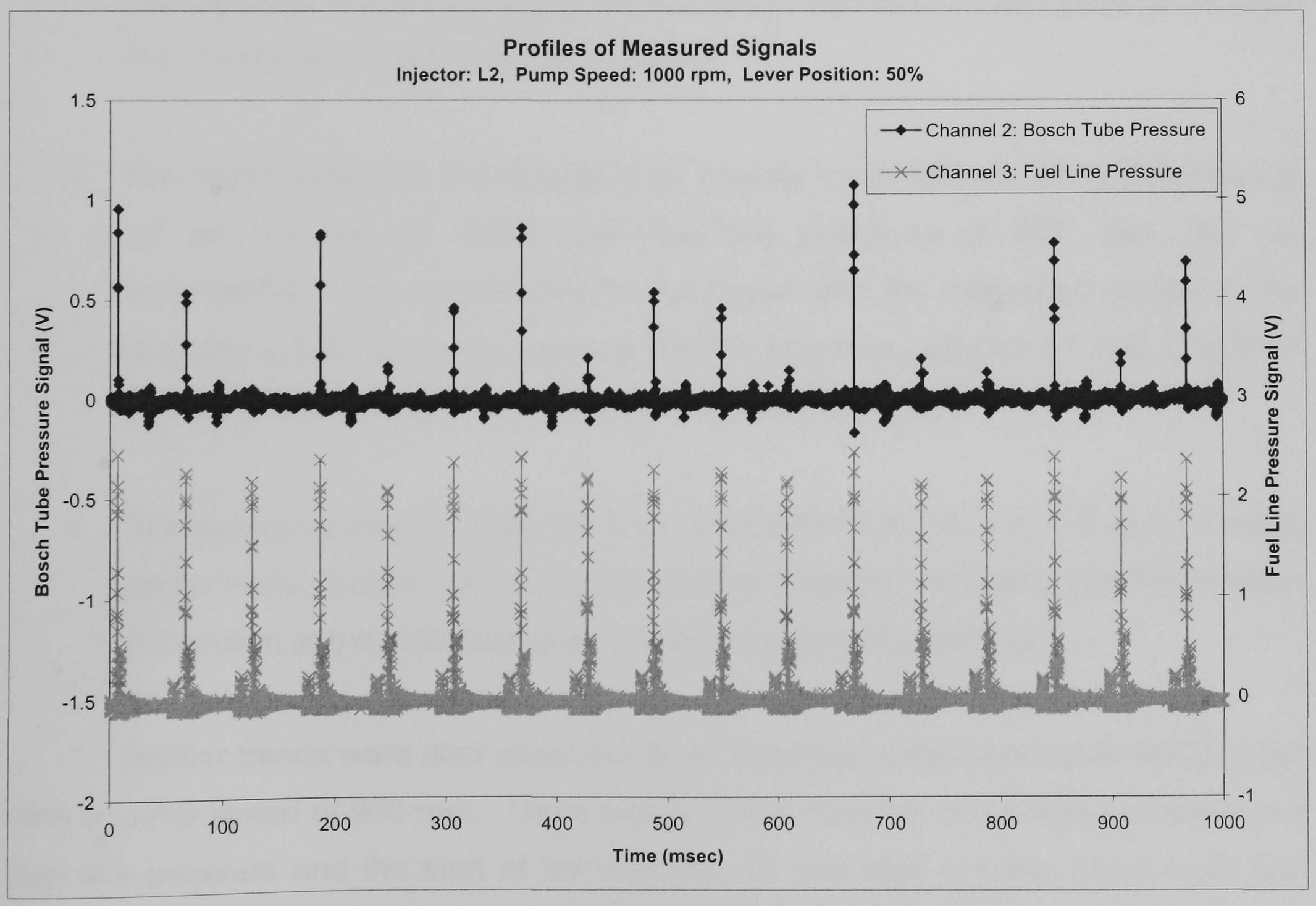

Figure 3.18: An example of the measured pressure signal profiles

(a) Injection and Fuel Line Pressure Profiles

Profiles of the injection and fuel line pressures for all four injectors at full load condition with a pump speed of 1000 rpm are shown in Figures 3.19 (a) to (d). Both curves are plotted with the pressure in bar against time in msec. The injection pressure as measured at the Bosch Tube meter is represented by the top curve while the fuel line pressure measured at the inlet to the injector is represented by the bottom curve. The signals from the injection pressure measurement show large variations in signal magnitude. This is believed due to the transducer being able only to sense the injection pressures that are above the back pressure value, i.e. 50 bar. As such, the injection pressure signals were filtered to select only signals above 0.65 volts. From the figures, the following observations can be made for the four injectors:

- The Bosch Tube pressure started to rise after a 0.3 msec delay behind the fuel line pressure curve change from a negative slope to a positive slope. The time lag between the fuel line pressure and the injection pressure is consistent for all four injectors and is believed to be due to the difference in the distance between the measurement points for each signal.

- The mean peak fuel line pressure for injector L1 is 322 bar while injectors L2, L3, and L4 showed mean peak fuel line pressures of 361, 364, 362 bar respectively. This observation is consistent with the measured values of the injectors nozzle opening pressure (NOP), where by, injector L1 has a NOP of 235 bar while the other injectors have a NOP of 240 bar.

- The injection period for injectors L1, L2, L3 and L4 is 1.6, 1.6, 1.5 and 1.7 msec respectively. These values are remarkably constant, indicating that the duration of injection at the indicated lever position are virtually identical.

Similar trends were also observed for all injectors at the same lever position but with a pump speed of 900 rpm. There was a similar time lag of 0.3 msec between the fuel line pressure and the start of the injection, L1 exhibited a lower mean peak fuel line pressure as compared to the other three injectors and the injection period for the four injectors were the same as shown in Figures 3.20 (a) to (d).

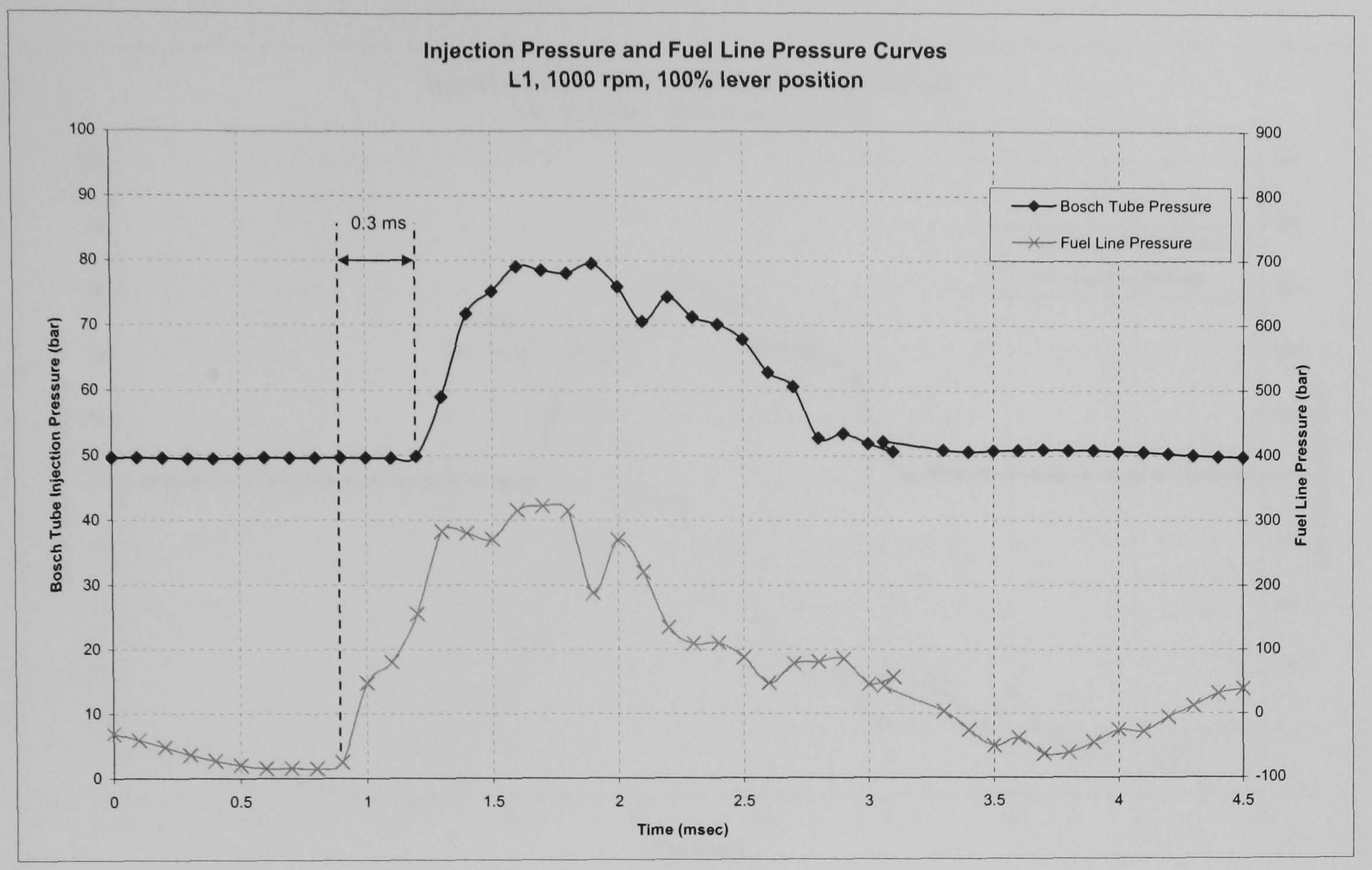

(a)

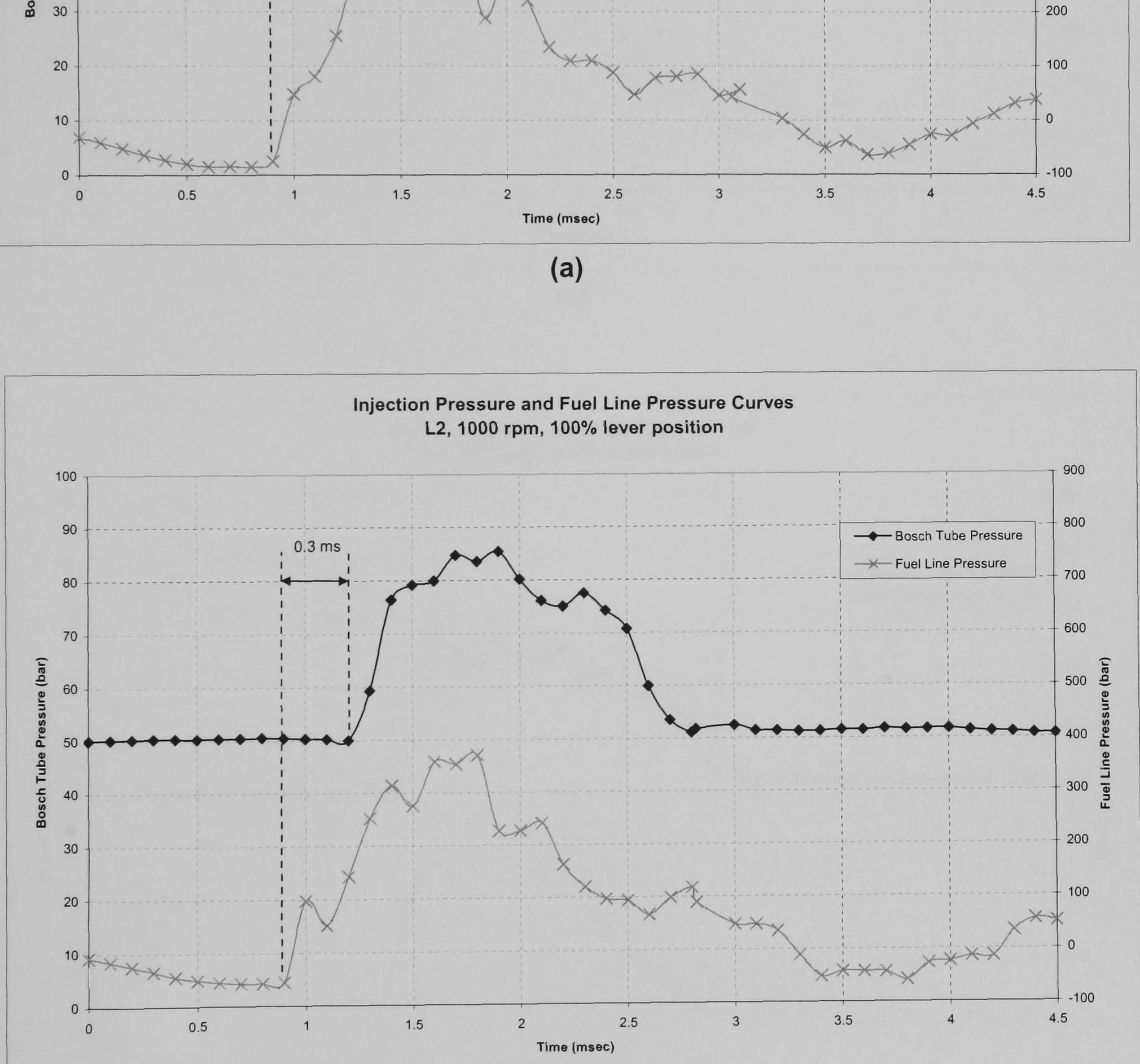

(b)

Figure 3.19 (a) and (b): Injection and fuel line pressure profiles of injectors L1 and L2 at full load condition with pump speed of 1000 rpm

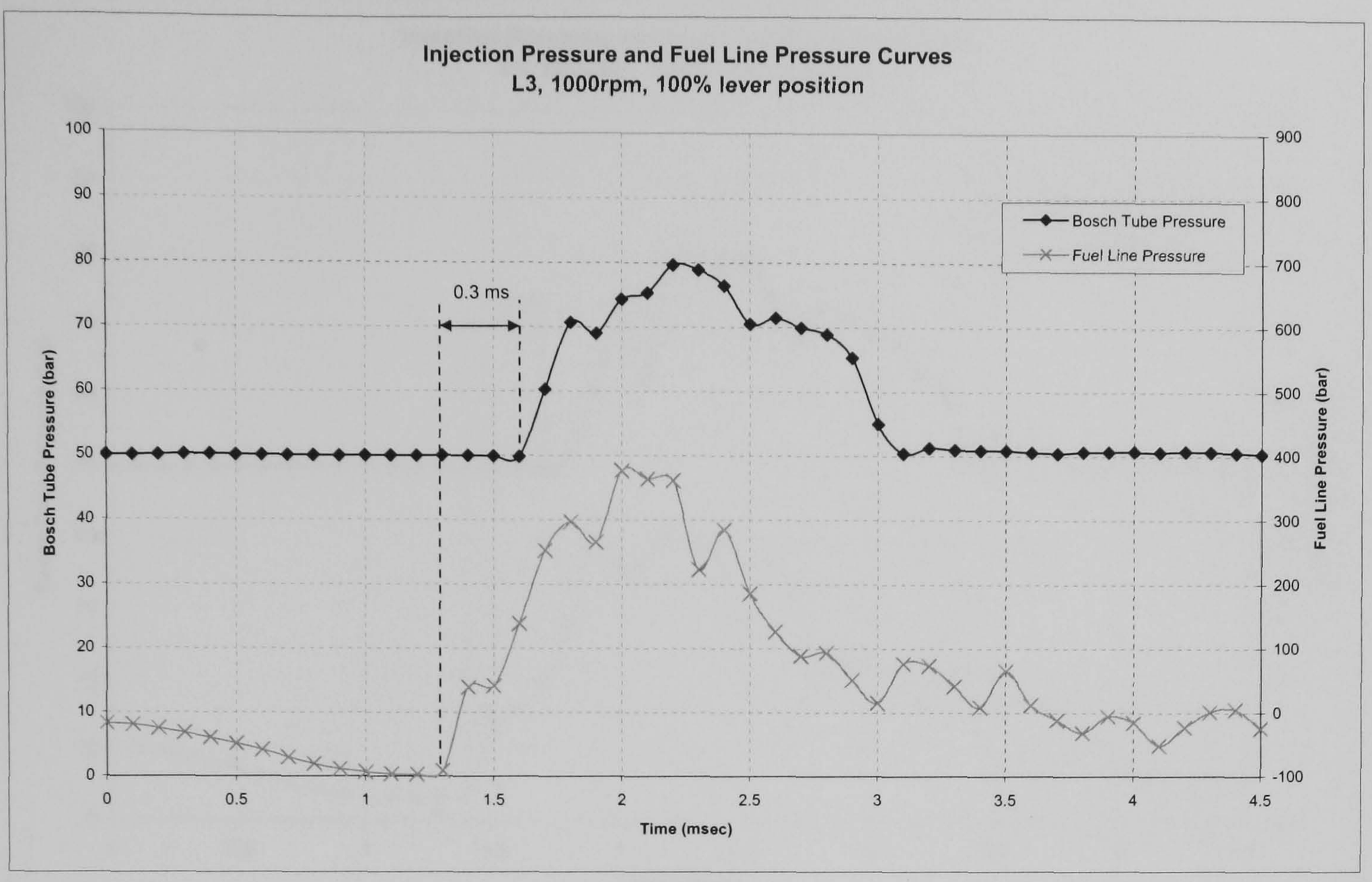

(c)

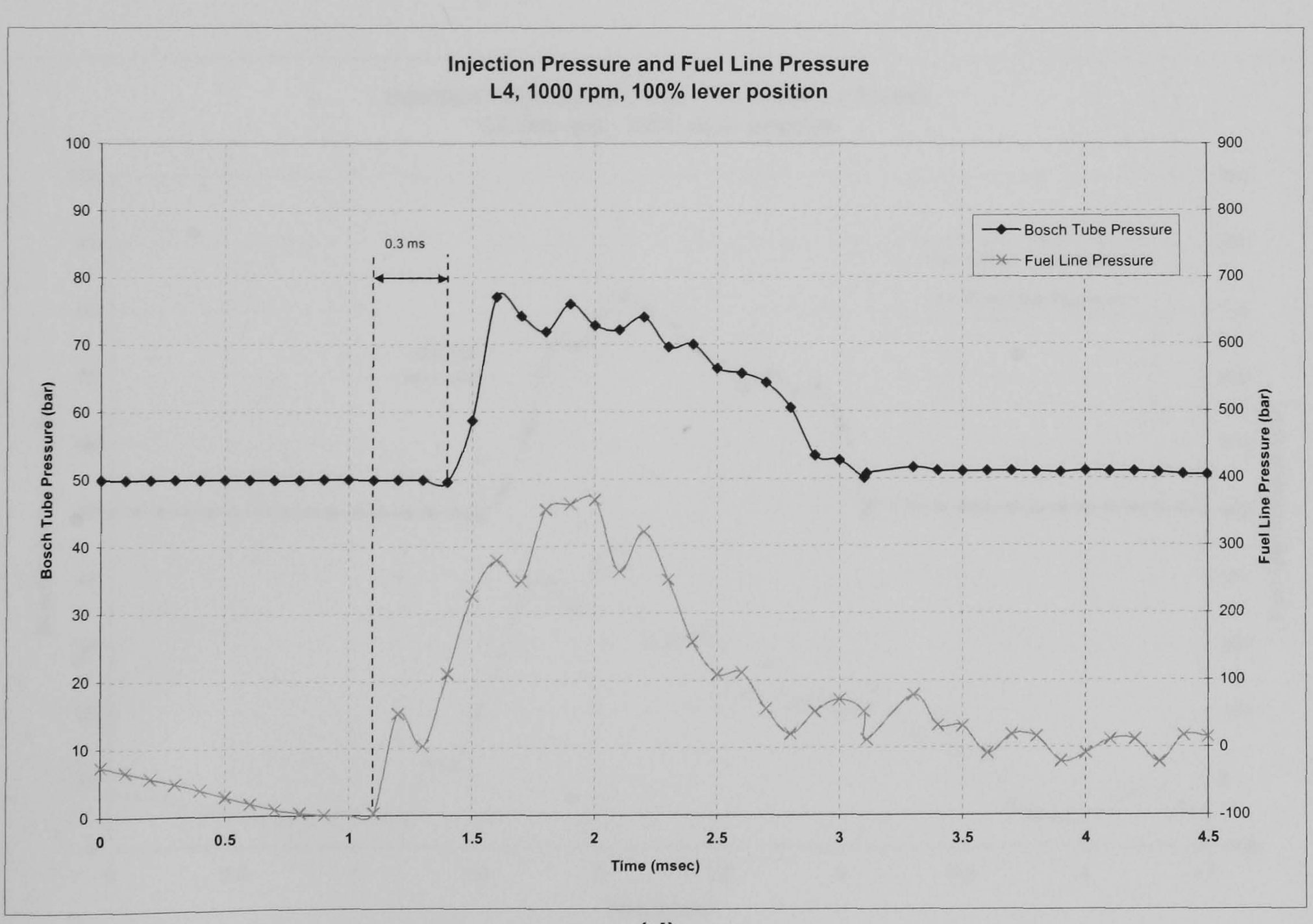

(d)

Figure 3.19 (c) and (d): Injection and fuel line pressure profiles of injectors L3 and L4 at full load condition with pump speed of 1000 rpm

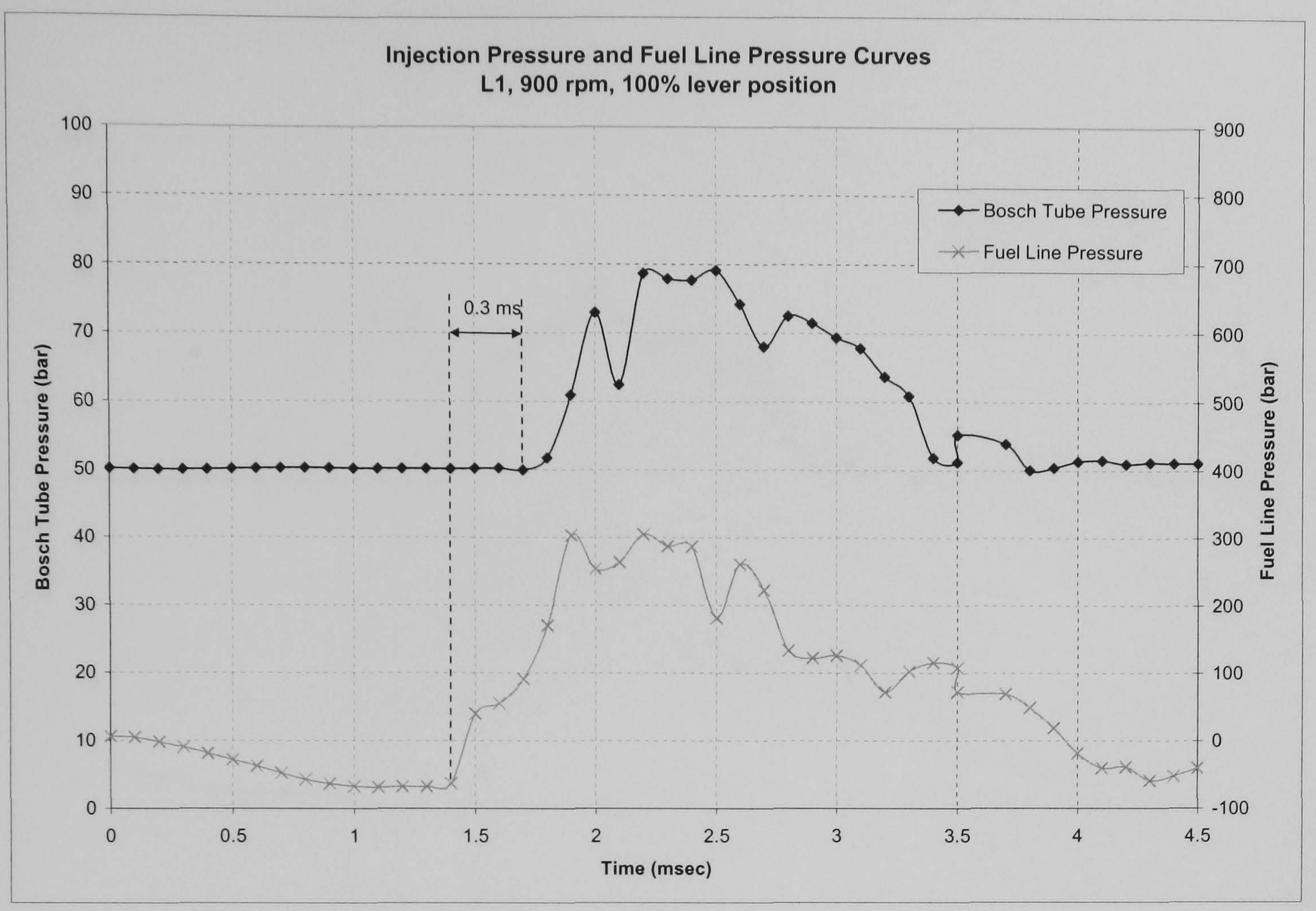

(a)

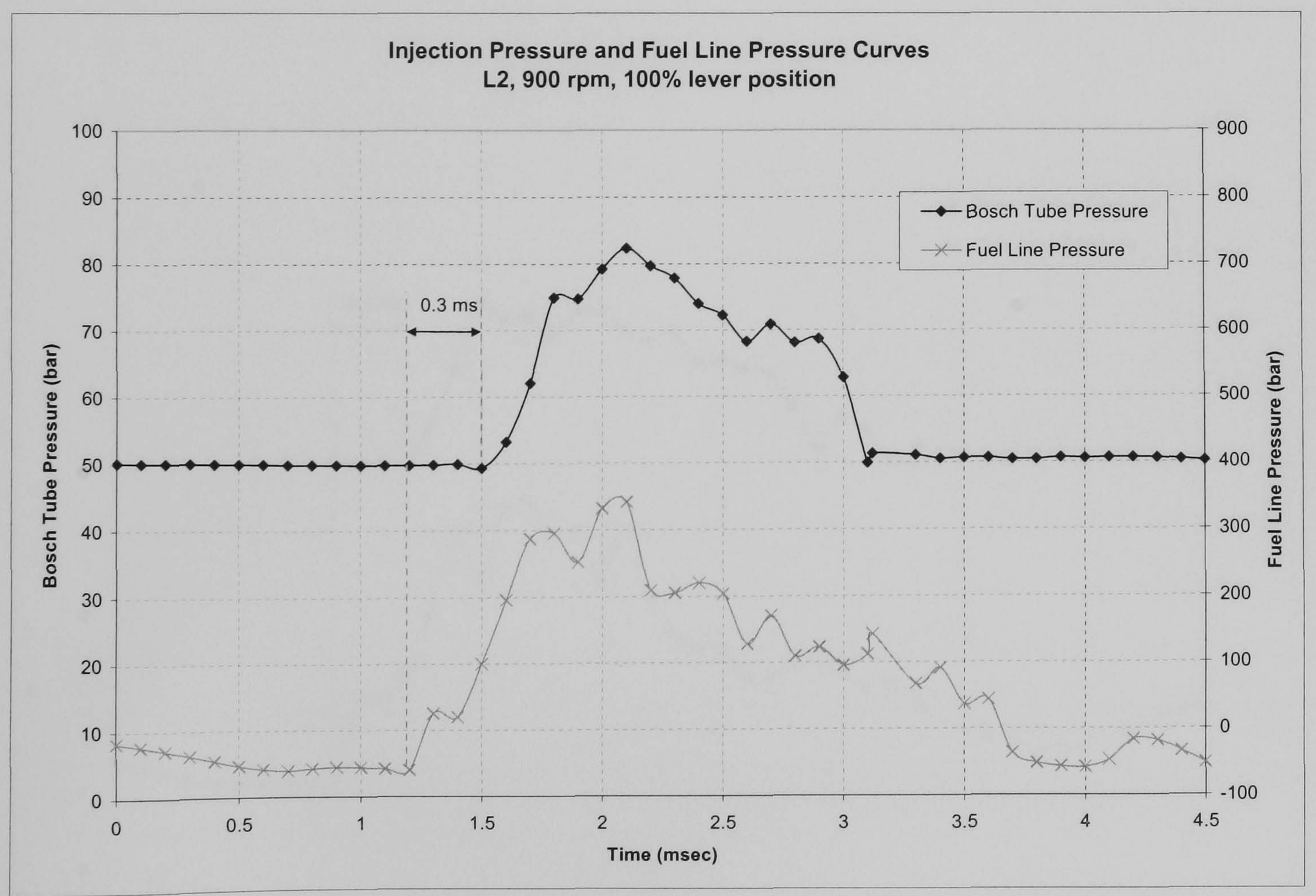

(b)

Figure 3.20 (a) and (b): Injection and fuel line pressure profiles of injectors L1 and L2 at full load condition with pump speed of 900 rpm

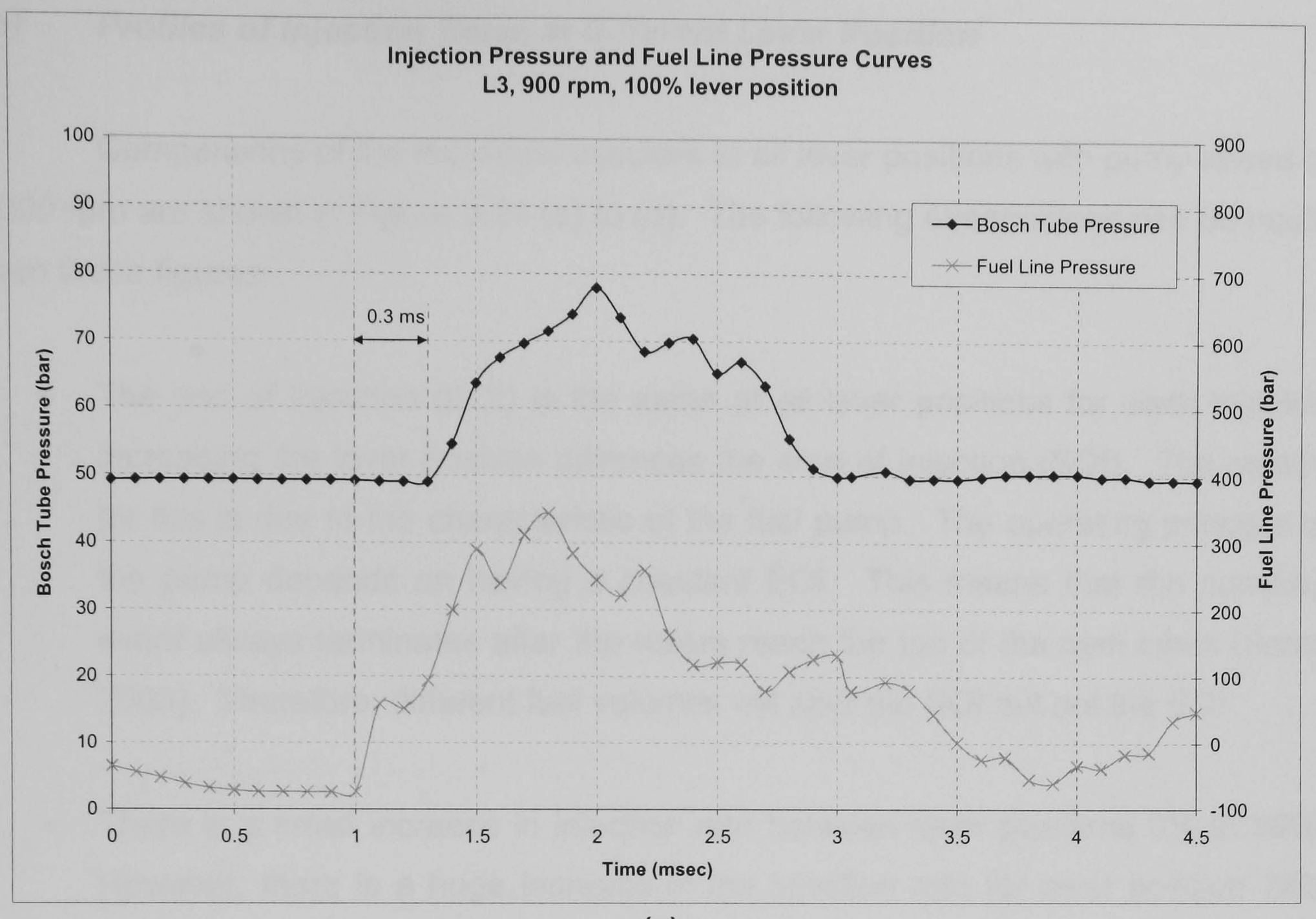

(c)

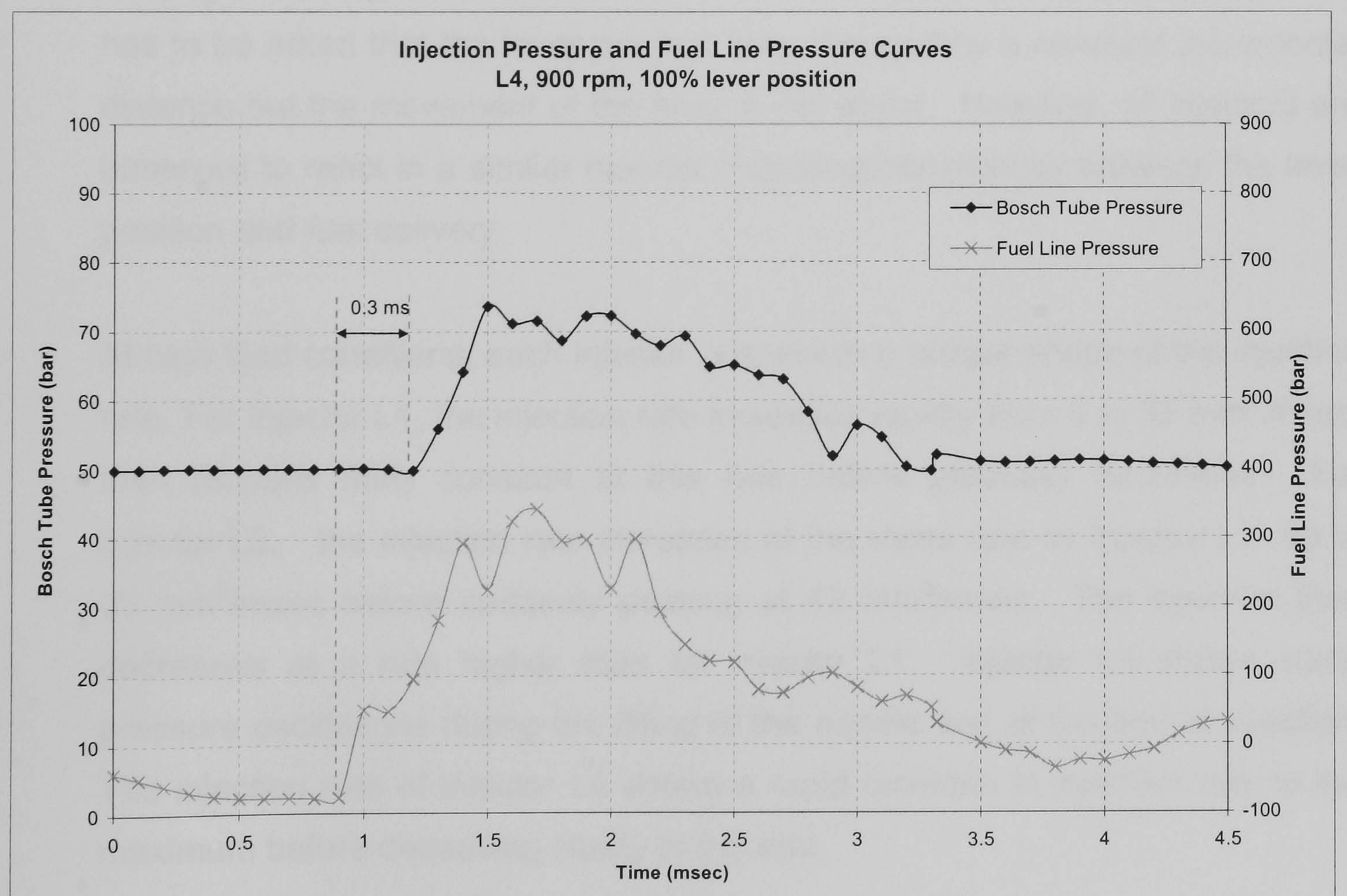

(d)

Figure 3.20 (c) and (d): Injection and fuel line pressure profiles of injectors L3 and L4 at full load condition with pump speed of 900 rpm

(b) Profiles of Injection Rates at Different Lever Position

Comparisons of the individual injectors at all lever positions with pump speed of 1000 rpm are shown in Figure 3.21 (a) to (d). The following observations can be made from these figures:

- The end of injection (EOI) is the same at all lever positions for each injector. Increasing the lever position advances the start of injection (SOI). The reason for this is due to the characteristic of the fuel pump. The operating principle of the pump depends on having a constant EOI. This means that the pumping event always terminates after the rollers reach the top of the cam lobes (Scott, 2003). Therefore, different fuel volumes will alter the SOI but not the EOI.

- There is a small increase in injection rate between lever positions 0% to 50%. However, there is a huge increase in the injection rate for lever position 75% and 100%. The difference in the injection rate is due to the difficulties in relating the pump fuel amount deliveries with respect to the lever position. It has to be noted that the lever position was changed by a constant incremental distance but the movement of the lever is not linear. However, all injectors are observed to react in a similar manner indicating consistency between the lever position and fuel delivery.

- At high load conditions, each injector possesses a unique shape of the injection rate. For injector L1, the injection rate increases rapidly from 0 to 35 mm^3/msec, then remains fairly constant at this rate before gradually decreases. For injector L2, the injection rate increases at the same rate as injector L1 up to 35 mm^3/msec before suddenly peaking at 42 mm^3/msec. The injection then decreases at a rate higher than for injector L1. Injector L3 shows some pressure oscillations during the lifting of the needle and at the end of injection. The injection rate of injector L4 shows a rapid increase in injection rate to the maximum before deceasing slowly to the end.

- Injection durations at each lever position are also very consistent from injector to injector.

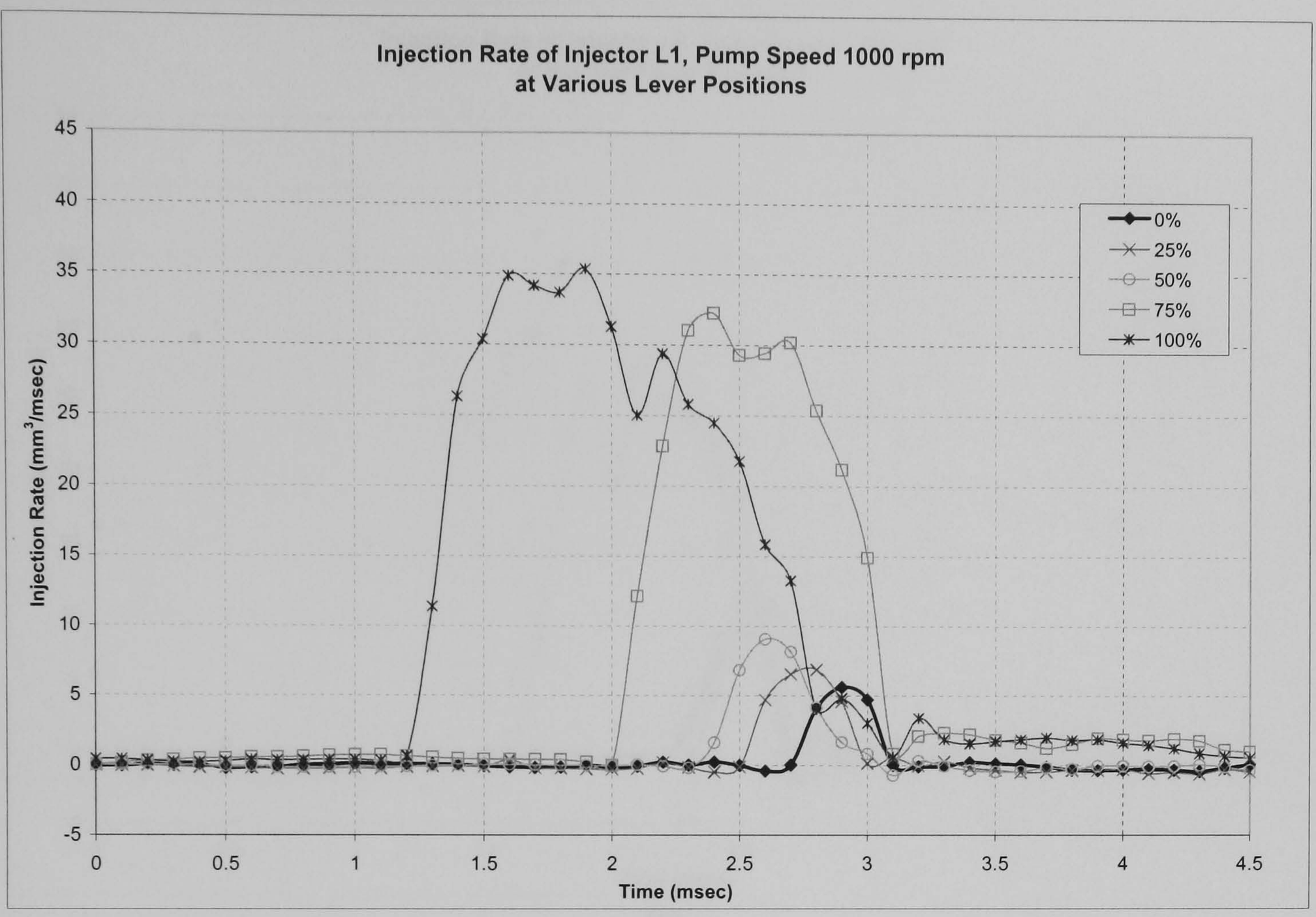

(a)

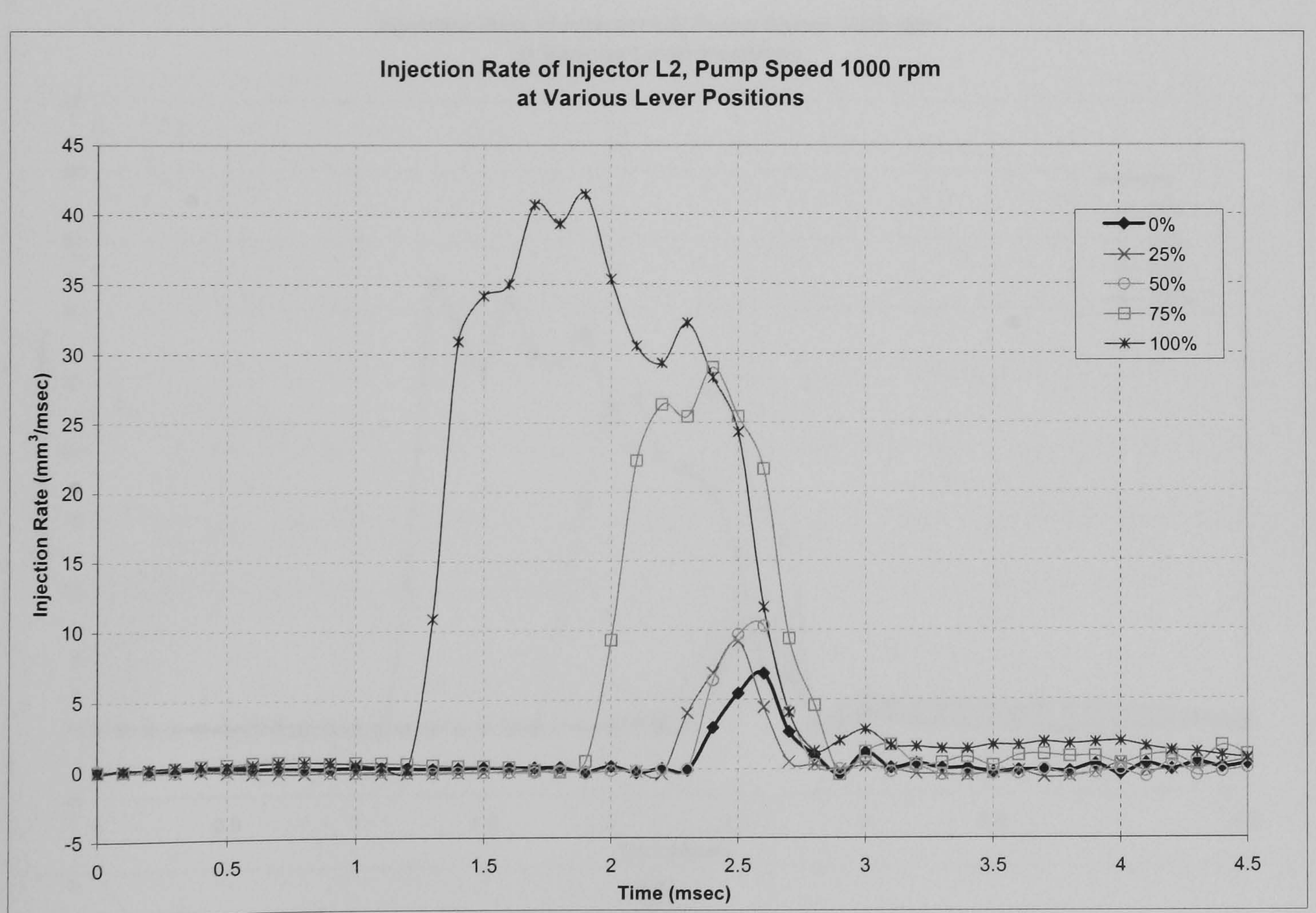

(b)

Figure 3.21 (a) and (b): Injection rate profiles of injectors L1 and L2

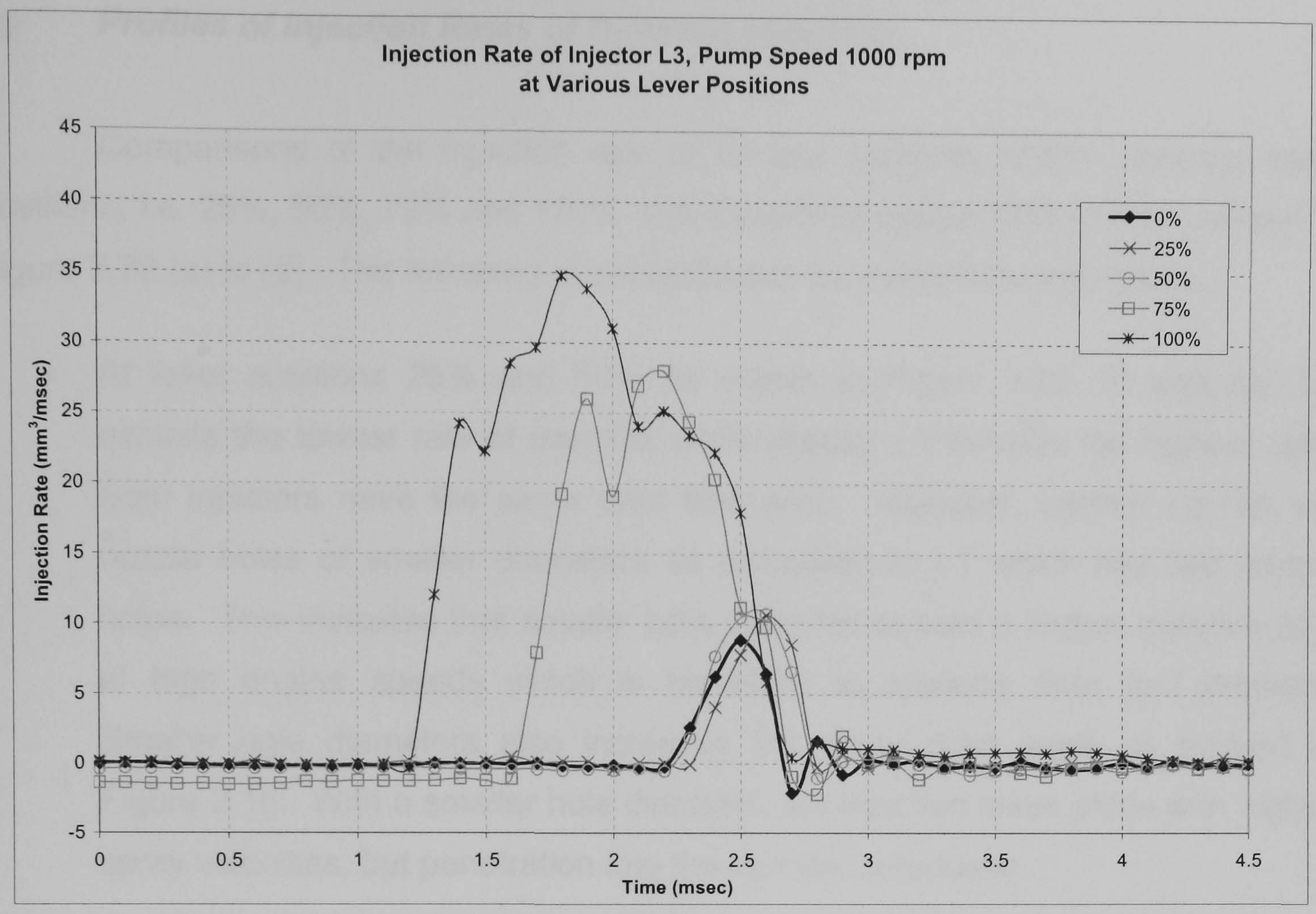

(c)

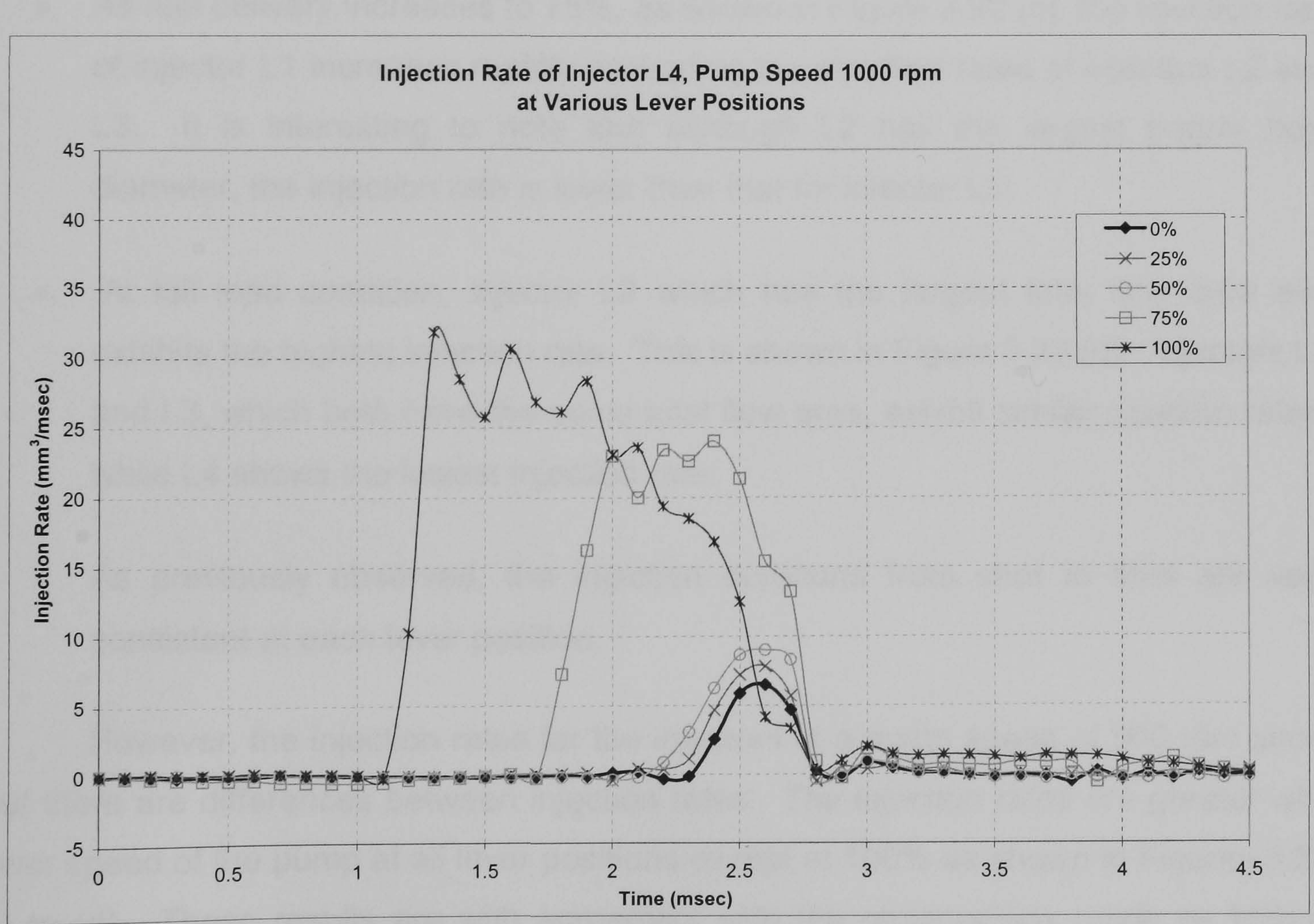

(d)

Figure 3.21 (c) and (d): Injection rate profiles of injectors L3 and L4

(c) Profiles of Injection Rates of Different Injectors

Comparisons of the injection rate of all four injectors at the separate lever positions, i.e. 25%, 50%, 75% and 100% with a pump speed of 1000 rpm are shown in Figure 3.22 (a) to (d). The following observation can be made from the figures:

- At lever positions 25% and 50% as shown in Figure 3.22 (a) and (b), L1 exhibits the lowest rate of injection while injector L3 exhibits the highest rate. Both injectors have the same total flow area. However, injector L3 has six nozzle holes of smaller diameters as compared to L1 which has five nozzle holes. This indicates that smaller hole diameter causes a higher injection rate at high engine speeds which is beneficial to produce finer fuel droplets. Smaller hole diameters also increases the spray cone angle as evident in Figure 3.16. With a smaller hole diameter, the injection takes place with higher spray velocities, but penetration into the cylinder is reduced.

- As fuel delivery increases to 75%, as shown in Figure 3.22 (c), the injection rate of injector L1 increases rapidly exceeding the injection rates of injectors L2 and L3. It is interesting to note that although L2 has the largest nozzle hole diameter, the injection rate is lower than that for injector L3.

- At full load condition, injector L2 which has the largest total flow area and exhibits the highest injection rate. This is shown in Figure 3.22 (d). Injectors L1 and L3, which both have the same total flow area, exhibit similar injection rates, while L4 shows the lowest injection rate.

- As previously observed, the injection durations from shot to shot are very consistent at each lever position.

However, the injection rates for the injectors at a pump speed of 900 rpm show that there are differences between injection rates. The injection rates are greater with lower speed of the pump at all lever positions except at 100% as shown in Figures 3.23 (a) to (d). These results are with agreement with the observations made by Marcic (Marcic, 2003) who reasoned the cause to be due to the difference in injection pressure in the nozzle. The results from the spray penetration length measurement as shown in Figure 3.15 also are in consistent with the above observation.

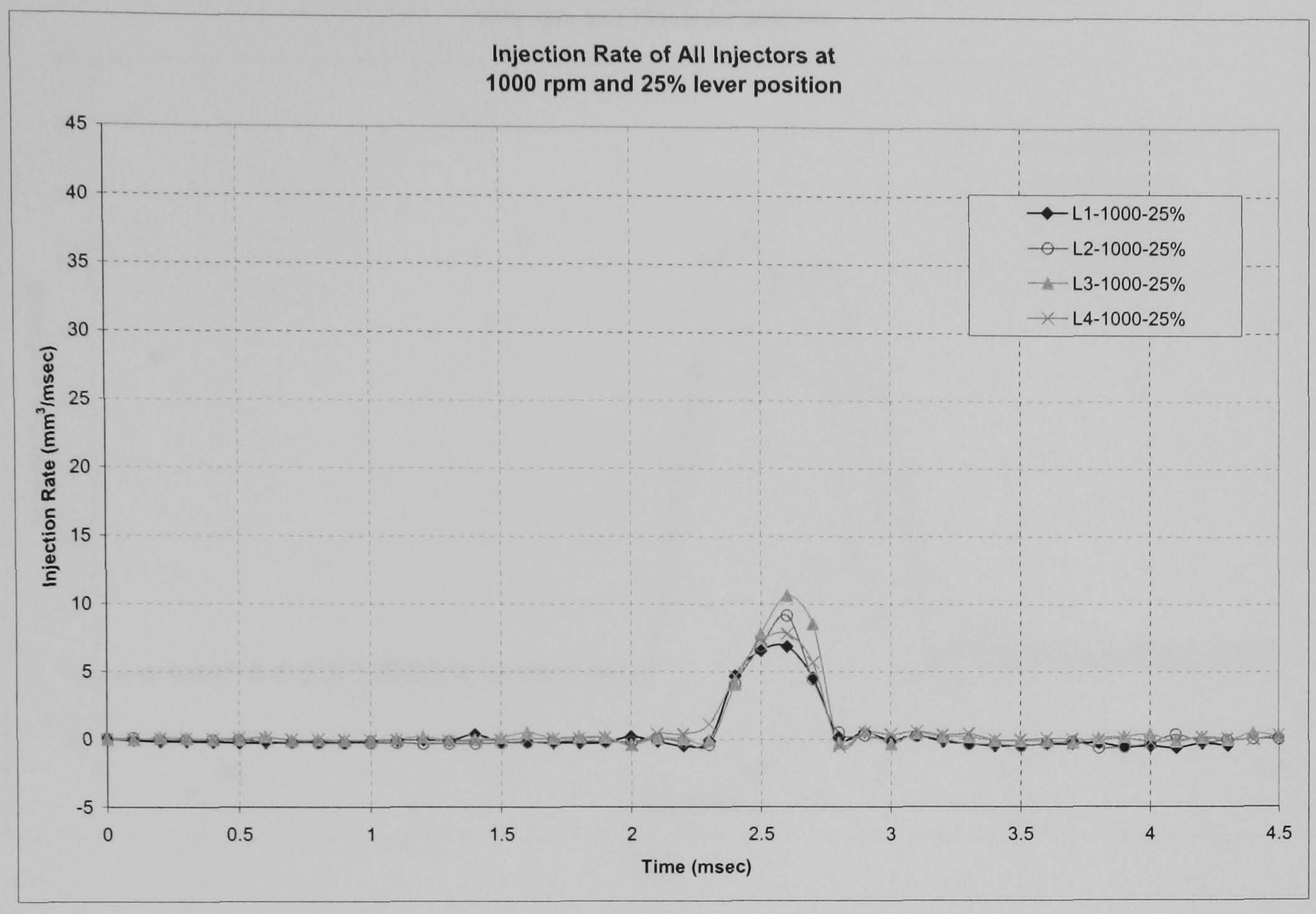

(a)

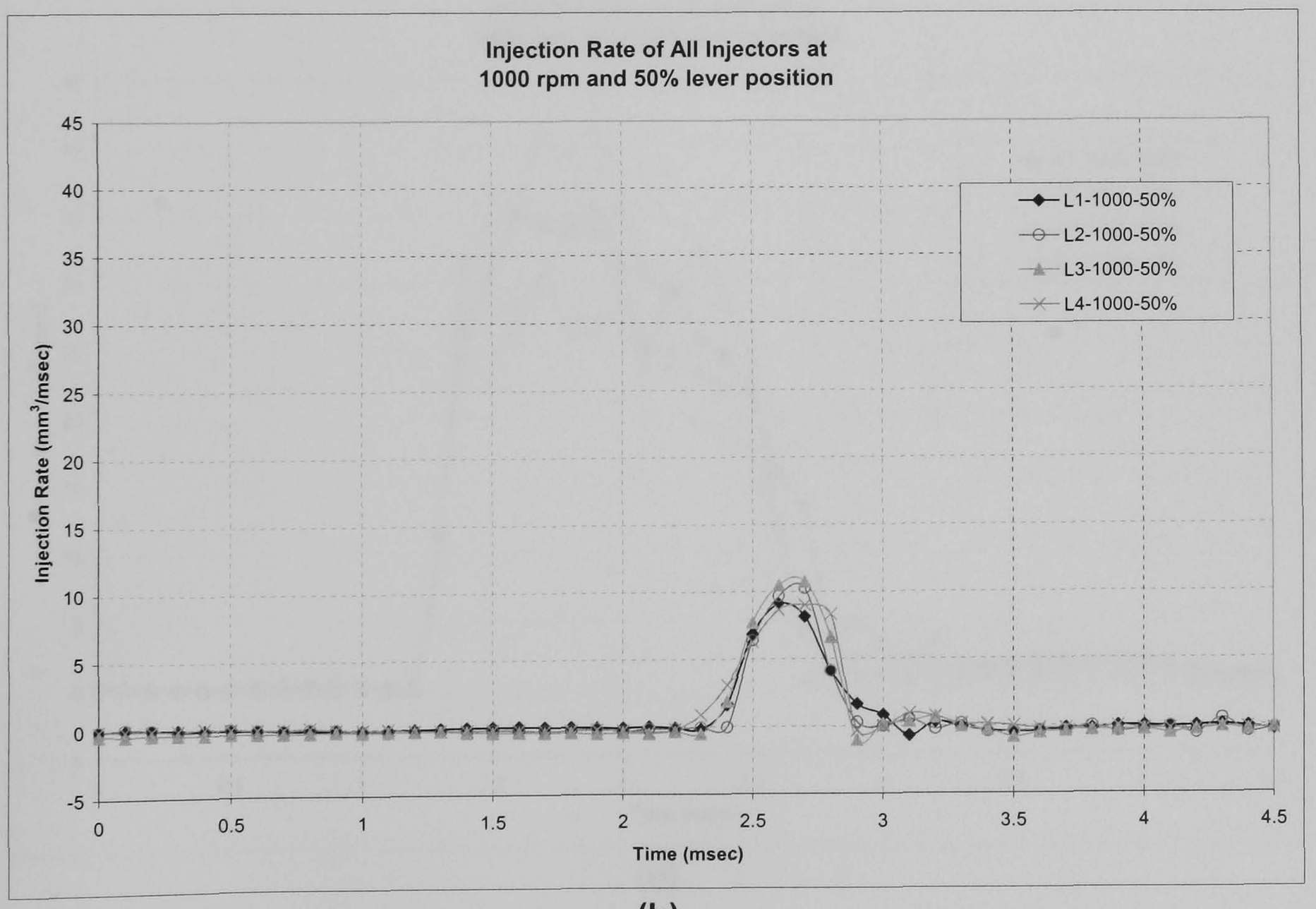

(b)

Figure 3.22 (a) and (b): Injection rate profiles of 25% and 50% lever positions for different injectors at 1000 rpm

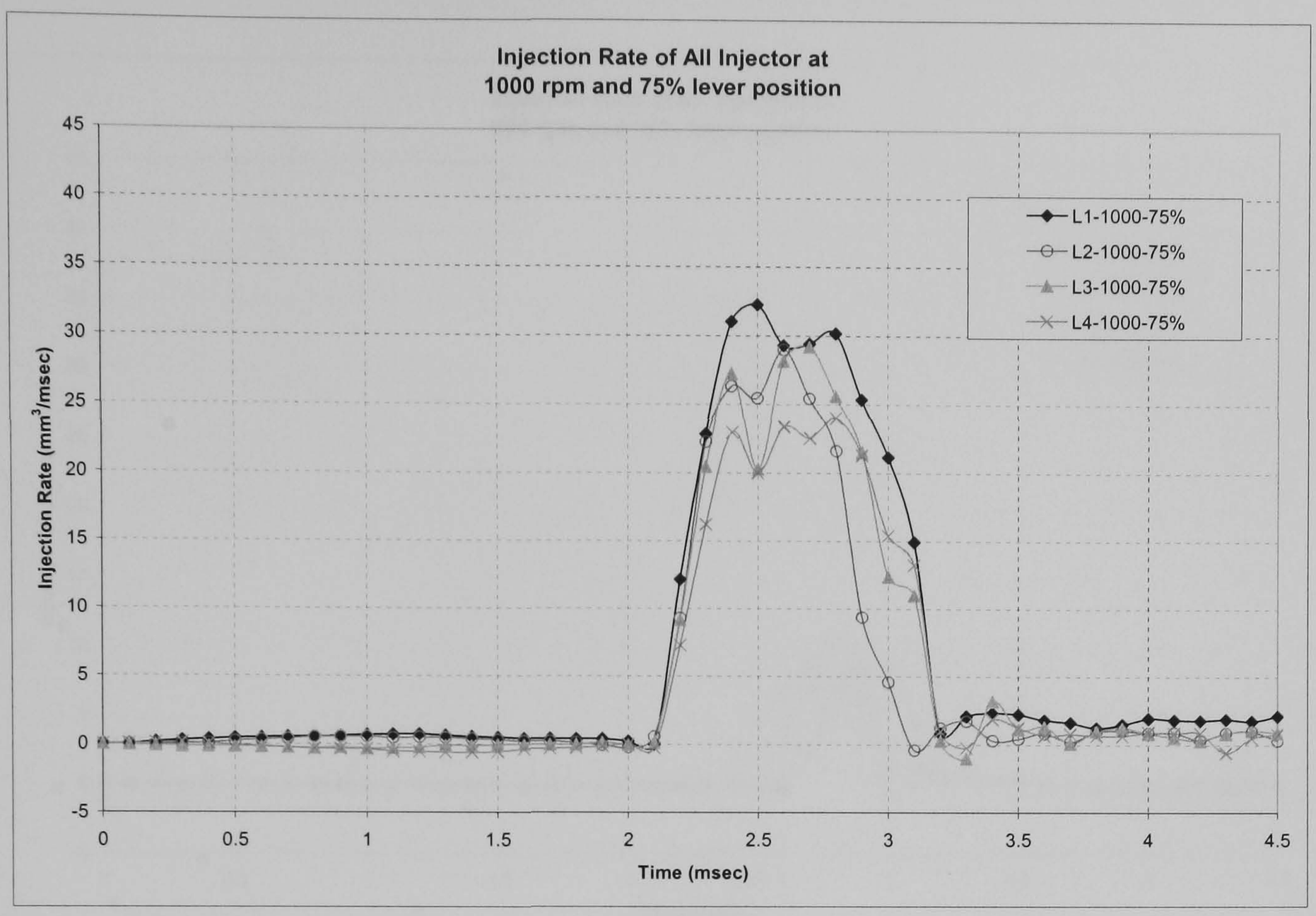

(c)

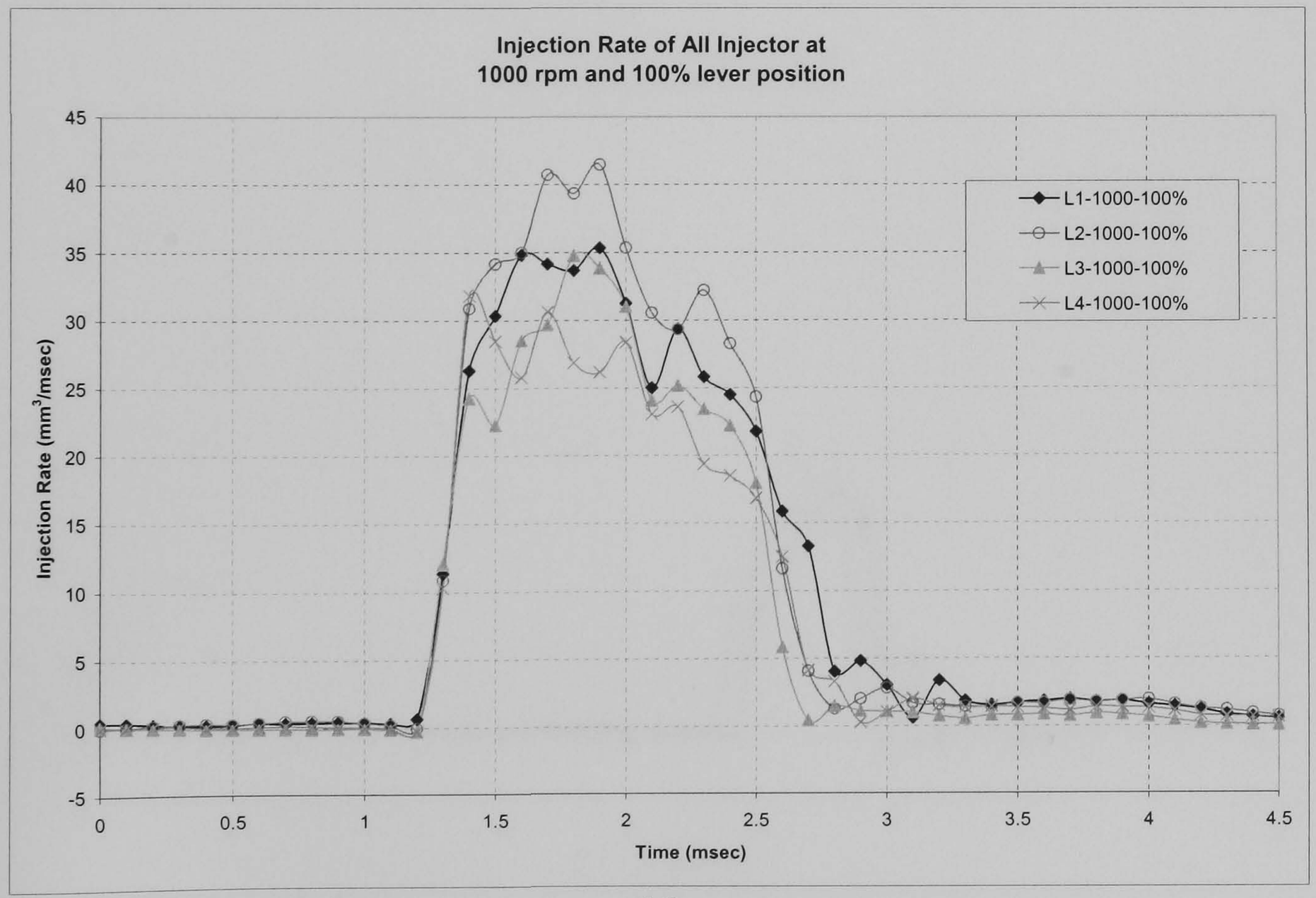

(d)

Figure 3.22 (c) and (d): Injection rate profiles of 75% and 100% lever positions for different injectors at 1000 rpm

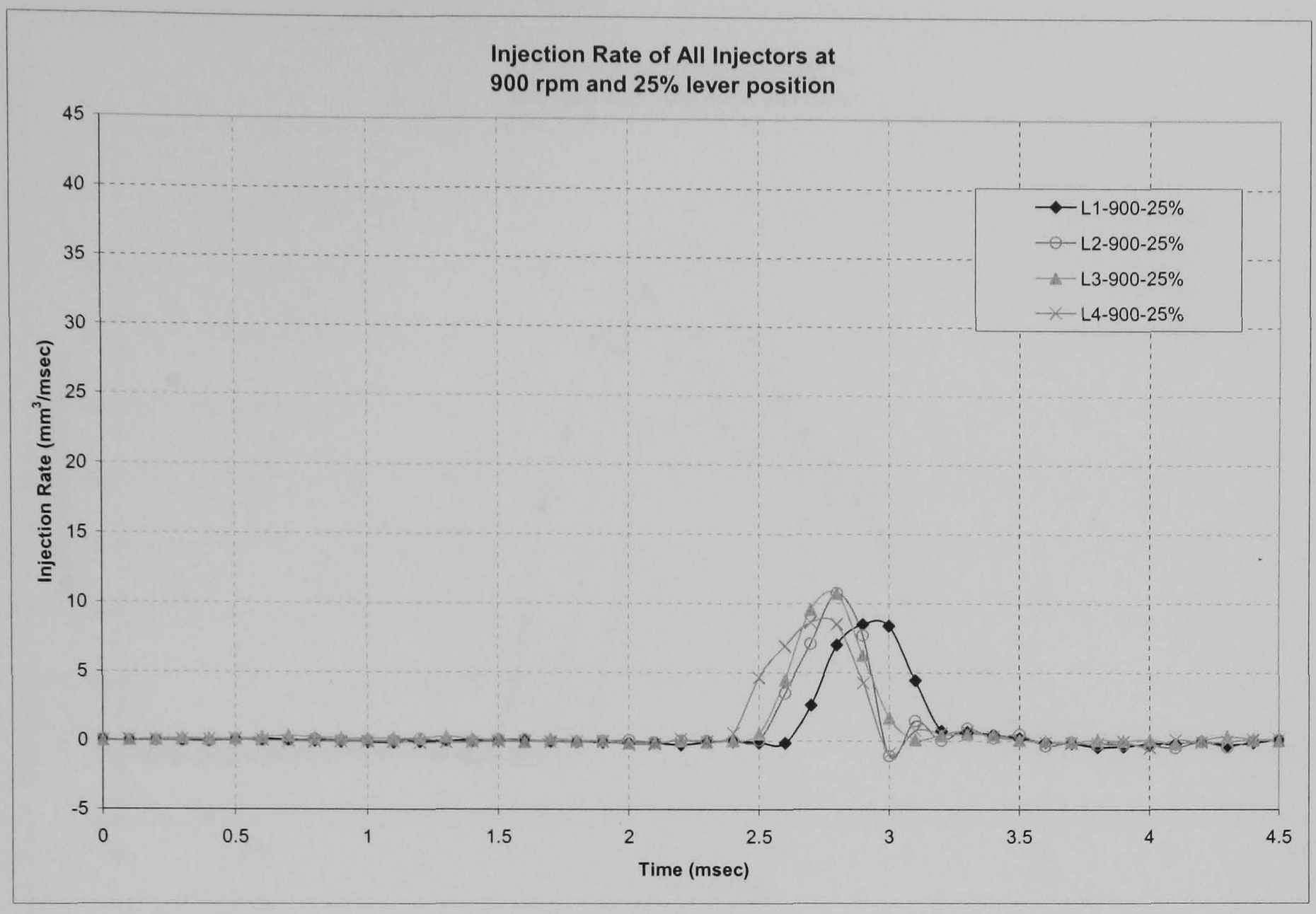

(a)

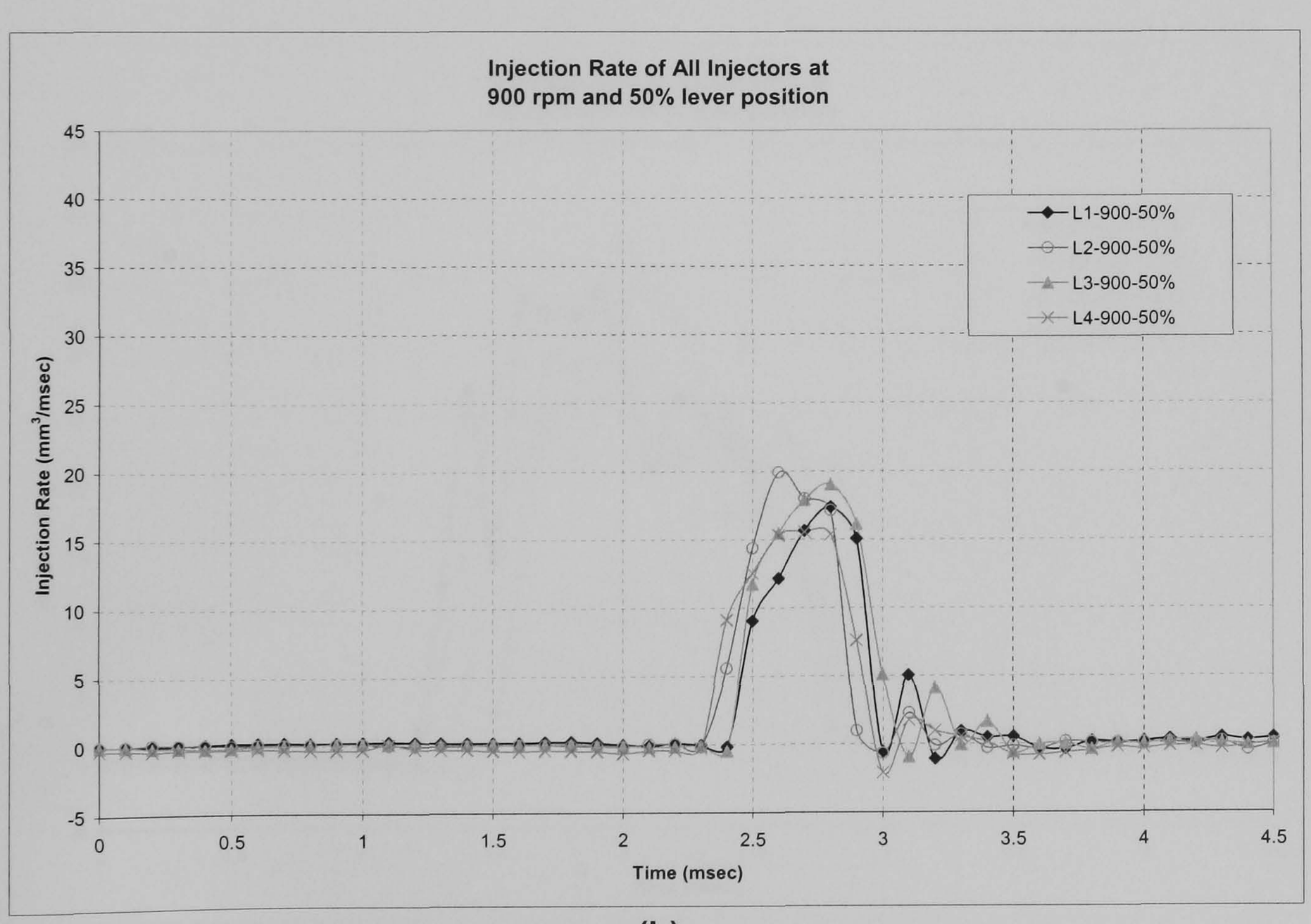

(b)

Figure 3.23 (a) and (b): Injection rate profiles of 25% and 50% lever positions for different injectors at 900 rpm

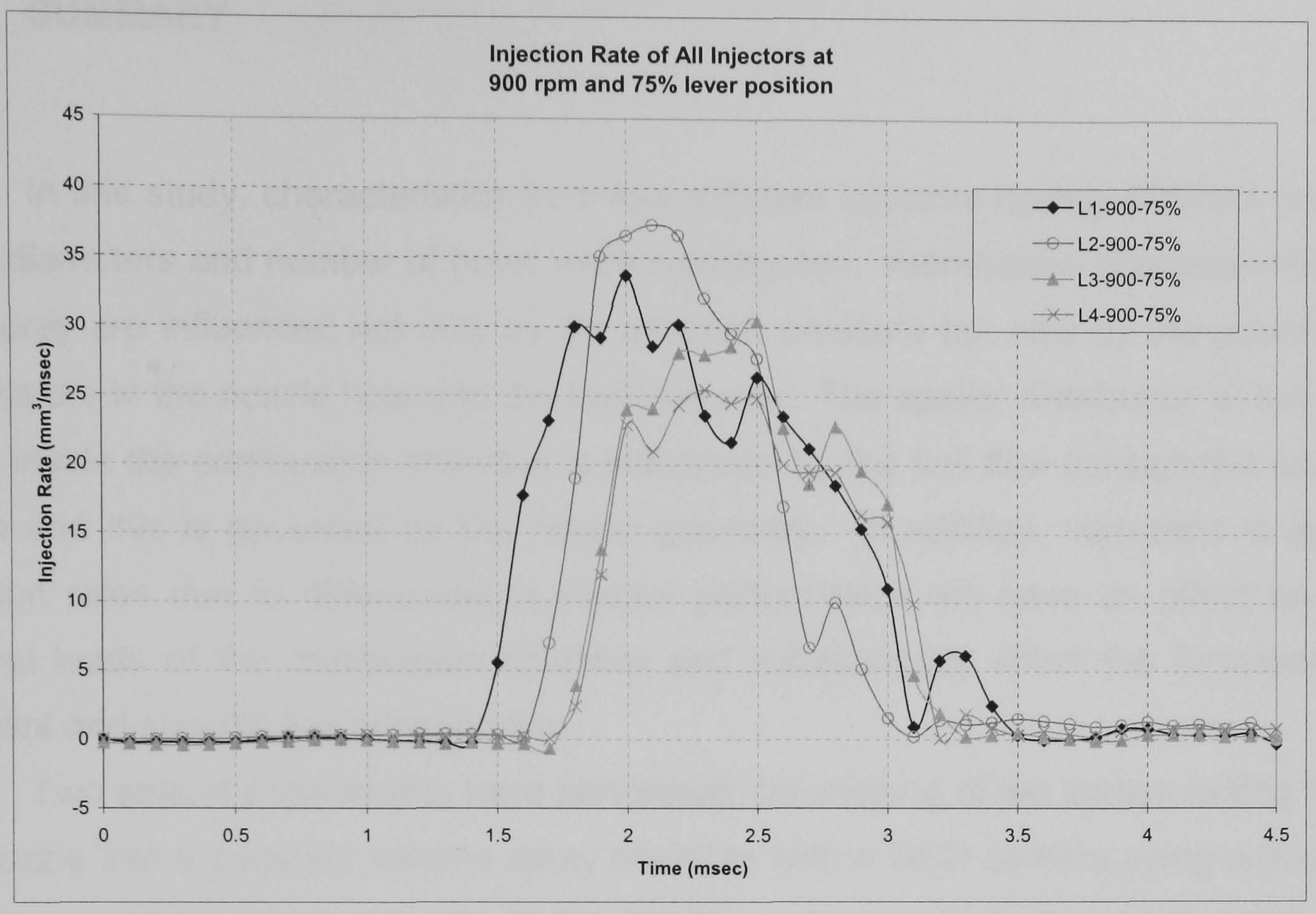

(c)

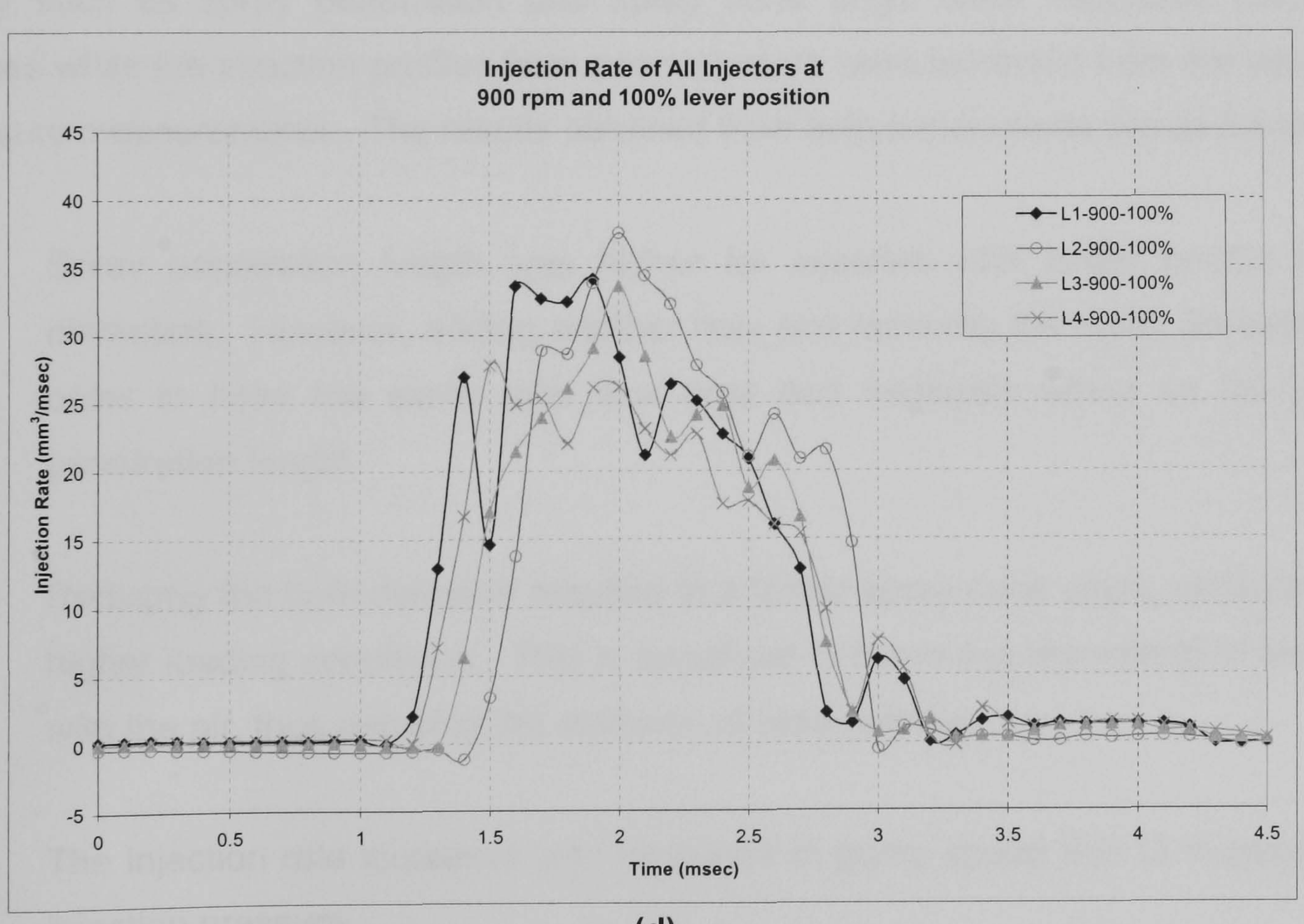

(d)

Figure 3.23 (c) and (d): Injection rate profiles of 75% and 100% lever positions for different injectors at 900 rpm

3.5 SUMMARY

In this study, characteristics from four different injectors having different nozzle holes diameters and number of holes were investigated. Atomisation characteristics of fuel spray are influenced not only by the injection pressure but also by the geometric parameters in the nozzle hole and the injection rate. The spatial distribution of the fuel spray inside the combustion chamber is influenced by the fuel flow through the nozzle orifice and this is governed by the nozzle geometry. In addition, variations in spray injection rates due to differences in injector performance will have an effect on the thermal loads of the combustion chamber and subsequently affect the formation of pollutant and specific fuel consumption.

Two sets of experiments were performed; (a) imaging of the sprays exiting from the nozzle into a constant volume spray chamber with a CCD camera using a back-lit technique and (b) measurements of the injection pressure from the nozzle using the Bosch Tube meter. From the imaging experiments, global characteristics of a diesel spray such as spray penetration and spray cone angle were measured from the images while the injection profiles from each injectors were extracted from the injection pressure measurements. The results obtained from both experiments are as follows:

- Spray penetration length was higher for injectors with larger nozzle holes diameters. However, adding another hole and reducing the holes diameters in order to have the same total flow area had negligible effect on the spray penetration length.

- Reducing the hole diameter resulted in a larger spray cone angle, especially at higher loading conditions. This is beneficial in improving the mixing of the fuel with the air, thus reducing the emission of black smoke.

- The injection rate increases with increases in pump speed due to increases in injection pressure.

- The injection rates for injectors having smaller holes diameters were higher at low load conditions but were lower at high load conditions.

CHAPTER 4: ENGINE FACILTY AND TESTING

This chapter discusses the test engine, equipment and instrumentation employed during the experiments, in addition to the exhaust gas emission measurements. The engine operating conditions were selected in order to enable the investigation of the effects of using injectors having different geometry on the combustion process of the test engine.

4.1 TEST ENGINE

The test engine used in the current research was a production Lister Petter 4X90, high speed, four-cylinder direct injection diesel engine, having a total displacement of 2.29 litres. This engine was one of Lister Petter X-series family, which could be used in a variety of set ups such as stationary generator set. The engine employed two valves per cylinder and was fitted with a re-entrant type piston. The injector was mounted in the cylinder head with a 1 mm offset and a 10° inclination relative to the centre line of the cylinder. The piston bowl was 4.22 mm off-centred from the piston centre. The engine was provided with a glow plug to each cylinder which was positioned with a 30° inclination to the normal to the cylinder head. A cross-sectional sketch of the cylinder head and piston are shown in Figure 4.1, with details of the fuel injector and glow plug positions with respect to the combustion chamber. Details of the engine specifications are given in Table 4.1. The engine power output is rated as 32.7 kW at 3000 rpm with 119.4 Nm torque, while the maximum torque is 143.0 Nm at 2000 rpm. The torque curve as a function of engine speed for this engine in the standard configuration is shown in Appendix IV.

The engine was coupled to a Heenan-Dynamatic MkII, 220 KW eddy current dynamometer. The operation to control the engine and dynamometer was performed either from the control console located outside the test cell or, from the control panel located inside the test cell. The control operation provided engine starting, running and stopping facilities by means of pushbuttons. Control modes included speed, torque or throttle position control in conjunction with a matched throttle actuator. An over-speed

trip facility was incorporated into the control system which could shutdown the engine and dynamometer in the event of engine over-speed. The engine could also be shutdown in the event of failure of the mains power or the dynamometer services and any fault connected to the engine test cell alarm system.

The engine torque was measured by a strain gauge load cell connected to the lever arm of the dynamometer. The load cell was calibrated by hanging known weights at the lever arm fixed to the dynamometer and then recording of the torque values which were provided by both a digital and an analogue readout. A magnetic pickup generated a signal with the passing of each gear tooth of a 60 toothed wheel attached to the rotating shaft for speed measurement. The frequency of the periodic signal generated is proportional to engine speed. An AVL 364 angle encoder was mounted on the flywheel shaft to provide a single marker pulse per cycle, as the trigger output, and 900 pulses for the crank degree marker, CDM.

A viscous air flow meter equipped with manometers was used to measure the airflow into the inlet manifold. The atmospheric air pressure was provided by a barometer in the control area, while the air pressure in the test cell was measured using a hand held 2022P Digitron differential manometer. Air temperature in the test cell was measured using a K-type thermocouple, which was placed at the same location for the test cell air pressure measurement. Fuel flow rate was determined by measuring the time for a known quantity of fuel to be consumed. This was provided by the gravimetric fuel measurement system equipped with a solenoid valve to fill the measuring tube, level sensors, and a timer. The fuel used was ESSO Ultra Low Sulphur Diesel, and the complete fuel properties are given in Appendix V. Some of the more important fuel properties are presented in Table 4.2. The in-cylinder pressure was measured using a Kistler Type 6053 B60 pressure transducer. A Kistler Type 5011 B10 charge amplifier was used to convert the charge signal from the transducer to an analog voltage of 0 to 10 volts for all the pressure measurements. The in-cylinder pressure transducer was flush-mounted in the fire deck of cylinder number 1 of the engine. The pressure transducer was calibrated using a dead weight tester and the calibration curve is shown in Appendix III. The in-cylinder pressure was referenced to the inlet manifold pressure. Temperatures of the inlet air, exhaust gas and cooling water were also taken at the relevant points using K-type thermocouples.

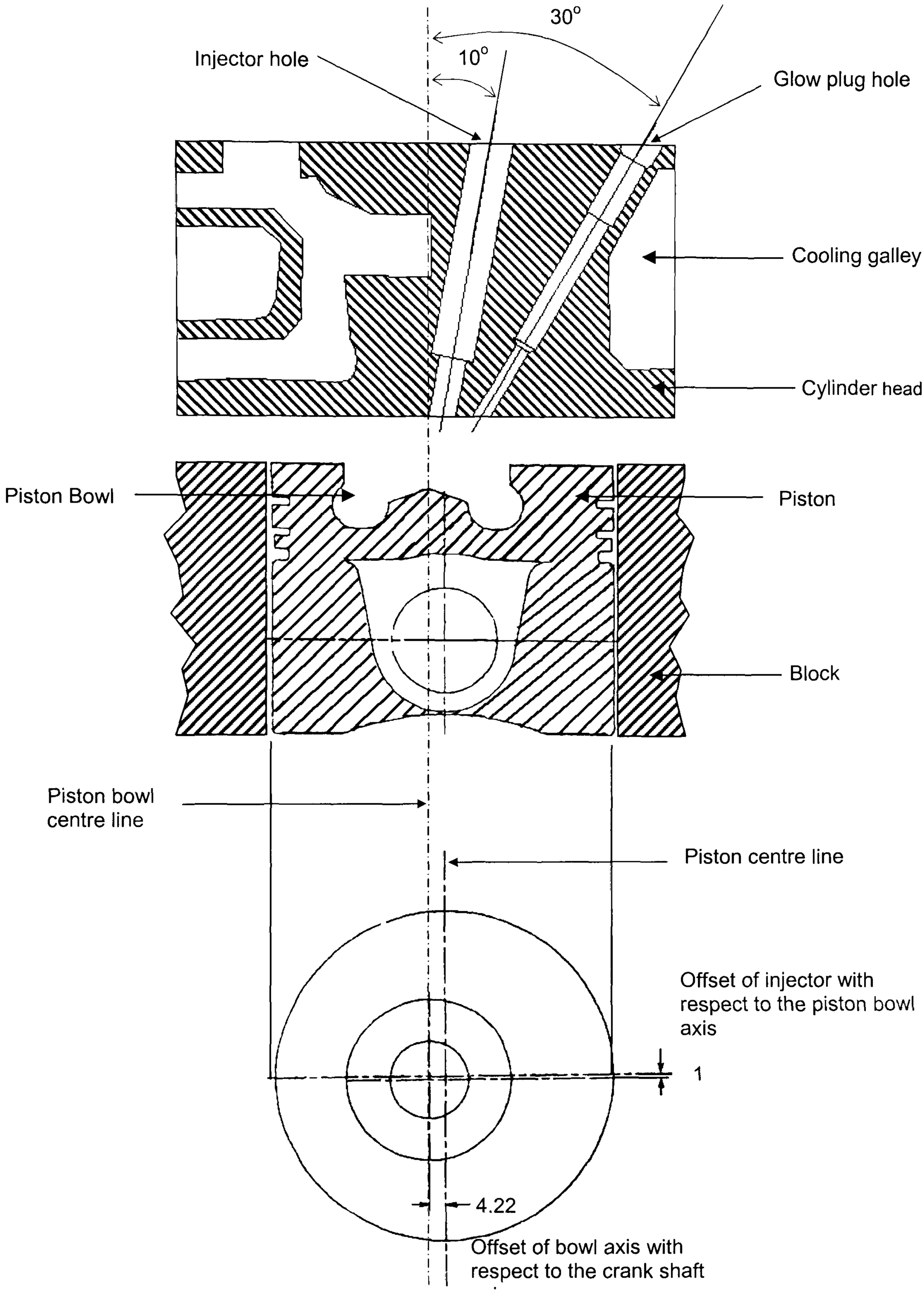

Figure 4.1 Schematic diagram of the combustion chamber

Table 4.1 Test engine specifications

Engine Type	Lister-Petter X90, DI, 4 stroke diesel
Configuration	Vertical, 4 cylinder in line
Cylinder Bore	90 mm
Stroke	90 mm
Connecting Rod Length	138 mm
Compression ratio	18.5:1
Combustion Chamber Type	Re-entrant
Swept volume (Displacement)	2.29 litres (2.29 x 10^{-3} m^3)
Min Full Load Speed	1500 rpm
Idle Speed	900 rpm
Min. Exhaust Back Pressure @ 3000rpm	75 mbar
Max. Intake Depression @ 3000 rpm	25 mbar
Rated Power	37.5 kW @ 3000 rpm
Maximum Torque	143 Nm @ 2000 rpm
Fuel Injection Pump	Lucas Rotary
Governing	Fixed or Variable Speed

Table 4.2 Diesel fuel specifications

PROPERTY	VALUE
Appearance	Light yellow
Cetane Number	54
Cetane Index	54
Density @ 15°C (kg/m^3)	834
Viscosity @ 40°C (mm^2/s)	2.69
Polycyclic Aromatic Hydrocarbons (% mass)	5.2
Sulphur Content (mg/kg)	40
Flash Point (°C)	64
Carbon Residue (% mass)	0.01
Ash Content (% mass)	<0.005
Water Content (mg/kg)	54
Particulate Matter (mg/kg)	2.9

4.2 INJECTION SYSTEM

The injectors used in this experiment were the same set of injectors used in the previous experiment for injection rate measurements. Descriptions of the injectors were given in Chapter 3 of this thesis. These injectors were also tested on the Hartridge Nozzle Testmaster prior to the engine test for visual inspection of the sprays and the nozzle opening pressure (NOP). The results of the test were the same as the results discussed in Section 3.3.1. A Kistler 4065 A1000 pressure transducer was installed to the high-pressure fuel line at a location 80 mm from the injector connector. The pressure-charge signals from the pressure transducer were measured and converted into a 0 to 10 volts output voltage using a Kistler 4617 AD piezoresistive amplifier. The pressure transducer was calibrated using a dead weight tester and the calibration data is shown in Appendix II. The engine was supplied with a Lucas rotary fuel injection pump Type 1333, having peak pumping pressures up to 720 bar. The pump was the same type as used for the injection rate measurements. Details of the pump were given in Section 3.3.1 of Chapter 3.

4.3 DATA ACQUISITION SYSTEM

The data received from the fuel line pressure transducer, the in-cylinder pressure transducer and the shaft encoder were acquired at intervals of 0.5° crank angle, using an AVL 670 Indimaster data acquisition system. These data were stored on the machine hard disk and were later transferred to a desktop personal computer for subsequent analysis.

The Indimaster data acquisition system allowed continuous monitoring of the test run as well as displaying both measurement and evaluation curves. These evaluation functions include statistical and thermodynamic analysis in real-time and on-line evaluation of the combustion chamber pressure (AVL-LIST, 2000). Images of the engine in the test cell and the equipment in the control room which were used during the experiments are shown in Figures 4.2 and 4.3.

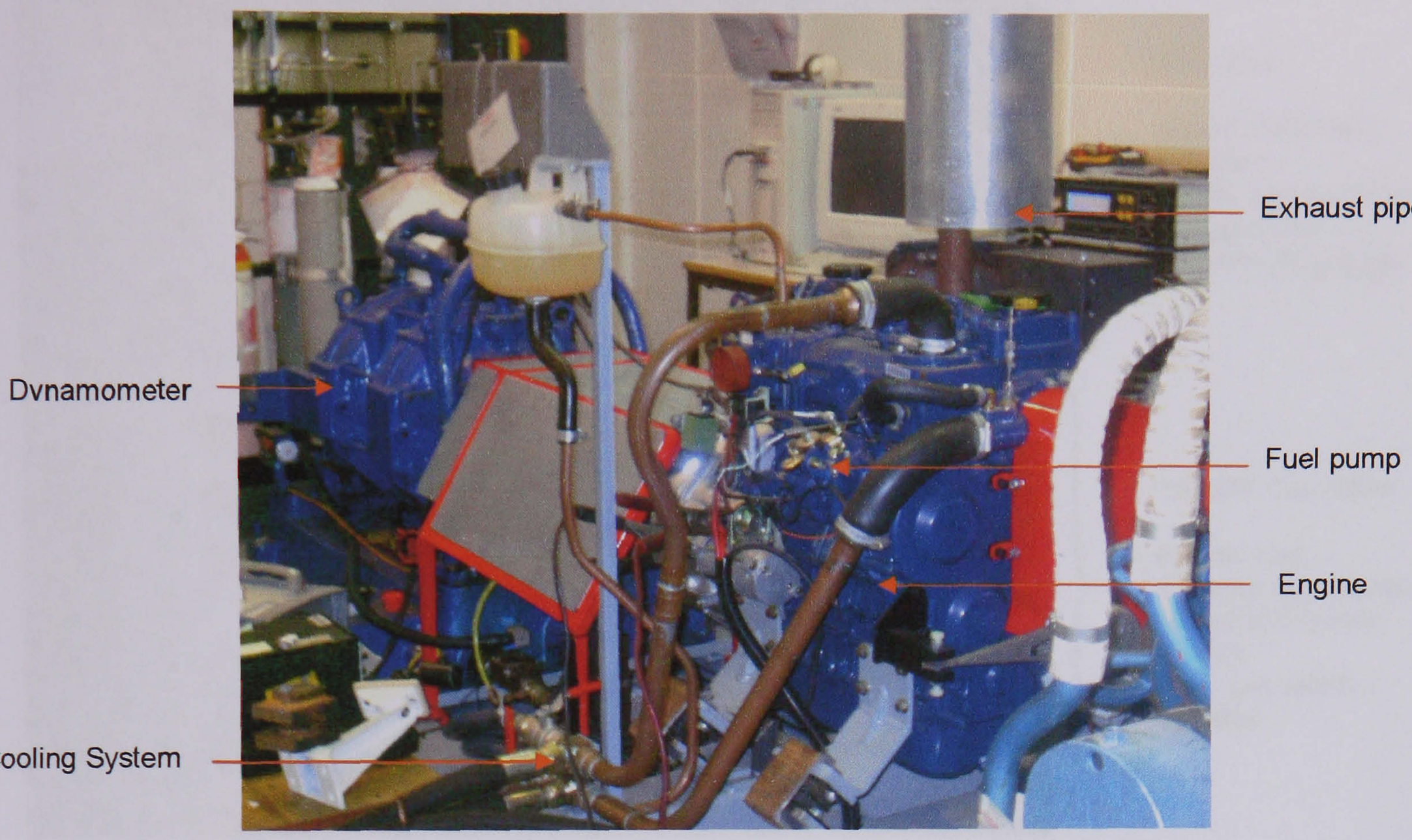

(a) View from the engine side

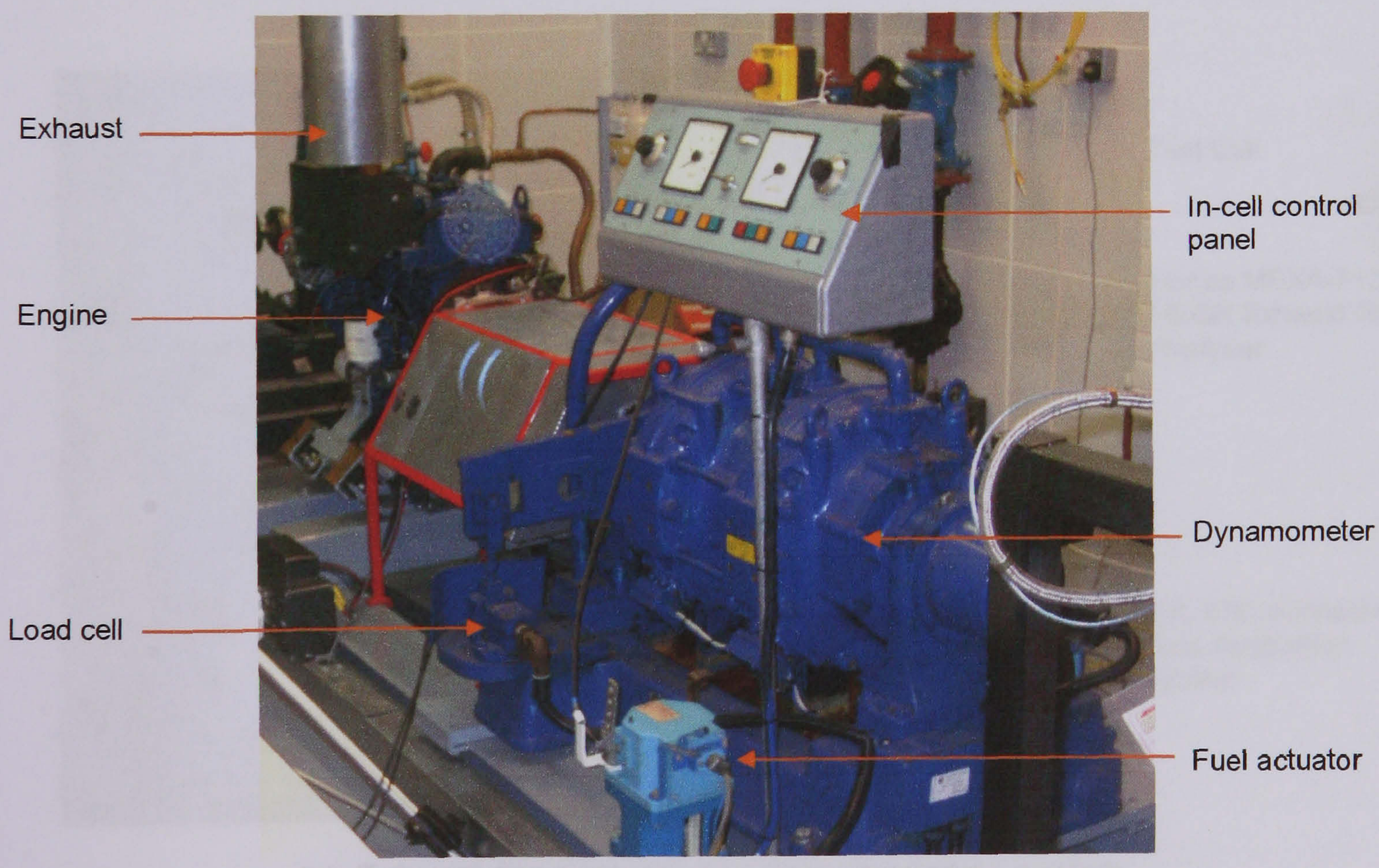

(b) View from the dynamometer side

Figure 4.2: Lister Petter 4X90 on the test bed coupled to the dynamometer in the test cell

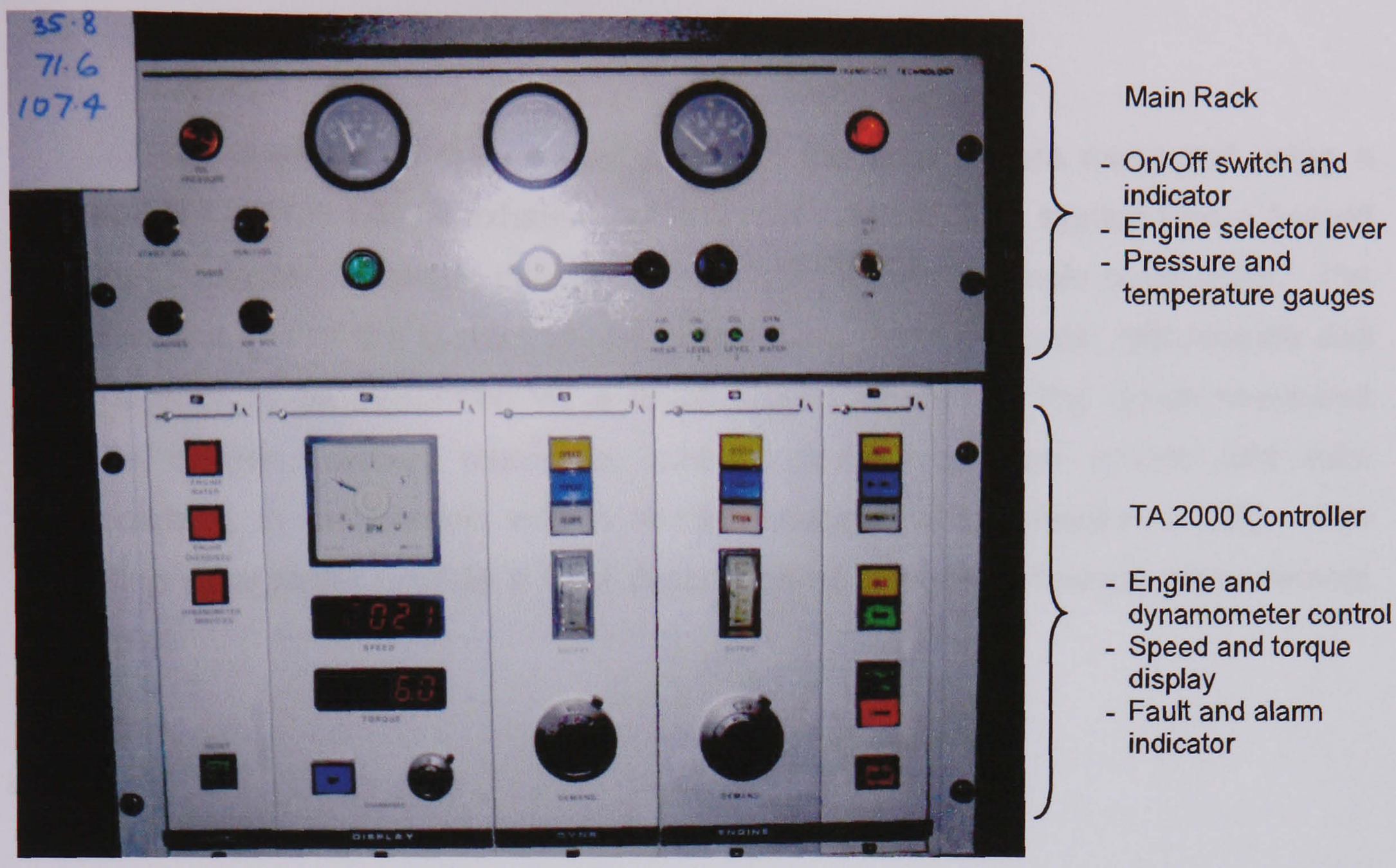

(a) Main control panel

(b) Exhaust gas analyser and data acquisition system

Figure 4.3: Equipment in the control room which were used for the engine test

4.4 EXHAUST EMISSIONS MEASUREMENT

The emissions in the exhaust gases of the engine were measured using a Horiba MEXA-7100 HEGR exhaust gas analyser system. The system had a heated line that could be connected directly to the engine exhaust sample outlet point. The main control unit of the system allowed calibration, measurements, adjustments and data storage to be performed via a touch screen interface. The gases measured include oxygen, carbon monoxide, carbon dioxide, nitrogen oxides and total hydrocarbon, in conjunction with a heated analyser which measures NO_2. The following paragraphs provide a brief description of the gas emissions measurement principles

4.4.1 Oxygen

Oxygen (O_2), is a paramagnetic substance which will align itself with the lines of force in a magnetic field. The analyser takes advantage of the magnetic properties of O_2 to measure the oxygen in a sample by passing the sample in a nitrogen stream, past an alternating magnetic field. The pressure between two detector plates varies according to the presence of O_2 in the sample.

4.4.2 Oxides of Nitrogen

The system utilises the chemiluminescent method for detection of nitric oxide, (NO) in the sample. A photo-diode is used to observe the reaction between NO and ozone, (O_3) in the reaction chamber in producing nitrogen dioxide (NO_2). The reaction emits photons of radiation with the number of photons proportional to the concentration of NO. For detection of oxides of nitrogen, (NOx), the sample containing NO and NO_2 is routed through a converter, instead of being passed directly into the reaction chamber, where all of the NO_2 is converted to NO. The total NO content is the sum of the NO produced from the NO_2 and the NO originally in the exhaust. This sum is referred to as oxides of nitrogen, NOx.

4.4.3 Total Hydrocarbons

Hydrocarbons, (HC) in the sample are measured using a heated flame ionisation detector (FID). When hydrocarbons are burned in an electric field, electrons and positive ions are formed producing an ionisation current. The measurement of total hydrocarbons, (THC) in a sample is accomplished by passing the sample through a hydrogen flame (the fuel used is a hydrogen/helium mixture). The hydrocarbons in the sample produce an ionisation current proportional to the total amount of carbon atoms present. A collector electrode surrounding the flame measures this change in the ionisation current. The results are specified as parts per million carbons.

4.4.4 Carbon Monoxide and Carbon Dioxide

Both carbon monoxide (CO) and carbon dioxide (CO_2) was measured using a non-dispersive infrared detector (NDIR) to measure. The analyser works on the principle that infrared radiation is absorbed in the wavelength band associated with the different gases. The analyser consists of four elements, i.e. an infrared radiation source, a reference cell, sample cell, and a detector. The sample gas is pumped into a sample cell through which infrared light is passed. The wavelength of the light is specifically selected depending on the component to be detected. The components of carbon monoxide or carbon dioxide, if present in the sample, absorbs the light and decreases the intensity of the light transmitted through the sample cell. This intensity is compared to a reference light source by the detector and the resulting difference is expressed in concentration of the specific components.

4.4.5 Smoke Measurement

The smoke content of the exhaust gas is measured using an AVL 415 Variable Sampling Smoke Meter. The soot concentration value is given as a smoke opacity in terms of the Bosch Filter Smoke Number (FSN), smoke density in unit mg/m^3, or % pollution level. The system extracts a sample of the exhaust gas through a probe inserted in the exhaust pipe. The sample is then passed through a clean filter paper. The blackness of the filter paper due to soot deposits is determined by a reflectometer head which then converts this into FSN. The entire measurement process from purging of the flow path, sampling transport and filtration to the determination of the paper blackening is controlled and monitored by a microprocessor in the system.

4.5 EXPERIMENTAL SET-UP

Engine performance and emissions data were obtained under steady state operating conditions at engine speeds of 1800 rpm and 2000 rpm, and a coolant temperature of 80 °C. Two engine speeds were chosen to simulate important operating conditions. The engine speed of 1800 rpm was the minimum speed at full load of the engine while 2000 rpm was the speed of the engine at maximum torque. The engine loads were determined based on the percentage of the maximum torque at the respective speed, i.e. full load represented the maximum torque, 50% load was 50% of the maximum torque while 0% load was the engine operating condition at the respective speed without any applied torque (neglecting small frictional force). The fuel injection pump was set for a fixed injection timing.

The smoke measurement was obtained by reading the digital readout on the AVL 415 Variable Sampling Smoke Meter. The concentration of THC, NOx, CO, CO_2 and O_2 were measured with the Horiba MEXA-7100 HEGR exhaust gas analyser system at all the test conditions. Cylinder pressure and fuel line pressure were measured at a resolution of 0.5° crank angle using the AVL 670 Indimaster data acquisition system. These data were saved into the system's hard disk.

The influence of nozzle hole diameter and number of nozzle hole on heat release rate and combustion were investigated. Parameters such as engine speed and engine load were varied to determine the effect of using the different injectors on the performance of the engine. The operating conditions for the test are listed in Table 4.3, while the experimental set-up is shown schematically in Figure 4.4.

Table 4.3: Operating conditions for the test matrix

Test No	Engine Speed (rpm)		Engine Load (%)						Injector			
1	1800	2000	0	25	-	50	-	75	L1	L2	L3	L4
2	1800	2000	0	25	-	50	-	75	L1	-	L3	-
3	1800	2000	0	25	37	50	63	75	L1	L2	L3	L4

1	AVL 364 Shaft Encoder
2	Kistler 6053 B60 In-Cylinder Pressure Transducer
3	Kistler 4065 A 1000 Fuel Line Pressure Transducer
4	Kistler 5011 B10 Charge Amplifier
5	Kistler 4617 AD Piezoresistive Amplifier

Figure 4.4: Experimental set-up for the engine test

CHAPTER 5: HEAT RELEASE RATE MODELLING

5.1 INTRODUCTION

Combustion models based on the thermodynamic energy conservation can be categorised into three different approaches, as suggested by Heywood (Heywood, 1988). They are labelled as (a) zero-dimensional models, in which flow characteristics or fluid motion are not taken into account, (b) phenomenological models, in which additional phenomena such as ignition delay period, are considered in the energy conservation equations, and (c) quasi-dimensional in which specific features such as fuel droplet distribution, are added to the basic thermodynamic approach. The following paragraphs will describe three zero-dimensional models, found in the literature, which were developed in an attempt to determine the energy release during the combustion process of a diesel engine. This energy is known as the heat release rate and the models are all based on the First Law of Thermodynamics.

Heat release rate is an important parameter of the combustion process since it can be used to describe the combustion characteristics of fuel in gasoline and diesel engines. Brunt and Platts (Brunt and Platts, 1999) reported that the heat release rate has significant influence on combustion noise, rate of pressure rise and NOx emissions. Heat release rate modelling is used here in support of combustion analysis for investigating of the combustion process in a diesel engine. The rate of heat release during combustion is obtained by computing the thermodynamic and ideal gases equations with measured cylinder pressure-crank angle data as an input parameter. However, the thermodynamics and ideal gases equations are only applicable to the part of the working cycle at which the inlet and outlet valves are closed, i.e. during the compression and expansion stroke. Because they are thermodynamic models, it is necessary therefore to define the "control volumes", i.e. single zone, two-zone or three-zones on which the thermodynamic analysis is to be performed and assumptions that are made. The following parameters are information that is required when developing a model to determine the rate of heat release;

- Data describing the geometry of the engine.
- Experimental data of the cylinder pressure versus time (or crank angle).
- Expressions for the internal energy, enthalpy and gas constant for the combustion products, unburned mixture and the fuel.
- Correlation for the gas-side heat transfer coefficient.
- Set of initial conditions - temperature, pressure, residual fraction and equivalent ratio.
- An estimate of metal temperatures for the exposed combustion chamber surfaces.
- Mass of intake air and injected fuel.

In the model, irrespective of the number of zones, Heywood (Heywood, 1988) stated that it is sufficiently accurate to assume that the composition is 'frozen' since the composition of the unburned mixture does not change significantly during intake and compression.

5.2 SINGLE-ZONE MODEL

Single-zone models are the least complex models when compared to multi-zone models. The control volume for the single-zone model is defined to be coincident with the entire combustion chamber volume. The model consists of the terms for work, chemical energy change and change in internal energy of the control volume contents. The term for heat transfer of the charge gas to the combustion chamber wall could also be included. However, the model does not include spatial variation in the combustion chamber and the fuel enthalpy. Hence, the model assumes uniform charge temperature and composition at all time during the cycle. Single-zone models have been described by Watson (Watson and Janota, 1982), Heywood (Heywood, 1988), and Brunt (Brunt and Platts, 1999).

The single-zone models are based on the First Law of Thermodynamics applied to the entire cylinder contents and can be defined as the following.

$$dQ = dW + dU$$

Where dQ describes the difference between the heat released by combustion of the fuel, dQ_{comb}, and the heat transfer from the system, dQ_{wall} (heat loss to the combustion chamber wall in this case). Substituting these terms into the above equation, we have;

$$dQ_{comb} = dW + dU + dQ_{wall} \tag{5.1}$$

The following simplifying assumptions are made at this stage;

1. The contents of the control volume are homogeneous.
2. Effects of chemical dissociation are neglected.
3. The ideal gas law is applicable to the contents in the control volume.

The term dW in equation (5.1) defines the work done onto the piston, such that $dW = PdV$ while dU is the internal energy of the cylinder contents, which is a function of temperature only, and is written as;

$$dU = mc_v dT$$

Where m and c_v are mass and specific heat of the cylinder contents respectively. Rewriting equation (5.1), we have;

$$dQ_{comb} = PdV + mc_v dT + dQ_{wall} \tag{5.2}$$

The term dT can also be replaced by;

$$d(PV) = mRdT$$

Where R is the universal gas constant.

$$dT = \frac{PdV}{mR} + \frac{VdP}{mR}$$

Substituting dT into equation (5.2), the heat release due to combustion can be written as;

$$dQ_{comb} = PdV + mc_v\left(\frac{PdV}{mR} + \frac{VdP}{mR}\right) + dQ_{wall}$$

$$dQ_{comb} = PdV + \frac{c_v}{R}PdV + \frac{c_v}{R}VdP + dQ_{wall}$$

Also,

$$\frac{c_v}{R} = \frac{1}{\gamma - 1}$$

$$dQ_{comb} = PdV + \left(\frac{1}{\gamma - 1}\right)PdV + \left(\frac{1}{\gamma - 1}\right)VdP + dQ_{wall}$$

Thus, the heat release due to combustion that would result in the experimental cylinder pressure trace is given by;

$$dQ_{comb} = \left(1 + \frac{1}{\gamma - 1}\right)PdV + \left(\frac{1}{\gamma - 1}\right)VdP + dQ_{wall} \qquad (5.3a)$$

or written as rate of heat release with respect to crank angle, θ;

$$\frac{dQ_{comb}}{d\theta} = \left(1 + \frac{1}{\gamma - 1}\right)P\frac{dV}{d\theta} + \left(\frac{1}{\gamma - 1}\right)V\frac{dP}{d\theta} + \frac{dQ_{wall}}{d\theta} \qquad (5.3b)$$

Therefore, the solution to the equation requires data of the in-cylinder pressure-crank angle histories, the combustion chamber volume at each crank angle and a correlation for the combustion chamber wall heat transfer.

5.3 TWO-ZONE MODEL

In a two-zone heat release rate model, the burned and unburned gases are treated as two separate zones. This type of model could provide information on the temperatures, volumes and mass fractions of both the burned and unburned zones, in addition to the heat release rate.

The example of a two-zone model described here is the heat release rate model based on the First Law of Thermodynamics as described by Kamimoto et al. (Kamimoto and Minagawa, 2000). Their analysis of the heat release of diesel fuel combustion model assumed that at any instant during combustion, the control volume (combustion chamber) could be divided into a burned gas zone and unburned air zone. Both zones are assumed to be at the same pressure at any instant and the mixtures are assumed to be in thermodynamic equilibrium. Zone 1 is defined as the burned zone and composed of two types of gaseous mixtures, i.e. unburned fuel and unburned air at temperature, T_u, and burned gas at temperature, T_b. Whereas zone 2 is defined as the unburned zone and composed of only air at temperature T_2. The two-zone model is schematically shown in Figure 5.1.

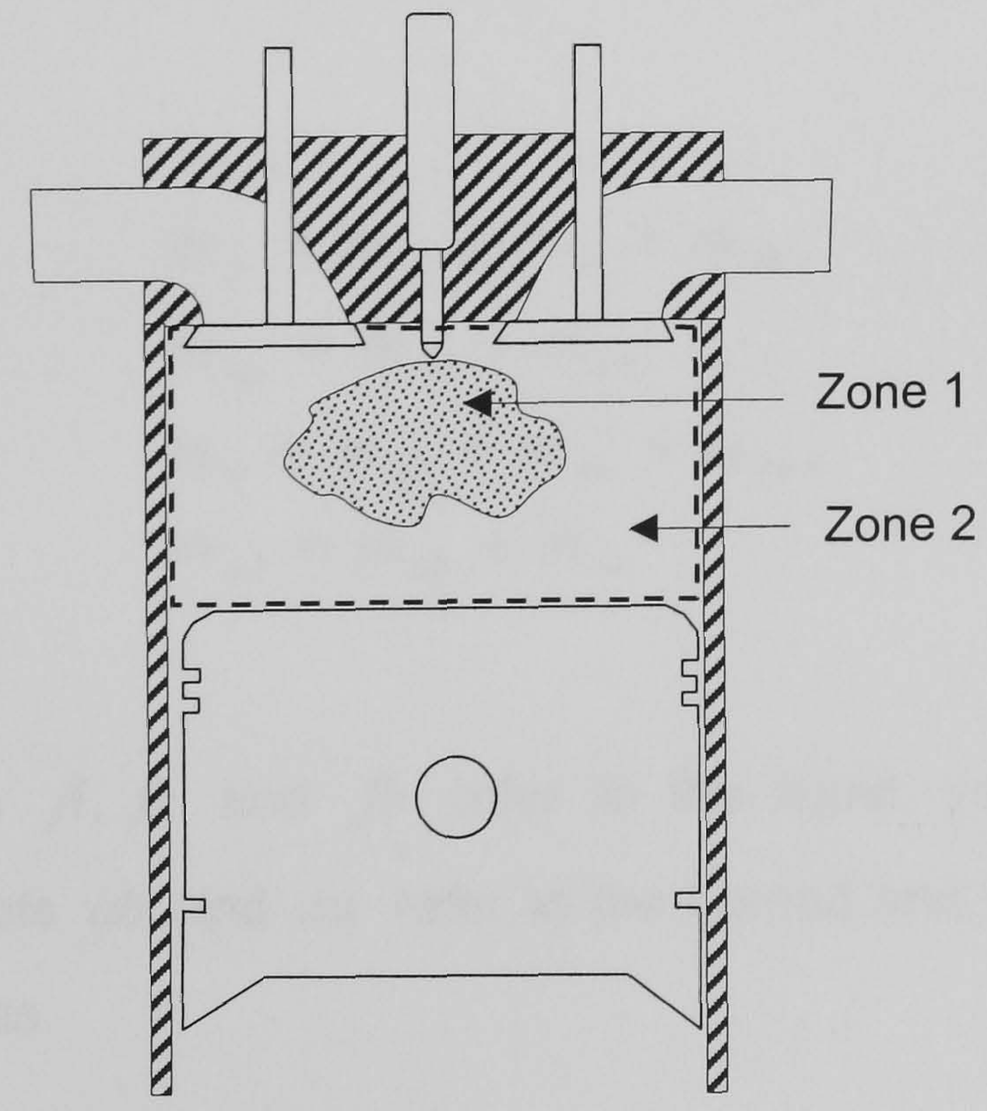

Figure 5.1: Two-zone heat release model

The energy equations for zone 1 and zone 2 are given by;

$$dU_1 = dH_1 - dQ_{wall_1} - dW_1 \qquad dU_2 = -dQ_{wall_2} - dW_2$$

Where dH_1 is the enthalpy energy in zone one, dQ_{wall_1} and dQ_{wall_2} are both heat losses to the combustion chamber wall, while dW_1 and dW_2 define the work done onto the piston in zone 1 and zone 2 respectively. Since the pressure in the combustion chamber is assumed to be constant, both work terms can be substituted by PdV. The total energy in the combustion chamber can then be written as;

$$dU_1 + dU_2 = dH_1 - dQ_{loss} - PdV \tag{5.4}$$

Kamimoto (Kamimoto and Minagawa, 2000) defined the mass in zone 1 to be made of the mass of fuel in three different phases, liquid, vapour and burned, and the mass of burned and unburned air. However, in zone 2, the mass is only of the air. The masses are defined by the following mass conservation equations;

$$m_f = m_{fl} + m_{fv} + m_{fb}$$
$$m_{bg} = m_{fb} + m_{ab}$$
$$m_a = m_{ab} + m_{au} + m_{au\,2}$$
$$m_{a\,1} = m_{ab} + m_{au}$$

Where the subscripts fl, fv and fb refer to the liquid, vapour and burned fuel respectively. Subscripts ab and au refer to the burned and unburned air, while bg refers to the burned gas.

By substituting the above mass equations into equation (5.4) and further simplifications, Kamimoto at al. (Kamimoto and Minagawa, 2000) derived the following equation;

$$\begin{aligned} &m_{fl}du_{fl} + m_{fv}du_{fv} + m_{bg}du_{bg} + m_{a2}du_{a2} + (u_{au} - u_{a2})dm_{a1} \\ &+ (u_{bgTb} - u_{bgTu})dm_{bg} + pdV = dQ_{comb} - dQ_{loss} \end{aligned} \tag{5.5}$$

At this junction, the following assumptions were made;

1. The injected fuel evaporates instantly, i.e. $m_{fl} = 0$.
2. Combustion takes place at stoichiometric air-fuel ratio.
3. Fuel vapour and unburned air in zone 1 have an identical temperature T_2.

With these assumptions, equation (5.5) can be written for the heat release as;

$$\begin{aligned} dQ_{comb} = m_{fv}c_{vfv}dT_2 + m_{bg}c_{vbg}dT_b + (m_a - m_{ab})c_{va}dT_2 \\ + (u_{bgT_b} - u_{bgT_u})dm_{bg} + PdV + dQ_{loss} \end{aligned} \tag{5.6a}$$

or written as rate of heat release with respect to crank angle, θ;

$$\begin{aligned} \frac{dQ_{comb}}{d\theta} = m_{fv}c_{vfv}\frac{dT_2}{d\theta} + m_{bg}c_{vbg}\frac{dT_b}{d\theta} + (m_a - m_{ab})c_{va}\frac{dT_2}{d\theta} \\ + (u_{bgT_b} - u_{bgT_u})\frac{dm_{bg}}{d\theta} + P\frac{dV}{d\theta} + \frac{dQ_{loss}}{d\theta} \end{aligned} \tag{5.6b}$$

The solution to the two-zone heat release rate equation requires similar data as for the single-zone model, i.e. in-cylinder pressure-crank angle histories, combustion chamber volume and a heat transfer correlation. In addition, the two-zone model also requires equations for the internal energy, u_{bg}, and specific heat constants calculation, values of the temperatures T_u and T_b, and the masses of components in each zones, $m_{fv}, m_{bg}, m_{ab}, m_a$.

5.4 THREE-ZONE MODEL

The discussion of the three-zone model is based on the model developed by Timoney et al. (Timoney et al., 2000). As with the previous two models, the First Law of Thermodynamics was employed to describe the heat release rate of diesel fuel combustion in the combustion chamber. For the three-zone model, the combustion chamber is divided into three discrete zones. Zone 1 consists of only fuel, which is assumed to vapourise into gaseous fuel upon injection into the combustion chamber. Zone 2 contains unburned gas mixture of the intake air and a small fraction of unburned gas that was recirculated into the intake air. Zone 3 represents the burned zone and only comes into existence upon combustion of the fuel in zone 1 with the unburned gases in zone 2. Each zone is represented by the subscripts u, b and f for the unburned, burned and fuel respectively. A schematic diagram of the three-zone heat release model is shown in Figure 5.2.

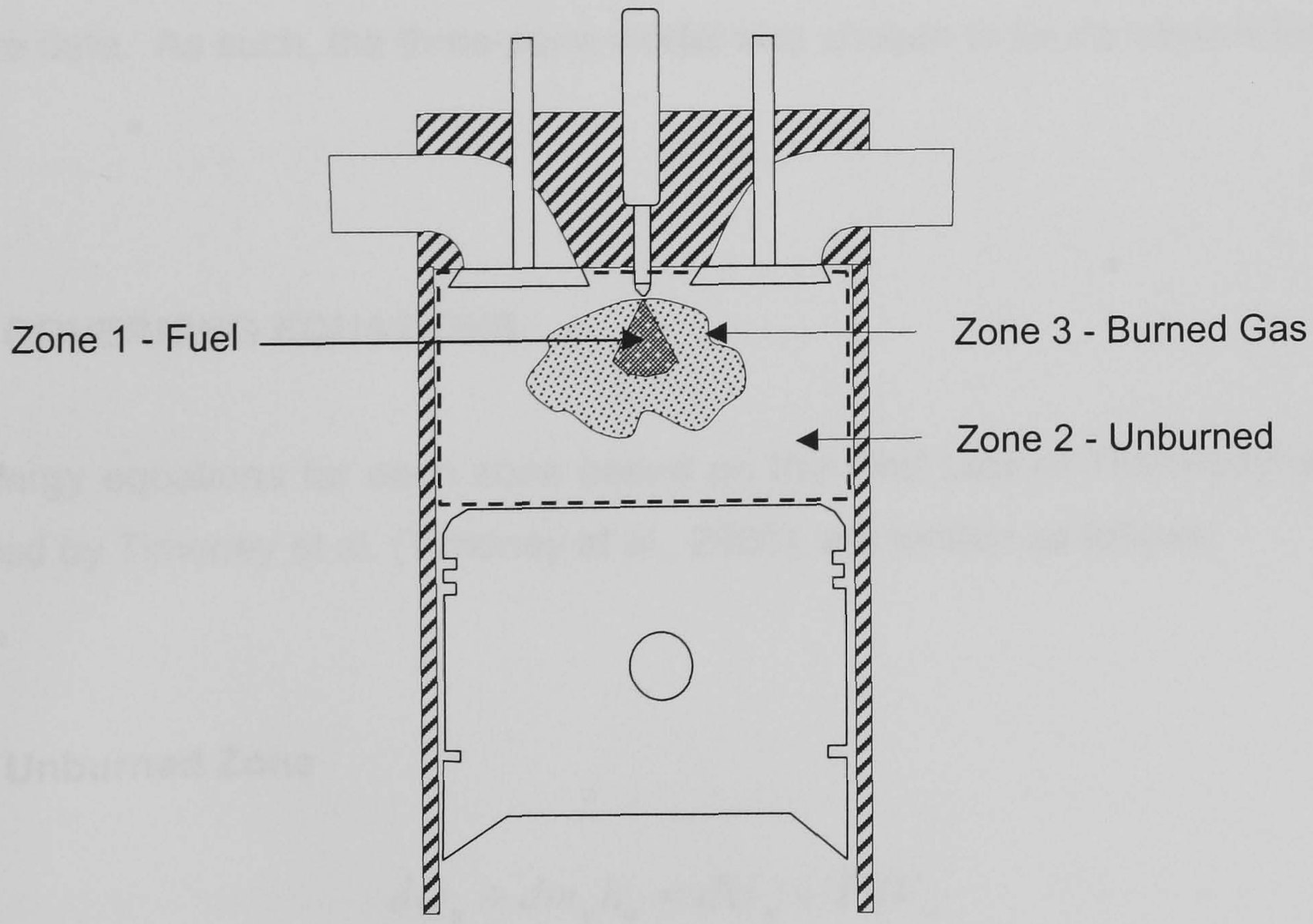

Figure 5.2: Three-zone heat release model

The following assumptions are made for the three-zone model;

- The mixture in each zone is instantaneously and completely mixed. Hence, each zone is uniform in temperature and composition.
- The contents of the control volume are homogeneous.
- The combustion chamber pressure is uniform at any instant in time.
- Effects of chemical dissociation are neglected.
- The individual species in the burnt, unburned and fuel vapour can be modelled as ideal gases.
- The fuel and oxygen burn immediately to form products of stoichiometric combustion.
- The products of combustion consist of four species, i.e. oxygen (O_2), nitrogen (N_2), carbon dioxide (CO_2) and water vapour (H_2O).

The three-zone model described here provides an opportunity to extend the model by applying the acquired fuel injection rate data as input to the fuel zone. This would be the second input data to the model, in addition to the available in-cylinder pressure data. As such, the three-zone model was chosen to be developed further.

5.5 GOVERNING EQUATIONS

The energy equations for each zone based on the First Law of Thermodynamics, as described by Timoney et al. (Timoney et al., 2000), are written as follows;

5.5.1 Unburned Zone

$$dQ_u + dm_u h_u = dU_u + PdV_u \tag{5.7}$$

The internal energy, $U_u = m_u h_u - PV_u$. Thus, a change in internal energy is given by;

$$dU_u = m_u dh_u + h_u dm_u - PdV_u - V_u dP \tag{5.8}$$

Substituting equation (5.8) into (5.7), we have;

$$dQ_u + dm_u h_u = m_u dh_u + h_u dm_u - PdV_u - V_u dP + PdV_u \tag{5.9}$$

Since $dh_u = c_{pu} dT_u$, equation (5.9) becomes;

$$dQ_u = m_u c_{pu} dT_u - V_u dP \tag{5.10a}$$

or written as a rate equation with respect to change in crank angle, θ;

$$\frac{dQ_u}{d\theta} = m_u c_{pu} \frac{dT_u}{d\theta} - V_u \frac{dP}{d\theta} \tag{5.10b}$$

Equation (5.10b) represents the rate of heat addition to the unburned zone.

5.5.2 Fuel Zone

$$dQ_f + dm_f\left(h_f + \frac{1}{2}V_{inj}^2\right) = dU_f + PdV_f \tag{5.11}$$

Where $dm_f\left(h_f + 1/2V_{inj}^2\right)$ represents the enthalpy and kinetic energy added to the fuel zone due to the injection of fuel in the combustion chamber. The internal energy can be written as, $U_f = m_f h_f - PV_f$.

The change in internal energy is therefore given by;

$$dU_f = m_f dh_f + h_f dm_f - PdV_f - V_f dP \tag{5.12}$$

Substituting equation (5.12) into (5.11). we have;

$$dQ_f + dm_f\left(h_f + \frac{1}{2}V_{inj}^2\right) = m_f dh_f + h_f dm_f - PdV_f - V_f dP + PdV_f \tag{5.13}$$

Since $dh_f = c_{pf} dT_f$, equation (5.13) becomes;

$$dQ_f + dm_f\left(\frac{1}{2}V_{inj}^2\right) = m_f c_{pf} dT_f - V_f dP \tag{5.14a}$$

or written as a rate equation with respect to change in crank angle, θ;

$$\frac{dQ_f}{d\theta} + \frac{dm_f}{d\theta}\left(\frac{1}{2}V_{inj}^2\right) = m_f c_{pf}\frac{dT_f}{d\theta} - V_f\frac{dP}{d\theta} \tag{5.14b}$$

Equation (5.14b) represents the rate of heat addition to the fuel zone.

5.5.3 Burned Zone

The burned zone only comes into existence upon combustion of the fuel vapour with the unburned gas mixture. The energy equation for the burned zone is given by;

$$dQ_b + dm_b h_b = dU_b + PdV_b \tag{5.15}$$

The internal energy for the burned zone $U_b = m_b h_b - PV_b$. Therefore, the change in internal energy is given by;

$$dU_b = m_b dh_b + h_b dm_b - PdV_b - V_b dP \tag{5.16}$$

Substituting equation (5.16) into (5.15), we have;

$$dQ_b + dm_b h_b = m_b dh_b + h_b dm_b - PdV_b - V_b dP + PdV_b \tag{5.17}$$

Since $dh_b = c_{pb} dT_b$, equation (5.17) becomes;

$$dQ_b = m_b c_{pb} dT_b - V_b dP \tag{5.18a}$$

or written as a rate equation with respect to change in crank angle, θ;

$$\frac{dQ_b}{d\theta} = m_b c_{pb} \frac{dT_b}{d\theta} - V_b \frac{dP}{d\theta} \tag{5.18b}$$

Equation (5.18b) represents the rate of heat addition to the burned zone.

In order to solve equations (5.10), (5.14) and (5.18), the mass balance and volume of the zones must be defined.

5.5.4 Mass in Each Zone

The total mass in the combustion chamber consists of the mass of the trapped air in the cylinder, m_{trap}, plus the total mass of fuel injected, m_{fi}. The mass of mixture

in the unburned zone, burned zone and in the fuel zone also represents the total mass in the combustion chamber. Therefore, we have;

$$m_{cyl} = m_{trap} + m_{fi} = m_u + m_f + m_b \tag{5.19}$$

The difference between the mass of fuel injected at any instant and current fuel mass in the fuel zones defines the mass of fuel burned, m_{fb};

$$m_{fb} = m_{fi} - m_f \tag{5.20}$$

For the burned zone, both fuel and unburned gases are drawn into the burned zone such that the oxygen content of these gases bears a stoichiometric relationship to one another. The mass of the burned zone can therefore be written as;

$$m_b = \left(m_{fi} - m_f\right)\left(1 + \frac{\alpha}{x_{uO2}}\right) \tag{5.21}$$

Where x_{uO2} is the mass fraction of oxygen in the unburned zone and α is the stoichiometric oxygen-fuel ratio.

Substituting equation (5.21) into equation (5.19) gives;

$$m_{cyl} = m_u + m_f + \left(m_{fi} - m_f\right)\left(1 + \frac{\alpha}{x_{uO2}}\right) \tag{5.22}$$

5.5.5 Volume of Each Zone

The combustion chamber volume at any instant is equal to the sum of the volume in each zone, and is given by;

$$V = V_u + V_f + V_b \tag{5.23}$$

Assuming pressure is uniform across the combustion chamber and the gases in each zone behave as ideal gases, i.e. $PV = mRT$, equation (5.23) can be written as;

$$P\left(V_u + V_f + V_b\right) = PV_u + PV_f + PV_b$$

such that

$$PV = m_u R_u T_u + m_f R_f T_f + m_b R_b T_b \tag{5.24}$$

Substituting equation (5.21) into (5.24) yields;

$$PV = m_u R_u T_u + m_f R_f T_f + \left(1 + \frac{\alpha}{x_{uO2}}\right)\left(m_{fi} - m_f\right)R_b T_b \tag{5.25}$$

5.5.6 Energy Balance

The energy balance for all three zones in the combustion chamber based on the First Law of Thermodynamics, can be written as;

$$\frac{dQ_t}{d\theta} + \frac{dm_f}{d\theta}\left(h_f + \tfrac{1}{2}V_{inj}{}^2\right) = \frac{dU}{d\theta} + P\frac{dV}{d\theta} \tag{5.26}$$

Integrating equation (5.26) between the limits $\theta =$ SOI to crank angle position θ , yields;

$$\int_{SOI}^{\theta} \frac{dQ_t}{d\theta} d\theta = \int_{SOI}^{\theta} \left(\frac{dQ_u}{d\theta} + \frac{dQ_b}{d\theta} + \frac{dQ_f}{d\theta}\right) d\theta \tag{5.27}$$

$$\int_{SOI}^{\theta} \frac{dm_f}{d\theta}\left(h_f + \tfrac{1}{2}V_{inj}^2\right) d\theta = m_f\left(h_f + \tfrac{1}{2}V_{inj}^2\right) \tag{5.28}$$

$$\int_{SOI}^{\theta} \frac{dU}{d\theta} d\theta = U_\theta - U_{SOI} = \left(m_u u_u + m_b u_b + u_f u_f\right) - U_o \tag{5.29}$$

$$\int_{SOI}^{\theta} P\frac{dV}{d\theta} = W_t \tag{5.30}$$

Where, U_o defines the internal energy of the cylinder contents at start of injection (SOI) and W_t defines the total work done by the cylinder contents.

5.6 COMBUSTION EQUATION

The species considered in the model are limited to only oxygen (O_2), nitrogen (N_2), carbon dioxide (CO_2) and water vapour (H_2O). Challen (Challen and Baranecsu, 1999) reported that this would be adequate for calculations of gas properties with air-fuel ratio above stoichiometric, which is the case in this model. In addition, species dissociation and emission formation are not considered in the current model. The concentrations of species in each zone are found by first determining the equation for combustion of the fuel with air and calculating the mixture composition in each zone. Heywood (Heywood, 1988) described the mixture composition as follows;

The equation for complete combustion of a hydrocarbon fuel having molecular composition $C_a H_b$ with air is written as;

$$C_a H_b + \left(a + \frac{b}{4}\right)(O_2 + 3.773\, N_2) = aCO_2 + \frac{b}{2} H_2O + 3.773\left(a + \frac{b}{4}\right) N_2 \qquad (5.31)$$

The fuel composition can be written as CH_y, where $y = b/a$, which is also known as the molar H/C ratio of the fuel. The stoichiometric air/fuel ratio on a mass basis is given by:

$$\left(\frac{Air}{Fuel}\right)_s = \frac{\frac{1}{a}\left(a + \frac{b}{4}\right)\left[O_2 + 3.773\, N_2\right]}{\frac{1}{a}(C_a H_b)}$$

$$\left(A/F\right)_s = \frac{\left(1 + y/4\right)\left[32 + 3.773\,(28.16)\right]}{12.011 + 1.008\, y} \qquad (5.32)$$

Conversely, the stoichiometric fuel/air ratio, on a molar basis, is written as:

$$\left(F/A\right)_s = \frac{1}{1+y/4} = \frac{4}{4+y} = \varepsilon \tag{5.33}$$

While, the molar fuel-air equivalence ratio, ϕ , is defined as;

$$\phi = \frac{(F/A)_{actual}}{(F/A)_s} \tag{5.34}$$

Thus, the actual molar fuel-air ratio becomes; $\left(F/A\right)_{actual} = \varepsilon\phi$ (5.35)

5.7 MIXTURE COMPOSITION

The composition of the mixture of each zone in the combustion chamber consists of unburned mixture, burned mixture and fuel. However, the trapped air in the combustion chamber during the initial compression stroke could also contain residual gases left over from the previous cycle. This residual mass fraction is defined by;

$$x_b = \frac{m_{residual}}{m_{trap}} \tag{5.36}$$

The combustion equation can be rewritten, per mole O_2, as;

$$\varepsilon\phi C + 2(1-\varepsilon)\phi H_2 + O_2 + \psi N_2 \rightarrow n_{CO_2}CO_2 + n_{H_2O}H_2O + n_{CO}CO + n_{H_2}H_2 + n_{O_2}O_2 + n_{N_2}N_2$$

Where;

ψ = molar N/O ratio

ε = stoichiometric molar fuel-air ratio

y = molar H/C ratio

ϕ = molar fuel-air equivalence ratio

n_i = moles of species i per mole O_2

The number of moles of each species per mole O_2, for lean and stoichiometric mixtures $(\phi \leq 1)$ can be found from Table 5.1. The mole fractions of each species can be derived by dividing the moles of each species by the total moles of the mixture. Additionally, the mass fractions of each species can be calculated as follows;

$$x_i = \frac{n_i M_i}{\sum (n_i M_i)} \tag{5.37}$$

Where, $\sum (n_i M_i)$ defines the mass of mixture (burned or unburned) per mole O_2 in the mixture, m_{RP}, and is given by;

$$m_{RP} = 32 + 4\phi(1 + 2\varepsilon) + 28.16\psi \quad \text{(kg/kmol)} \tag{5.38}$$

5.8 THERMODYNAMIC GAS PROPERTIES

Thermodynamic properties of each species in the mixture are polynomial functions of temperature and are based on curve fits of experimental data as represented by the thermodynamic properties coefficients table found in Heywood (Heywood, 1988). The values of the coefficients are reproduced in Table 5.2. The unit is kJ/kmolK for specific heat, c_p, and kJ/kmol for both enthalpy, h, and internal energy, u. The enthalpy datum is taken as zero at 298.15 K. For each species, i, the specific heat on a mass basis is given by;

$$c_{p,i} = \frac{R_o}{M_i}\left(A_{i,1} + B_{i,2}T + C_{i,3}T^2 + D_{i,4}T^3 + E_{i,5}T^4\right)$$

Substituting equations (5.37) and (5.38) for the mixture properties yields;

$$c_{p,i} = n_i \cdot R_o \left(A_{i,1} + B_{i,2}T + C_{i,3}T^2 + D_{i,4}T^3 + E_{i,5}T^4 \right) / m_{RP} \quad \text{(kJ/kgK)} \qquad (5.39)$$

$$h_i = n_i \cdot R_o \left(A_{i,1} + \frac{B_{i,2}}{2}T^2 + \frac{C_{i,3}}{3}T^3 + \frac{D_{i,4}}{4}T^4 + \frac{E_{i,5}}{5}T^5 \right) / m_{RP} \quad \text{(kJ/kg)} \qquad (5.40)$$

$$u_i = h_i - n_i R_o T / m_{RP} \quad \text{(kJ/kg)} \qquad (5.41)$$

Coefficients for unburned mixture properties calculation are taken from the temperature range of 300 to 1000K range, while for the burned mixture, properties are taken from the 1000 to 5000K range.

The values of the coefficients for selected type of diesel fuels extracted from Ferguson (Ferguson, 1986), Heywood (Heywood, 1988) and Reid (Reid et al., 1987) are shown in Table 5.3. The fuel properties were calculated by;

$$c_{p,f} = \left(A_{f,1} + B_{f,2}T + C_{f,3}T^2 + D_{f,4}T^3 \right) / M_f \quad \text{(kJ/kgK)} \qquad (5.42)$$

$$h_f = \left(A_{f,1}T + \frac{B_{f,2}}{2}T^2 + \frac{C_{f,3}}{3}T^3 + \frac{D_{f,4}}{4}T^4 \right) / M_f \quad \text{(kJ/kg)} \qquad (5.43)$$

Table 5.1: Gas composition for burned and unburned mixture

Species	Burned Gas Composition, n_{bi} (kmoles/kmole O_2)	Unburned Gas Composition, n_{ui} (kmoles/kmole O_2)
CO_2	$n_b CO_2 = \varepsilon\phi$	$n_u CO_2 = y_b \varepsilon\phi$
H_2O	$n_b H_2O = 2(1-\varepsilon)\phi$	$n_u H_2O = 2y_b(1-\varepsilon)\phi$
CO	$n_b CO = 0$	$n_u CO = 0$
H_2	$n_b H_2 = 0$	$n_u H_2 = 0$
O_2	$n_b O_2 = 1-\phi$	$n_u O_2 = 1 - y_b\phi$
N_2	$n_b N_2 = \psi$	$n_u N_2 = \psi$
Fuel	-	$n_u f = 4(1-y_b)(1+2\varepsilon)\phi / M_f$
Sum	$n_b = (1-\varepsilon)\phi + 1 + \psi$	$n_u = (1-y_b)(4(1+2\varepsilon)\phi/M_f + 1 + \psi) + y_b n_b$

Table 5.2: Coefficients of selected species properties

Species	*M, kg/kmol*	*T range, K*	A_1	B_2	C_3	D_4	E_5
CO_2	44.01	1000-5000	4.4608	3.0982e-3	-1.2393e-6	0.2274e-9	-1.553e-14
		300-1000	2.4008	8.735e-3	-6.607e-6	2.002e-9	6.327e-16
H_2O	18.02	1000-5000	2.7168	2.945e-3	-0.8022e-6	0.1023e-9	4.847e-15
		300-1000	4.070	-1.108e-3	4.152e-9	-2.964e-9	0.807e-12
CO	28.01	1000-5000	2.9841	1.489e-3	-0.579e-6	0.1036e-9	-6.935e-15
		300-1000	3.7101	-1.619e-3	3.692e-6	-2.032e-9	2.395e-12
H_2	2.02	1000-5000	3.1002	0.5112e-3	0.0526e-6	-3.491e-11	3.694e-15
		300-1000	3.0574	2.6765e-3	-5.810e-6	5.521e-9	-1.181e-12
O_2	32.00	1000-5000	3.622	0.7362e-3	-0.196e-6	0.0362e-9	-2.895e-15
		300-1000	3.626	-1.878e-3	7.055e-6	-6.764e-9	2.156e-12
N_2	28.01	1000-5000	2.896	1.5156e-3	-0.572e-6	0.0998e-9	-6.522e-15
		300-1000	3.675	-1.208e-3	2.324e-6	-0.632e-9	-0.226e-12

Table 5.3: Coefficients of selected diesel fuel for specific heat and enthalpy

Fuel	M	A_1	B_2	C_3	D_4
$C_{14.4}H_{24.9}$ [a]	198.06	7.9710	1.1954 e-01	-3.6858 e-05	-1.9385 e+04
$C_{10.8}H_{18.7}$ [b]	148.57	-38.126	1.0340	-6.0181e-04	1.3536e-07
$C_{12}H_{26}$ [c]	170.34	-9.328	1.149	-6.344e-04	1.359e-07

[a] Ferguson (Ferguson, 1986)

[b] Heywood (Heywood, 1988)

[c] Reid (Reid et al., 1987)

5.9 HEAT TRANSFER

Two correlations for determining heat transfer that are commonly used in engine modelling are that of Annand and Woschni. The heat transfer correlation described in this chapter will follow that of Annand (Annand, 1963).

The heat transfer in an engine combustion chamber is correlated with the fluid conditions using non-dimensional parameters, known as Nusselt number, Nu, Reynolds number, Re, and Prandtl number, Pr, which describe the properties, viscosity and thermal conductivity of the fluid. Nusselt number is defined as the ratio of the convection to the conduction heat transfer for the same temperature difference, and is written as;

$$Nu = \frac{hx}{k} \tag{5.44}$$

Where h is a heat transfer coefficient (W/m^{2}K), x is the characteristic length (m) and k is the gas thermal conductivity (W/mK).

The Reynolds number is a ratio of the inertial to viscous fluid forces and is expressed as;

$$Re = \frac{\rho U x}{\mu} \tag{5.45}$$

Where ρ is the gas density (kg/m^3), U is the characteristic gas velocity (m/s), and μ is the gas dynamic viscosity (kg/ms). Annand (Annand, 1963) uses the cylinder bore as the characteristic length and mean piston speed in place of the characteristic gas velocity. The gas thermal conductivity is defined as;

$$k = \frac{c_p \mu}{Pr} \tag{5.46}$$

Heywood (Heywood, 1988) expressed the Prandtl number and the dynamic viscosity of lean hydrocarbon-air combustion product mixture respectively by;

$$Pr = 0.05 + 4.2(n-1) - 6.7(n-1)^2 \tag{5.47}$$

and,
$$\mu_{mix} = \frac{\mu_{air}}{1 + 0.027\phi} \tag{5.48}$$

where $\mu_{air} = 3.3\,x\,10^{-7} T^{0.7}$

Annand (Annand, 1963) suggested that the empirical heat transfer correlation can be represented by the relationship;

$$Nu = a\,Re^b \tag{5.49}$$

Substituting equation (5.44) into equations (5.49) yields;

$$\frac{hx}{k} = a\,Re^b$$

Replacing the characteristic length, x, with the cylinder bore, B, the heat transfer coefficient in the combustion chamber can be written as ;

$$h = a\frac{k}{B}Re^b \tag{5.50}$$

Heat is transferred from the gas in the cylinder, by convection at the cylinder wall, and by radiation from flame and luminous carbon particles. Heat transfer from the gas-to-wall will depend on the temperature gradient in the boundary layer at the surface and the surface area. The equation for convective heat transfer rate per unit area is given as;

$$\frac{\dot{Q}}{A_{comb}} = h(T_g - T_{wall}) \tag{5.51}$$

Where A_{comb} is the surface area of the combustion chamber, T_g represents the bulk mean gas temperature and T_{wall}, is the local surface temperature on the cylinder wall. Substituting equation (5.50) into (5.51), we have;

$$\frac{\dot{Q}}{A_{comb}} = a\frac{k}{B}Re^b\left(T_g - T_{wall}\right) \tag{5.52}$$

Annand (Annand, 1963) added a radiation term into the heat transfer rate equation, hence the equation becomes;

$$\frac{\dot{Q}}{A_{comb}} = a\frac{k}{B}Re^b(T_g - T_{wall}) + c(T_g^4 - T_{wall}^4) \tag{5.53}$$

The value of the radiant heat transfer constant, c, for a diesel engine is $c = 1.6\text{x}10^{-12}$ W/m^2 K^4 (Annand, 1963). This constant value is derived from the product of emissivity, ε, and Stefan-Boltzmann constant, σ.

Where ε = 0 to 1 (1 for blackbody) and $\sigma = 5.6703x10^{-8} W/m^2K^4$.

5.10 ENGINE GEOMETRY

The area and volume of the combustion chamber for a given crank angle can be derived from the geometry of the engine as shown in Figure 5.3.

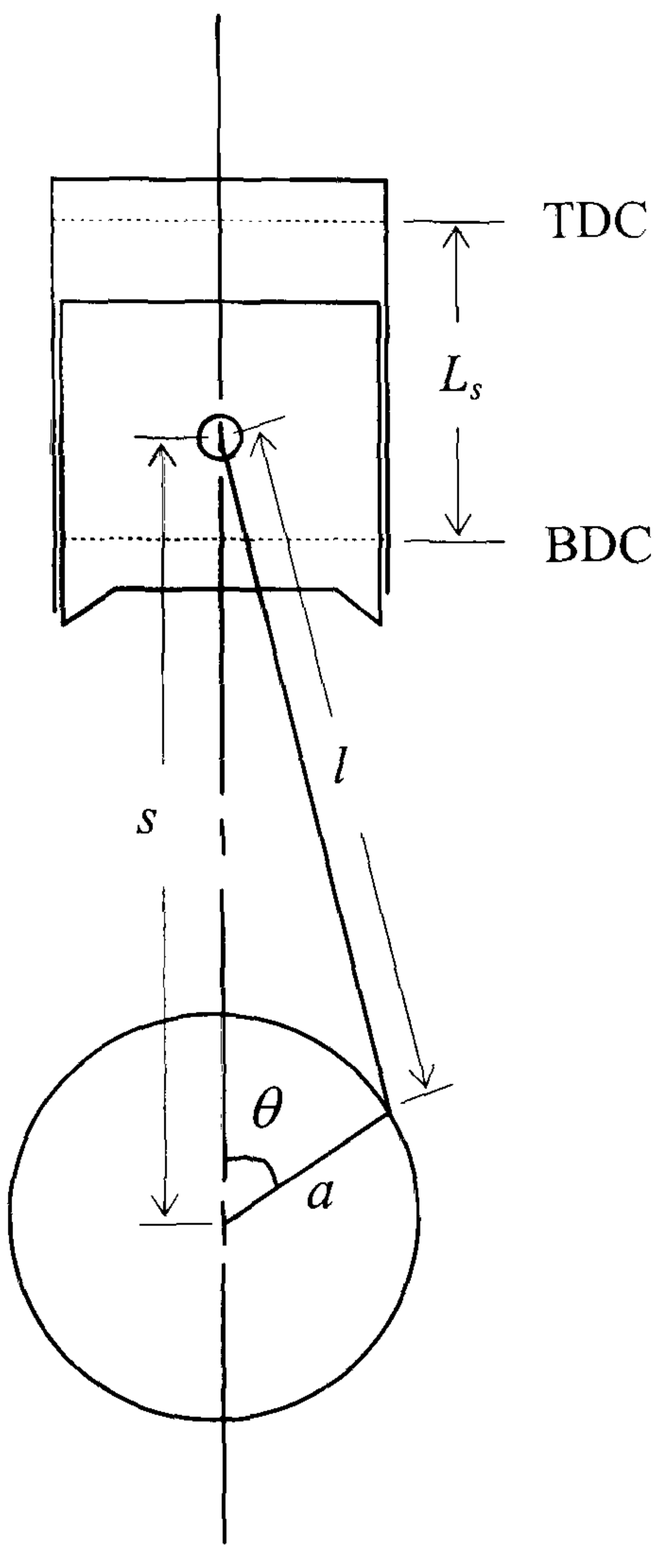

TDC	Top Dead Centre
BDC	Bottom Dead Centre
L_s	Stroke
l	Connecting Rod Length
θ	Crank Angle
a	Crank Radius

Figure 5.3: Schematic diagram showing engine geometry definitions

The combustion chamber surface area A_{comb} at crank angle θ is comprised of the surface area of the cylinder head, A_{cyl}, surface area of the piston crown, A_p, and the surface area of the wall. Hence;

$$A_{comb} = A_{cyl} + A_p + \pi B\left(l + a - s\right) \tag{5.54}$$

Where s refers to the distance between the piston pin axis and the engine crank axis and is defined as;

$$s = a\cos\theta + \left(l^2 - a^2 \sin^2\theta\right)^{1/2}$$

Substituting s into equation (5.54), the area of the combustion chamber can be written as;

$$A_{comb} = A_{cyl} + A_p + \pi B\left(l + a - a\cos\theta - \sqrt{\left(l^2 - a^2 \sin^2\theta\right)}\right) \tag{5.55}$$

Volume of the combustion chamber is the sum of the clearance volume, V_c at TDC and the swept volume, which is written as;

$$V = V_c + \frac{\pi B^2}{4}\left(l + a - s\right) \tag{5.56}$$

Similarly, by substituting s into equation (5.56), the volume of the combustion chamber can be written as;

$$V = V_c + A_{cyl}\left(l + a - a\cos\theta - \sqrt{\left(l^2 - a^2 \sin^2\theta\right)}\right) \tag{5.57}$$

In the model, the change in the combustion volume with respect to crank angle is required in the computation of the work done on the piston. Thus, the derivative of equation (5.57) yields;

$$\frac{dV}{d\theta} = \frac{\pi B^2}{4}\left[a\sin\theta + \frac{\left(a^2 \sin\theta\cos\theta\right)}{\sqrt{\left(l^2 - a^2 \sin^2\theta\right)}}\right] \tag{5.58}$$

5.11 THE COMPUTER PROGRAMME

The three-zone heat release rate model described above is implemented in the Matlab programming language. The Matlab software allows commands to be written in text files called script files. These script files can be initiated in the Matlab command window and the programme written in the script files will be evaluated exactly as they would, if written directly at the Matlab command window prompt.

The model presents twelve unknown variables that need to be numerically solved, namely the mixture properties u_u, u_f, u_b, which are all functions of the temperatures T_u, T_f, T_b respectively, together with the mass and volume in each zone, $m_u, m_f, m_b, V_u, V_f, V_b$. All these variables are solved using the appropriate equation during the evaluation of each zone.

In the Matlab programme, the engine geometry information, the cylinder pressure data and the injection rate data are written in three separate sub-routine script files, named EngineGeometry.m, CylinderPressure.m and InjectionRate.m, respectively. The computation of the combustion area A_{comb}, combustion chamber volume V, and the derivative of the combustion chamber volume $dV/d\theta$, with respect to the crank angle are performed using equations (5.55), (5.57) and (5.58) respectively, within the EngineGeometry.m script file. The script files CylinderPressure.m contains the cylinder pressure data and the evaluation of the derivative of the cylinder pressure with respect to the crank angle, $dP/d\theta$. The script file InjectionRate.m contains the timing and rate of fuel injection data, which was obtained from the injection rate measurement. In addition to the three script files, another script file was written to define the values of all the relevant constants and species coefficients in the burned zone, unburned zone and the fuel. This file is named Constant.m. By placing these sub-routine script files at the beginning of the main script file, they will be executed first when the main script file is initiated. The flow chart for the heat release programme is shown in Figure 5.4.

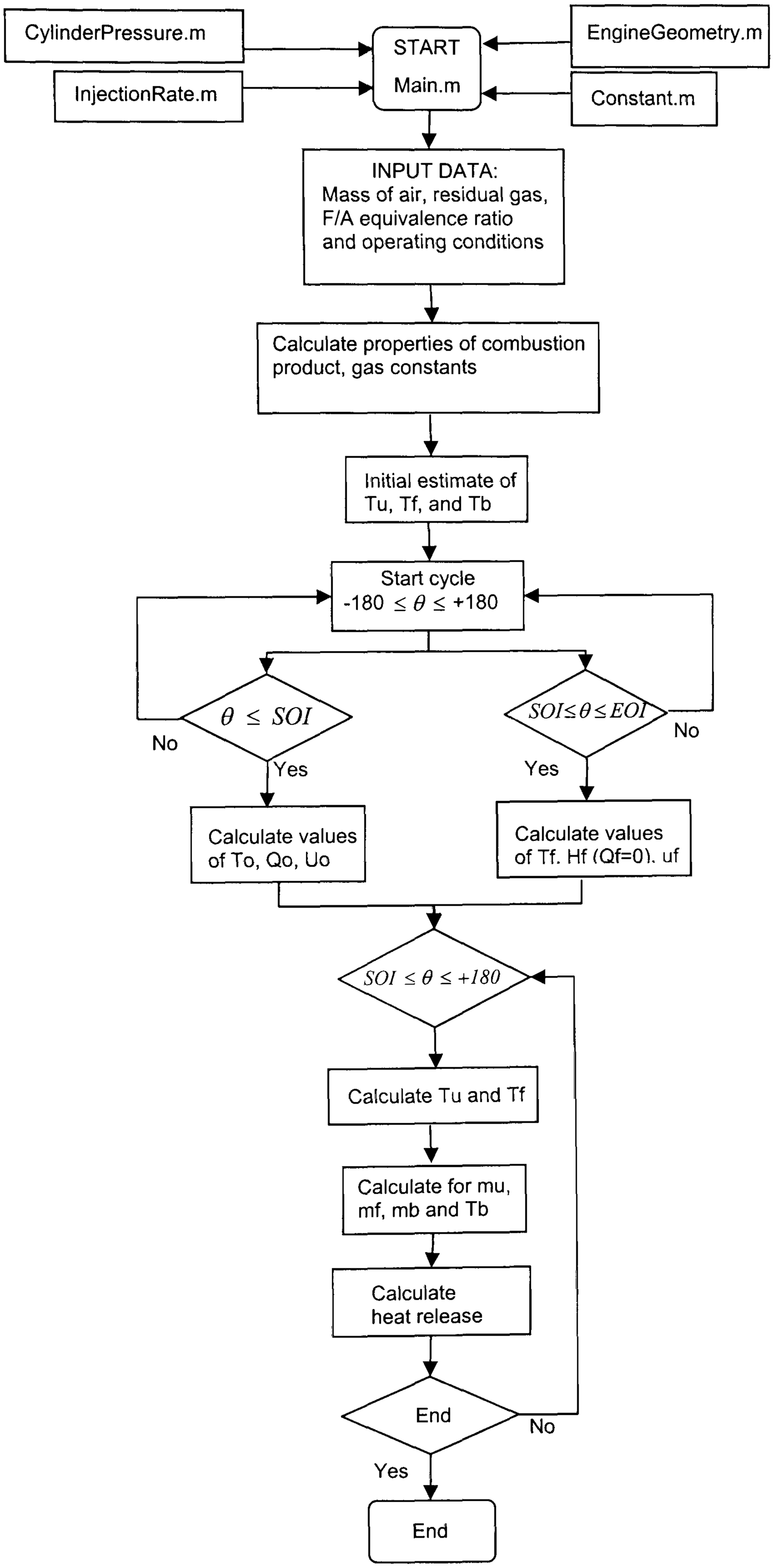

Figure 5.4: Flow chart for the heat release rate programme

The first part of the main programme executes the four sub-routine script files, which form the initial input into the programme. Then, the engine speed, mass of inducted air, mass of the residual gas, the fuel-air equivalent ratio and the cylinder wall surface temperature are defined. These data are used to determine the piston speed, the total trapped charge in the combustion chamber, stoichiometric molar fuel-air ratio and the residual gas mass fraction.

The inducted air mass of 3.6×10^{-3} kg, is computed from the measured mass flow rate of air, while the trapped air in the cylinder is the sum of the inducted air mass and the residual gas mass. The residual gas is estimated to be 5 percent of the inducted air, i.e.0.18×10^{-3} kg. The initial temperature of the unburned zone is calculated using the ideal gas law from the measured cylinder pressure and volume at the start of fuel injection. This value varies between the different injectors and the load conditions. The fuel dodecane with chemical formula $C_{12}H_{26}$ is used as representative of the diesel fuel. The fuel thermodynamic properties are given in Table 5.3 in section 5.8 of the thesis. The initial temperature of fuel is estimated to be at 400K at the time of injection.

The statements that follow, define the mixture properties in the initial unburned zone, from the equilibrium composition of the product of combustion. The calculations of the moles of each species per mole of oxygen in the unburned zones, including the burned mixture in the residual gas are based on the equations listed in Table 5.1. Molecular weight and gas constant of the burned and unburned zones are then computed at this point based on the values of the moles of each species obtained earlier.

The iteration loops commence after specifying the step size (h) and initial values of the temperatures, i.e. T_u, T_f, and T_b at the crank angle -180°. The programme first calculates the mixture properties, transport properties and the heat transfer rate in the unburned zone prior to fuel injection, based on initial unburned temperature and the pressure data using the ideal gas law. These resulted with values for the initial internal energy, u_o, initial compression work of the unburned mixture, W_o, and the initial heat transfer during the compression stage, Q_o. These values are later added to the unburned mixture during combustion to give the total energy of the unburned zone. The burned zone comes into existence when the fuel burn with the unburned mixture. Since equation (5.21) already defines the mass in the burned zone,

the only unknown variables are the mass of the unburned, m_u, mass of the fuel zones, m_f, and the burned zone temperature, T_b.

In order to calculated the internal energies of species in the three zones, temperatures T_u and T_f are evaluated from the following two ordinary differential equations, derived from equations (5.10b) and (5.14b) respectively. These equations are rewritten as the followings;

$$\frac{dT_u}{d\theta} = \frac{1}{m_u c_{pu}}\left[\frac{dQ_u}{d\theta} + \frac{m_u R_u T_u}{P}\frac{dP}{d\theta}\right] \tag{5.59}$$

$$\frac{dT_f}{d\theta} = \frac{1}{m_f c_{pf}}\left[\frac{dQ_f}{d\theta} + \frac{dm_f}{d\theta}\left(\frac{1}{2}V_{inj}^2\right) + \frac{m_f R_f T_f}{P}\frac{dP}{d\theta}\right] \tag{5.60}$$

Both the differential equations are solved using the fourth order Runge-Kutta method as outlined by Mathews and Fink (Mathews and Fink, 1998), which has the form as follows;

$$k_1 = hf\left(t_n, y_n\right)$$

$$k_2 = hf\left(t_n + \frac{h}{2}, y_n + \frac{k_1}{2}\right)$$

$$k_3 = hf\left(t_n + \frac{h}{2}, y_n + \frac{k_2}{2}\right)$$

$$k_4 = hf\left(t_n + h, y_n + k_3\right)$$

$$y_{n+1} = y_n + \frac{h\left(k_1 + 2k_2 + 2k_3 + k_4\right)}{6}$$

The Newton-Raphson iterative techniques by Press et al. (Press et al., 1994) and by Mathews and Fink (Mathews and Fink, 1998) were used to define the functions in equations (5.22), (5.25) and (5.26) as follows;

$$f_1(m_u, m_f, T_b) = m_u + m_f + \left(m_{fi} - m_f\right)\left(1 + \frac{\alpha}{x_{uO2}}\right) - m_{cyl} = 0 \qquad (5.61)$$

$$f_2(m_u, m_f, T_b) = m_u R_u T_u + m_f R_f T_f + \left(1 + \frac{\alpha}{x_{uO2}}\right) \cdot \left(m_{fi} - m_f\right) R_b T_b - PV = 0 \qquad (5.62)$$

$$f_3(m_u, m_f, T_b) = \left(m_u u_u + m_f u_f + m_b u_b\right) - Q_t - m_{fi}\left(h_f + \tfrac{1}{2} V_{inj}{}^2\right) - U_o + W = 0 \qquad (5.63)$$

This method has the matrix form of;

$$\begin{bmatrix} m_{u\,i+1} \\ m_{fi+1} \\ T_{bi+1} \end{bmatrix} = \begin{bmatrix} m_u \\ m_f \\ T_b \end{bmatrix} - \begin{bmatrix} \frac{\partial f_1}{\partial(m_u)} & \frac{\partial f_1}{\partial(m_f)} & \frac{\partial f_1}{\partial(T_b)} \\ \frac{\partial f_2}{\partial(m_u)} & \frac{\partial f_2}{\partial(m_f)} & \frac{\partial f_2}{\partial(T_b)} \\ \frac{\partial f_3}{\partial(m_u)} & \frac{\partial f_3}{\partial(m_f)} & \frac{\partial f_3}{\partial(T_b)} \end{bmatrix}^{-1} * \begin{bmatrix} f_1 \\ f_2 \\ f_3 \end{bmatrix}$$

The new values of m_u, m_f, m_b, T_u, T_f, and T_b are then reassigned to the differential equations and the non-linear equations for calculation of the new values at the next time step, until convergence are achieved.

The complete computer code for the determination of the heat release rate based on the three-zone model is provided in Appendix VIII. The sub-routine script files CylinderPressure.m and InjectionRate.m provided in the appendix, only displayed one set of data from the experiment when using injector L1 at 2000 rpm and 25% load.

CHAPTER 6: RESULTS AND DISCUSSIONS

The discussions of the results from the experimental work are presented in two separate sections. Sections 6.1 will discuss the results that were generated from the implementation of the three-zone heat release rate model. These results include the temperature calculation of the three zones and the heat release rate calculation. The heat release rate profile produced by the three-zone model is labelled as the 'three-zone heat release rate'. Section 6.2 will discuss the results obtained from the engine experiments, which include the in-cylinder pressure measurements, the exhaust gas emissions measurements, and the heat release rate calculation. The calculation of the heat release rate was performed by the subroutine program 'Thermodynamic 1' of the AVL Indimaster data acquisition system, using the measured cylinder pressure data. The calculation is based on the principles of the first law of thermodynamics applied to a single-zone model. This model is similar to the single-zone model described in section 5.2 of this thesis. The heat release rate profile produced by the AVL Indimaster is labelled as the 'experimental heat release rate'.

6.1 RESULTS FROM THE THREE-ZONE MODEL

Pressure data from the engine experiments as outlined in section 4.5, and the injection rate data from the Bosch Tube measurement, from section 3.4.2 of this thesis, were used as inputs into the model. The injection rate profiles at the various engine operating conditions were discussed in section 3.2.2 of Chapter 3. However, in order to assist with the discussion of the results, several terms with regards to the cylinder pressure curve are defined. This includes the definitions of start of injection (SOI), ignition delay period and start of combustion (SOC), which are shown graphically on the cylinder pressure against crank angle curve in Figure 6.1.

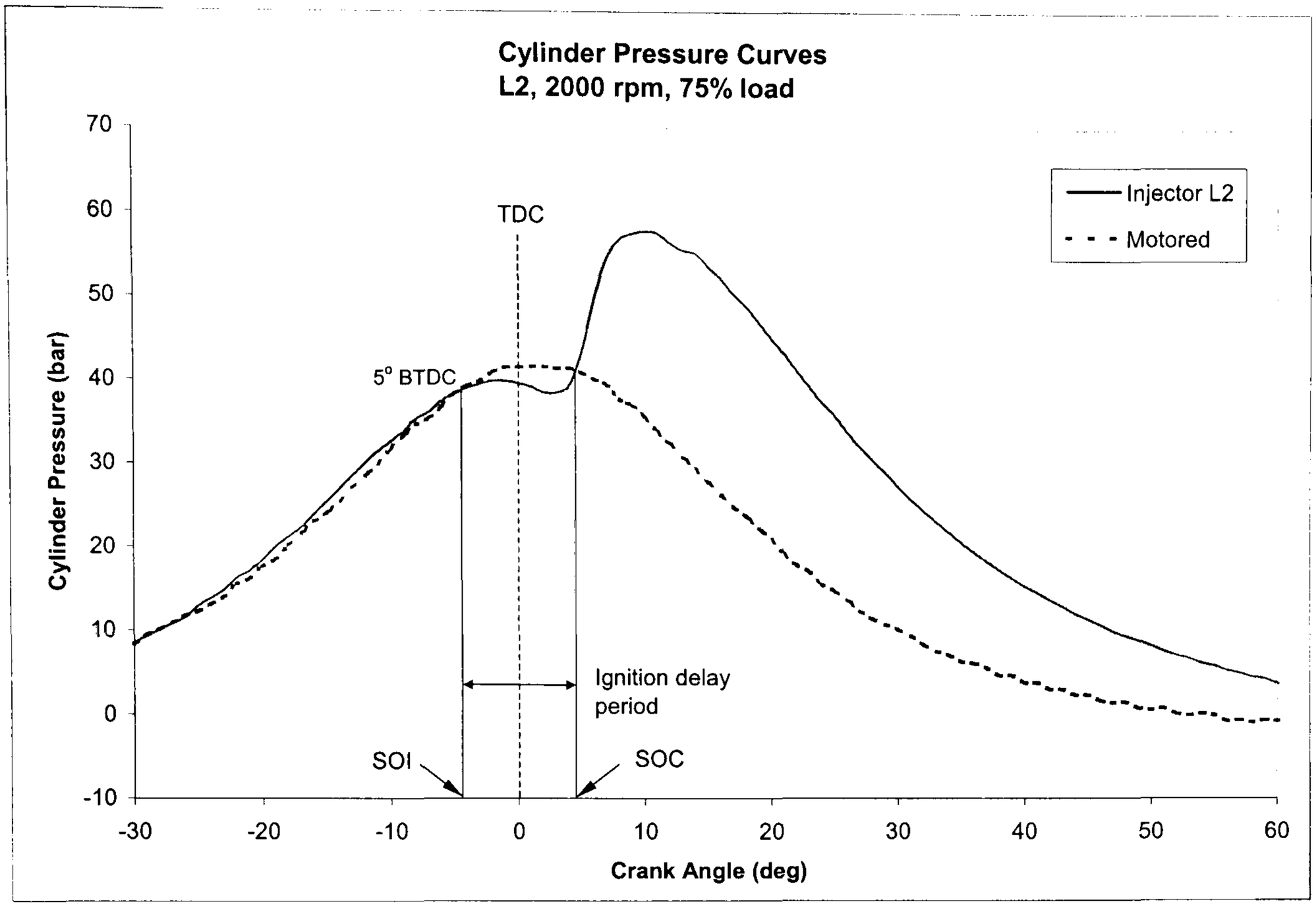

Figure 6.1: Definition of start of injection, ignition delay and start of combustion

The figure shows the plot of two cylinder pressure curve measurements. The curve plotted with the dotted lines represents the cylinder compression pressure curve when no fuel injection or combustion occurs. This curve is labelled as the 'motored' cylinder pressure. The full line curve represents the cylinder pressure of combustion when injector L2 was used at an engine speed of 2000 rpm with a 75% engine load. From these two curves, the SOI is defined as the point at which the cylinder pressure of combustion starts to depart the compression only cylinder pressure. This is the point at which the cylinder pressure shows a drop in pressure due to the cooling effect of the injected fuel. For the condition shown in the figure, the SOI occurs at 5° CA before top dead centre (BTDC). While, the SOC is defined as the point at which the cylinder pressure rises rapidly due to combustion of the fuel. In this case, the SOC is found to be at 4° CA after top dead centre (ATDC). The ignition delay period is therefore defined as the time from SOI to SOC. The piston TDC, which is shown in the figure, is observed to coincide with the crank angle at 0°.

The implementation of the model was performed using Matlab. The model enabled the calculation of the temperatures in each zone as well as the heat release rate of combustion. Due to the large amount of data collected, only the results when

using injector L1 were chosen to be presented in this section. The other reason for choosing only the results from injector L1 is due to the fact that the results from injectors L2, L3 and L4 showed similar trends, thus avoiding a repetitive discussion. However, the differences in the rates and magnitudes of heat release from using these injectors will be discussed in the following sections.

6.1.1 Zone Temperature Calculations

The values of temperatures and heat release rate with respect to crank angle, generated from the Matlab program were copied into Excel. This provided the flexibility to plot several parameter curves onto the same plot. The temperatures of the unburned, T_u, burned, T_b, and fuel zones, T_f, based on the data obtained when using injector L1, at an engine speed of 2000 rpm and various load conditions are shown in Figure 6.2 (a) to (d).

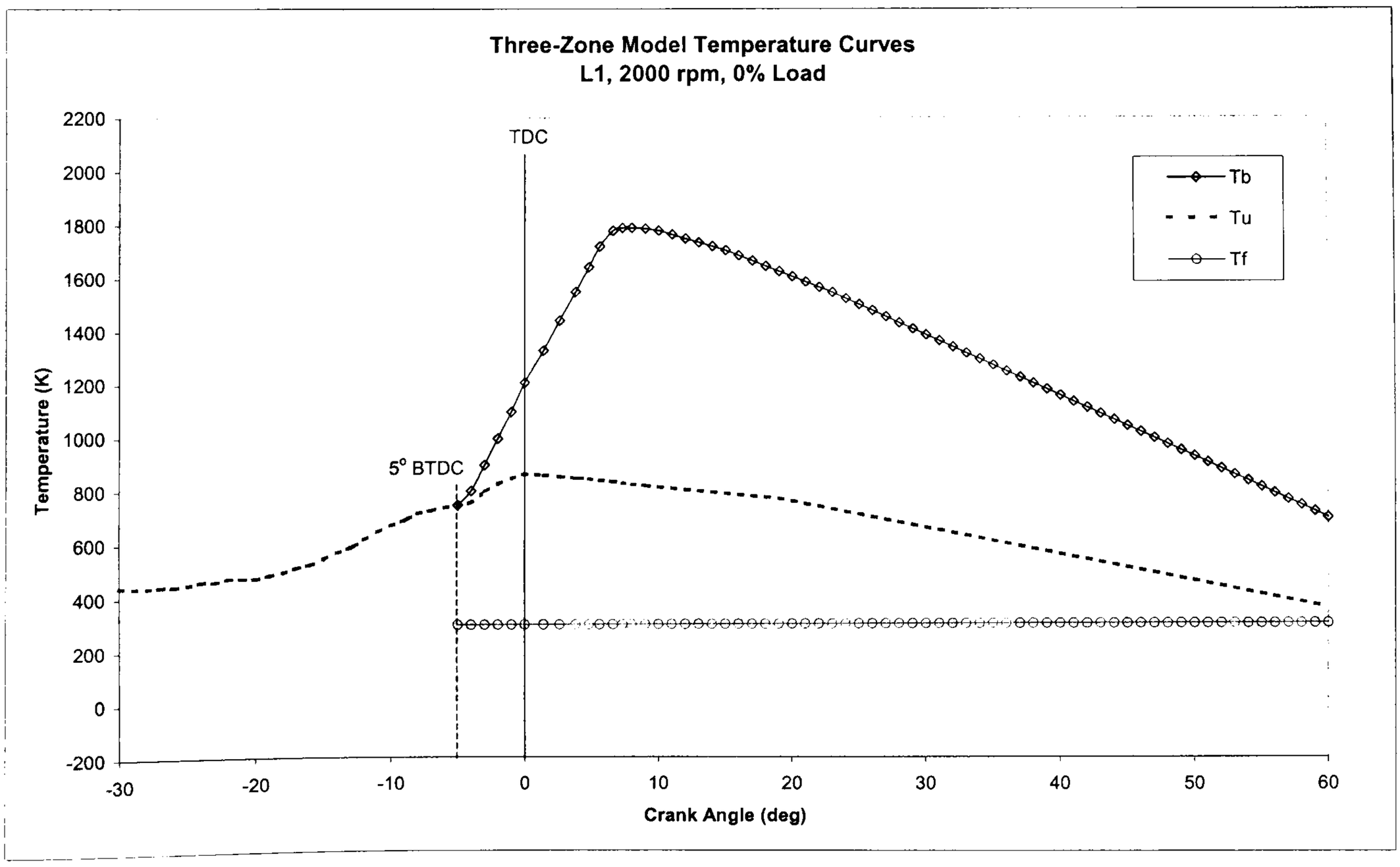

Figure 6.2 (a): Temperatures of unburned, burned and fuel zones at 2000 rpm and 0% engine load

The initial estimate for T_f was 300K, while T_u, was calculated from the unburned zone before SOI such that T_u = T_0 at SOI. The temperature profiles in Figure 6.2 (a) shows that the burned zone temperatures, T_b, only start when fuel is introduced into the combustion chamber at -5° CA. After a 1° CA ignition delay period, the temperatures increase rapidly to a peak temperature of 1750K at 7° CA, before gradually decreasing to the exhaust temperature. The unburned temperatures increase only a small amount, to a peak temperature of 860K at the end of the compression stroke. The reason for this is due to the compression of the burned zone and the fact that there is no heat addition to the unburned zone from the burned zone. The model assumes that all the heat from the burned zone is transferred to the cylinder wall. The temperatures of the fuel zone remain constant throughout the event due to no heat transfer to or from the fuel zone.

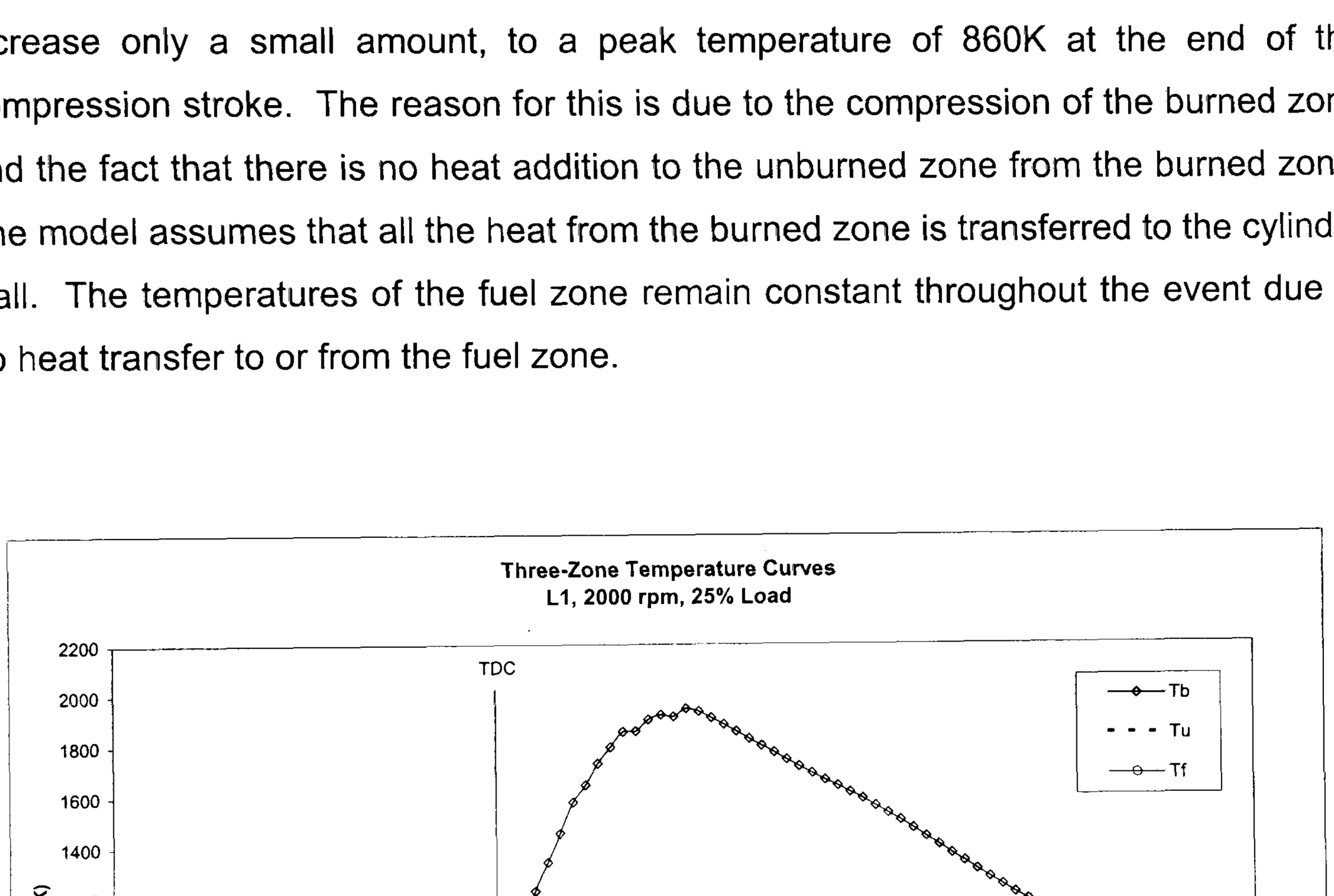

Figure 6.2(b): Temperatures of unburned, burned and fuel zones at 2000 rpm and 25% engine load

The temperatures profiles at an engine load of 25% are shown in Figure 6.2 (b). The burned zone temperatures are observed to initially increase slowly at a rate of 9K/° CA, upon injection at -5° CA. The temperatures then start to increase rapidly at a

rate of 102K/° CA at 0° CA to a peak temperature of 1946K at 15° CA. This phenomenon is due to the fact that, upon injection of the fuel, some of the heat of the in-cylinder charge are transferred to the fuel causing a reduction in cylinder pressure. The temperatures then rise due to combustion of the fuel. The unburned zone also exhibits small increase in temperatures, to a peak temperature of 897K at 4° CA, before gradually decreasing. The small increase in temperatures is expected since the calculation of unburned temperature is only a function of the cylinder pressure. As for the fuel zone, the temperatures remain constant due to no heat exchange between the zones.

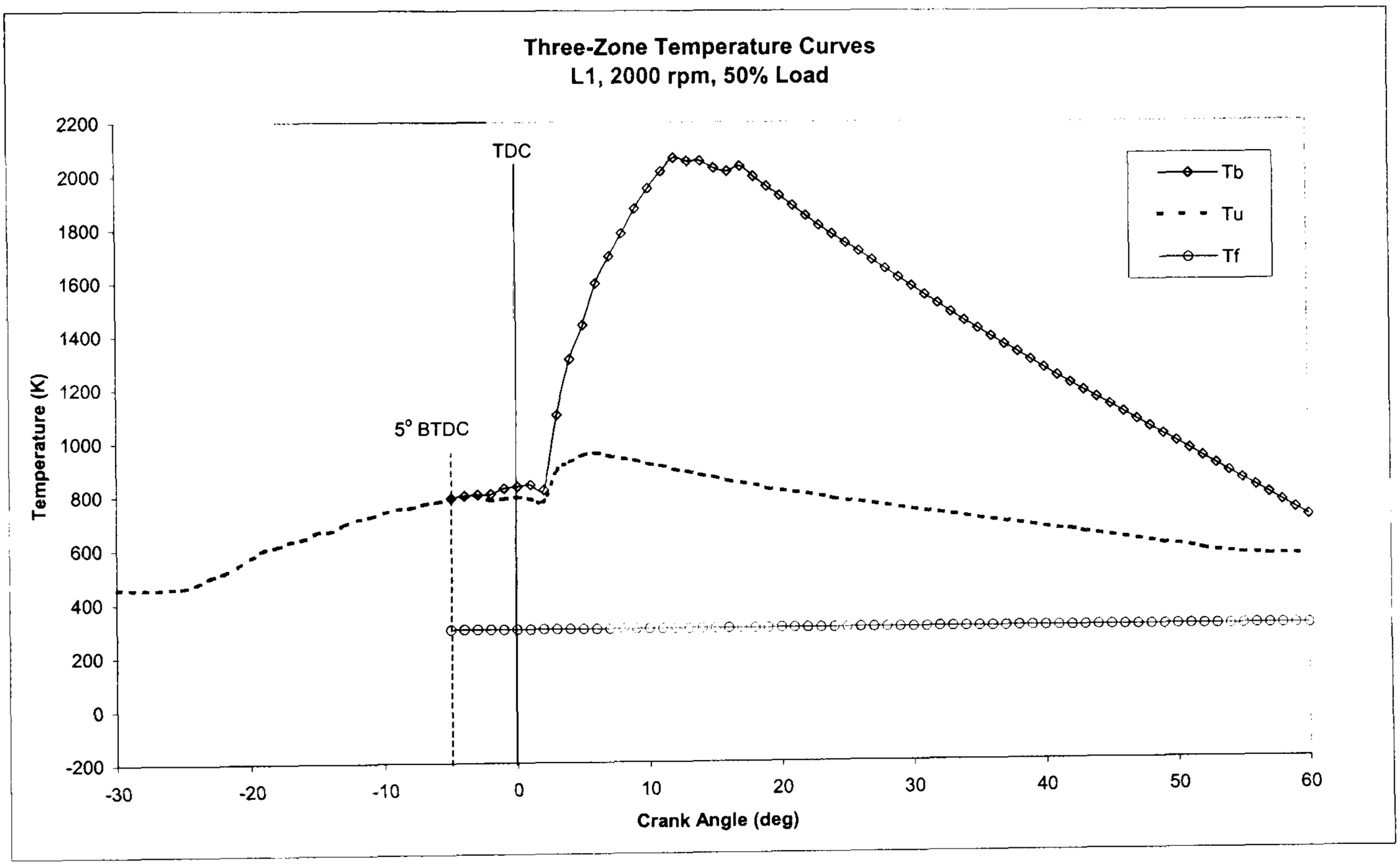

Figure 6.2(c): Temperatures of unburned, burned and fuel zones at 2000 rpm and 50% engine load

The temperature profiles at the engine load of 50% are shown in Figure 6.2 (c). The curve trends are similar to the previous two figures. However, the magnitude of the burned temperature peaks, to a temperature of 2066K at 12° CA, while the unburned zone does not exhibit a significant increase, even though the fuelling level in this case is higher. As for the fuel zone, the temperature remains constant. As mentioned earlier, the inputs to the model are the cylinder pressure and the measured

fuel injection rate data. The measured fuel injection rate at pump lever positions of 0%, 25% and 50% were observed to have similar magnitude due to the inability, during the measurement, to relate the lever position to the amount of fuel delivery. Therefore, the only significant variable to the model is the cylinder pressure data. Consequently, the temperature curves tend to follow that of the cylinder pressure, as observed in Figure 6.2 (c).

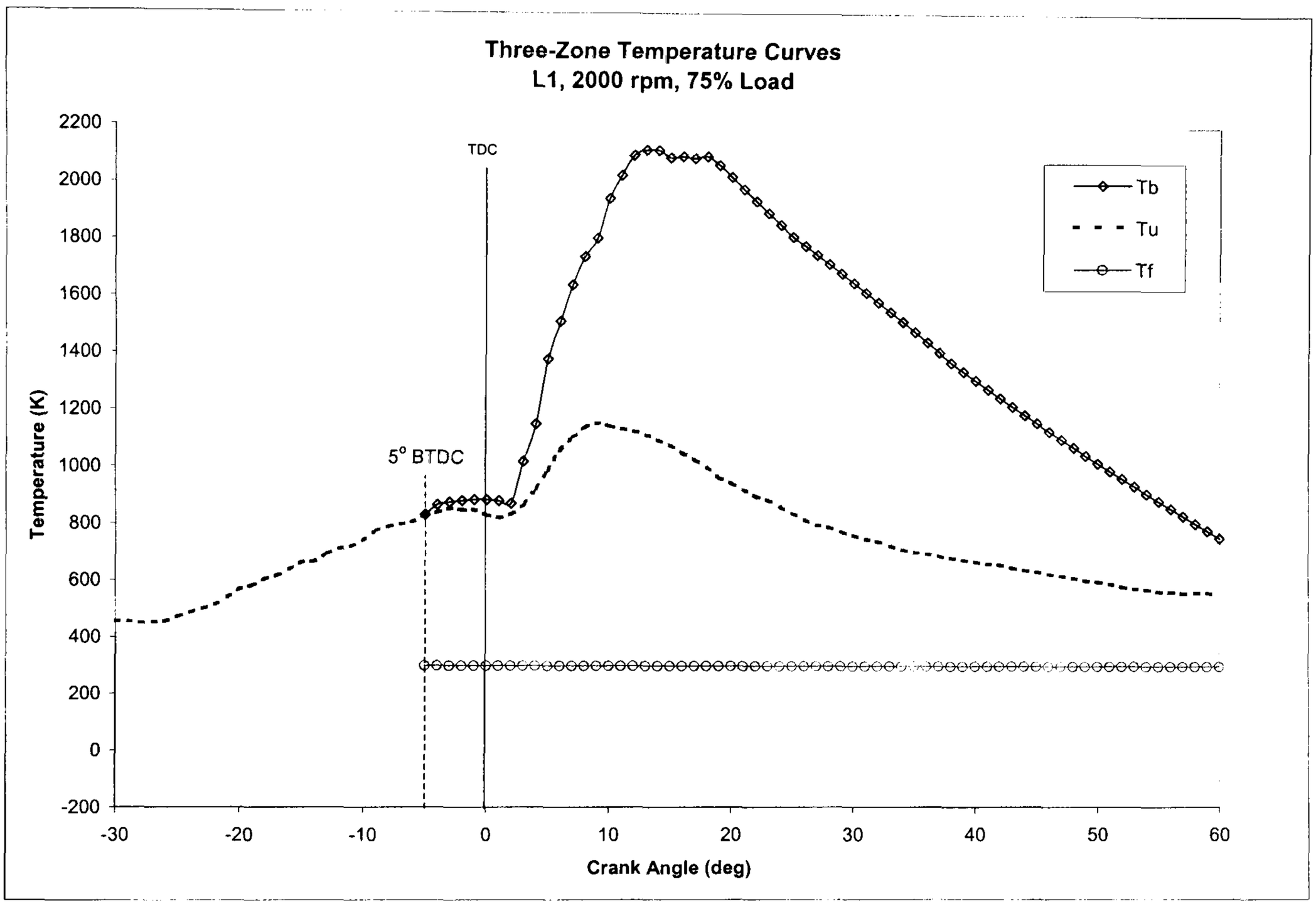

Figure 6.2(d): Temperatures of unburned, burned and fuel zones at 2000 rpm and 75% engine load

The temperature profiles at 75% engine load are shown in Figure 6.2 (d). The burned temperatures start at –5° CA but only increase at a rate of 10K/deg to 2° CA. Upon this, the temperature rises rapidly to a peak temperature of 2118K at 13° CA. It is believed that the long ignition delay period, of 7° CA in this case, would provide time for the fuel to evaporate and mix with the air, causing larger premixed combustion. Consequently, the unburned temperature also rises to a peak temperature of 1155K at 9° CA, corresponding to the increased cylinder pressure. As expected, the fuel zone temperatures remain constant.

6.1.2 Effects of Load Level on Heat Release Rate

The effects of the 0%, 25%, 50% and 75% engine load on the heat release rate (HRR) are investigated and the results are shown graphically in Figures 6.3 (a) to (d). The measured cylinder pressure, the experimental and the three-zone heat release rate curves for the 0% load are shown in Figure 6.3 (a). From these figures, it is observed that the experimental heat release rate curves show large fluctuations, especially at higher load conditions. While, the three-zone heat release rate curves are smooth. The reasons for this are that the experimental heat release rate calculation was performed by the AVL 670 Indimaster sub-routine single zone model program using data from a raw single cycle of the measured in-cylinder pressure. While, for the three-zone model, the in-cylinder pressure data was first smoothed average from 50 cycles and these new sets of data were saved as a new file. As a result of using the new sets of data, a smoother curve was obtained for the three-zone heat release rate.

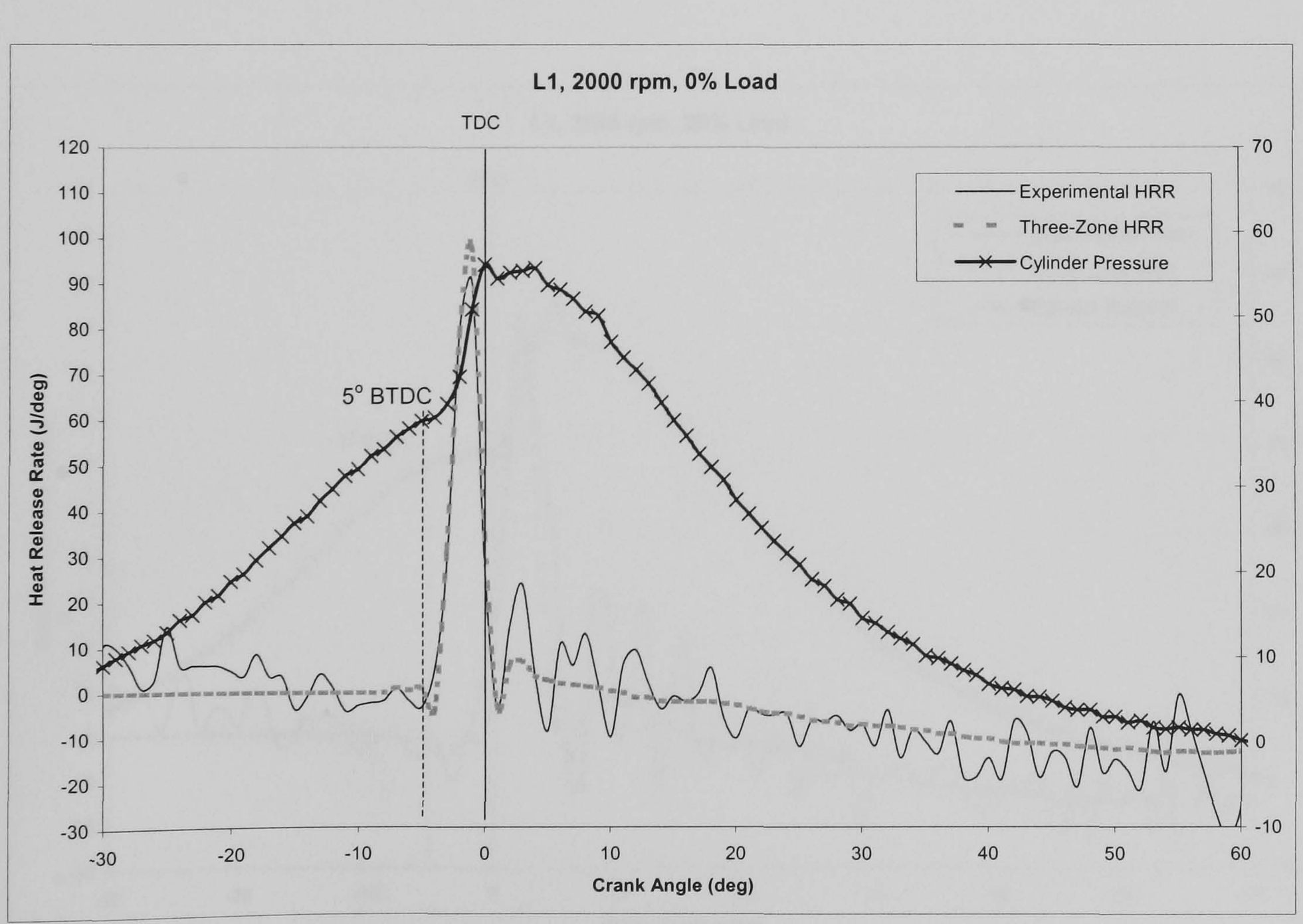

Figure 6.3(a): Cylinder pressure and heat release rate profiles at 0% load

From the cylinder pressure curve, the injection is found to start at –5° CA. The ignition delay period is only 1° CA and the cylinder pressure starts to increase rapidly at –4° CA. At the SOI, the three-zone heat release rate curve is observed to decrease to –5 J, before rapidly increases at a rate of approximately 34 J/° CA. This decrease is due to the injection of fuel at a lower temperature than the bulk charge temperature at –5° CA, causing heat transfer to the fuel. Both the heat release rate curves exhibit a distinctive premixed burn fraction while the diffusion burn fraction is negligible. Since the amount of fuel injection at 0% load is small, it is believe that of all the injected fuel are burned in the premixed combustion phase. The heat release rate during the premixed burn phase peaks to 97.8 J/deg for the three-zone model and 90.4 J/deg for the experimental heat release rate. The three-zone heat release rate during the premixed combustion phase shows good correspondence to the experimental heat release rate.

The cylinder pressure and heat release rate profiles for the 25% load are shown in Figure 6.3 (b).

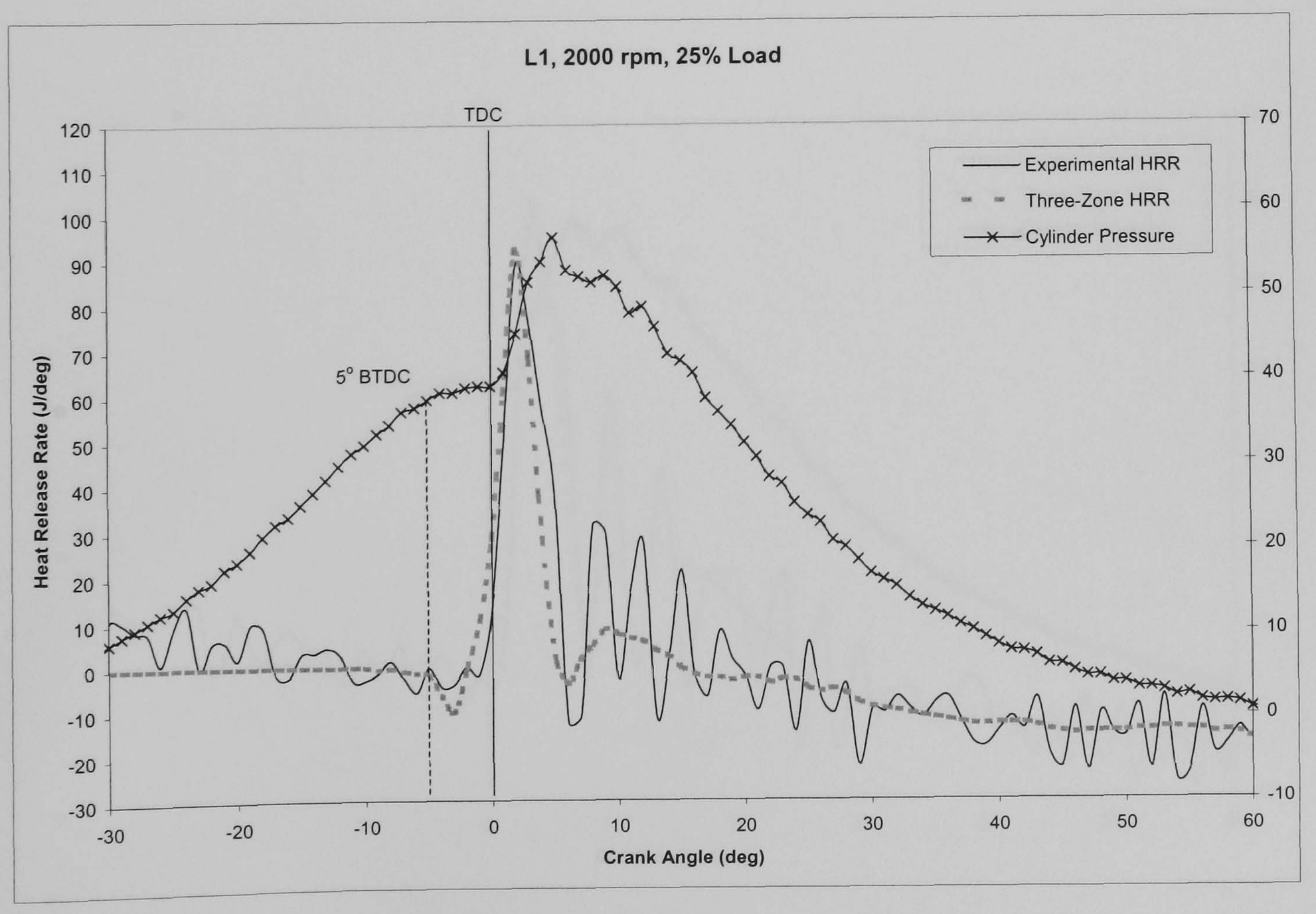

Figure 6.3(b): Cylinder pressure and heat release rate profiles at 25% load

The SOI is observed to start at –5° CA with an ignition delay period of 5° CA. The three-zone heat release rate exhibits a reduction of –10 J/deg at SOI due to the larger amount of fuel injected at this load condition. The experimental heat release rate is observed to start at 0° CA, corresponding to the increase in the cylinder pressure. However, the three-zone heat release rate is observed to start at 2° CA after fuel is injected, and rise at an initial rate of 12 J/° CA. The rate increases to 34 J/° CA from 0° CA. Both heat release rate models correspond well during the premixed combustion phase. However, it is observed that the diffusion combustion fraction of experimental heat release rate is larger than the three-zone heat release rate. The reason for this is due to the fuel injection rate data used in the model at 25% loading condition has a rate closed to the rate at 0%. The discrepancy of the fuel injection rate measurement was due to the lever setting of the fuel pump as discussed in Chapter 4 of this thesis.

The cylinder pressure and the heat release rate profiles at 50% load condition are shown in Figure 6.3 (c).

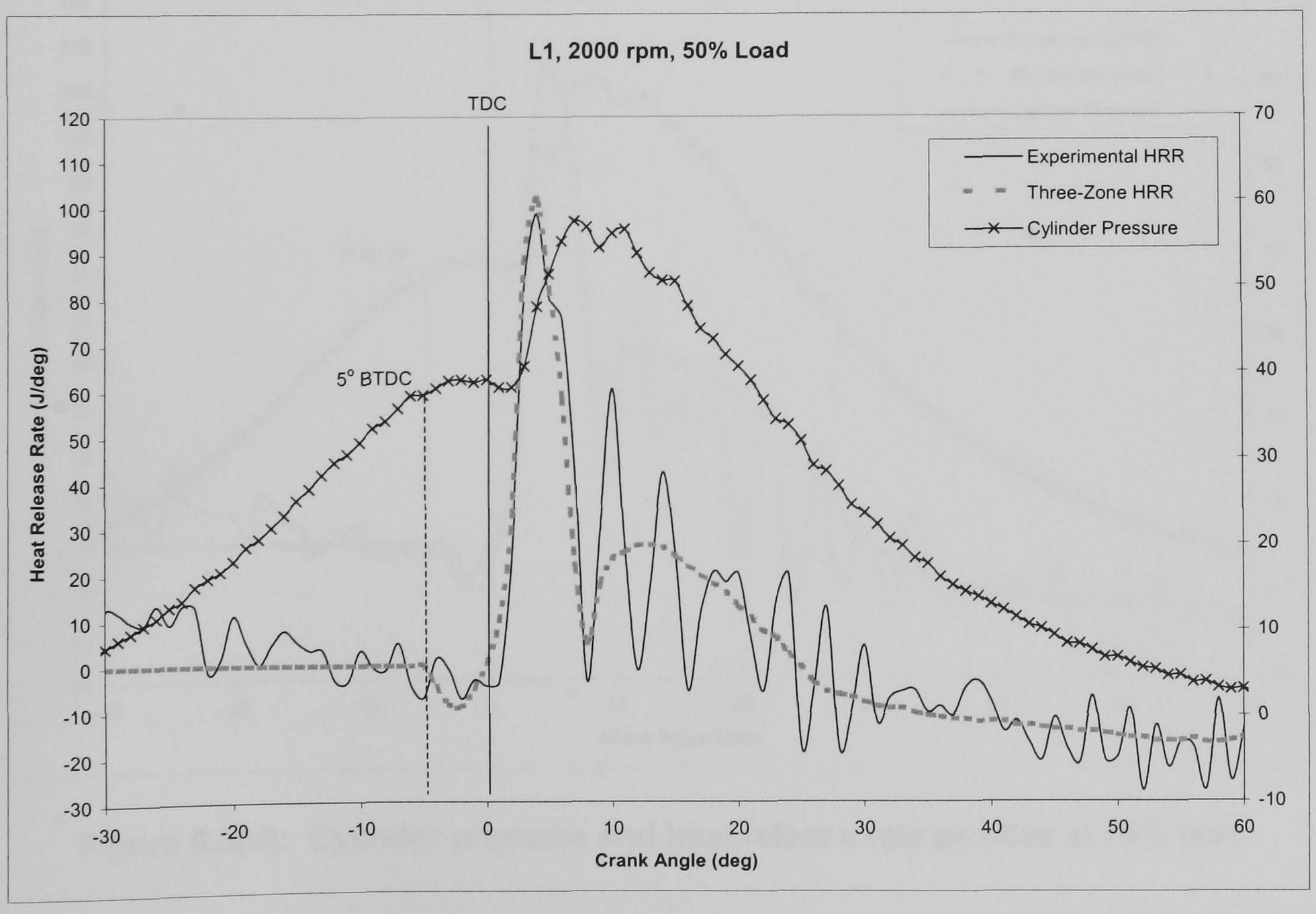

Figure 6.3(c): Cylinder pressure and heat release rate profiles at 50% load

As with the previous two load cases, the SOI starts at –5° CA. The cylinder pressure only starts to rise at 2° CA with an ignition delay period of 7° CA. The three-zone heat release rate exhibits a larger heat reduction upon SOI, corresponding to the amount of fuel injected. The three-zone heat release rate curve also exhibits a prominent diffusion burn fraction, which is commonly associated with direct injection diesel combustion. This give an indication that the three-zone heat release rate model is able to predict the amount of diffusion combustion corresponding to the later occurrence of combustion and the larger amount of fuel being burned in the diffusion combustion phase. Both the three-zone and the experimental heat release rate show a high premixed burn fraction which peak to 102.2 and 98.7 J/deg at 4° CA, respectively.

The profiles of the cylinder pressure and heat release rate at 75% load are shown in Figure 6.3 (d).

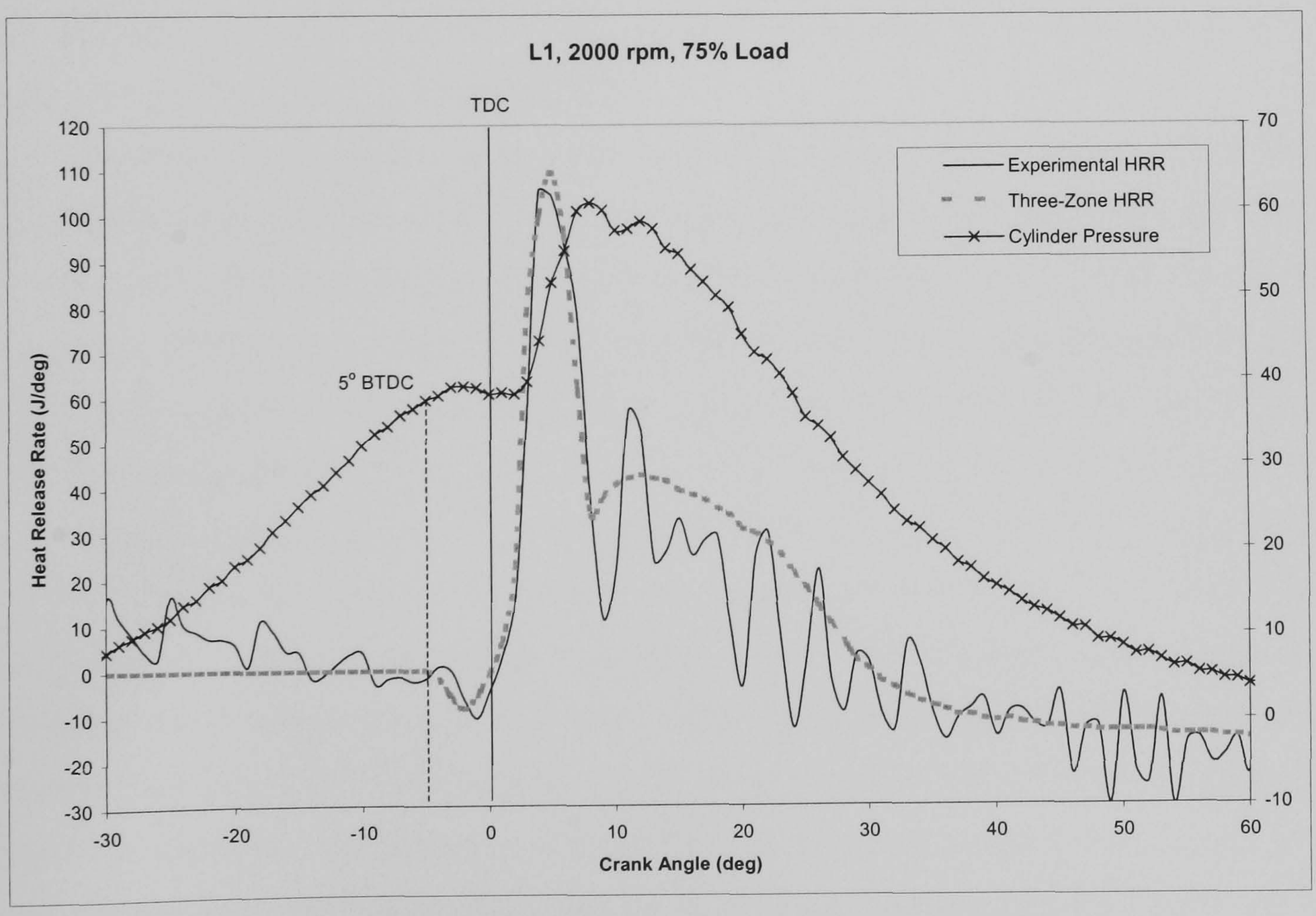

Figure 6.3(d): Cylinder pressure and heat release rate profiles at 75% load

The cylinder pressure curve exhibits a significant decrease in the cylinder pressure after TDC due to fuel injection that continues when the piston is past TDC. Consequently, much heat transfer from the compressed charge has already occurred. The cylinder pressure only peaks to 60.9 bar due to the late combustion. However, the premixed burn fraction is still large and peaks to 109.5 J/deg at 4° CA for the three-zone heat release rate, and 105.4 J/deg at 5° CA for the experimental heat release rate. This is due to the lower in-cylinder temperatures as a result of the pressure drop after TDC, which causes long ignition delay period and the subsequent delay in commencement of the combustion. The large premixed burn, in turn, causes high in-cylinder temperatures late in the cycle, which would improve soot oxidation. The three-zone heat release rate also exhibits a large diffusion burn fraction as a result of combustion of the large amount of fuel not burned during the premixed combustion phase.

6.2 RESULTS FROM THE ENGINE EXPERIMENTS

In order to understand and explain the emissions of the exhaust gases as measured from the engine experiment, cylinder pressure data and heat release rate are used in the combustion analysis. Prior to the engine experiment, a compression test was performed on all cylinders using a Compression Tester Gauge. This was to determine whether there were any significant variations in the compression pressure, especially from cylinder number 1, in which the pressure transducer was installed. The results from the compression test showed that the pressures of the four cylinders varied between ± 2 bar, which is within an acceptable range.

In the first engine experiment, measurements of the exhaust emissions and cylinder pressure for all four injectors were performed at two different engine speeds, i.e. 1800 rpm and 2000 rpm. The engine load was varied from 0% to 75% load conditions. The in-cylinder pressure data obtained were averaged from 100 cycles and a smoothing function was performed on the pressure data. The values of THC, NOx, CO_2, CO and O_2 were recorded. The smoke meter reading was selected to give smoke value in filter smoke number (FSN).

The measured cylinder pressures for each injector at the respective load setting were plotted against crank angle. Comparisons of the cylinder pressure traces for all four injectors at loading conditions of 25% and 75% with an engine speed of 1800 rpm were made as shown in Figure 6.4 (a) and (b) respectively. This comparison was a preliminary analysis of the acquired data to observe if there were any discrepancies or major differences in the experiment results. The motored cylinder pressure curve is also plotted on these graphs. From the graphs, the piston TDC is observed to coincide at 0^{o} CA. In general, injector L1 exhibits the highest cylinder pressure at both engine load conditions, while L2, which has the largest nozzle hole diameter, shows the lowest peak pressure amongst the four injectors. Injector L3, which has smaller nozzle hole diameter than injector L1, shows lower peak pressure than injector L1 but higher than injector L2. Another interesting observation is that the peak pressure of L4, which has the smallest nozzle hole diameter, exhibits a higher peak pressure value than injectors L2 and L3, especially at higher engine loads. Further investigation into the heat release rates and exhaust emission concentration of all these injectors are required in order to provide a satisfactory explanation to these observations.

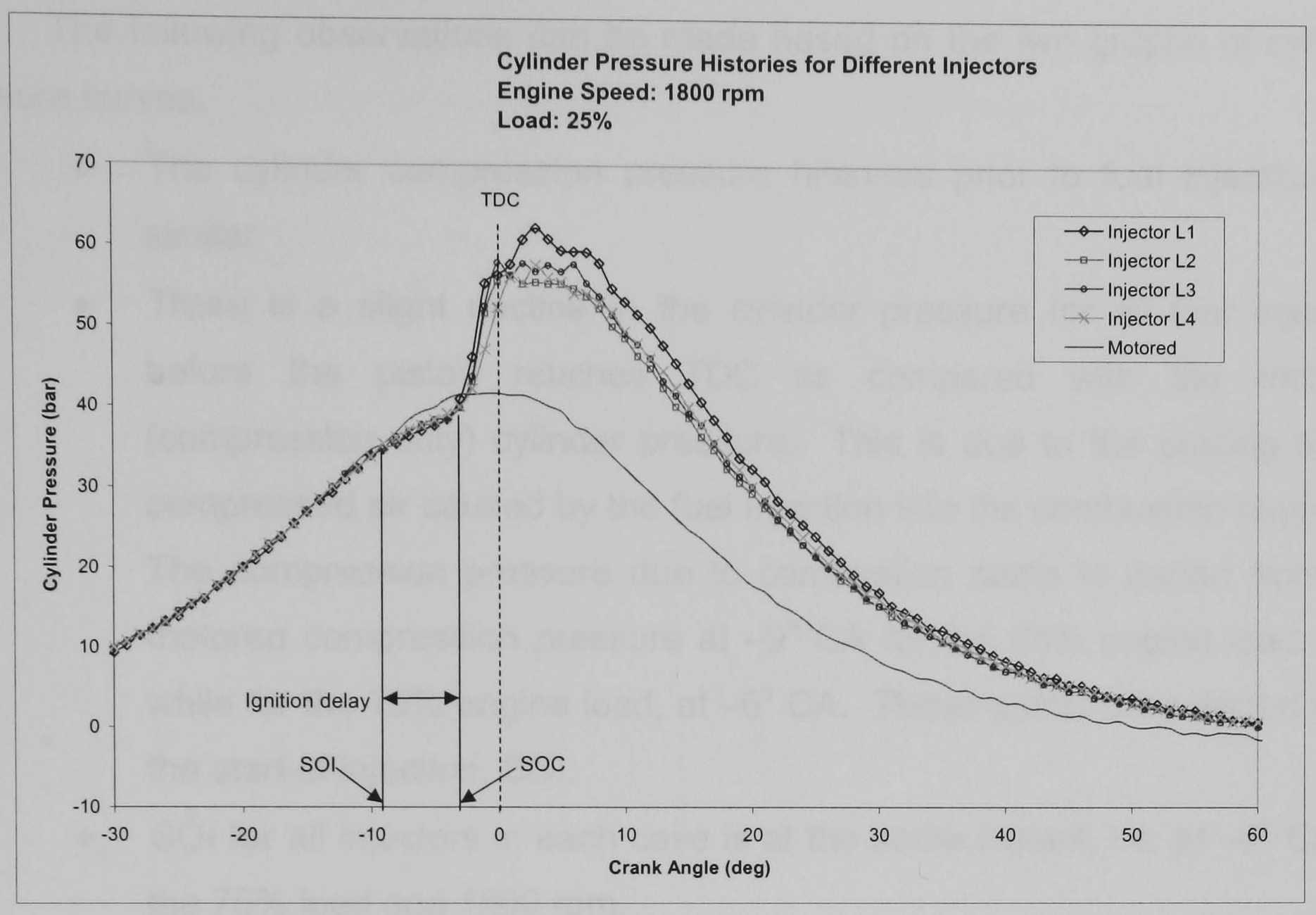

(a)

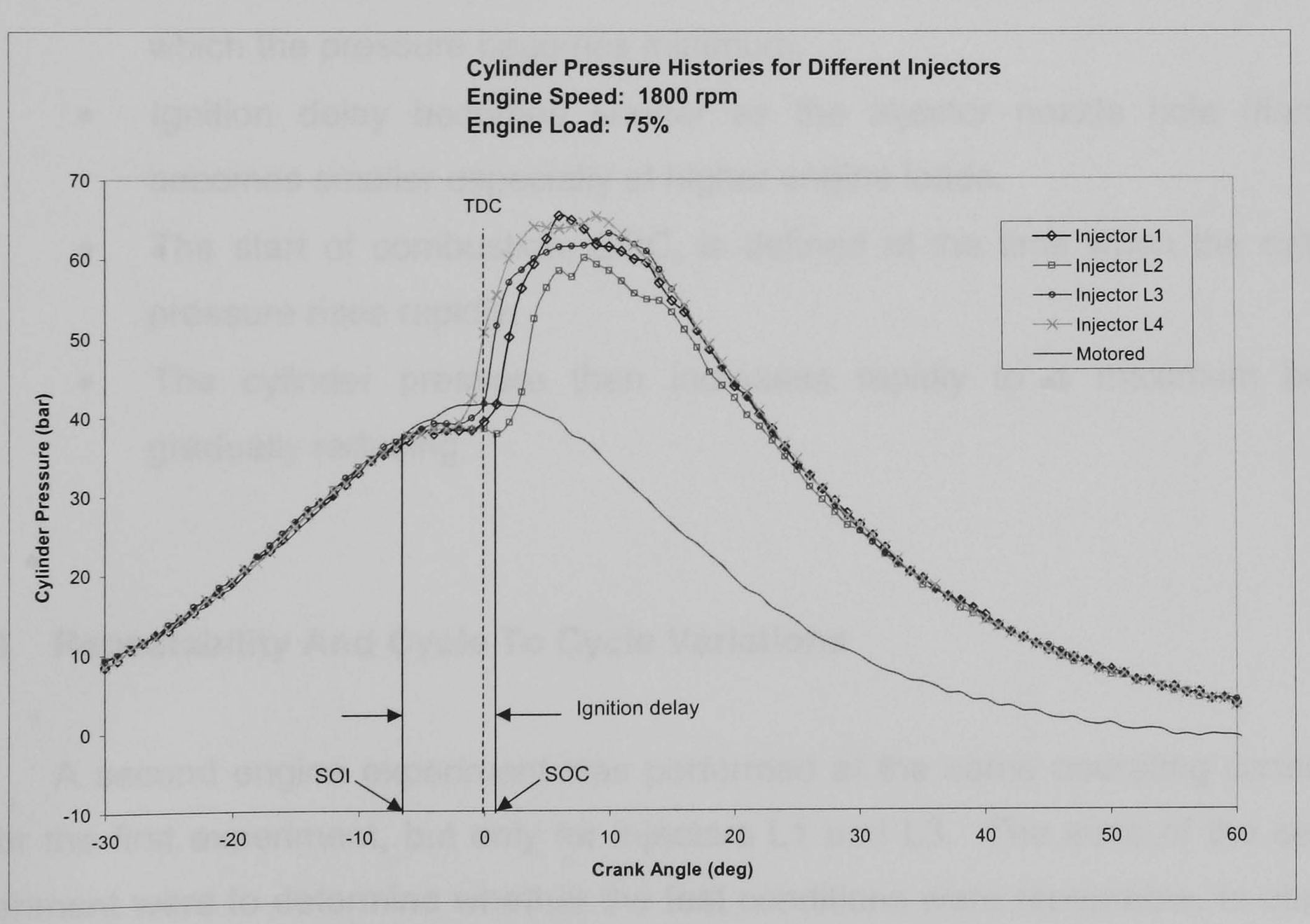

(b)

Figure 6.4: Comparison of the cylinder pressure curves of all the injectors at an engine speed of 1800 rpm and engine load of (a) 25% and (b) 75%

The following observations can be made based on the two graphs of cylinder pressure curves.

- The cylinder compression pressure histories prior to fuel injection are similar.
- There is a slight decline in the cylinder pressure for all four injectors before the piston reaches TDC as compared with the motored (compression only) cylinder pressure. This is due to the cooling of the compressed air caused by the fuel injection into the combustion chamber. The compression pressure due to combustion starts to depart from the motored compression pressure at –9° CA for the 25% engine load case while for the 75% engine load, at –6° CA. These points are referred to as the start of injection, SOI.
- SOI for all injectors in each case is at the same instant, i.e. at –6° CA for the 75% load and 1800 rpm.
- The ignition delay period is defined as the time from the point at which the pressure departed from the compression-only pressure to the point at which the pressure becomes minimum.
- Ignition delay becomes shorter as the injector nozzle hole diameter becomes smaller especially at higher engine loads.
- The start of combustion, SOC, is defined at the time when the cylinder pressure rises rapidly.
- The cylinder pressure then increases rapidly to a maximum before gradually reducing.

6.2.1 Repeatability And Cycle To Cycle Variations

A second engine experiment was performed at the same operating conditions as for the first experiment, but only for injectors L1 and L3. The aims of the second experiment were to determine whether the test conditions were repeatable, to observe if there were any cycle-to-cycle variations to the cylinder pressure and to determine if the results were consistent. In-cylinder compression pressure measurements of 50 cycles were taken with no smoothing operations performed on the pressure data for all load conditions. The results of the pressure histories and exhaust gas measurements

of the second experiment were compared with the results obtained from the first experiment for all the relevant conditions. Comparison between two load conditions, i.e. 25% and 75%, at the engine speed of 1800 rpm, for the pressure data of injector L1 are shown in Figure 6.5 (a) and (b).

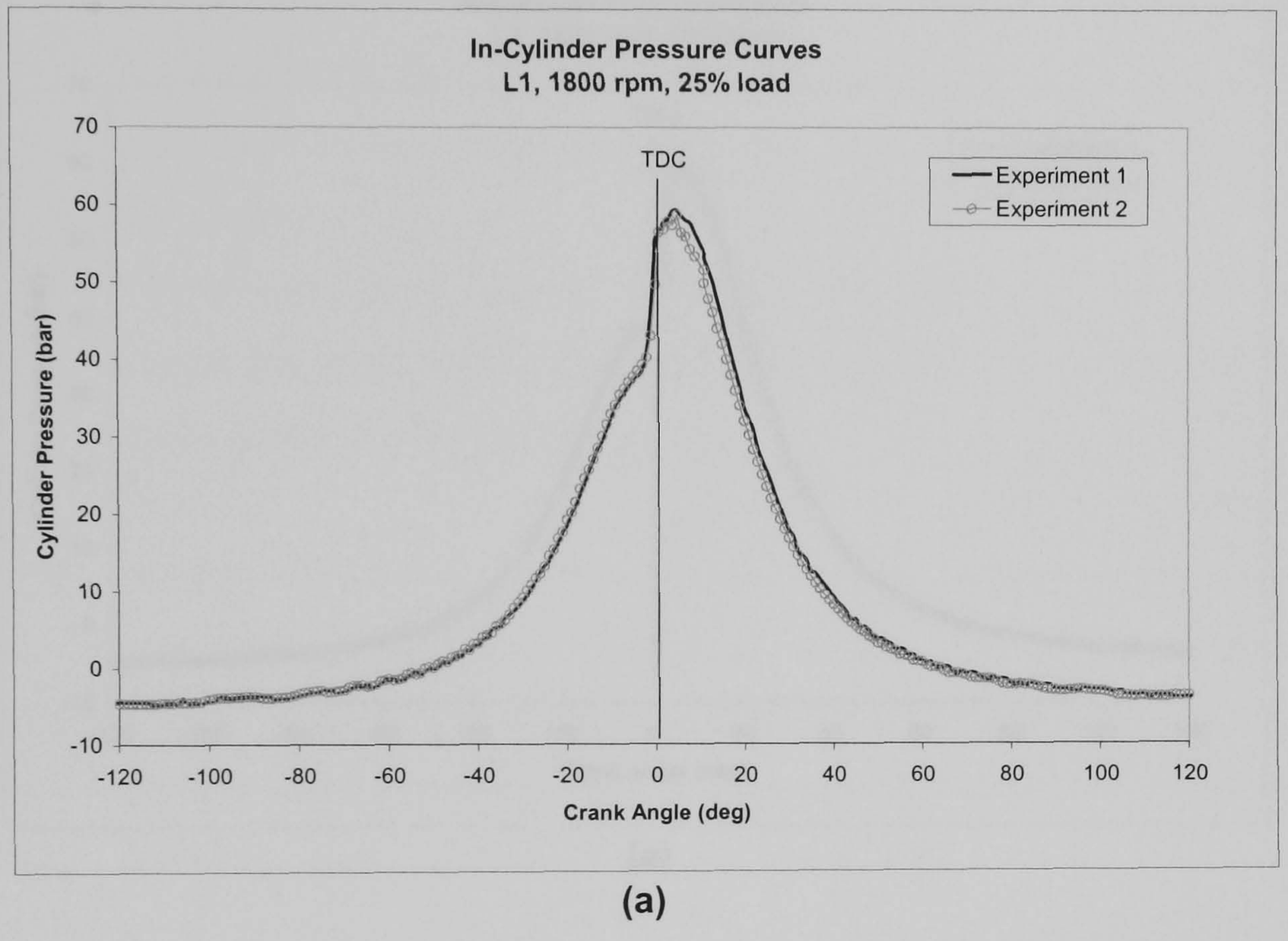

(a)

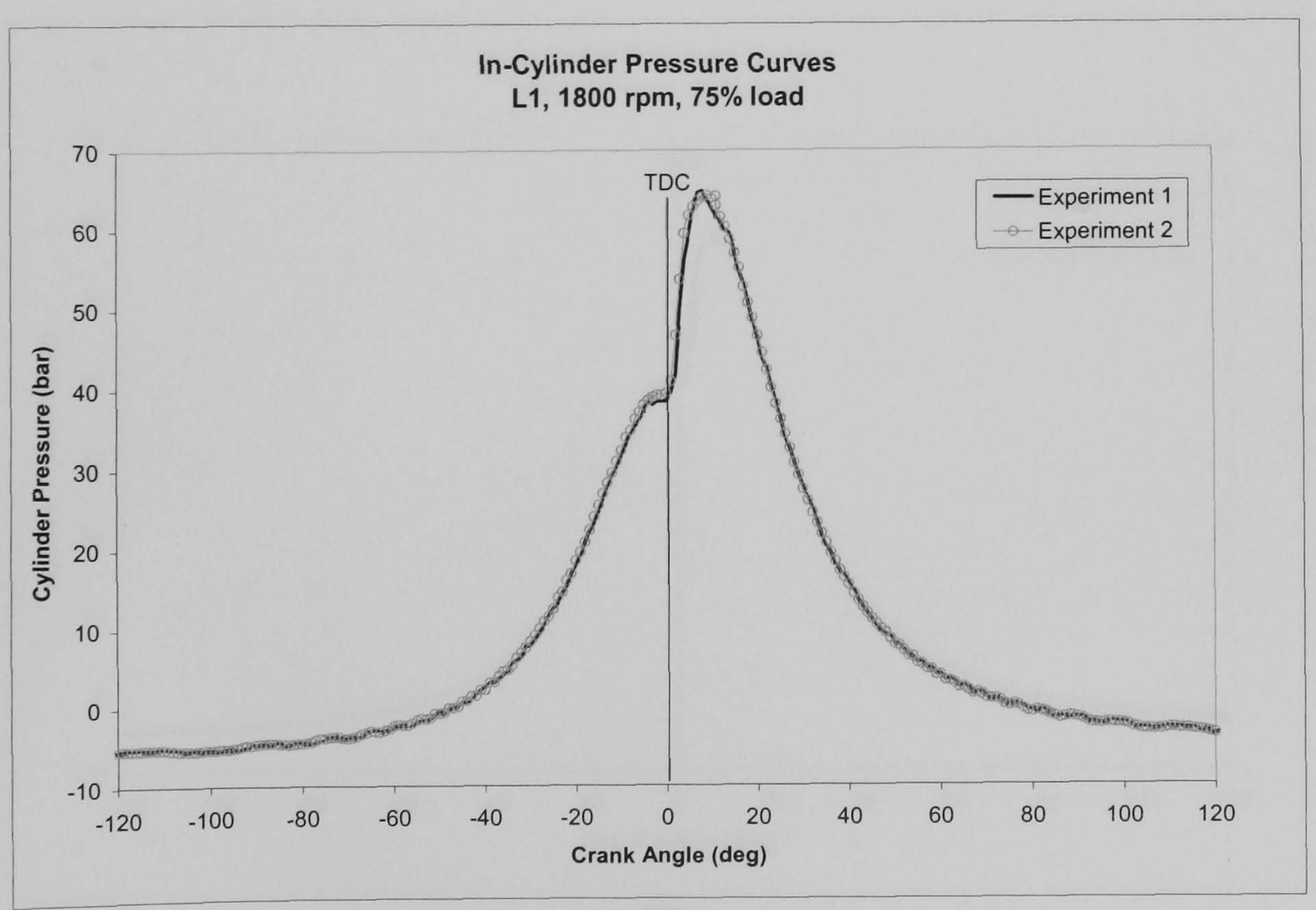

(b)

Figure 6.5: Comparison of cylinder pressure curves between experiments 1 and 2 for injector L1 at two load positions with an engine speed of 1800 rpm

Comparison between two engine speeds, i.e. of 1800 and 2000 rpm for injector L3 over the same load conditions are shown in Figure 6.6 (a) and (b).

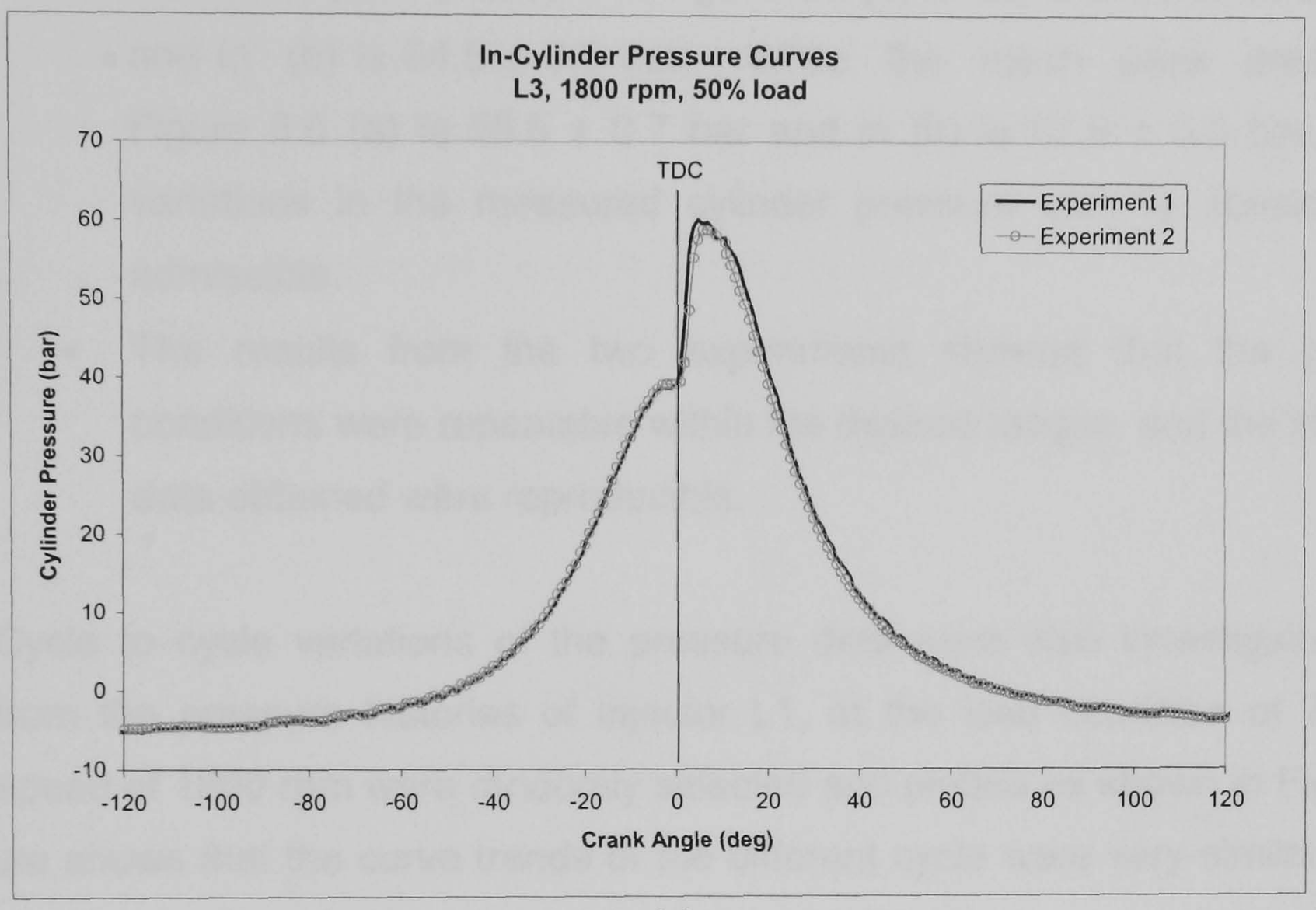

(a)

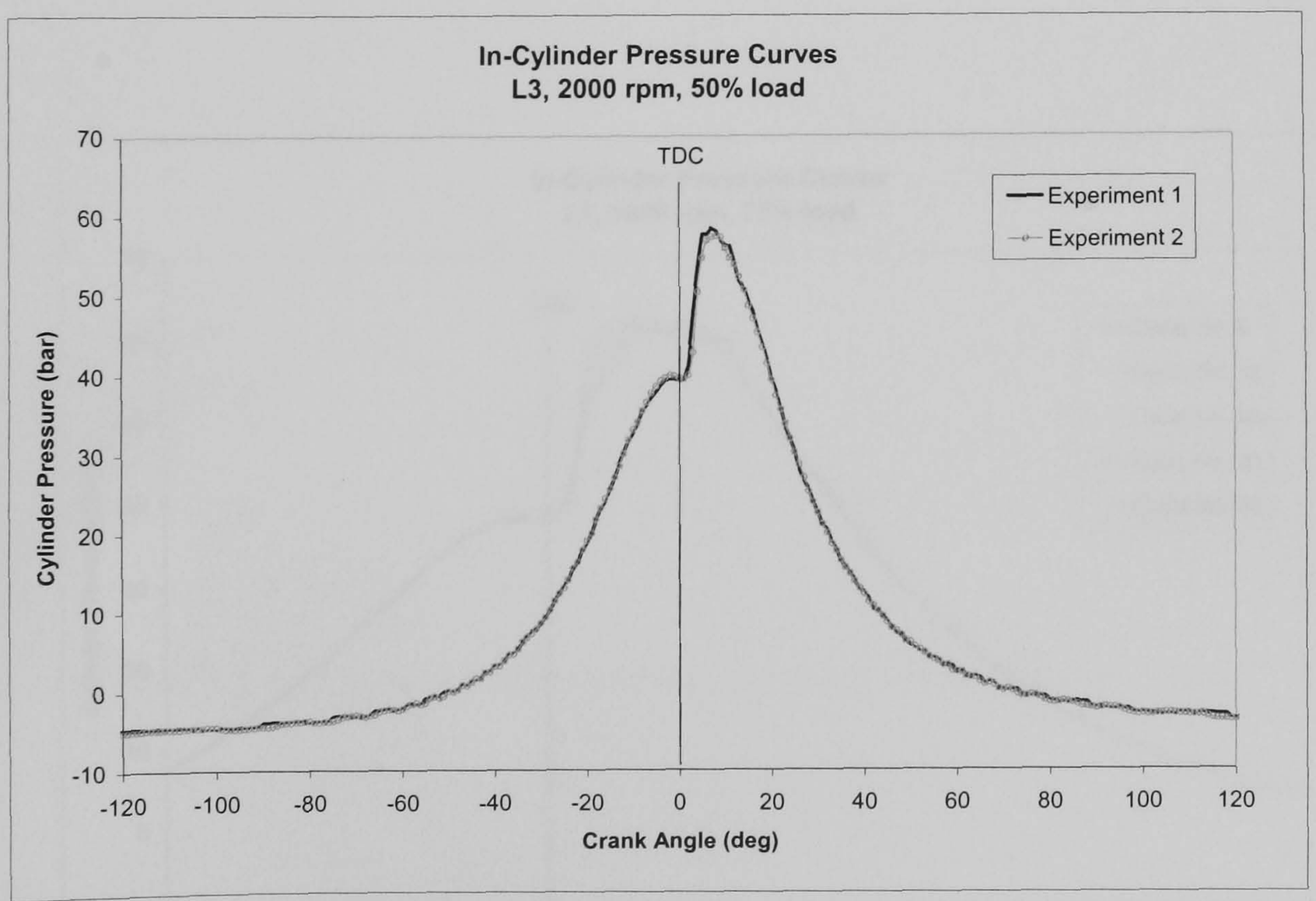

(b)

Figure 6.6: Comparison of cylinder pressure curves between experiments 1 and 2 for injector L3 at 50% engine load and engine speeds of 1800 and 2000 rpm

The following observations can be made from Figure 6.5 and Figure 6.6:

- The pressure curve trends for the two load conditions at constant speed as shown in Figure 6.5, and for the different engine speed but at the same engine load as shown in Figure 6.6, are very similar.
- The mean peak pressure in Figure 6.5 (a) is found to be at 59 ± 0.3 bar, and in (b) is 64.5 ± 0.3 bar. While the mean peak pressure in Figure 6.6 (a) is 59.5 ± 0.7 bar and in (b) is 57.9 ± 0.5 bar. These variations in the measured cylinder pressure can be considered as admissible.
- The results from the two experiments showed that the operating conditions were repeatable within the desired ranges, and the measured data obtained were reproducible.

Cycle to cycle variations of the pressure data were also investigated. Five cycles from the pressure histories of injector L1, at the load condition of 75% and engine speed of 1800 rpm were randomly selected and plotted as shown in Figure 6.7. The figure shows that the curve trends of the different cycle were very similar and the cycle-to-cycle variations observed were not to be significant.

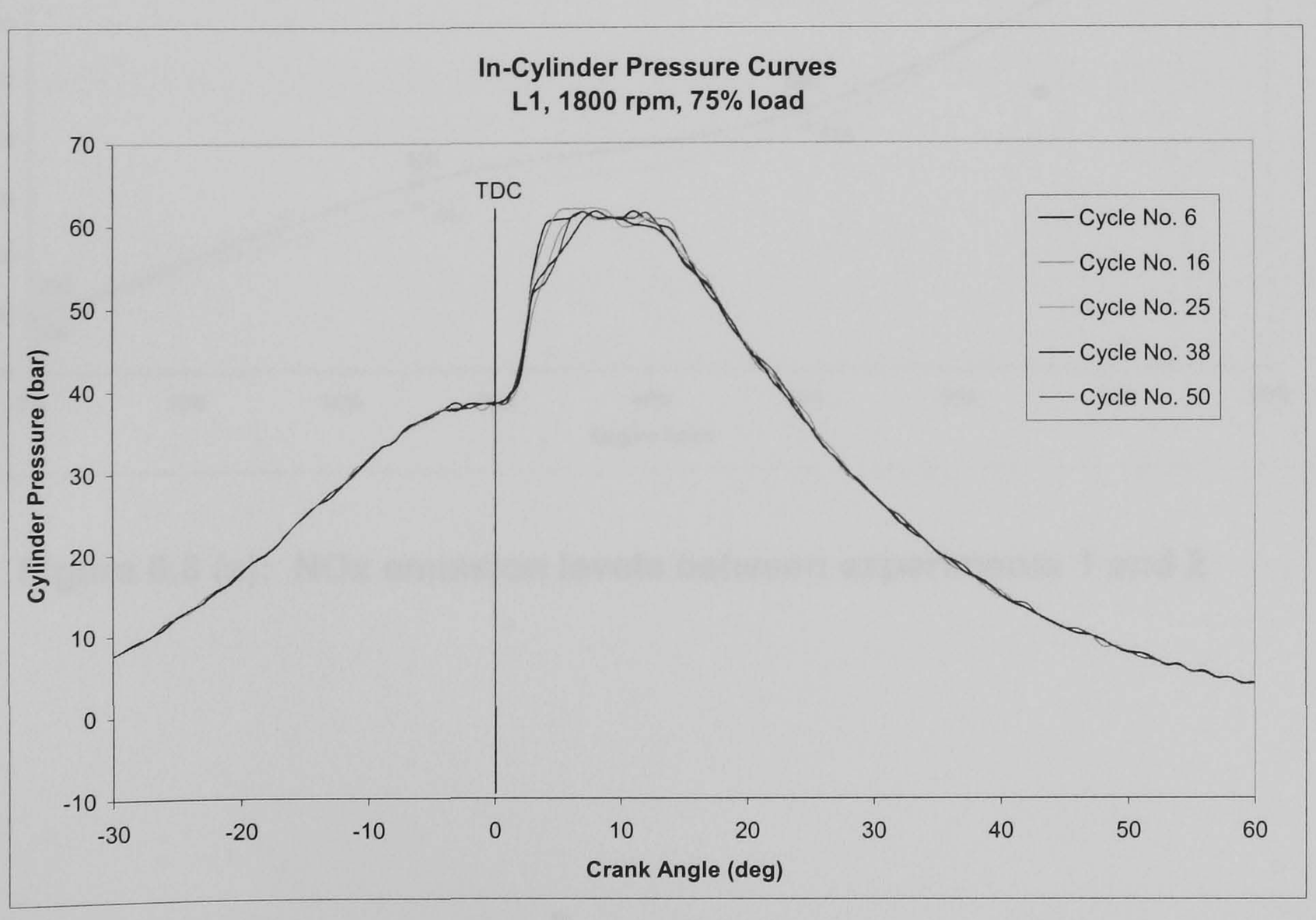

Figure 6.7: Cylinder pressure curves for injector L1 from different cycles

Variations in the exhaust gas emissions were also investigated by comparing the measured emission levels recorded from the two experiments. The emission results of nitrogen oxides (NOx) and total hydrocarbon (THC) for injector L3, at the engine speed of 2000 rpm, from the two experiments were plotted as shown in Figure 6.8 (a) and (b) respectively. The mean values of the pollutants were plotted against engine load at fixed engine speed. The values for the fluctuations are also shown on these curves. Results in Figure 6.8 (a) from the NOx measurements show that the NOx levels from the two experiments have an increasing trend when engine load is increased. However, the second experiment shows a greater increase in NOx levels at higher engine loads.

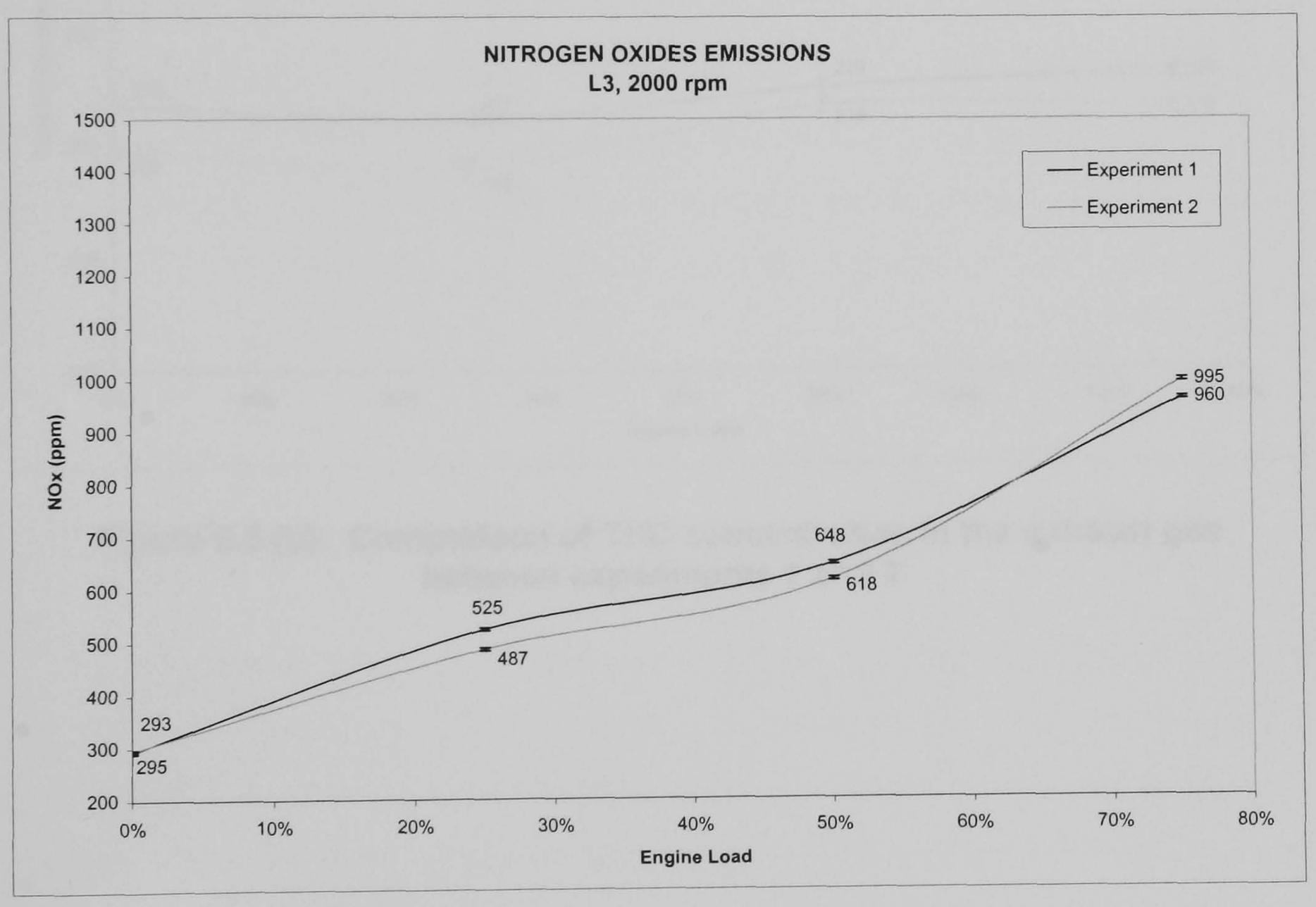

Figure 6.8 (a): NOx emission levels between experiments 1 and 2

Measurements of the THC emissions from the two experiments are shown in Figure 6.8 (b). Although the results exhibit some variations in the pollutant concentration, they show that the curve trends are very similar between the two experiments. Hence, establishing that the experiments are highly reproducible.

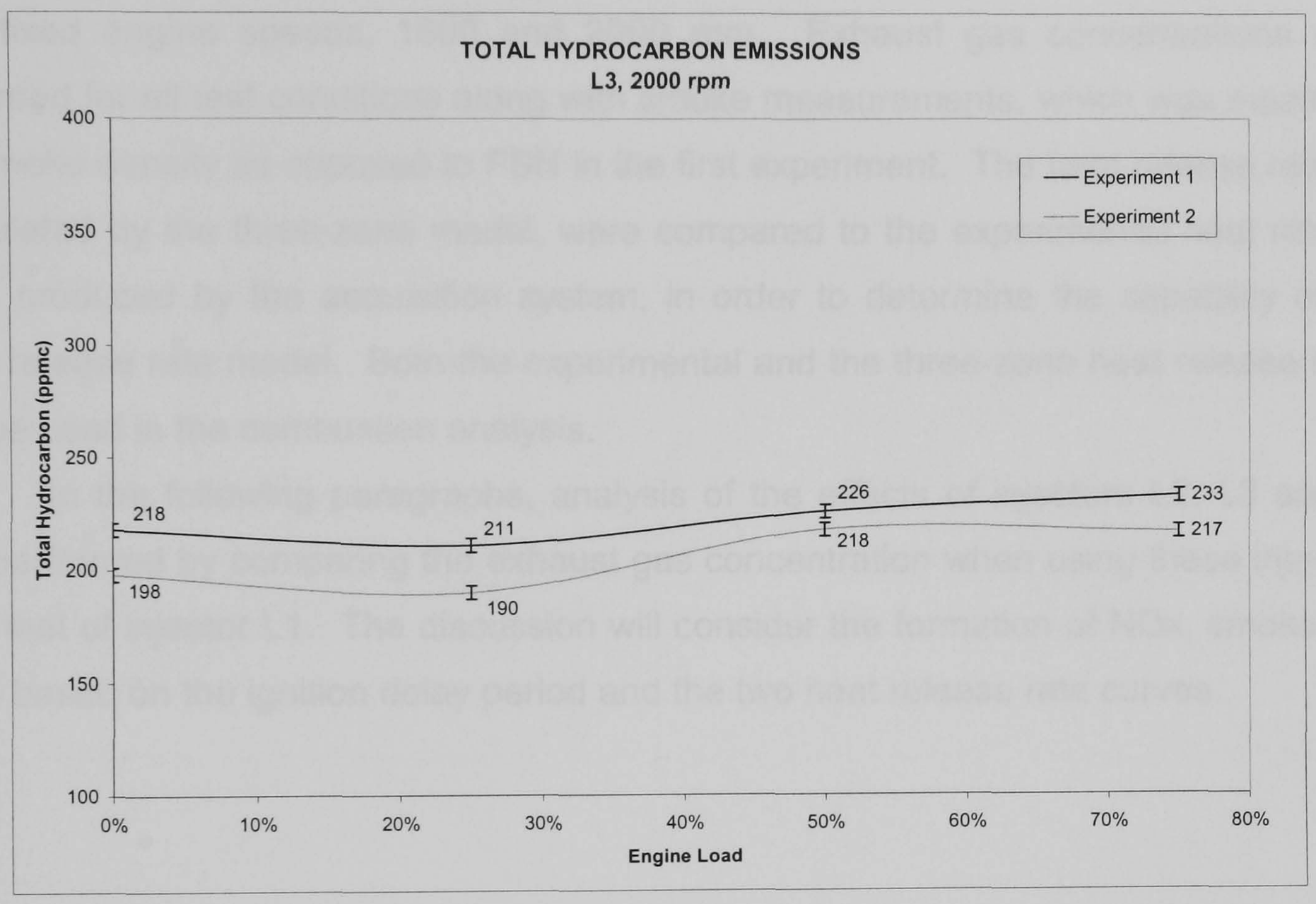

Figure 6.8 (b): Comparison of THC concentration in the exhaust gas between experiments 1 and 2

6.3 COMBUSTION ANALYSIS

Upon satisfactory completion of the analysis of experiments 1 and 2, a third experiment was performed for all four injectors. Two additional engine load conditions were included in the current experiment, i.e. 37% and 63% loads, giving a total of six load conditions. As with the previous two experiments, the engine was operated at the two fixed engine speeds, 1800 and 2000 rpm. Exhaust gas concentrations were recorded for all test conditions along with smoke measurements, which was measured as smoke density as opposed to FSN in the first experiment. The heat release rate, as calculated by the three-zone model, were compared to the experimental heat release rate, produced by the acquisition system, in order to determine the capability of the heat release rate model. Both the experimental and the three-zone heat release rates will be used in the combustion analysis.

In the following paragraphs, analysis of the effects of injectors L2, L3 and L4 are performed by comparing the exhaust gas concentration when using these injectors with that of injector L1. The discussion will consider the formation of NOx, smoke and THC based on the ignition delay period and the two heat release rate curves.

6.3.1 Emissions Concentration

The emissions of NOx, smoke and THC for all four injectors at both engine speeds are shown in Figure 6.9, 6.10 and 6.11 respectively. The curves display the effects of varying engine load and engine speed on the formation of pollutant in the exhaust gas when different injectors were used in the engine. For each curve, the concentration of the pollutant was plotted against engine load. Each line with different marker represents different injectors while for the two engine speeds, the dotted lines represent engine speed of 1800 rpm and the full lines for the 2000 rpm.

(a) Emission of NOx

The concentration of NOx in the exhaust gas for all four injectors and at both engine speeds are shown in Figure 6.9.

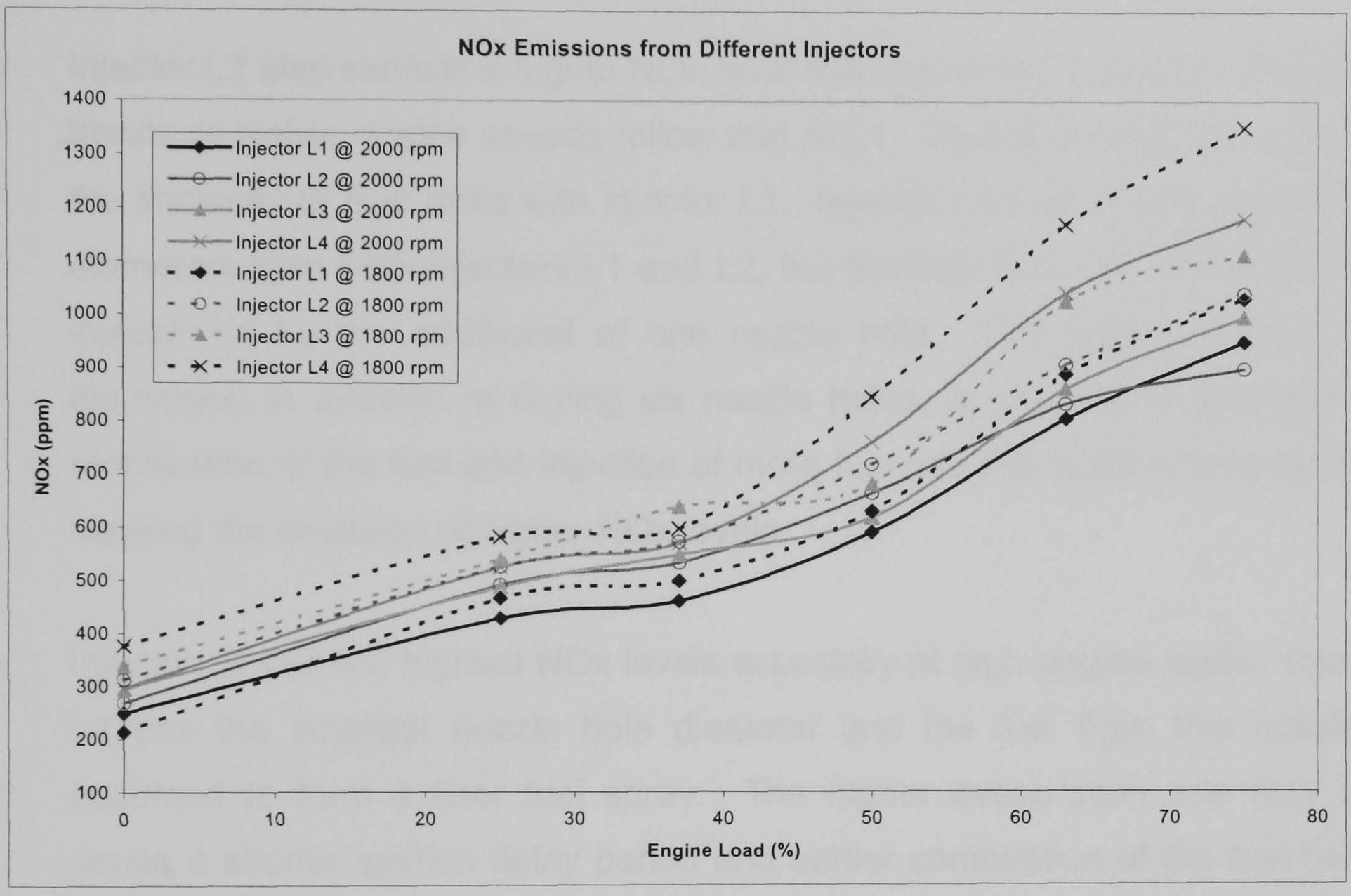

Figure 6.9: Plot showing the concentration of NOx

The following observations can be made from the curve trends:

- NOx increases with engine load for all injectors. The NOx emission is also higher at the lower engine speed.

- For injector L1, the NOx concentration was the lowest amongst the other injectors, at most load conditions and at both engine speeds.

- The NOx concentration, using injector L2, exhibits a higher level than injector L1, but lower than injectors L3 and L4. However, there is a decreasing trend at the 75% engine load and at 2000 rpm. The higher level of NOx concentration is expected from an injector having larger nozzle hole diameters, due to larger rate of fuel injected into the combustion chamber which would cause bigger burn fraction in the initial combustion phase.

- Injector L3 also exhibits a higher NOx level than injectors L1 and L2. The curve trends at higher engine speeds follow that of L1. This is believed to be due to the similarity of flow rates with injector L1. Injector L3 has smaller nozzle hole diameters than both injectors L1 and L2, but the total flow rate is the same as injector L1 by the additional of one nozzle hole. The smaller nozzle hole diameters, in addition to having six nozzle holes, is believed to enhance the atomisation of the fuel and injection of more fuel into the combustion chamber, causing the emission of higher NOx levels.

- Injector L4 has the highest NOx levels especially at high engine loads. Injector L4 has the smallest nozzle hole diameter and the fuel from this nozzle is assumed to form a finer fuel spray. The higher evaporation rate may also cause a shorter ignition delay period and earlier combustion of the fuel before the piston reaches TDC. This produces a high compression pressure and temperature, which promotes the formation of NOx.

(b) Emission of smoke

The density of smoke measured in the exhaust gas for all the four injectors and at the two engine speeds are shown in Figure 6.10.

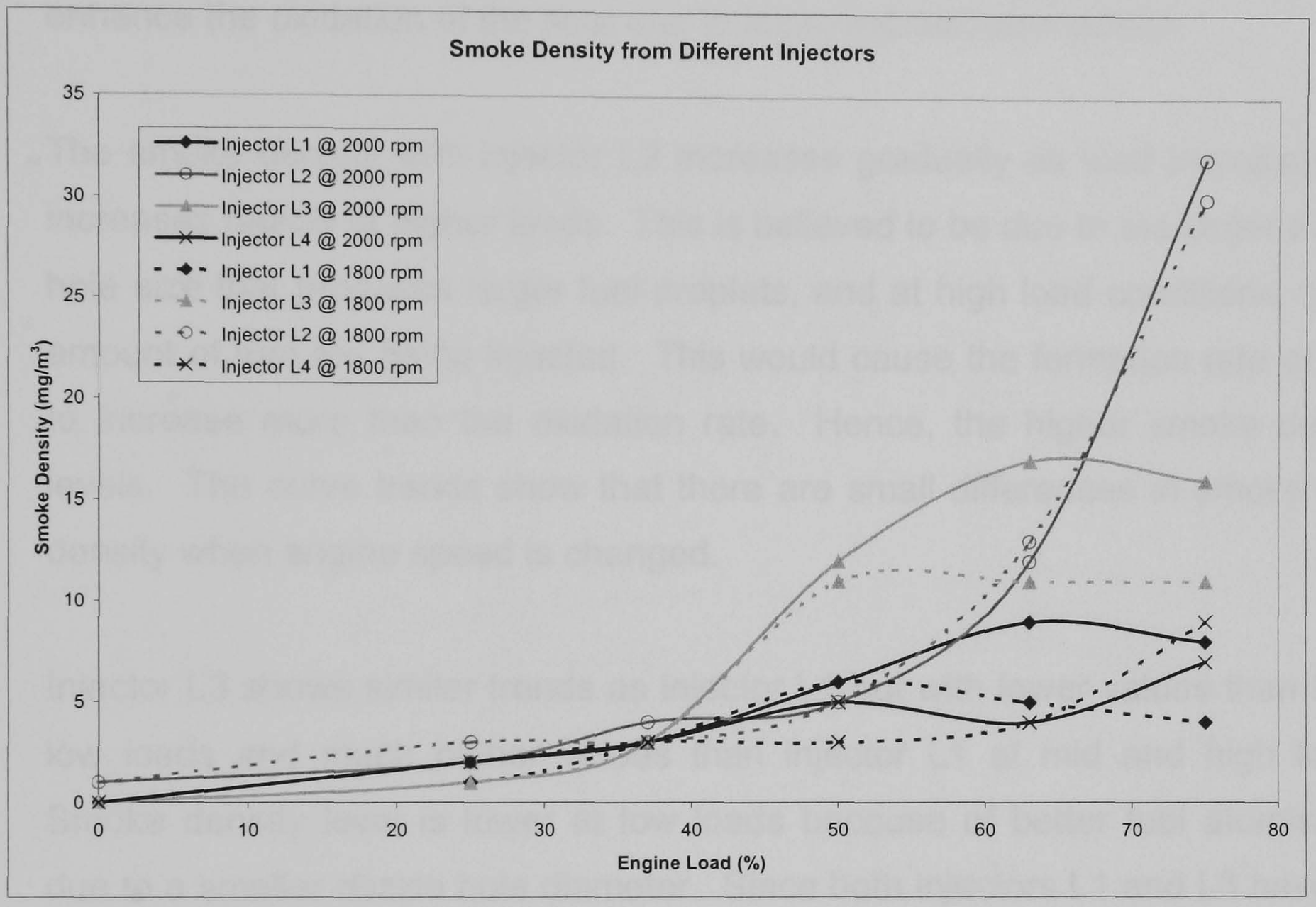

Figure 6.10: Plot showing smoke density

The smoke emission trends show that:

- The smoke density is low at low engine loads and increases at load conditions higher than 40%. Increasing the engine speed at high load conditions causes a higher smoke density for injectors L1 and L3 while the level when using injector L4 reduces. Changing engine speed has no significant effect on the smoke density for injector L2.

- Injector L1 shows a gradual increase in smoke density as engine load increases with higher density levels of 9 mg/m^3, at mid-load. Then the trends show a decreasing smoke density at high load condition. At lower engine speed, the smoke density decreases at a faster rate. It is believed that the smoke levels increases as more fuel is injected into the combustion chamber. However, at higher load conditions, the higher energy of the injected fuel could enhance the oxidation of the soot due to improved fuel atomisation.

- The smoke density with injector L2 increases gradually as load increases but increases rapidly at higher loads. This is believed to be due to the larger nozzle hole size that produces larger fuel droplets, and at high load conditions, larger amount of fuel are being injected. This would cause the formation rate of soot to increase more than the oxidation rate. Hence, the higher smoke density levels. The curve trends show that there are small differences in smoke level density when engine speed is changed.

- Injector L3 shows similar trends as injector L1 but with lower values than L1 at low loads and much higher values than injector L1 at mid and high loads. Smoke density level is lower at low loads because of better fuel atomisation due to a smaller nozzle hole diameter. Since both injectors L1 and L3 have the same total flow area, higher smoke density is observed at high load conditions due to the larger amount of fuel injected.

- Injector L4 exhibits the lowest smoke density levels. The smoke density increases gradually with no significant increase at mid-loads but show a small increase at high loads. The low smoke density level is believed to be due to the small nozzle hole diameter and the low amount of fuel injected which enhances air utilization, thus promoting oxidation of the soot.

(c) Emission of THC

Curve trends of THC concentrations as measured from the exhaust gas are shown in Figure 6.11.

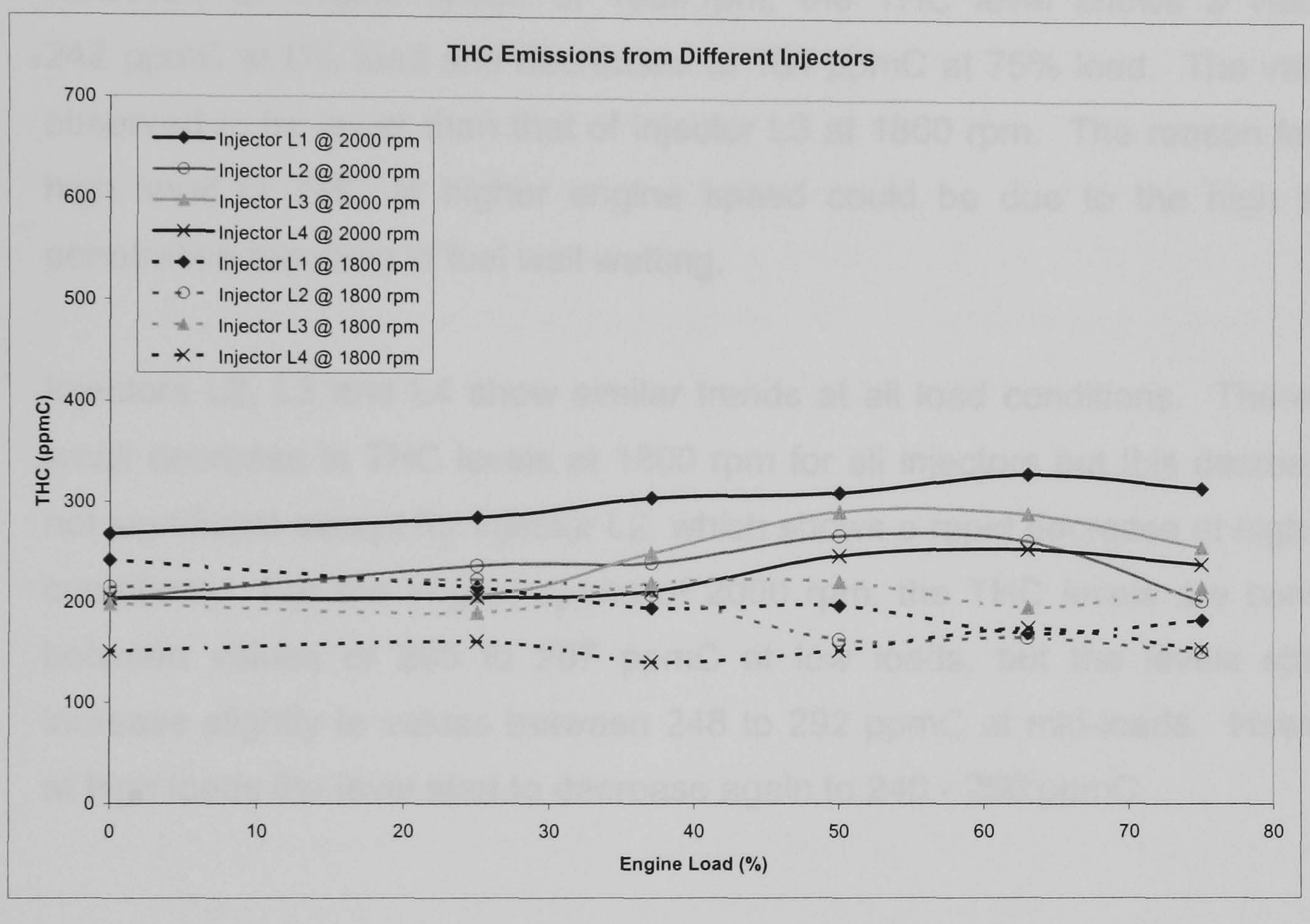

Figure 6.11: Emission of THC for the four injectors at all load levels and engine speeds

The curves show that:

- The concentrations of THC for all injectors exhibit almost a constant value at all load conditions especially at lower engine speed. This give an indication that the combustion occurs at a condition where there is no significant change in the overall equivalent ratio.

- The concentrations of THC are higher at higher engine speed for all injectors. However, this observation is expected as the fuel amount increases at higher load conditions and the THC increase is not too significant that would indicate an unexpected phenomenon.

- Injector L1 shows the highest level of THC at engine speed of 2000 rpm with a minimum THC value of 268 ppmC at 0% load to 316 ppmC at 75% load. However, at engine speed of 1800 rpm, the THC level shows a value of 242 ppmC at 0% load and decreases to 184 ppmC at 75% load. The value is observed to be lower than that of injector L3 at 1800 rpm. The reason for this high level of THC at higher engine speed could be due to the high spray penetration resulting in fuel wall wetting.

- Injectors L2, L3 and L4 show similar trends at all load conditions. There is a small decrease in THC levels at 1800 rpm for all injectors but this decrease is not significant except for injector L2, which shows a rapid decrease at high load conditions. For the engine speed of 2000 rpm, the THC levels are constant between values of 205 to 207 ppmC at low loads, but the levels start to increase slightly to values between 248 to 292 ppmC at mid-loads. However, at high loads the level start to decrease again to 240 - 250 ppmC.

6.3.2 Cylinder Pressure and Heat Release Rate

Comparison of the in-cylinder pressure with the heat release rate curves would enable a description of the combustion process with relation to the emissions results. The measured cylinder pressure and the experimental heat release rate from each operating condition are plotted as a function of crank angle for each injector. The three-zone heat release rate curves are plotted in a different figure. This enables a comparison to be made between the two models to determine the capabilities of the three-zone model. From the plots, it was found that the start of injection (SOI) of all the injectors is at the same crank angle before engine TDC, i.e. at 5° before TDC, for the engine speed of 2000 rpm. This observation was anticipated since the injection timing was not changed in all the experimental conditions. The change in engine load causes a corresponding change in the injection rate but not to the SOI.

(a) Effects of engine load on cylinder pressure and heat release rate

The effects of changing the engine loads on the cylinder pressure and heat release rate of different injectors were investigated in order to provide a logical explanation to the formation of the measured pollutants in the exhaust gas. Only four load conditions, i.e. 0%, 25%, 50% and 75% are presented for discussion. The reason for selecting only these four engine load conditions is for simplicity and clarity in the presentation of the curves especially for the heat release rate curves. In addition, the heat release rate trends of the 37% and 63% loads were similar to that of the 25% and 75% respectively, so these curves were not plotted. The motored cylinder pressure is also included in each plot. It is observed that the cylinder pressure show constant increasing trends when the engine load is increased. The heat release rate curve, on the other hand, show different trends with respect to the engine load.

(i) Injector L1

The measured cylinder pressure and heat release rate curves for injector L1, are shown in Figure 6.12.

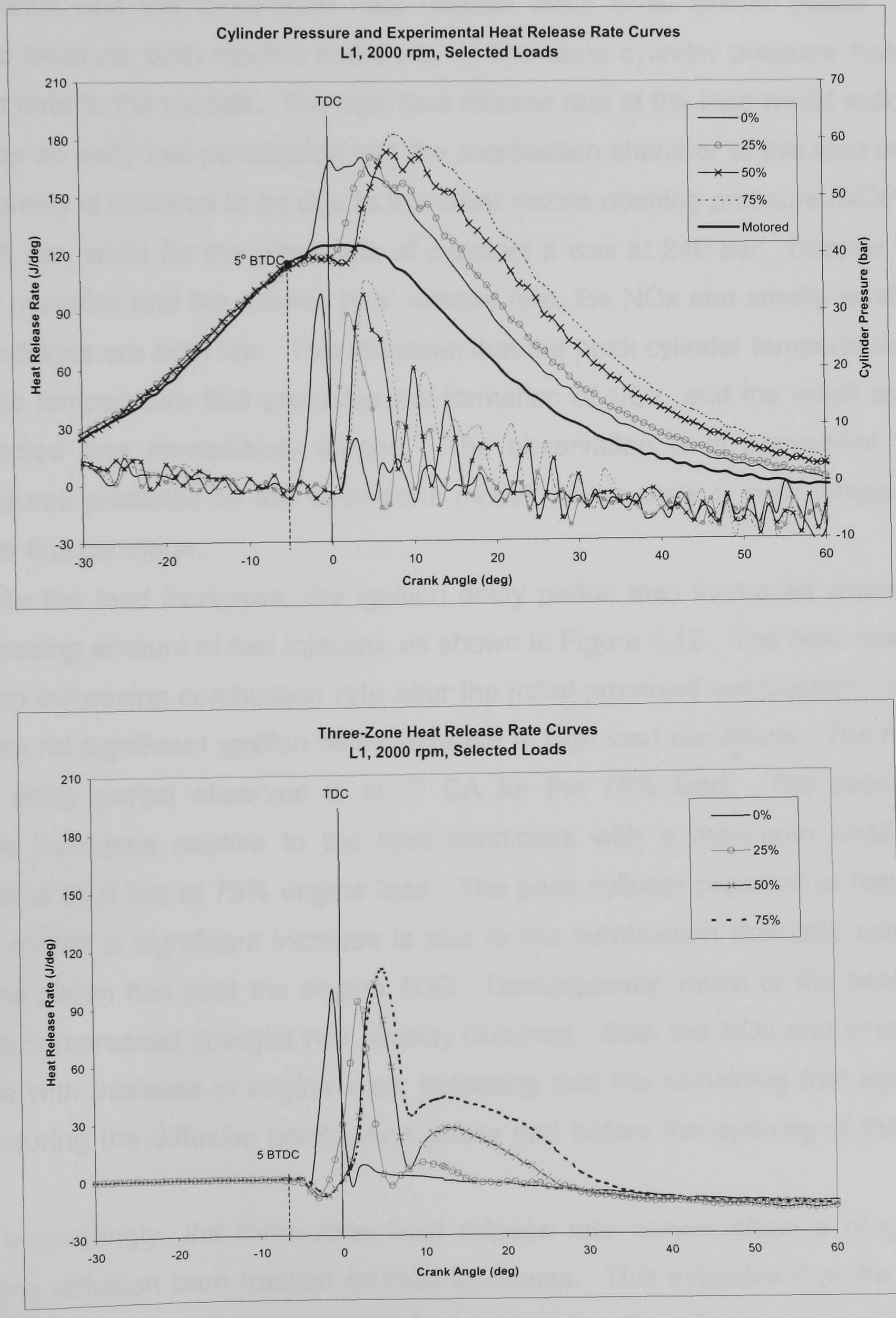

Figure 6.12: Combustion characteristics of injector L1

Injector L1 exhibits a peak cylinder pressure of 56.8 bar, at both 0% and 25% loads, 57.8 bar at 50% load and 60.9 bar at 75% load. The peak cylinder pressure at 0% load is found to be relatively high. The ignition delay period at 0% load is observed to be short, i.e. 2° CA, and combustion starts before TDC. The magnitude of the premixed burn fraction at all loading conditions, except at 75% load, do not exhibit a progressive increasing trends with respect to the increasing fuelling levels. Both the experimental and the three-zone heat release rates show similar trends. This is expected because both models make use of the same cylinder pressure histories as the input data to the models. The high heat release rate at 0% load would indicate that there was an early fuel penetration into the combustion chamber at this load condition. This anomaly is believed to be due to the lower nozzle opening pressure (NOP), which is at 235 bar, while for the other sets of injectors it was at 240 bar. Despite the high cylinder pressure and the intense heat release rate, the NOx and smoke levels at this load conditions are both low. This indicates that the peak cylinder temperature did not reach the temperature that promotes the formation of NOx, and the small amount of fuel injected was immediately burned. The observation is in agreement with the temperatures predicted by the three-zone model, which show a peak temperature of 1750K at this condition.

As the load increases, the ignition delay period also increases which reflects the increasing amount of fuel injected, as shown in Figure 6.12. The heat release rate shows an increasing combustion rate after the initial premixed combustion. However, there was no significant ignition delay increase at high load conditions. The maximum ignition delay period observed is at 7° CA for the 75% load. The peak cylinder pressure increases relative to the load conditions with a maximum peak cylinder pressure of 60.9 bar at 75% engine load. The peak cylinder pressure at higher loads did not exhibit a significant increase is due to the combustion that only commences when the piston has past the engine TDC. Consequently, much of the heat transfer from the compressed charged has already occurred. Both the NOx and smoke levels increase with increase in engine load, indicating that the remaining fuel injected are burned during the diffusion combustion phase and before the opening of the exhaust valve.

Interestingly, the three-zone heat release rate curves show a progressively increasing diffusion burn fraction as load increases. This indicates that the model is able to predict well the combustion processes based on the cylinder pressure histories.

(ii) Injector L2

The trends of cylinder pressure and heat release rate curves for injector L2 are shown in Figure 6.13.

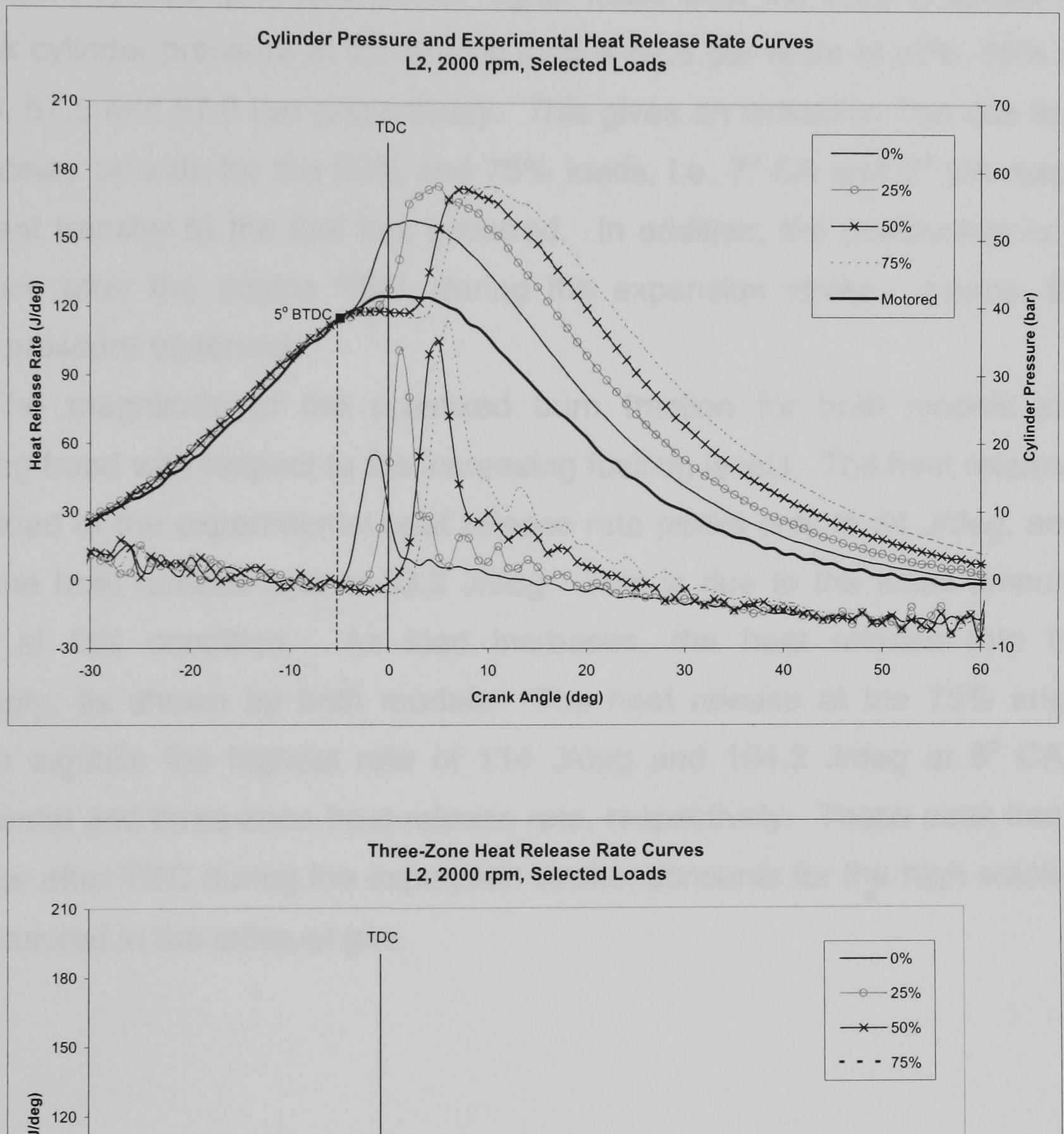

Figure 6.13: Combustion characteristics of injector L2

The ignition delay period for injector L2, in Figure 6.13, shows a progressively increasing trend with loads, from 1° CA at 0% load to 8° CA at 75% load. The ignition delay periods are however shorter than the ignition delay periods of injector L1, indicating that the SOC for injector L2 occurs at an earlier crank angle. This is due to the larger nozzle hole diameters of injector L2, causing more fuel to be injected and evaporated during the ignition delay period. The peak cylinder pressure curves show no significant cylinder pressure rise at higher loads after the initial pressure increase. The peak cylinder pressure at 0% engine load is 52.8 bar while at 25%, 50% and 75% are 57.3, 57.5 and 57.8 bar respectively. This gives an indication that due to the long ignition delay periods for the 50% and 75% loads, i.e. 7° CA and 8° CA respectively, much heat transfer to the fuel has occurred. In addition, the combustion is found to commence after the engine TDC, during the expansion stroke. Hence, the lower cylinder pressure observed.

The magnitude of the premixed burn fraction for both models shows an increasing trend with respect to the increasing fuelling levels. The heat release rate for the 0% load of the experimental heat release rate peaks only to 54 J/deg, and for the three-zone heat release rate to 53.2 J/deg. This is due to the small amount of fuel injected at this condition. As load increases, the heat release rate increases accordingly, as shown by both models. The heat release at the 75% engine load condition exhibits the highest rate of 114 J/deg and 104.2 J/deg at 6° CA, for the experimental and three-zone heat release rate, respectively. These peak heat release rate occur after TDC during the expansion stroke, accounts for the high smoke density level measured in the exhaust gas.

(iii) Injector L3

The measured cylinder pressure and heat release rate curves for injector L3 are shown in Figure 6.14.

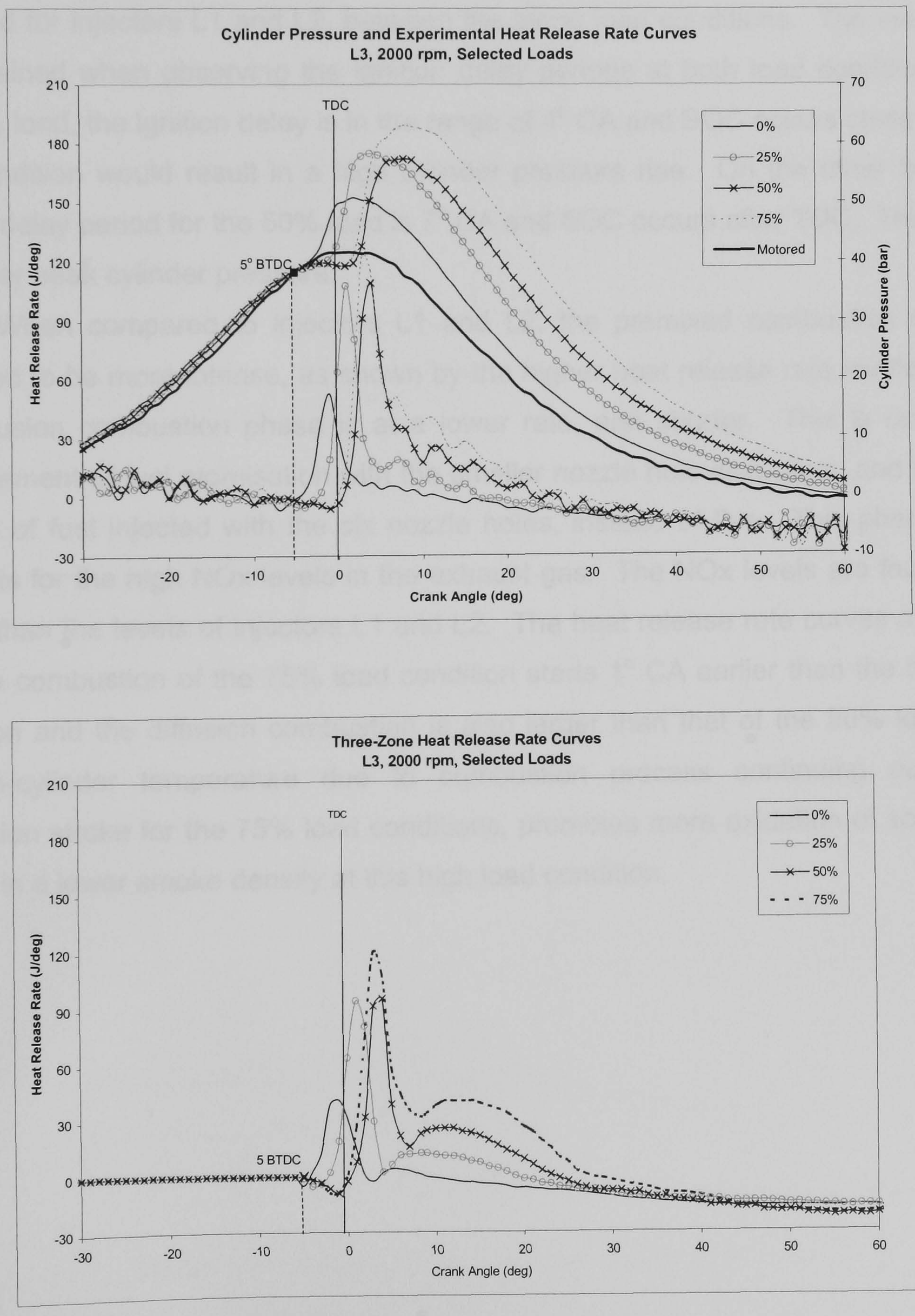

Figure 6.14: Combustion characteristics of injector L3

The ignition delay periods observed with injector L3, as shown in Figure 6.14, are shorter than those for injector L1. The longest delay period of 7° CA, is shown by the 50% engine load while the ignition delay period for the 75% load is 6° CA. The combustion is observed to start close to TDC producing high cylinder pressure. The peak cylinder pressure at 0%, 25%, 50% and 75% are found to be 50.9, 58.3, 57.4 and 63.1 bar respectively. It is also observed that the cylinder pressure at 25% and 50% loads do not exhibit any significant difference in magnitude. This characteristic is also observed for injectors L1 and L2, between the same load conditions. The reason can be explained when observing the ignition delay periods at both load conditions. For the 25% load, the ignition delay is in the range of 4° CA and SOC occurs close to TDC. This condition would result in a high cylinder pressure rise. On the other hand, the ignition delay period for the 50% load is 7° CA and SOC occurs after TDC. This results in a lower peak cylinder pressure.

When compared to injectors L1 and L2, the premixed combustion phase is observed to be more intense, as shown by the higher heat release rate levels. While, the diffusion combustion phase is at a lower rate, and shorter. This is due to the enhancement of fuel atomisation with the smaller nozzle hole diameters, and the large amount of fuel injected with the six nozzle holes, instead of five. This phenomenon accounts for the high NOx levels in the exhaust gas. The NOx levels are found to be higher than the levels of injectors L1 and L2. The heat release rate curves also show that the combustion of the 75% load condition starts 1° CA earlier than the 50% load condition and the diffusion combustion is also larger than that of the 50% load. The high in-cylinder temperature due to combustion process continuing during the expansion stroke for the 75% load conditions, promotes more oxidation of soot, which results in a lower smoke density at this high load condition.

(iv) Injector L4

The combustion characteristics for injector L4 are shown in Figure 6.15.

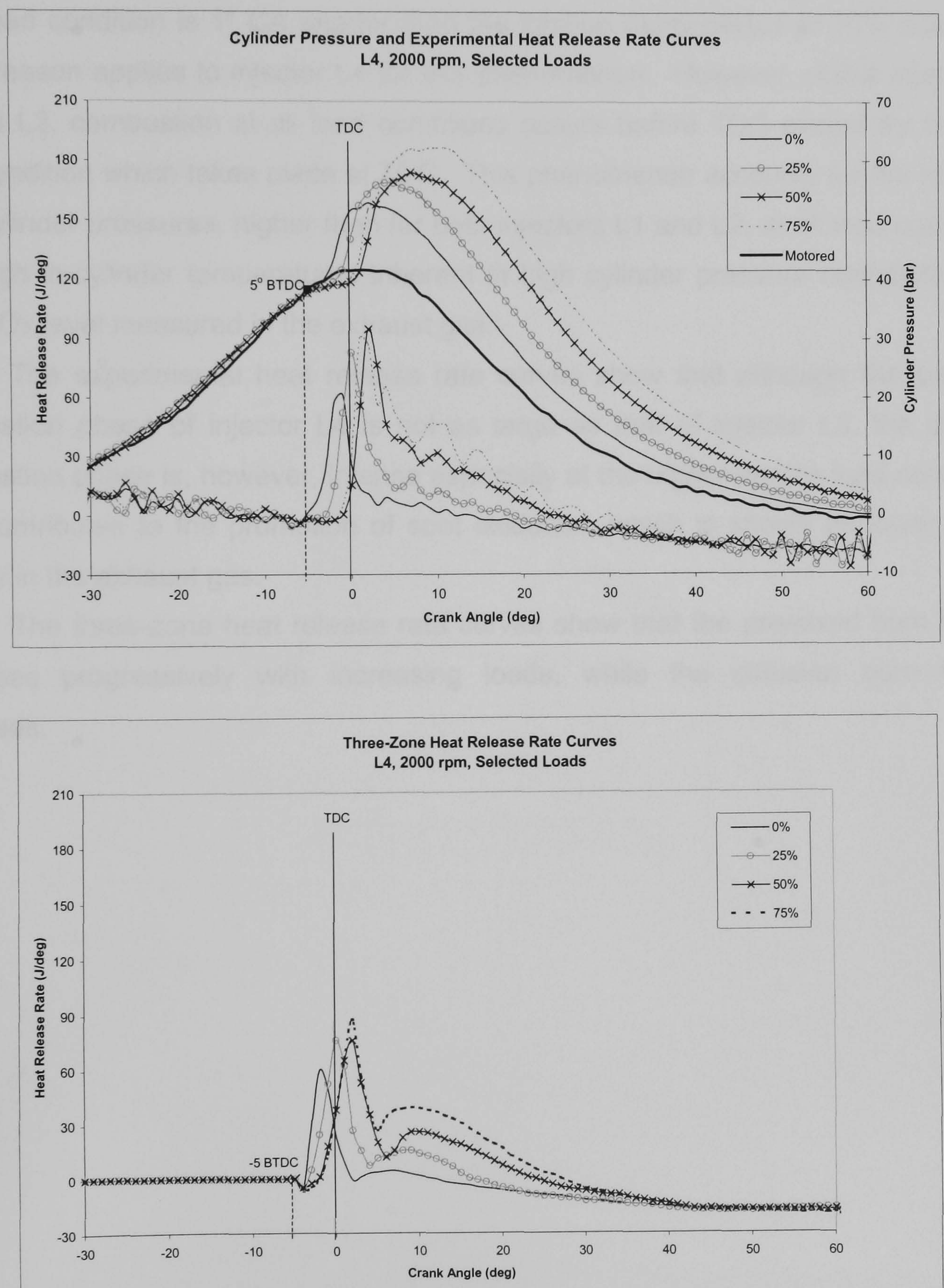

Figure 6.15: Combustion characteristics of injector L4

Injector L4 exhibits the shortest ignition delay periods at all engine load conditions as shown in Figure 6.15. In general, the peak cylinder pressure and peak heat release rates for injector L4 are lower than those of injectors L1, L2 and L3. Since injector L4 has the smallest nozzle hole diameter of 0.171 mm, the observed trends are expected. Similar to the trend observed in injector L3, the ignition delay period of the 75% load condition is 1° CA shorter than the ignition delay period at 50% load. The same reason applies to injector L4 for this phenomenon. However, unlike injector L1, L2 and L3, combustion at all load conditions occurs before TDC except for the 50% load condition which takes place at TDC. This phenomenon accounts for the relatively high cylinder pressures, higher than for both injectors L1 and L2, at all load conditions. The high in-cylinder temperatures inherent in high cylinder pressure contribute to the high NOx level measured in the exhaust gas.

The experimental heat release rate curves show that although the premixed combustion phase of injector L4 is not as large as that of injector L3, the diffusion combustion phase is, however, intense especially at the higher engine load conditions. This contributes to the promotion of soot oxidation, which is shown as lower smoke density in the exhaust gas.

The three-zone heat release rate curves show that the premixed burn fraction deceases progressively with increasing loads, while the diffusion burn fraction increases.

(b) Effects of different injectors on cylinder pressure and heat release rate.

The effects of nozzle hole diameter and number of holes on the cylinder pressure and heat release rate at different engine loads are shown in Figure 6.16 to 6.19. The information provided by these curves at the engine speed of 2000 rpm is then used to explain the formation of emissions in the exhaust gas. The combustion characteristics at 0% engine load for all the injectors are shown in Figure 6.16.

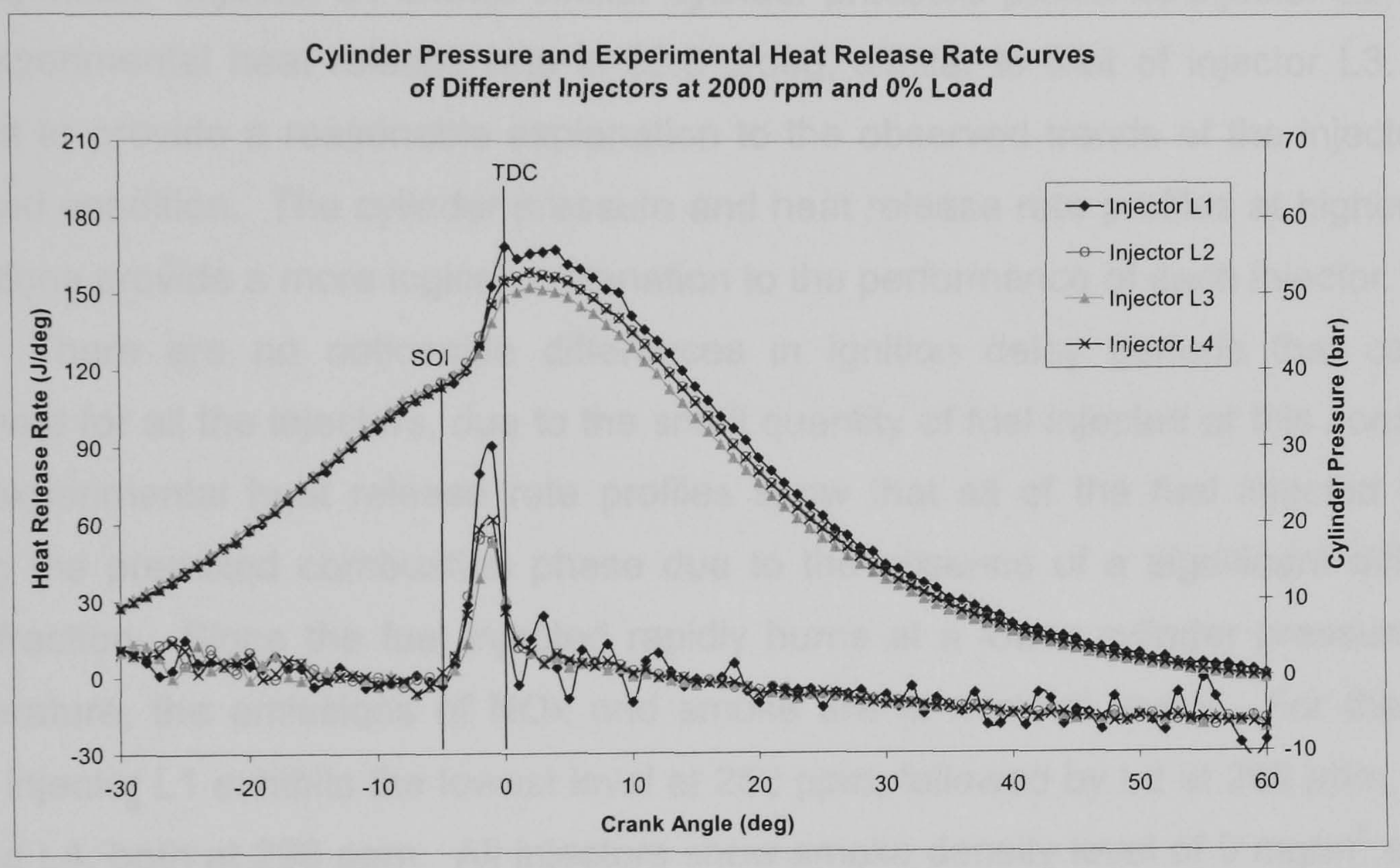

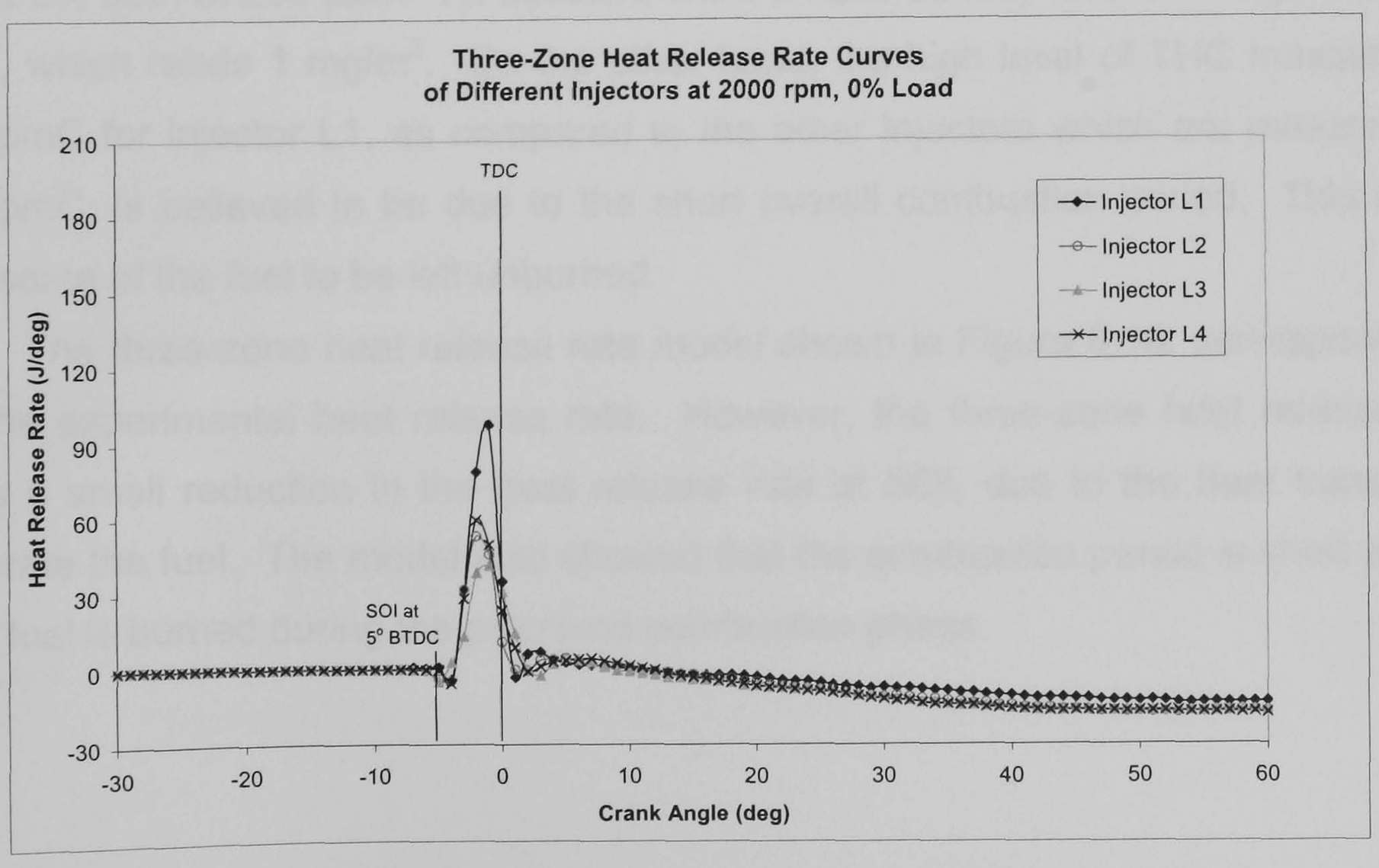

Figure 6.16: Combustion characteristics at 0% engine load

The compression cylinder pressures before SOI, shown in Figure 6.16, for all four injectors are found to be similar. Injector L1 shows the highest peak cylinder pressure of 56.8 bar and peak experimental heat release rate of 97.9 J/deg. This is believed to be due to the fuel spray penetration occurring earlier, caused by the lower NOP of injector L1. For injector L2, which has the largest nozzle hole diameter of 0.225 mm, the cylinder pressure and experimental heat release rate curves at 0% load condition are lower than that of injector L1. Injector L3 exhibits the lowest peak cylinder pressure of 50.9 bar and peak experimental heat release rate of 52.8 J/deg at this condition. Injector L4 shows similar cylinder pressure profile as injector L2, while the experimental heat release rate is 52.8 J/deg, similar to that of injector L3. It is difficult to provide a reasonable explanation to the observed trends of the injectors at 0% load condition. The cylinder pressure and heat release rate profiles at higher load conditions provide a more logical explanation to the performance of each injector.

There are no noticeable differences in ignition delay periods that can be observed for all the injectors, due to the small quantity of fuel injected at this condition. The experimental heat release rate profiles show that all of the fuel injected burns during the premixed combustion phase due to the absence of a significant diffusion burn fraction. Since the fuel injected rapidly burns at a lower cylinder pressure and temperature, the emissions of NOx and smoke are at minimal levels. For the NOx level, injector L1 exhibits the lowest level at 250 ppm, followed by L2 at 269 ppm, while L3 and L4, both at 296 ppm. All injectors show smoke density level of 0 mg/m^3 except for L2, which reads 1 mg/m^3. On the other hand, the high level of THC measured at 268 ppmC for injector L1, as compared to the other injectors which are measured at 203 ppmC, is believed to be due to the short overall combustion period. This would allow some of the fuel to be left unburned.

The three-zone heat release rate model shown in Figure 6.16, correspond well with the experimental heat release rate. However, the three-zone heat release rate shows a small reduction in the heat release rate at SOI, due to the heat transfer to evaporate the fuel. The model also showed that the combustion period is short and all of the fuel is burned during the premixed combustion phase.

The combustion characteristics at 25% load for the four injectors are shown in Figure 6.17.

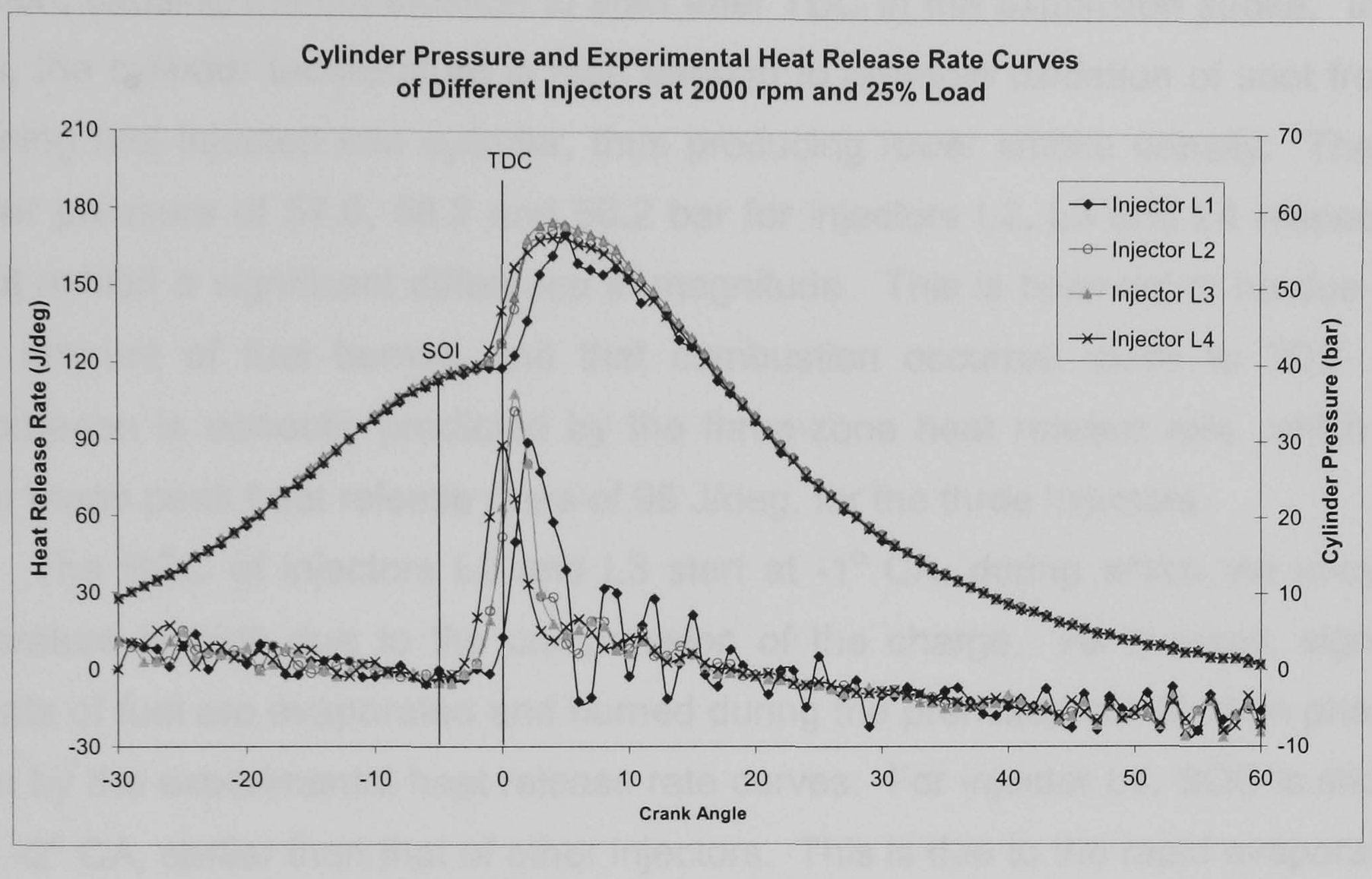

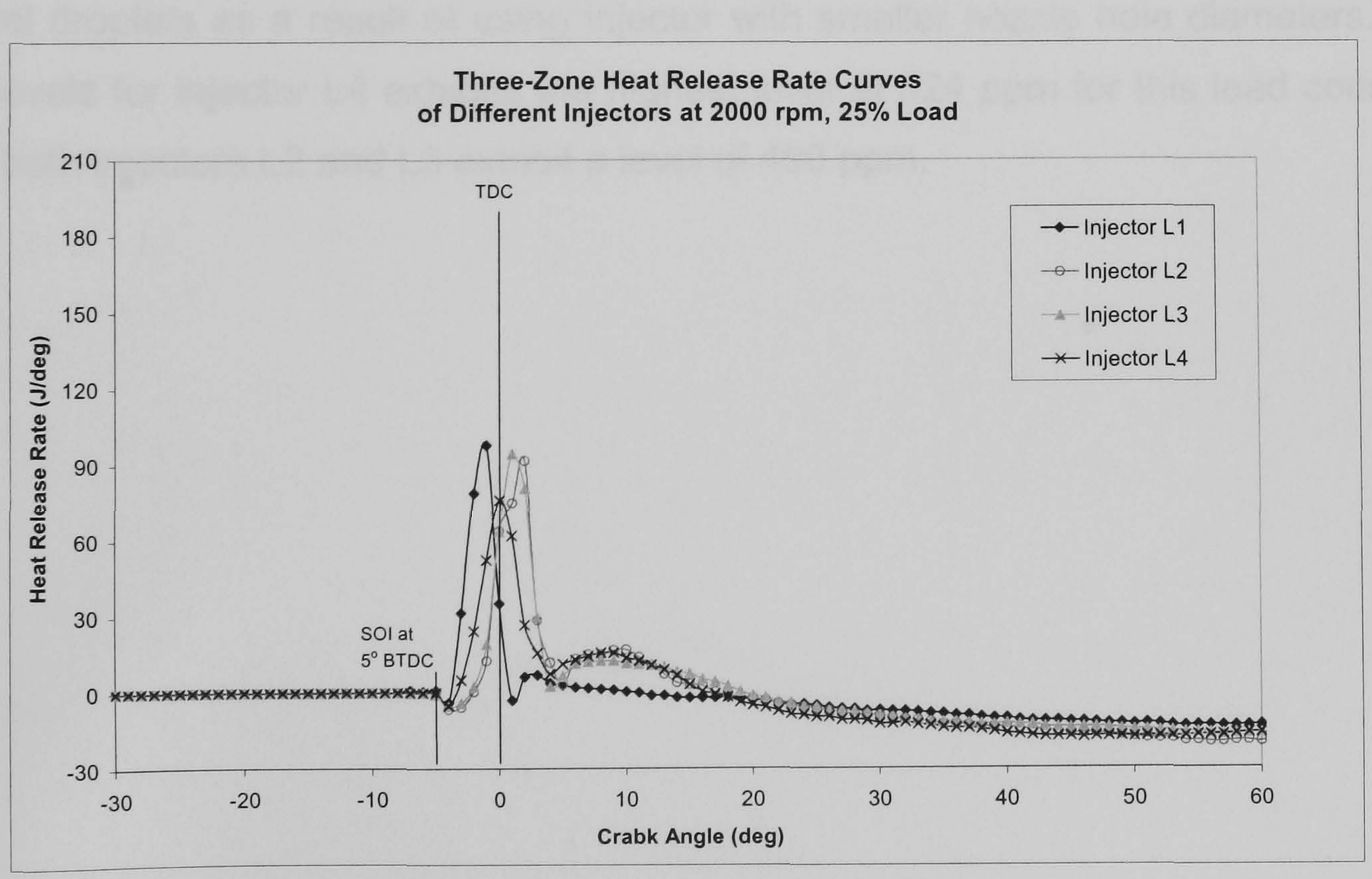

Figure 6.17: Combustion characteristics at 25% engine load

The peak cylinder pressure and the experimental heat release rate for injector L1, shown in Figure 6.17, are found to be lower than injectors L2 and L3. This can be explained by the long ignition delay period experienced by injector L1 at this load condition, causing the combustion to start after TDC in the expansion stroke. In spite of this, the cylinder temperature is high enough to promote oxidation of soot from the remaining fuel injected into cylinder, thus producing lower smoke density. The peak cylinder pressure of 57.8, 58.2 and 56.2 bar for injectors L2, L3 and L4 respectively, did not exhibit a significant difference in magnitude. This is believed to be due to the same amount of fuel burned and that combustion occurred close to TDC. This phenomenon is correctly predicted by the three-zone heat release rate, which show similar mean peak heat release rates of 95 J/deg, for the three injectors.

The SOC of injectors L2 and L3 start at -1° CA, during which the in-cylinder temperature is high due to the compression of the charge. As a result, significant amounts of fuel are evaporated and burned during the premixed combustion phase, as shown by the experimental heat release rate curves. For injector L4, SOC is shown to be at -2° CA, earlier than that of other injectors. This is due to the rapid evaporation of the fuel droplets as a result of using injector with smaller nozzle hole diameters. The NOx levels for injector L4 exhibits the highest level at 524 ppm for this load condition, while both injectors L2 and L3 exhibit a level of 490 ppm.

The combustion characteristics at 50% load for the four injectors are shown in Figure 6.18.

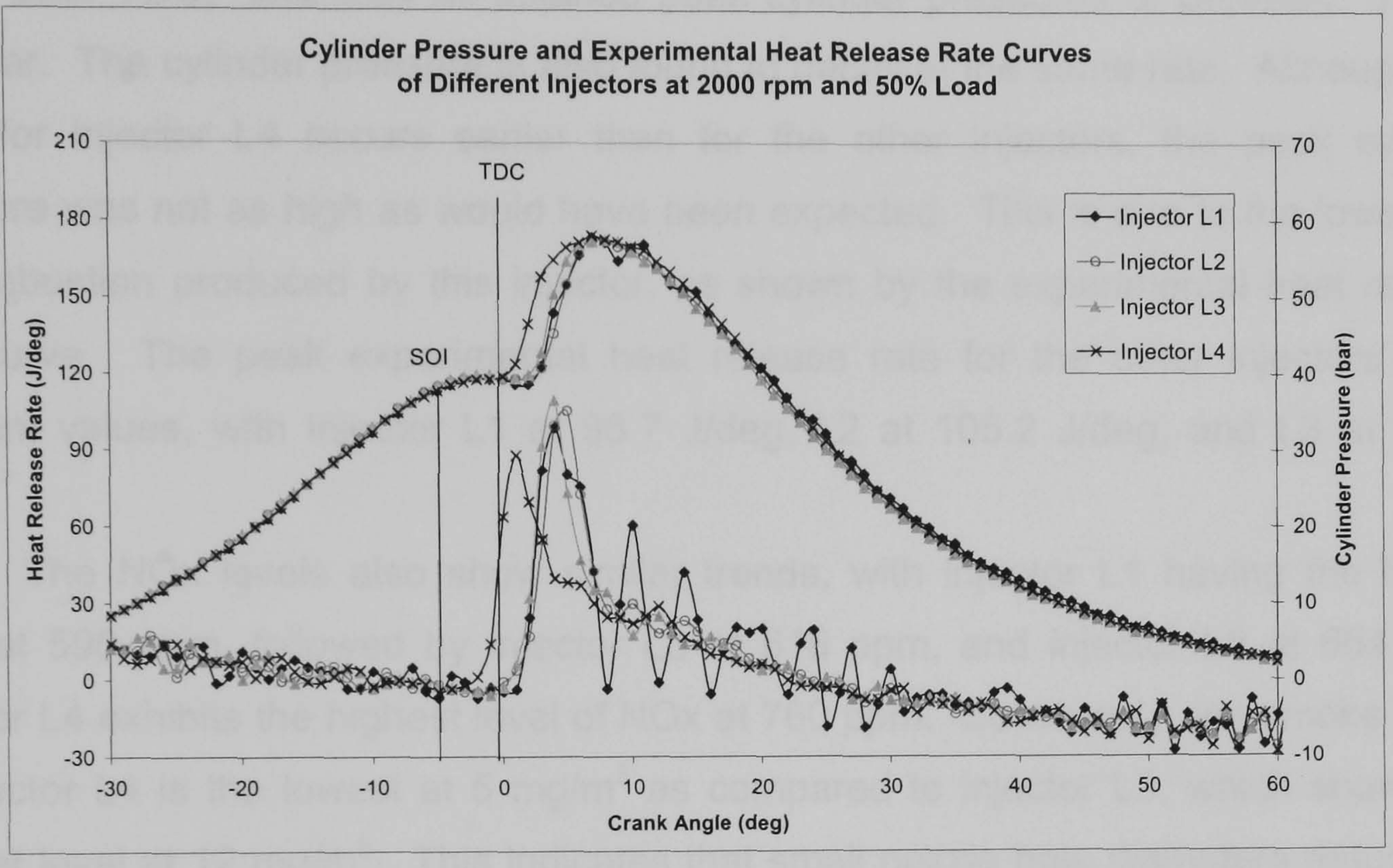

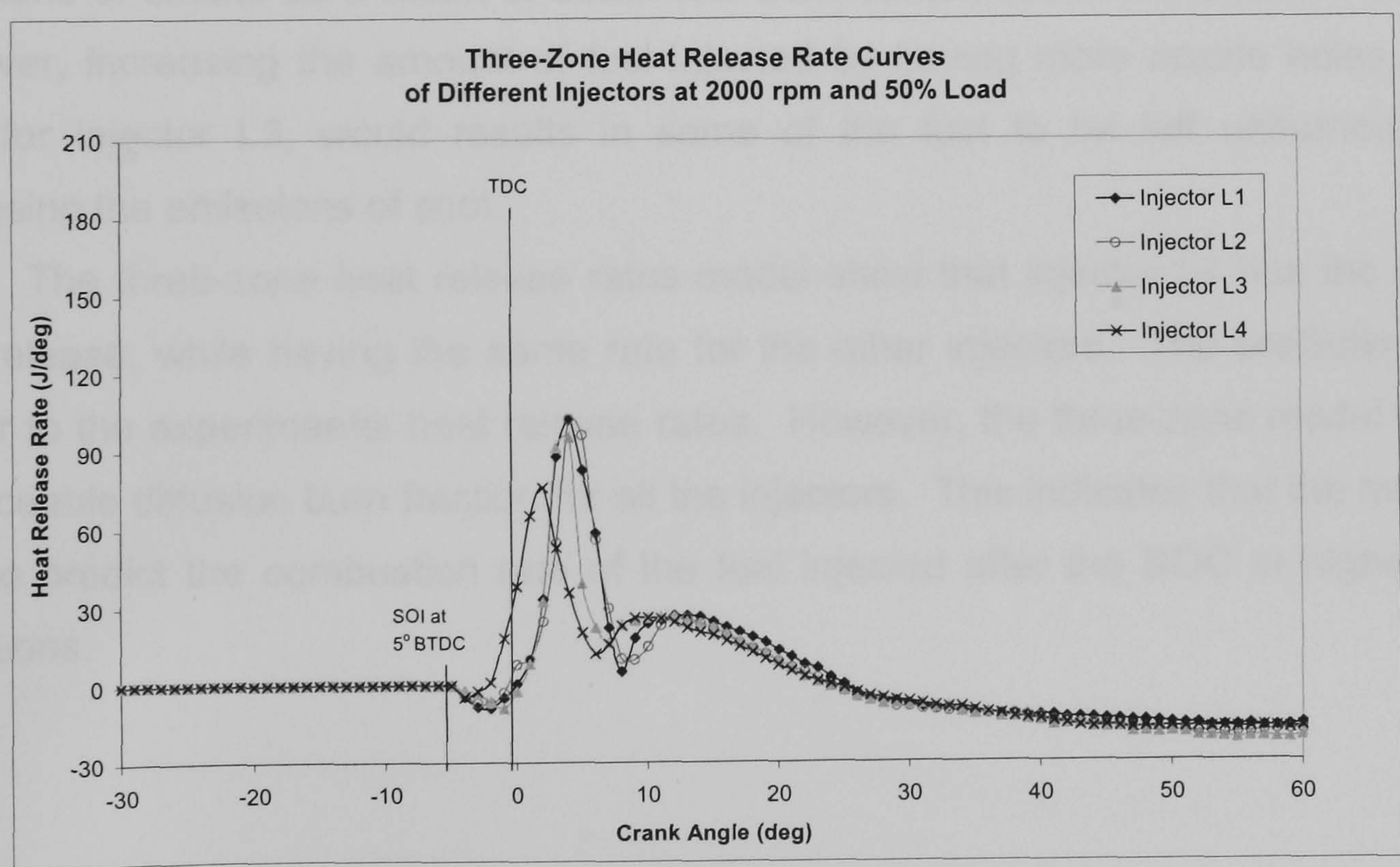

Figure 6.18: Combustion characteristics at 50% engine load

For the 50% load condition, injectors L1, L2 and L3 exhibit similar ignition delay periods of 7° CA, while injector L4, exhibits a shorter ignition delay period of 5° CA. The peak cylinder pressure for all four injectors is found to occur at the same instant, 7° CA after TDC, and they all attained peak cylinder pressures of between 57.8 to 58.0 bar. The cylinder pressure is also found to decay at the same rate. Although, the SOC for injector L4 occurs earlier than for the other injectors, the peak cylinder pressure was not as high as would have been expected. This is due to the lower rate of combustion produced by this injector, as shown by the experimental heat release rate curve. The peak experimental heat release rate for the other injectors show different values, with injector L1 at 98.7 J/deg, L2 at 105.2 J/deg, and L3 at 109.4 J/deg.

The NOx levels also show similar trends, with injector L1 having the lowest level at 590 ppm, followed by injector L3 at 618 ppm, and injector L2 at 664 ppm. Injector L4 exhibits the highest level of NOx at 760 ppm. Conversely, the smoke levels of injector L4 is the lowest at 5 mg/m^3 as compared to injector L3, which shows the highest level at 12 mg/m^3. This indicates that small nozzle hole diameters reduce the emissions of smoke as a result of better fuel atomisation, but at the expense of NOx. However, increasing the amount of fuel injected by having more nozzle holes, as in case for injector L3, would results in some of the fuel to be left unburned, thus increasing the emissions of soot.

The three-zone heat release rates model show that injector L4 has the lowest heat release, while having the same rate for the other injectors. The predictions are similar to the experimental heat release rates. However, the three-zone model shows a noticeable diffusion burn fraction for all the injectors. This indicates that the model is able to predict the combustion rate of the fuel injected after the SOC at higher load conditions.

The combustion characteristics at 75% load for the four injectors are shown in Figure 6.19.

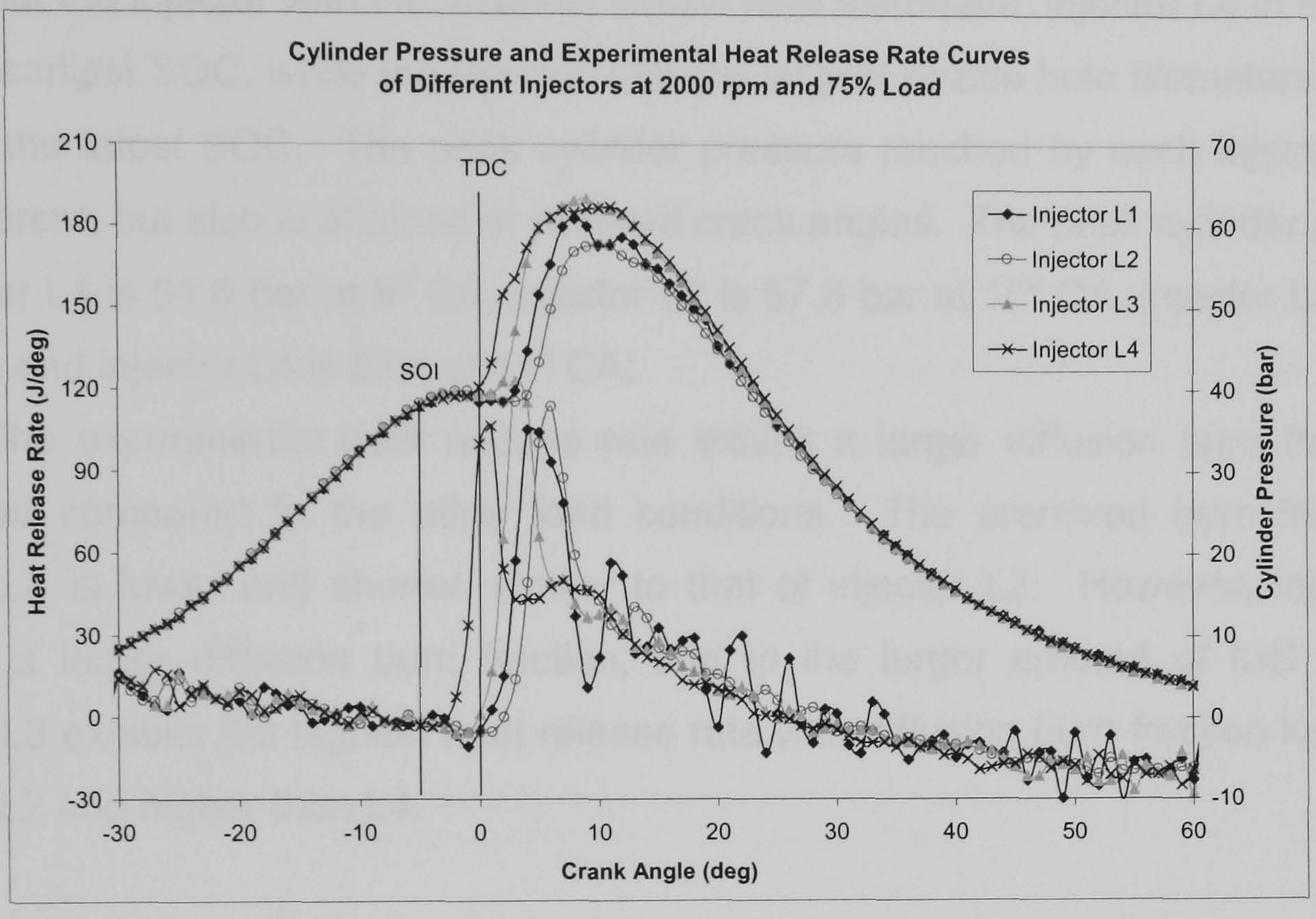

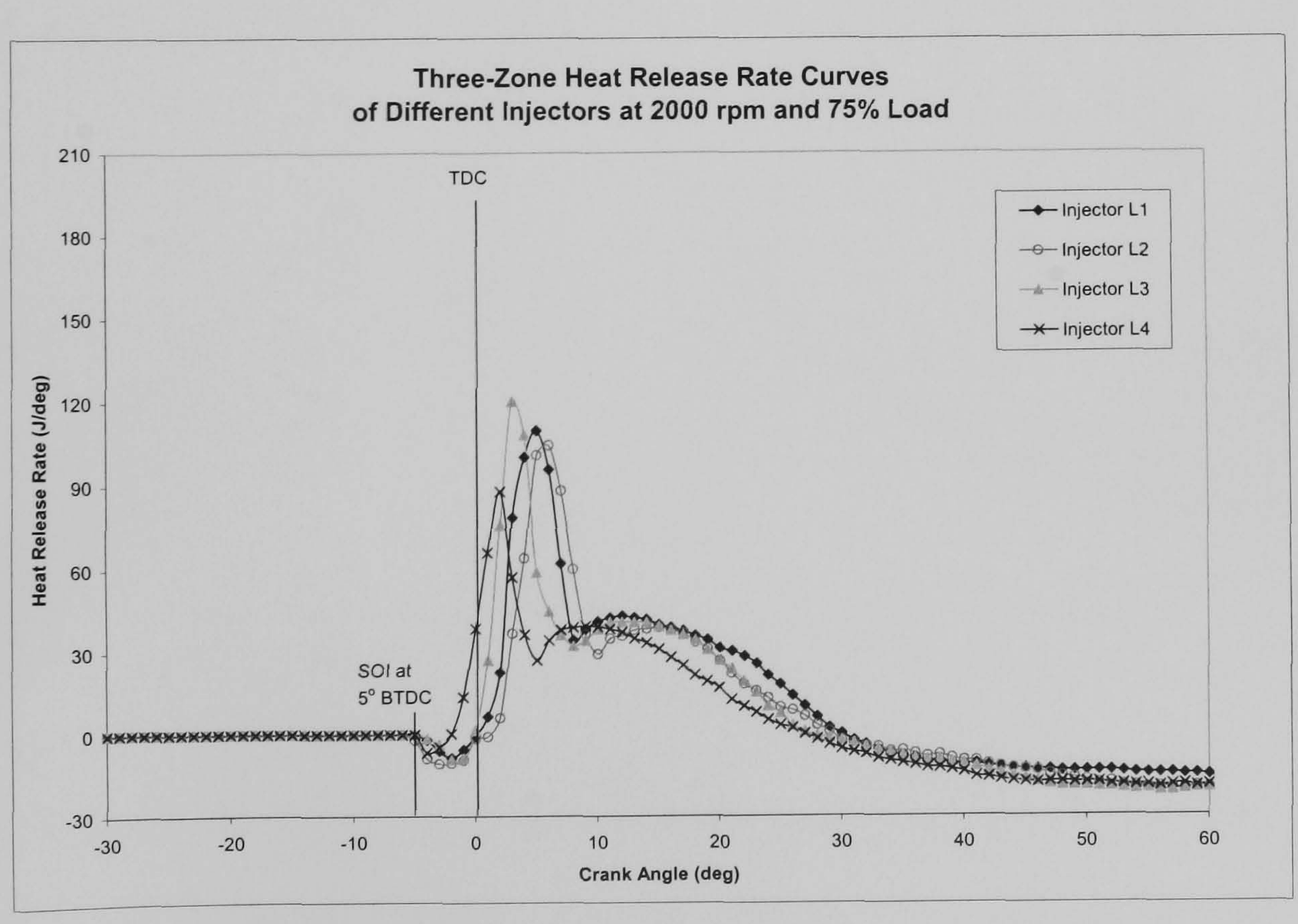

Figure 6.19: Combustion characteristics at 75% engine load

From the cylinder pressure curves shown in Figure 6.19, all the injectors exhibit different ignition delay periods. Injector L1 has an ignition delay period of 8° CA, injector L2 at 9° CA, injector L3 at 7° CA and injector L4 at 5° CA. This observation shows that the injector with the smallest nozzle hole diameters, injector L4 in this case, has the earliest SOC, while the injector with the largest nozzle hole diameters, injector L2, has the latest SOC. The peak cylinder pressure reached by each injector is not only different, but also is attained at different crank angles. The peak cylinder pressure of injector L1 is 61.6 bar at 8° CA, injector L2 is 57.8 bar at 10° CA, injector L3 is 63.4 at 9° CA and injector L4 is 62.4 at 11° CA.

The experimental heat release rate exhibit a larger diffusion burn fraction at 75% load compared to the other load conditions. The premixed burn fraction of injector L4 is lower and shorter, similar to that of injector L2. However, injector L2 exhibits a larger diffusion burn fraction, due to the larger amount of fuel injected. Injector L3 exhibits the highest heat release rate with diffusion burn fraction lower than injector L2 and higher than L4.

(c) Effects of engine speeds on cylinder pressure and heat release rate.

For comparisons between different engine speeds, Figure 6.20 shows the combustion characteristics for injector L1. It is observed that as engine speed increases at the same load conditions, the ignition delay period becomes longer and the cylinder peak pressure is lower. Similar trends are also observed with the other injectors. The NOx emissions show lower levels as engine speed increases for all injectors. The smoke density at low load conditions for all injectors show no change in emission levels at both engine speeds. However, at higher loads, injector L1 and L3 exhibit an increase in the smoke levels as engine speed increases, while for injectors L2 and L4, the levels remain the same. The THC for all injector increases at higher engine speeds.

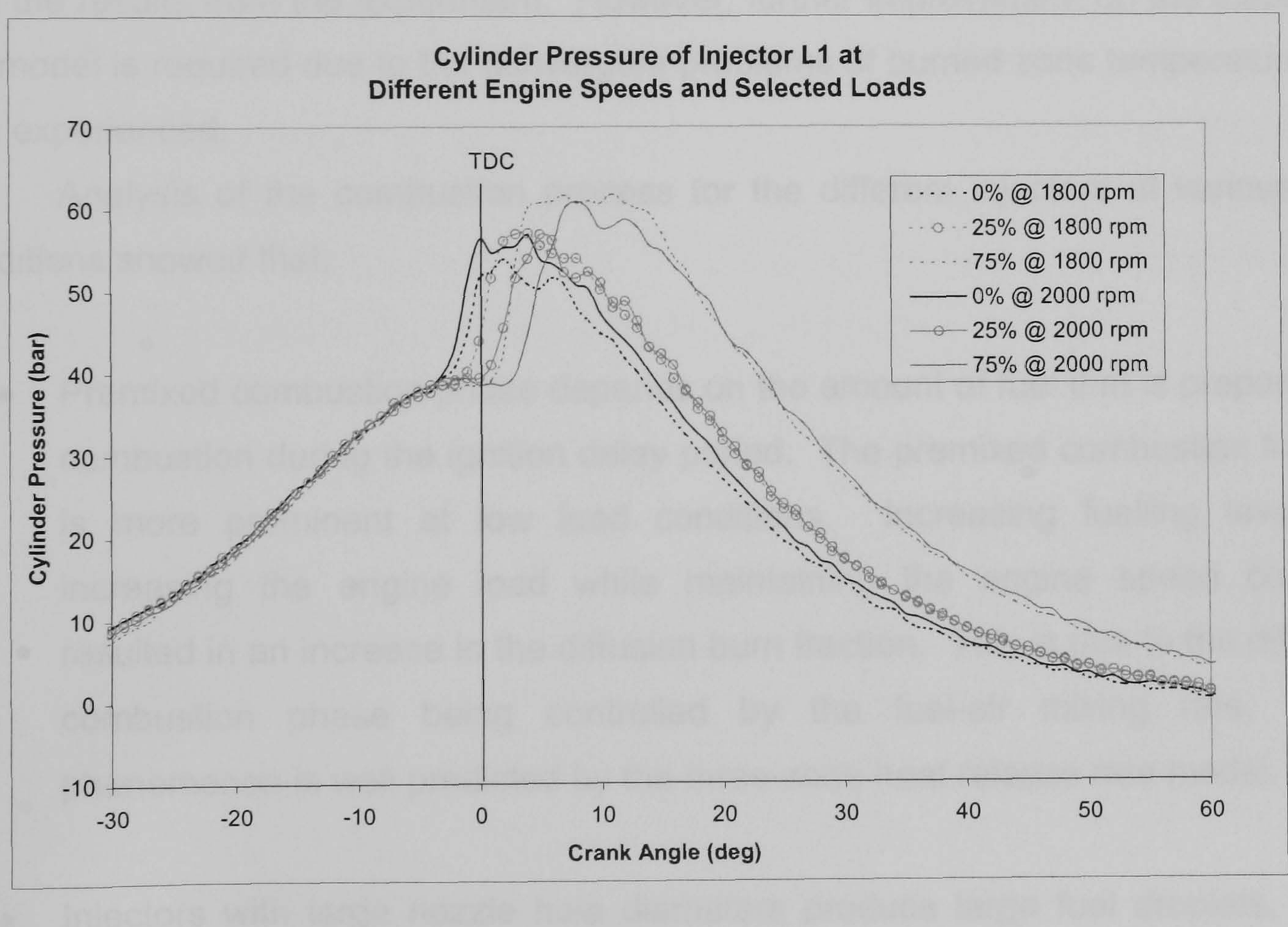

Figure 6.20: Effects of changing engine speeds on cylinder pressure

6.4 SUMMARY

The results generated from the implementation of the three-zone model to calculate the heat release rate were presented in this chapter. The model used the experimental in-cylinder pressure data and the fuel injection rate data as inputs to the program. In addition to the heat release rate, the model is also able to predict the bulk temperatures for each zone of the model.

Engine performance investigations using four injectors having different nozzle hole diameters were performed. Parameters such as in-cylinder pressure histories and exhaust gas emissions were measured and used to describe the combustion processes when using the different injectors.

The experimental heat release rate profiles were compared with the three-zone heat release rate model. The results showed that the model exhibits close correlation with the results from the experiment. However, further improvement on the stability of the model is required due to the convergent problems of burned zone temperature that was experienced.

Analysis of the combustion process for the different injectors at various load conditions showed that;

- Premixed combustion phase depends on the amount of fuel that is prepared for combustion during the ignition delay period. The premixed combustion fraction is more prominent at low load conditions. Increasing fuelling levels by increasing the engine load while maintaining the engine speed constant resulted in an increase in the diffusion burn fraction. This is due to the diffusion combustion phase being controlled by the fuel-air mixing rate. This phenomenon is well predicted by the three-zone heat release rate model.

- Injectors with large nozzle hole diameters produce large fuel droplets, which would decrease the fuel evaporation rate. This leads to a later and less homogeneous combustion. The locally high fuel concentration becomes an additional source of soot due to limitation for the soot oxidation. This condition is worsened at higher engine loads since the formation rate of soot is higher than the oxidation rate. The NOx emission is also relatively high due to the large amount of fuel injected during the ignition delay periods.

- Injectors with small nozzle hole diameters cause the combustion to start early, i.e. before TDC or at TDC. This is due to the enhancement of fuel atomisation and higher rate of fuel evaporation as a result of smaller fuel droplets. Subsequently, the in-cylinder pressure and temperature increase causing high levels of NOx emissions. On the other hand, soot oxidation is enhanced, resulting in lower smoke density levels in the exhaust gas emission.

- Injectors with small nozzle hole diameters which increase the fuel flow rate by adding more nozzle holes have the advantage of better fuel atomisation. At the same time, air utilisation is increased due to improved distribution of fuel in the combustion chamber. However, this increases the rate of soot formation during the early combustion phase but the soot oxidation is reduced in later combustion phases due to the richer fuel-mix mixture. As a results, both NOx and smoke levels increase.

- The concentration of THC for all injectors did not change significantly for all load conditions and both engine speeds. However, there is a small increase in THC at the higher engine speed. This gives an indication that the combustion occurs at a relatively constant overall equivalent ratio.

CHAPTER 7: CONCLUSIONS AND RECOMMENDATIONS FOR FUTURE WORK

7.1 SUMMARY OF CONCLUSIONS

The research work presented in this thesis involves the experimental investigation of four different injectors having various nozzle holes diameters and number of holes on the performance of a diesel engine. The research also includes a thermodynamic computational study of the heat release rate of combustion. The aim of the present research was to determine the effects of varying injection parameters on the fuel structure, combustion characteristics and the formation of pollutants in a diesel engine

In order to understand the relationship between fuel injection and the exhaust gas emissions of a diesel engine, the characteristics of the fuel injected from the various injectors had to be determined. These investigations include the imaging of the fuel sprays exiting from the injector nozzles into a constant volume spray chamber with a CCD camera using a back-lit technique and measurements of the fuel injection pressure at the nozzle using the Bosch Tube meter to determine the fuel injection rates.

Four different Lucas-Delphi diesel injectors were used in the investigations. The first injector, L1, had five nozzle holes, each with a diameter of 0.194mm, and the second injector, L2, also had five nozzle holes with larger nozzle hole diameters of 0.225mm. The third injector, L3, despite having smaller nozzle holes of 0.177mm each, had an additional hole so that the total flow area of injector L3 was the same as that of injector L1. The forth injector, L4, had five nozzle holes with the smallest hole diameters of 0.171mm.

Engine experiments were performed using a production Lister Petter 2.29 litres, four-cylinder, high-speed, direct injection diesel engine. The operating conditions were varied from 0% load to 75% load in steps of 25%, at two fixed engine speeds of 1800 rpm and 2000 rpm. Measurements of NOx, CO, CO_2 and THC emissions were obtained using the Horiba MEXA-7100 HEGR exhaust gas analyser system while the smoke density readings were obtained from the AVL-415 smoke meter.

The overall results showed that atomisation characteristics of fuel spray were influenced not only by the injection pressure but also by the geometric parameters in the nozzle hole and the injection rate. The spatial distribution of the fuel spray inside the combustion chamber was influenced by the fuel flow through the nozzle orifice and this was governed by the nozzle geometry. In addition, variations in spray injection rates due to differences in injector performance have an effect on the thermal loads of the combustion chamber and subsequently affect the formation of pollutant and specific fuel consumption. The results obtained from the current research has shown close agreement with the results obtained from other researches such as Zhang (Zhang et al., 1993, 1998), Baritaud (Baritaud et al., 1994), Greeves and Tullis (Greeves and Tullis, 1993), Arcoumanis (Arcoumanis et al., 1994), and Larsson (Larsson, 1999).

The results also showed that, for the injector with the largest nozzle hole diameters, i.e. injector L2, the spray penetration length was found to be longer with a reduction in the spray cone angle. The injection rates of this injector were high at all load conditions. These account for the high smoke levels measured in the exhaust gas especially at high load conditions. Reducing the size of the nozzle holes, i.e. injector L4, produced a shorter spray penetration length with an increase in the spray cone angle. The injection rates of smaller nozzle hole diameters were observed to be high at low load conditions but low at high load conditions. The emissions results from using these injectors, compared to the other injectors, showed that the NOx levels were highest while the smoke levels were the lowest. This is due to the improved fuel atomisation, which enhanced the fuel evaporation rate, causing high combustion rates during the initial combustion phase. On the other hand, reducing the nozzle diameter while maintaining the same total flow area, i.e. injector L3, had negligible effect on the spray penetration length but increased the spray cone angle. The emission results showed that this injector improved fuel atomisation and at the same time, air utilisation was increased due to improved distribution of fuel in the combustion chamber. This increased the rate of soot formation during the early combustion phase but the soot oxidation is reduced in later combustion phases due to the richer fuel-mix mixture. As a result, both NOx and smoke levels increase.

The cause and effect relationships implicit in the experimental results are often difficult to interpret. The application of modelling and simulation approaches, although less precise in predicting the outcome of a specific test, can effectively isolate one variable at a time and point out trends and causes. A computer programme to

determine the heat release rate of combustion was developed and implemented using Matlab. The mathematical model was based on a three-zone model, initially developed by Timoney et al. (Timoney et al., 2000). The current model made use of the experimentally obtained cylinder pressure and the fuel injection rate data as inputs into the model. The model was able to calculate the bulk temperatures in the unburned, burned and fuel zones.

The results from the heat release rate profiles generated by the model showed that a longer delay and a larger premixed burn caused a rapid cylinder pressure rise. Injectors with large nozzle hole diameters would lead to a later and less homogeneous combustion. The locally high fuel concentrations become an additional source of soot due to limited soot oxidation in the later stages of combustion. This condition was worsened at higher engine loads since the formation rate of soot was higher than the oxidation rate. The NOx emission was also relatively high due to the large amount of fuel injected during the ignition delay periods. Injectors with small nozzle hole diameters produce shorter ignition delay periods, causing combustion to start before TDC or at TDC. This was due to the enhancement of fuel atomisation and a higher rate of fuel evaporation as a result of smaller fuel droplets. Subsequently, the in-cylinder pressure and temperature increased, producing high levels of NOx emissions. On the other hand, soot oxidation was enhanced, resulting in lower smoke density levels in the exhaust gas emission. Injectors with small nozzle hole diameters which increase the fuel flow rate by adding more nozzle holes have the advantage of better fuel atomisation. At the same time, air utilisation was increased due to improved distribution of fuel in the combustion chamber. However, this increased the rate of soot formation during the early combustion phase but the soot oxidation was reduced in later combustion phases due to the richer fuel-mix mixture. As a result, both NOx and smoke levels increased.

Over all, this research has made a contribution to the understanding of the injection parameters on the combustion processes of a production high-speed diesel engine. The originality of the research work lies in the ability to consolidate the fuel spray characteristics results with the fuel rate of injection results of the various injectors in proving the observed trends in the direct injection diesel engine pollutant formation. This is further augmented by the capability of the three-zone model in using the in-cylinder pressure histories and injection rate data to validate the results obtained from the experimental work.

Although the present diagnostic methodology does not allow a comprehensive understanding of all the relevant features of combustion, useful information could be gathered to assist in the selection and improvement of diesel injectors, and further development of a more sophisticated combustion model. In is to the author believes that optimisation of the injection parameter, i.e. retarding the injection timing for injector L4 would prove that injector L4 could provide better performance, in terms of reducing both the NOx and smoke formation for this particular engine, as oppose to the standard injector L1.

7.2 RECOMMENDATIONS FOR FUTURE WORK

The research facilities shortly available in the department offer significant research potential in the future. The spray imaging investigation presented in this thesis only covers the liquid phase penetration and dispersion. It is thus recommended to extend the investigation to include the investigation of the fuel spray behaviour in the vapour phase using laser induced fluorescent imaging techniques. This would enable a more quantitative analysis of the fuel spray evaporation characteristics.

Injection rate measurement would be indispensable, not only in the development of high pressure injection and pilot injection, but also in the detection of irregular injection. The injection rate measurement performed in this research was obtained to represent the injection characteristics of each injector. Further research to investigate the variation of injections such as the fuel delivery quantity per stroke and injection rate uniformity from stroke-to-stroke and their effects on the engine performance should be assessed.

The current research employed the measurement of the exhaust gas emissions technique as a means to assess the influence of the injection parameters on the engine performance. However, this technique does not directly provide insights into the mechanisms leading to the formation of soot and NOx. Optical diagnostic techniques offer a better means for in-cylinder viewing of combustion phenomenon and for radiation measurements. Preliminary work to provide an optical access into the combustion chamber of the current research engine using an endoscopic system has

been carried out by the author. Due to time constraints and operation limitations imposed by the current research engine at the time, the optical research was proposed for future engine development research. The details of the work are provided in Appendix VI.

As for the three-zone heat release rate model, it is recommended to extent the computation scheme to incorporate the determination NO by inclusions of species dissociation calculations and the Zeldovich mechanism.

REFERENCES

1. Afzal, H., Arcoumanis, C., Gavaises, M. and Kampanis, N. (1999). *Internal Flow in Diesel Injector Nozzles: Modelling and Experiments*. Seminar on Fuel Injection System, London, Proceedings of the IMechE.

2. Ahmadi-Befrui, B., Wiesler, B. and Winklhofer, E. (1991). *The Propagation of Fuel Sprays in a Research Diesel Engine - A Joint Numerical and Experimental Analysis*. SAE 910181.

3. Annand, W. J. D. (1963). *Heat Transfer in the Cylinders of Reciprocating Internal Combustion Engines.* Proceedings of the IMechE, Vol. 177, (No. 36), pp. 973-996.

4. Araneo, L., Coghe, A., Brunello, G. and Cossali, G. E. (1999). *Experimental Investigation of Gas Density Effects on Diesel Spray Penetration and Entrainment*. SAE 1999-01-0525.

5. Arcoumanis, C., Bae, C., Nagwaney, A. and Whitelaw, J. H. (1995a). *Effect of EGR on Combustion Development in a 1.9L DI Diesel Optical Engine*. SAE 950850.

6. Arcoumanis, C., Baniasad, M. S. and Gibbins, J. R. (1992). *Measurement and Analysis of Injection Rate Variations in Diesel Engines*. Diesel Fuel Injection Systems. Mechanical Engineering Publication, pp. 17-21.

7. Arcoumanis, C., Cho, S. T. and Whitelaw, D. S. (1998). *The Effects of EGR and Supercharging on Fuel Sprays, Combustion and Emissions in a HSDI Diesel Engine*. IMechE C554/023/98.

8. Arcoumanis, C., Flora, H., Gavaises, M. and Badami, M. (2000). *Cavitation in Real-Size Multi-Hole Diesel Injector Nozzles*. SAE 2000-01-1249.

9. Arcoumanis, C., Flora, H., Gavaises, M., Kampanis, N. and Horrocks, R. (1999). *Investigation of Cavitation in a Vertical Multi-Hole Injector.* SAE 1999-01-0524.

10. Arcoumanis, C., Gavaises, M. and French, B. (1997). *Effect of Fuel Injection Processes on the Structure of Diesel Sprays*. SAE 970799.

11. Arcoumanis, C., Hu, Z. and Nagwaney, A. (1994). *Spray and Combustion Visualisation in Direct-Injection Diesel Engines*. Measurement and Observation Analysis of Combustion in Engines. IMechE Seminar Paper Publication, pp. 1-16.

12. Arcoumanis, C., Nagwaney, A., Hentschel, W. and Ropke, S. (1995b). *Effect of EGR on Spray Development, Combustion and Emissions in a 1.9L Direct-Injection Diesel Engine*. SAE 952356.

13. Arnold, M. L., Espey, C., Litzinger, T. A., Santavicca, D. A. and Santoro, R. J. (1990). *A Study of Non-Swirling and Swirling and Their Effects on Spray Flow Fields and Combustion in an Optically-Accessible, DI Diesel Engine*. SAE 900396.

14. Ashley, C., Kordesch, V., Raffelsberger, P. and Waras, H. (1995). *New Developments in Diesel Injection Systems for Powerful High-Speed DI Diesel Engines*. Diesel Fuel Injection Systems. Mechanical Engineering Publication, pp. 1 - 13.

15. Asou, Y., Fujimoto, H., Senda, J., Tsurutani, K. and Nagae, M. (1992). *Combustion in a Small DI Diesel Engine at Starting*, SAE 920697.

16. AVL-LIST (2000). *AVL 670 Indimaster Operating Instructions*.

17. Baert, R. S. G., Beckman, D. E. and Veen, A. (1999). *Efficient EGR Technology for Future HD Diesel Engine Emission Targets*. SAE 1999-01-0837.

18. Baritaud, T. A., Heinze, T. A. and Le Coz, J. F. (1994). *Spray and Self-Ignition Visualisation in a DI Diesel Engine*. SAE 940681.

19. Bayvel, L. and Orzechowski, Z. (1993). *Liquid Atomization*. Washington, Taylor and Francis.

20. Bazari, Z. and French, B. A. (1993). *Performance and Emissions Trade-Offs for a HSDI Diesel Engine - An Optimization Study*. SAE 930592.

21. Bergwerk, W. (1959). *Flow Pattern in Diesel Nozzle Spray Holes*. Proceedings of IMechE, Vol. 173, (No. 25), pp. 655-660.

22. Bi, X., Yang, M., Han, S. and Ma, Z. (1999). *A Multi-Zone Model for Diesel Spray Combustion*. SAE 1999-01-0916.

23. Boehner, W. and Hummel, K. (1997). *Common Rail Injection System for Commercial Diesel Vehicles*. SAE 970345.

24. Borman, G. L. and Ragland, K. W. (1998). *Combustion Engineering*. London, McGraw-Hill.

25. Bosch, W. (1966). *The Fuel Rate Indicator: A New Measuring Instrument for Display of the Characteristics of Individual Injection*. SAE 660749.

26. Brunt, M. F. J. and Platts, K. C. (1999). *Calculation of Heat Release in Direct Injection Diesel Engines.* SAE 1999-01-0187.

27. Bürgler, L., Herzog, P. L. and Winklhofer, E. (1992). *The Influence of Injection System Parameters on DI Diesel Spray Structure, Spray Ignition and Combustion.* Diesel Fuel Injection Systems. Mechanical Engineering Publication, pp. 75-83.

28. Cavaliere, A., Ragucci, R., D'Alessio, A. and Noviello, C. (1989). *Analysis of Diesel Sprays Through Two-Dimensional Laser Light Scattering*. Twenty-Second Symposium (International) on Combustion. The Combustion Institute, pp. 1973-1981.

29. Challen, B. and Baranecsu, R., Eds. (1999). *Diesel Engine Reference Book*. Oxford, Butterworth-Heinemann.

30. Chang, C. T. and Farrell, P. V. (1997). *A Study on the Effects of Fuel Viscosity and Nozzle Geometry on High Injection Pressure Diesel Spray Characteristics*. SAE 970353.

31. Chaves, H., Knapp, M., Kubitzek, A., Obermeier, F. and Schneider, T. (1995). *Experimental Study of Cavitation in the Nozzle Hole of Diesel Injectors Using Transparent Nozzles*. SAE 950290.

32. Chehroudi, B., Chen, S.-H., Bracco, F. V. and Onuma, Y. (1985). *On the Intact Core of Full-Cone Sprays*. SAE 850126.

33. Chehroudi, B., Sinko, K. M. and Shih, S. (1996). *A Novel Approach for Simultaneous NOx and Smoke Reduction: Interacting-Sprays Injection*. SAE 961678.

34. Chikahisa, T. and Araki, T. (1996). *In-Cylinder Control of Smoke and NOx by High Turbulent Two-Stage Combustion in Diesel Engines*. SAE 962113.

35. Chiu, W. S., Shahed, S. M. and Lyn, W. T. (1976). *A Transient Spray Mixing Model for Diesel Combustion*. SAE 760128.

36. Cho, S. T. (1999). *Spray Development and Combustion in Direct-Injection Diesel Engines*. PhD. Thesis: Department of Mechanical Engineering. Imperial College of Science, Technology and Medicine, University of London, London

37. Coghe, A. (2000). *Fuel Injection in Internal Combustion Engines*. ILASS - Europe 2000, Darmstadt.

38. Coghe, A. and Cossali, G. E. (1994). *Phase Doppler Characterization of a Diesel Spray Injected into a High Density Gas Under Vaporization Regimes*. Seventh International Symposium on Applications of Laser Techniques to Fluid Mechanics, Lisbon, Portugal.

39. Dan, T., Takagishi, S., Senda, J. and Fujimoto, H. (1997a). *Effects of Ambient Gas Properties for Characteristics of Non-Reacting Diesel Fuel Spray*. SAE 970352.

40. Dan, T., Yamamoto, T., Senda, J. and Fujimoto, H. (1997b). *Effect of Nozzle Configurations for Characteristics of Non-Reacting Diesel Fuel Spray*. SAE 970355.

41. Dec, J. E. (1997). *A Conceptual Model of DI Diesel Combustion Based on Laser-Sheet Imaging*, SAE 970873.

42. Dec, J. E. and Espey, C. (1995). *Ignition and Early Soot Formation in a DI Diesel Engine Using Multiple 2-D Imaging Diagnostics*. SAE 950456.

43. Dent, J. C. (1971). *A Basis for the Comparison of Various Experimental Methods for Studying Spray Penetration*. SAE 710571.

44. DiGiorgio, F., Laforgia, D. and Damiani, V. (1995). *Investigation of Drop Size Distribution in the Spray of a Five-Hole, V.C.O. Nozzle at High Feeding Pressure*. SAE 950087.

45. Edwards, C. F., Siebers, D. L. and Hoskin, D. H. (1992). *A Study of the Autoignition Process of a Diesel Spray Via High Speed Visualisation*. SAE 920108.

46. Erlach, H., Chmela, F., Cartellieri, W. and Herzog, P. L. (1995). *Pressure Modulated Injection and Its Effect on Combustion and Emissions of a HD Diesel Engine*. SAE 952059.

47. Espey, C. and Dec, J. E. (1995). *The Effect of TDC Temperature and Density on the Liquid-Phase Fuel Penetration in a DI Diesel Engine*. SAE 952456.

48. ExxonMobil (2001). *Esso Diesel ULS*. Marketing Technical Bulletin, ExxonMobil Fuels Marketing, Issued 16/07/01.

49. Faeth, G. M. (1990). *Structure and Atomization Properties of Dense Turbulent Sprays*. Twenty-Third Symposium (International) on Combustion. The Combustion Institute, pp. 1345-1352.

50. Ferguson, C. R. (1986). *Internal Combustion Engines: Applied Thermosciences*. New York, John Wiley & Sons.

51. Foster, D. E. (1985). *An Overview of Zero-Dimensional Thermodynamic Model for IC Engine Data Analysis*. SAE 852070.

52. Gill, D. W. (2002). *User Instructions - Injection Rate Gauge*, AVL-Graz.

53. Gong, Y. Y., You, L. H. and Liang, X. M. (1992). *An Investigation on Droplet Size Distribution and Evaporation of Diesel Fuel Sprays at High Injection Pressure by Using Laser Diagnostic Technique*. SAE 920090.

54. Greeves, G. and Tullis, S. (1993). *Contribution of EUI-200 and Quiescent Combustion System Towards US 94 Emissions*. SAE 930274.

55. Gülder, Ö. L., Smallwood, G. J. and Snelling, D. R. (1992). *Diesel Spray Structure Investigation by Laser Diffraction and Sheet Illumination*. SAE 920577.

56. Hampson, G. J. and Reitz, R. D. (1998). *Two-Colour Imaging of In-Cylinder Soot Concentration and Temperature in a Heavy-Duty DI Diesel Engine with Comparison to Multidimensional Modelling for Single and Split Injections*. SAE 980524.

57. Hashizume, T., Miyamoto, T., Akagawa, H. and Tsujimura, K. (1998). *Combustion and Emission Characteristics of Mutiple Stage Diesel Combustion*. SAE 980505.

58. Henein, N. A., Lai, M.-C., Singh, I., Wang, D. and Liu, L. (2001). *Emissions Trade-Off and Combustion Characteristics of a High-Speed Direct Injection Diesel Engine*. SAE 2001-01-0197.

59. Hentschel, W. (1996). *Modern Tools for Diesel Combustion Investigation*. Twenty-Sixth Symposium (International) on Combustion. The Combustion Institute, pp. 2503-2515.

60. Hentschel, W., Schindler, K. P. and Haahtela, O. (1994). *European Diesel Research IDEA - Experimental Results from DI Diesel Engine Investigations*. SAE 941954.

61. Herzog, P. L. (1998). *HSDI Diesel Engine Development Towards EURO IV*. Diesel Fuel Injection System. Mechanical Engineering Publication, pp. 21-32.

62. Herzog, P. L., Bürgler, L., Winklhofer, E., Zelenka, P. and Cartellieri, W. (1992). *NOx Reduction Strategies for DI Diesel Engines*. SAE 920470.

63. Heywood, J. B. (1988). *Internal Combustion Engine Fundamentals, International Edition*. Singapore, McGraw-Hill.

64. Hikosaka, N. (1997). *A View of the Future of Automotive Diesel Engines*. SAE 972682.

65. Hiroyasu, H. and Arai, M. (1990). *Structures of Fuel Sprays in Diesel Engines*. SAE 900475.

66. Horiba (2000). *Operating Manual: MEXA 7100 HEGR*.

67. Hottel, H. C. and Broughton, F. P. (1932). *Determination of True Temperature and Total Radiation from Luminous Gas Flames*. Industrial and Engineering Chemistry: Analytical Edition., Vol. 4, (No. 2), pp. 166-175.

68. Hwang, J. W., Kal, H. J., Kim, M. H., Park, J. K., Shenghua, L., Martychenko, A. A. and Chae, J. O. (1999). *Effect of Fuel Injection Rate on Pollutant Emissions in DI Diesel Engine*. SAE 1999-01-0195.

69. Ikegami, M., Nakatani, K., Tanaka, S. and Yamano, K. (1997). *Fuel Injection Rate Shaping and Its Effect on Exhaust Emissions in a Direct-Injection Diesel Engine Using a Spool Acceleration Type Injection System*. SAE 970347.

70. Ishikawa, N. and Zhang, L. (1999). *Characteristics of Air-Entrainment in a Diesel Spray*. SAE 1999-01-0522.

71. Johnson, T. V. (2000). *Diesel Emission Control in Review*. SAE 2000-01-0184.

72. Kamimoto, T. and Minagawa, T. (2000). *A Two-Zone Model Analysis of Heat Release Rate in Diesel Engines*. THIESEL 2000: Thermofluidynamic Processes in Diesel Engines, pp. 323-331.

73. Karimi, E. R. (1989). *High-Speed Photography of Fuel Spray and Combustion Events In a Production Diesel Engine and Combustion Bomb*. Proceedings of IMechE, Vol. 203, Part A, pp. 269-281.

74. Karimi, E. R. and Jane, P. A. H. (1993). *A Combustion System Investigation to Achieve Low Emissions on a Heavy Duty Diesel Engine*. Automotive Emissions and Combustion. London, Mechanical Engineering Publication, pp. 143-160.

75. Kato, S., Onishi, S., Tanabe, H. and Sato, G. T. (1992). *Development of Low NOx Emission Diesel Engine by Impingement of Fuel Jet*. SAE 921645.

76. Kato, T., Koyama, T., Sasaki, K. and Mori, K. (1998). *Common Rail Fuel Injection System for Improvement of Engine Performance on Heavy Duty Diesel Engine*. SAE 980806.

77. Kobayashi, S., Sakai, T., Nakahira, T., Komori, M. and Tsujimura, K. (1992). *Measurement of Flame Temperature Distribution in a DI Diesel Engine with High Pressure Fuel Injection*. SAE 920692.

78. Kobori, S., Kamimoto, T. and Kosaka, H. (1996). *Ignition, Combustion and Emissions in a DI Diesel Engine Equipped with a Micro-Hole Nozzle*. SAE 960321.

79. Konno, M., Chikahisa, T. and Murayama, T. (1992). *Reduction of Smoke and NOx by Strong Turbulence Generated During the Combustion Process in DI Diesel Engines*. SAE 920467.

80. Kosaka, H., Won, Y. H. and Kamimoto, T. (1992). *A Study of the Structure of Diesel Sprays Using 2-D Imaging Techniques*. SAE 920107.

81. Kozma, J. H. and Farrell, P. V. (1997). *Air Entrainment in a High Pressure Diesel Spray*. SAE 971620.

82. Kuniyoshi, H., Tanabe, H., Sato, G. T. and Fujimoto, H. (1980). *Investigation on the Characteristics of Diesel Fuel Spray*. SAE 800968.

83. Ladommatos, N. and Zhao, H. (1994a). *A Guide to Measurement of Flame Temperature and Soot Concentration in Diesel Engines Using the Two-Colour Method, Part 1: Principles*. SAE 941956.

84. Ladommatos, N. and Zhao, H. (1994b). *A Guide to Measurement of Flame Temperature and Soot Concentration in Diesel Engines Using the Two-Colour Method, Part 2: Implementation*. SAE 941957.

85. Lai, M.-C., Wang, T.-C., Xie, X., Han, J.-S., Henein, N. A., Schwarz, E. and Bryzik, W. (1998). *Microscopic Characterisation of Diesel Sprays at VCO Nozzle Exit*. SAE 982542.

86. Lapuerta, M., Armas, O. and Hernández, J. J. (1999). *Effect of the Injection Parameters of a Common Rail Injection System on Diesel Combustion Through Thermodynamic Diagnosis*. SAE 1999-01-0194.

87. Larsson, A. (1999). *Optical Studies in a DI Diesel Engine*. SAE 1999-01-3650.

88. Lee, T.-W. and Mitrovic, A. (1996). *Liquid Core Structure of Pressure-Atomized Sprays via Laser Tomographic Imaging*. Atomization and Sprays, Vol. 6, pp. 111-126.

89. Lefebvre, A. H. (1989). *Atomization and Spray*. New York, Hemisphere Publishing Corporation.

90. Li, X. and Wallace, J. S. (1995). *In-Cylinder Measurement of Temperature and Soot Concentration Using the Two-Colour Method*. SAE 950848.

91. Marcic, M. (2003). *Measuring Method for Diesel Multihole Injection Nozzles*. Sensors and Actuators A: Physical, Vol. 107, (Issue 2), pp. 152-158.

92. Mathews, J. H. and Fink, K. D. (1998). *Numerical Methods Using Matlab*. New Jersey, Prentice Hall.

93. Matsui, Y., Kamimoto, T. and Matsuoka, S. (1979). *A Study on the Time and Space Resolved Measurement of Flame Temperature and Soot Concentration in a DI Diesel Engine by the Two-Colour Method*. SAE 790491.

94. Matsui, Y., Kamimoto, T. and Matsuoka, S. (1980). *A Study on the Application of the Two-Colour Method to the Measurement of Flame Temperature and Soot Concentration in DI Diesel Engines*. SAE 800970.

95. Matsui, Y., Kamimoto, T. and Matsuoka, S. (1982). *Formation and Oxidation Processes of Soot Particulates in a DI Diesel Engine - An Experimental Study via the Two-Colour Method*. SAE 820464.

96. Miles, P. C. (2000). *The Influence of Swirl on HSDI Diesel Combustion at Moderate Speed and Load*. SAE 2000-01-1829.

97. Minami, T., Takeuchi, K. and Shimazaki, N. (1995). *Reduction of Diesel Engine NOx Using Pilot Injection*. SAE 950611.

98. Montgomery, D. T. and Reitz, R. D. (1996). *Six-Mode Cycle Evaluation of the Effect of EGR and Multiple Injections on Particulate and NOx Emissions from a DI Diesel Engine*. SAE 960316.

99. Morgan, R., Wray, J., Kennaird, D. A., Crua, C. and Heikal, M. R. (2001). *The Influence of Injector Parameters on the Formation and Break-up of a Diesel Spray*. SAE 2001-01-0529.

100. Mori, K. (1997). *Worldwide Trends in Heavy-Duty Diesel Engine Exhaust Emission Legislation and Compliance Technologies*. SAE 970753.

101. Murayama, T. (1994). *Simultaneous Reduction of NOx and Smoke of Diesel Engines without Sacrificing Thermal Efficiency*. JSME International Journal. Series B, Vol. 37, (No. 1), pp. 1-8.

102. Naber, J. D. and Siebers, D. L. (1996). *Effects of Gas Density and Vaporisation on Penetration and Dispersion of Diesel Sprays*. SAE 960034.

103. Needham, J. R. and Whelan, S. (1994). *Meeting The Challenge of Low Emission and Fuel Economy with the Ricardo Four-Valves High-Speed Direct Injection Engine*. Proceedings of IMechE, Part D: Journal of Automotive Engineering, Vol. 208, pp. 181-190.

104. Nehmer, D. A. and Reitz, R. D. (1994). *Measurement of the Effect of Injection Rate and Split Injections on Diesel Engine Soot and NOx Emissions*. SAE 940668.

105. Paul-Trading-Corp (2002).

106. Payri, F., Desantes, J. M. and Arrègle, J. (1996). *Characterization of D.I. Diesel Sprays in High Density Conditions*. SAE 960774.

107. Pierpont, D. A., Montgomery, D. T. and Reitz, R. D. (1995b). *Reducing Particulate and NOx Using Multiple Injections and EGR in a DI Diesel*. SAE 950217.

108. Pierpont, D. A. and Reitz, R. D. (1995a). *Effects of Injection Pressure and Nozzle Geometry on DI Diesel Emissions and Performance*. SAE 950604.

109. Pitcher, G. and Wigley, G. (1994). *Simultaneous Two-Component Velocity and Dropsize Measurements in a Combusting Diesel Fuel Spray*. Seventh International Symposium on Applications of Laser Techniques to Fluid Mechanics, Lisbon, Portugal.

110. Powell, C. F., Yue, Y., Poola, R., Wang, J., Lai, M.-C. and Schaller, J. (2001). *X-Ray Measurement of High Pressure Diesel Sprays*. SAE 2001-01-0531.

111. Press, W. H., Tenkolsky, S. A., Vetterling, W. T. and Flannery, B. P. (1994). *Numerical Recipes in C*. Cambridge University Press.

112. Rajalingam, B. V. and Farrell, P. V. (1999). *The Effect of Injection Pressure on Air Entrainment into Transient Diesel Sprays*. SAE 1999-01-0523.

113. Reid, R. C., Prausnitz, J. M. and Poling, B. E. (1987). *The Properties of Gases and Liquids*. New York, McGraw-Hill.

114. Reitz, R. D. and Bracco, F. V. (1982). *Mechanism of Atomization of a Liquid Jet*. The Physics of Fluids, Vol. 25, (No. 10), pp. 1730-1742.

115. Reitz, R. D. and Diwakar, R. (1987). *Structure of High-Pressure Fuel Sprays*. SAE 870598.

116. Ricardo (2002). *Ricardo Expects New Technology to Continue Fuelling Diesel Sales*. http://www.ricardo.com/

117. Ricart, L. M. and Reitz, R. D. (1996). *Visualization and Modeling of Pilot Injection and Combustion in Diesel Engines*. SAE 960833.

118. Ricart, L. M., Xin, J., Bower, G. R. and Reitz, R. D. (1997). *In-Cylinder Measurement and Modeling of Liquid Fuel Spray Penetration in a Heavy-Duty Diesel Engine*. SAE 971591.

119. Russell, M. F. and Lee, H. K. (1995). *Modelling Injection Rate Control Devices*. Diesel Fuel Injection System. London, Mechanical Engineering Publication, pp. 115-125.

120. Russell, M. F., Nicol, S. W. and Young, C. D. (1989). *Rate Modulation for Direct Injection Diesel Engines*. Diesel Fuel Injection Systems. London, Mechanical Engineering Publication, pp. 79-85.

121. Schindler, K. P. (2000). *Diesel Engines and the Environment*. THIESEL 2000: Thermofluidynamics Processes in Diesel Engines.

122. Schneider, B. (2002). *Manual and Help File for PCO-Pictures*. Switzerland.

123. Scott, A. (2003). *Personal correspondent with regards to DP203 Fuel Injection Pump*.

124. Sekar, R. (2000). *X-Ray Vision: Taking a Hard Look at Fuel Sprays and Combustion*. TransForum. Vol. 3, pp. 2-3.

125. Shimazaki, N., Hatanaka, H., Yokota, K. and Nakahira, T. (1996). *A Study of Diesel Combustion Process Under the Condition of EGR and High-Pressure Fuel Injection with Gas Sampling Method*. SAE 960030.

126. Shiozaki, T., Nakajima, H., Kudo, Y., Miyashita, A. and Aoyagi, Y. (1996). *The Analysis of Combustion Flame Under EGR Conditions in a DI Diesel Engine*. SAE 960323.

127. Shiozaki, T., Nakajima, H., Yokota, H. and Miyashita, A. (1998). *The Visualisation and Its Analysis of Combustion Flame in a DI Diesel Engine*. SAE 980141.

128. Shundoh, S., Komori, M., Tsujimura, K. and Kobayashi, S. (1992). *NOx Reduction from Diesel Combustion Using Pilot Injection with High Pressure Fuel Injection*. SAE 920461.

129. Siebers, D. L. (1998). *Liquid-Phase Fuel Penetration in Diesel Sprays*. SAE 980809.

130. Smallwood, G. J., Gülder, Ö. L. and Snelling, D. R. (1994). *The Structure of the Dense Core Region in Transient Diesel Sprays*. Twenty-Fifth Symposium (International) on Combustion. The Combustion Institute, pp. 371-379.

131. Soteriou, C., Andrews, R. and Smith, M. (1995). *Direct Injection Diesel Sprays and the Effect of Cavitation and Hydraulic Flip on Atomization*. SAE 950080.

132. Spikes, R. H. and Pennington, G. A. (1959). *Discharge Coefficient of Small Submerged Orifices*. Proceedings of IMechE, Vol. 173, (No. 25), pp. 661-665.

133. Stone, R. (1999). *Introduction to Internal Combustion Engines, 3rd. Edition*. Basingstoke, MacMillan Press Ltd.

134. Takaishi, T., Tateishi, M. and Kunimoto, E. (1989). *Control of Fuel Injection Characteristics in Small Diesel Engines*. Diesel Fuel Injection Systems. London, Mechanical Engineering Publication, pp. 71-78.

135. Takeda, Y. and Niimura, K. (1995). *Characteristics of Diesel Combustion and Emissions with a Multi-Injector System*. SAE 952511.

136. Tanin, K. V., Wickman, D. D., Montgomery, D. T., Das, S. and Reitz, R. D. (1999). *The Influence of Boost Pressure on Emissions and Fuel Consumption of a Heavy-Duty Single-Cylinder DI Diesel Engine*. SAE 1999-01-0840.

137. Timoney, D. J., McNally, C. P. and Doyle, C. T. (2000). *A Three-Zone Heat Release Model for Direct Injection Diesel Engines*. THIESEL 2000: Thermofluidynamic Processes in Diesel Engines, pp. 423-433.

138. Tow, T. C., Pierpont, D. A. and Reitz, R. D. (1994). *Reducing Particulate and NOx Emissions by Using Multiple Injections in a Heavy Duty DI Diesel Engine*. SAE 940897.

139. Tsunemoto, H., Montajir, R. M., Ishitani, H., Hayashi, T. and Harai, D. (1999). *The Influence of Pressure in the Nozzle Sac and Needle Lift on Fuel Spray Behaviour and HC Emissions in DI Diesel Engines*. SAE 1999-01-3491.

140. Tullis, S. and Greeves, G. (1996). *Improving NOx Versus BSFC with EUI 200 Using EGR and Pilot Injection for Heavy-Duty Diesel Engines*. SAE 960843.

141. Uchida, N., Daisho, Y., Saito, T. and Sugano, H. (1993). *Combined Effects of EGR and Supercharging on Diesel Combustion and Emissions*. SAE 930601.

142. Venkatesan, C. P. and Abraham, J. (2000). *An Investigation of the Dependence of NO and Soot Emissions from a Diesel Engine on Heat Release Rate Characteristics - I*. SAE 2000-01-0509.

143. Verhoeven, D., Vanhemelryck, J.-L. and Baritaud, T. (1998). *Macroscopic and Ignition Characteristics of High-Pressure Sprays of Single-Component Fuels.* SAE 981069.

144. Watson, N. and Janota, M. S. (1982). *Turbocharging the Internal Combustion Engine*. London, The MacMillan Press Ltd.

145. Way, R. J. B. (1977). *Investigation of Interaction Between Swirl and Jets in Direct Injection Diesel Engines Using a Water Model*. SAE 770412.

146. Weissbeck, H. (2002). *Technologies That Will Improve Diesels.* http://www.sae.org/congress/2003/executive-panels.htm.

147. Werlberger, P. and Cartellieri, W. P. (1987). *Fuel Injection and Combustion Phenomena in a High Speed DI Diesel Engine Observed by Means of Endoscopic High Speed Photography*. SAE 870097.

148. Winklhofer, E., Fuchs, H. and Philipp, H. (1993). *Diesel Spray Combustion - An Optical Imaging Analysis.* SAE 930862.

149. Winterbone, D. E., Yates, D. A., Clough, E., Rao, K. K., Gomes, P. and Sun, J.-H. (1994). *Combustion in High-Speed Direct Injection Diesel Engines - A Comprehensive Study*. Proceedings of IMechE, Vol. 208, Part C, pp. 223-240.

150. Yamaguchi, I., Nakahira, T., Komori, M. and Kobayashi, S. (1990). *An Image Analysis of High Speed Combustion Photographs for DI Diesel Engine with High Pressure Fuel Injection*. SAE 901577.

151. Yan, J. and Borman, G. L. (1988). *Analysis and In-Cylinder Measurement of Particulate Radiant Emissions and Temperature in a Direct Injection Diesel Engine*. SAE 881315.

152. Yoda, T. and Tsuda, T. (1997). *Influence of Injection Nozzle Improvement on DI Diesel Engine*. SAE 970356.

153. Yule, A. J. and Salters, D. G. (1995). *The Breakup Zone of a Diesel Spray: Part 1, Length of Zone and Volume of Unatomized Liquid.* Atomization and Sprays, Vol. 5, pp. 157-174.

154. Zelenka, P., Kriegler, W., Herzog, P. L. and Cartellieri, W. P. (1990). *Ways Toward the Clean Heavy-Duty Diesel*. SAE 900602.

155. Zhang, L., Minami, T., Takatsuki, T. and Yokota, K. (1993). *An Analysis of the Combustion of a DI Diesel Engine by Photography Processing*. SAE 930594.

156. Zhang, L., Tsurushima, T., Ueda, T., Ishii, Y., Itou, T., Minami, T. and Yokota, K. (1997). *Measurement of Liquid Phase Penetration of Evaporating Spray in a DI Diesel Engine*. SAE 971645.

157. Zhang, L., Ueda, T., Ishii, Y. and Yokota, K. (1998). *Observation and Calculation of the Combustion Characteristics of a HSDI Engine: Effects of Combustion Chambers and Injection Specifications.* The Fourth International Symposium COMODIA 98.

BOSCH TUBE PRESSURE CALIBRATION DATA

Transducer: AVL GM12D

Date: 11/09/03

Item	Description	Model	Serial No	Setting
1	Pressure Transducer	AVL GM12D		
2	Kistler Charge Amplifier	Type 5011 B10	629609	T=15.7pc/bar S=10
3	Digital Multimeter	3435A	1606A-11035	DC 20 V

Weight (kg/cm2)	Voltage Output (V)		Average (V)	Pressure (bar)
	Added	Removed		
0	0	0	0	0.00
10	0.9	0.9	0.9	9.81
20	1.9	1.9	1.9	19.62
30	2.8	2.8	2.8	29.43
35	3.3	3.3	3.3	34.34
40	3.8	3.8	3.8	39.24
50	4.8	4.7	4.75	49.05
55	5.3	5.3	5.3	53.96
60	5.8	5.7	5.75	58.86
65	6.2	6.2	6.2	63.77
70	6.7	6.7	6.7	68.67
80	7.7	7.7	7.7	78.48
90	8.6	8.6	8.6	88.29

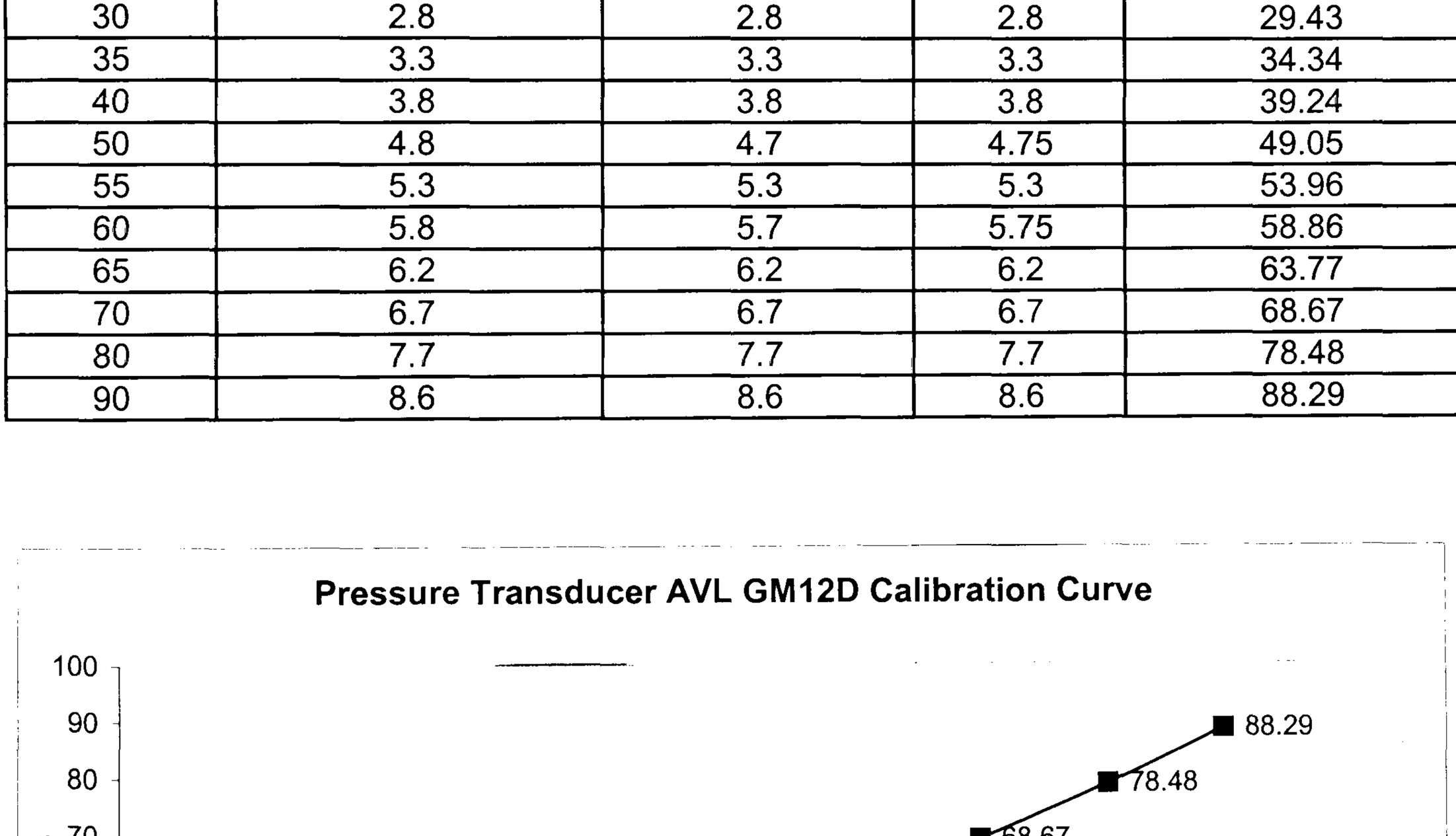

FUEL LINE PRESSURE CALIBRATION DATA

Transducer: Kistler 4065 A1000

Date: 21/05/03

Item	Description	Model	Serial No	Setting
1	Pressure Transducer	Kistler 4065 A1000	352996	
2	Kistler Charge Amplifier	Kistler 4617 AD	343491	
3	Digital Multimeter		MM1210	DC 20 V
4	Power Supply Unit		MM1210	

Weight (kg/cm2)	Voltage Output (V)		Average (V)	Pressure (bar)
	Added	Removed		
0	0.26	0.26	0.26	0.00
50	0.74	0.74	0.74	49.05
100	1.23	1.23	1.23	98.10
150	1.72	1.72	1.72	147.15
200	2.22	2.22	2.22	196.20
250	2.71	2.71	2.71	245.25
300	3.21	3.21	3.21	294.30
350	3.71	3.71	3.71	343.35
400	4.21	4.21	4.21	392.40
450	4.7	4.71	4.705	441.45
500	5.2	5.2	5.2	490.50
550	5.7	5.7	5.7	539.55

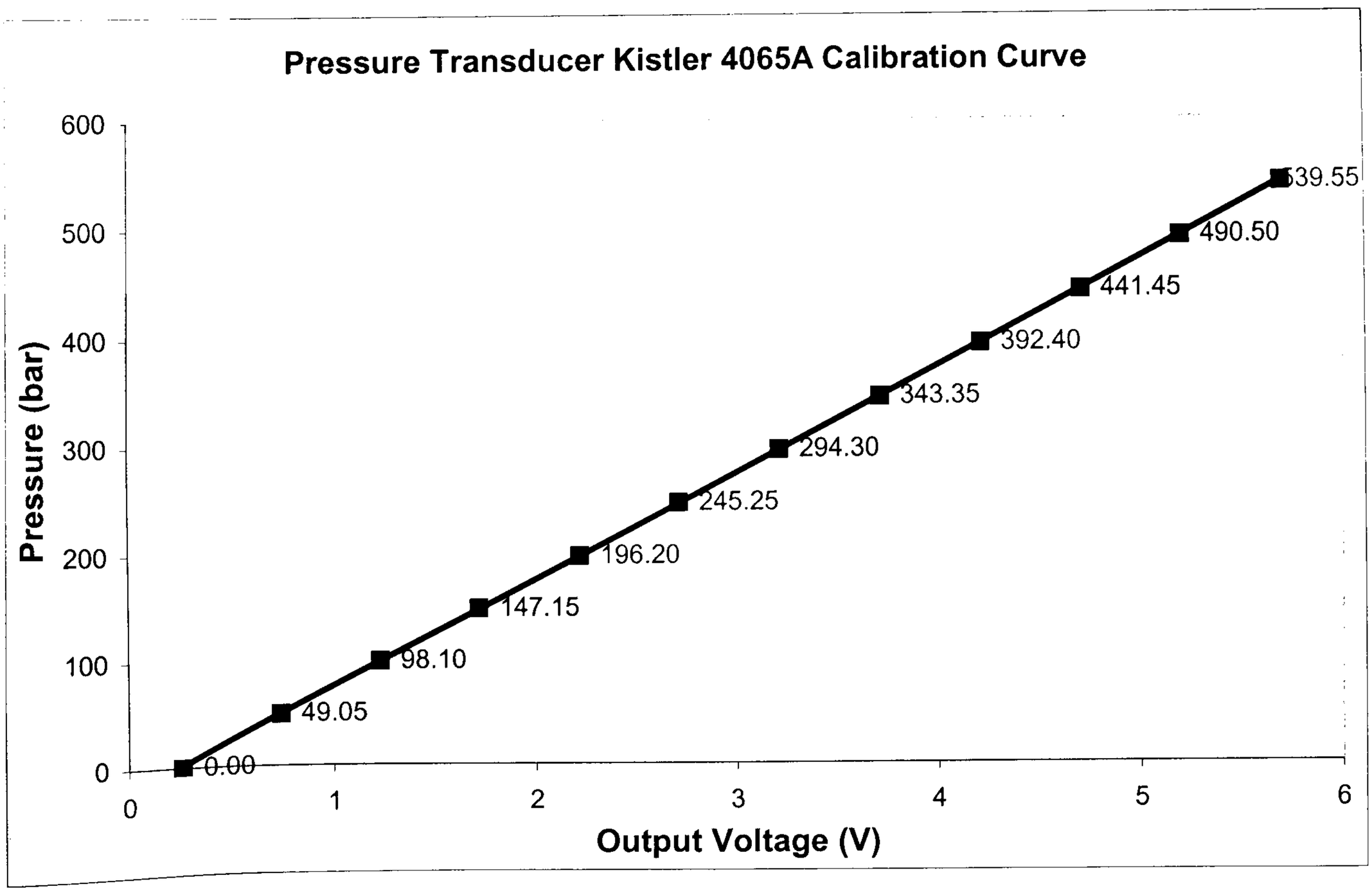

IN-CYLINDER PRESSURE CALIBRATION DATA

Transducer: Kistler 6053 B60
Date: 18/08/03

Item	Description	Model	Serial No	Setting
1	Pressure Transducer	Kistler 6053 B60	564707	
2	Kistler Charge Amplifier	Kistler 5011 B10	629609	T=6.5pC/bar S=20
3	Digital Multimeter	3435A	1606A-11035	DC 20 V

Weight (kg/cm2)	Voltage Output (V)		Average (V)	Pressure (bar)
	Added	Removed		
0	0	0	0.00	0.00
10	0.46	0.45	0.46	9.81
20	0.96	0.95	0.96	19.62
30	1.46	1.46	1.46	29.43
40	1.97	1.97	1.97	39.24
50	2.48	2.47	2.48	49.05
60	2.98	2.98	2.98	58.86
70	3.49	3.49	3.49	68.67
80	4	4	4.00	78.48
90	4.5	4.51	4.51	88.29
100	5.1	5.01	5.06	98.10
110	5.52	5.53	5.53	107.91
120	6.03	6.04	6.04	117.72
130	6.54	6.54	6.54	127.53
140	7.05	7.06	7.06	137.34
150	7.56	7.57	7.57	147.15
160	8.07	8.08	8.08	156.96
170	8.58	8.59	8.59	166.77
180	9.09	9.09	9.09	176.58
190	9.6	9.6	9.60	186.39
200	10.11	10.11	10.11	196.20

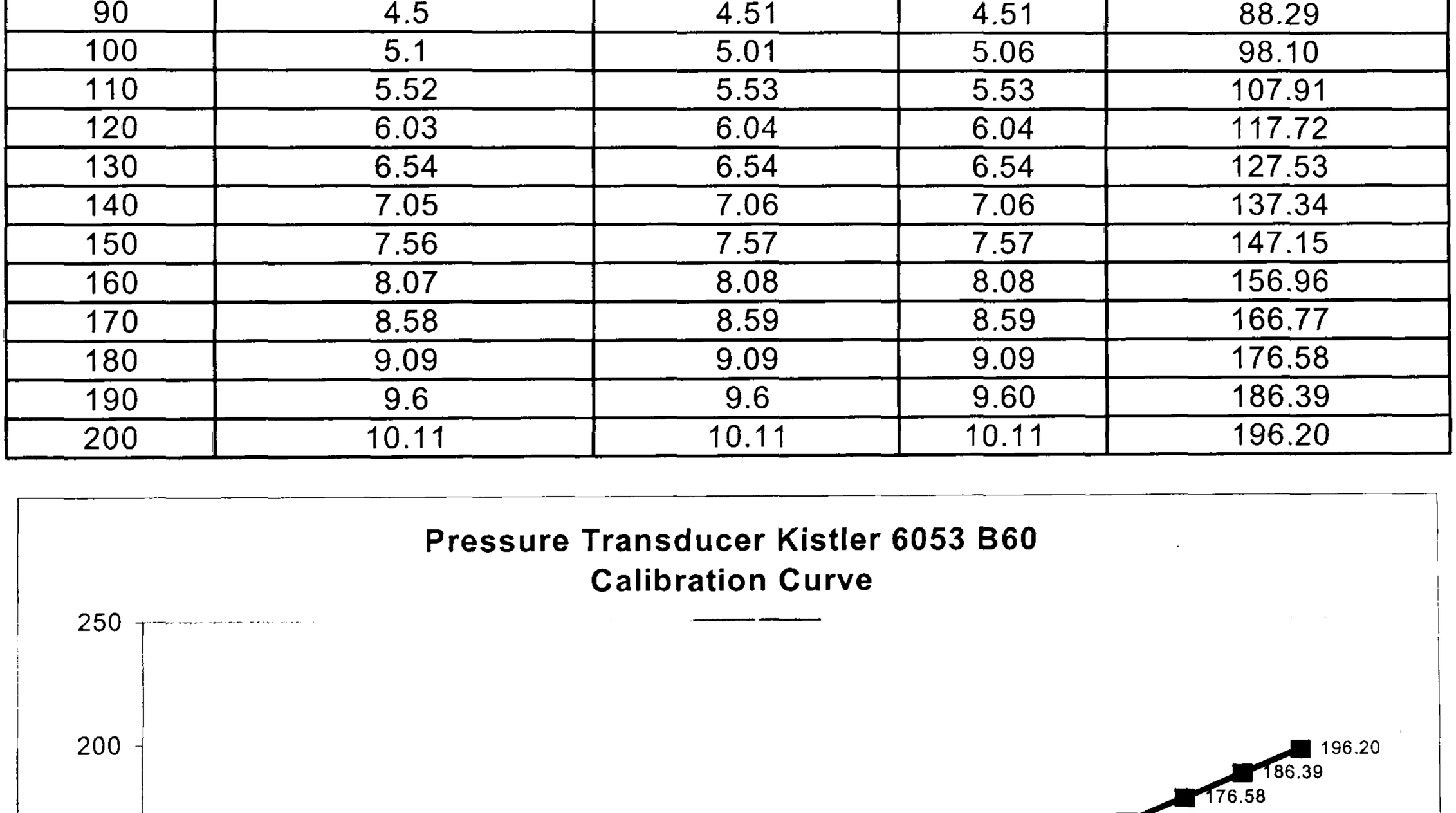

4X90 VARIABLE SPEED PERFORMANCE 94381EUG

TEST DESCRIPTION	:-	3000 TORQUE CURVE	COMMENTS	:-	4 Deg BTOC @ 3000r/min
DATE	:-	30/7/01			6 Deg BTDC @ 2000r/min
X No.	:-				
TRIAL No.	:-				FUELLING RESET TO NEW
ENGINE TYPE	:-	X904			MASTER SETTINGS BY DELPHI
ENGINE No.	:-	AD 1795			
ENGINE BLD.SCHED.	:-	V3000			
TIMING	:-	SEE NOTES BELOW			
ENGINEER	:-	A.WELLS			

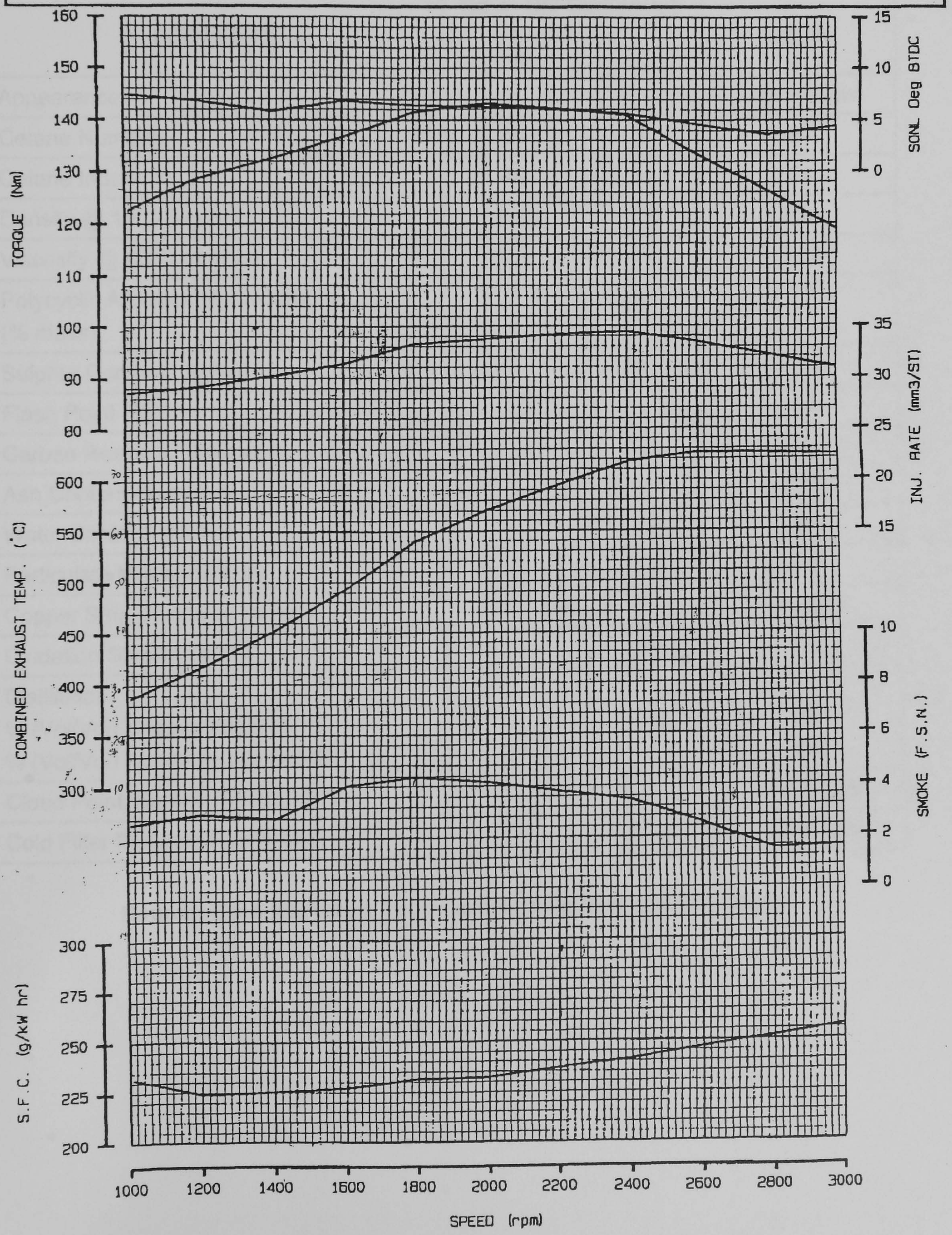

ESSO Diesel Ultra Low Sulphur

PROPERTY	BS or HM Customs & Excise Limit		VALUE
	Min	Low	
Appearance			Light yellow
Cetane Number	51	-	54
Cetane Index	46	-	54
Density @ 15°C (kg/m^3)	820	835	834
Viscosity @ 40°C (mm^2/s)	2.0	4.4	2.69
Polycyclic Aromatic Hydrocarbons (% mass)	-	11	5.2
Sulphur Content (mg/kg)	-	50	40
Flash Point (°C)	55	-	64
Carbon Residue (% mass)	-	0.3	0.01
Ash Content (% mass)	-	0.01	<0.005
Water Content (mg/kg)	-	200	54
Particulate Matter (mg/kg)	-	24	2.9
Copper Strip Corrosion (rating)	Class 1		Class 1
Oxidation Stability (g/m^3)	-	25	< 16
Distillation % (Vol/Vol) Recovered @ 250°C % (Vol/Vol) Recovered @ 345°C	 - 85	 < 65 -	 33 98
Cloud Point; Summer/Winter (°C)	-	-	-11S/-12W
Cold Filter Plugging Point (°C)	-	-5S/-15W	-12S/-18W

Source: Esso Marketing Technical Bulletin (ExxonMobil, 2001)

APPENDIX VI

OPTICAL ACCESS INTO THE COMBUSTION CHAMBER FOR ENDOSCOPE

Two cylinder heads were available for the engine. The original cylinder head was drilled with a 12 mm hole to fit the adaptor for the pressure transducer while the other cylinder head was prepared to provide the optical access into the combustion chamber. The optical access into the combustion chamber was achieved by employing an endoscopic optical system. Endoscopy is a technique that allows optical access to the combustion chamber of a real engine with minimal interference to the combustion process and insignificant alterations to the design of the cylinder head. In-cylinder and combustion chamber views and imaging of the fuel injection and combustion phenomena under actual engine conditions are made possible with this system. It takes advantage of fitting a pressure window into the cylinder head of an engine in a similar way as is common practice with cylinder pressure transducers, while providing relatively wide angle of view into the combustion chamber. The endoscope and window assembly is easy to mount and to remove for changing and cleaning purpose, without having to remove the cylinder head from the engine. The system only requires a 15 mm hole to be drilled into the engine cylinder head to accommodate the cylinder head sleeve for inserting the endoscope assembly. To accomplish this, the original glow plug hole of cylinder number one was enlarged to the required dimensions in order to fit the cylinder head sleeve. Figure A1 shows the details for enlarging the glow plug access hole, while Figure A2 shows a drawing of the cylinder insert. The modified cylinder head sleeve, shown in Figure A3 (a) was then fitted into the cylinder head and secured by applying loctite to the surfaces. A blanking plug was also machined which was inserted into the sleeve when the endoscope was not in use. Both the cylinder head sleeve and the blanking plug were machined flush to the cylinder head surface. The blanking plug was used during the engine warm-up period and when the imaging operation was not performed.

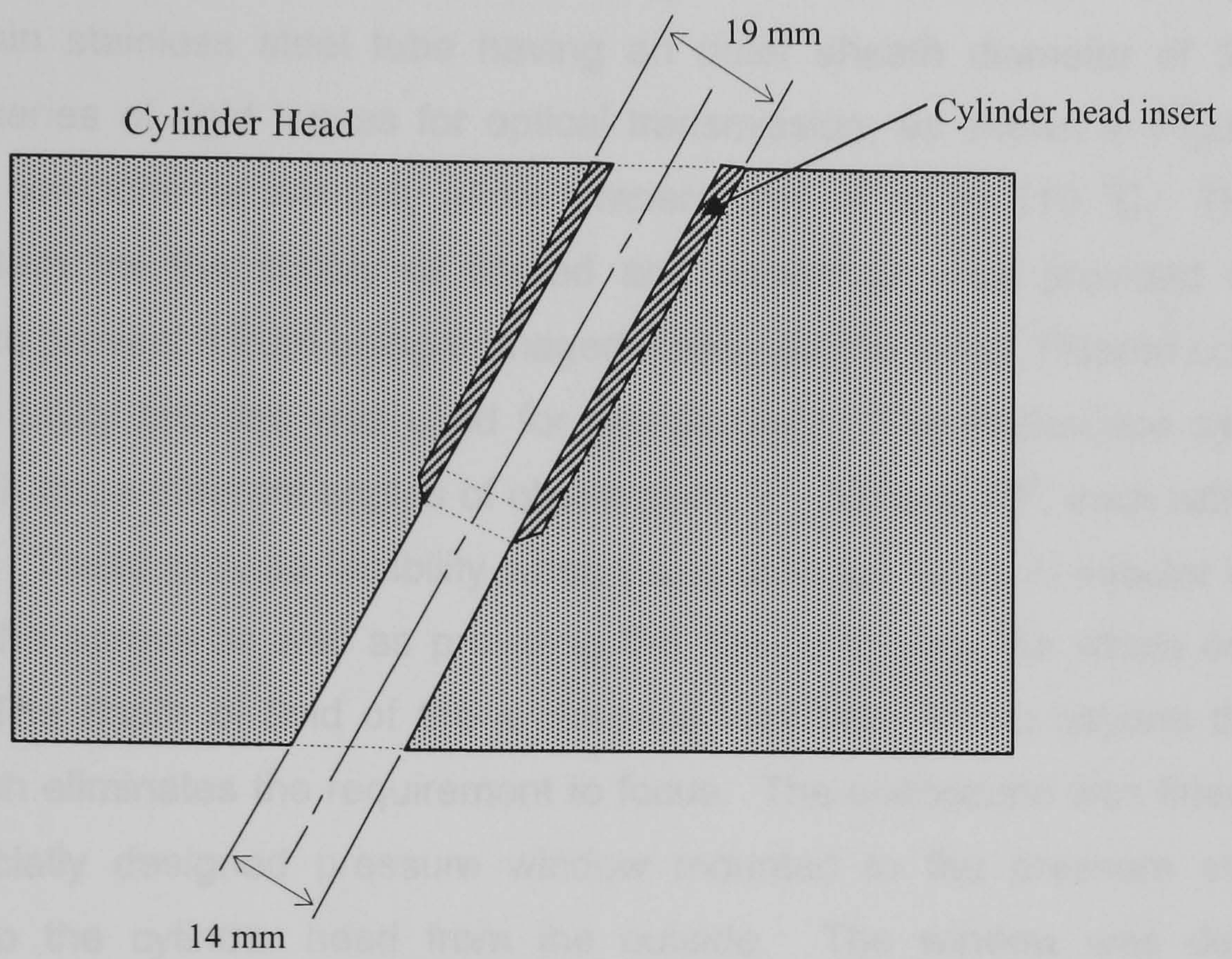

Figure A1: Drawing showing details of the hole drilling through the cylinder head

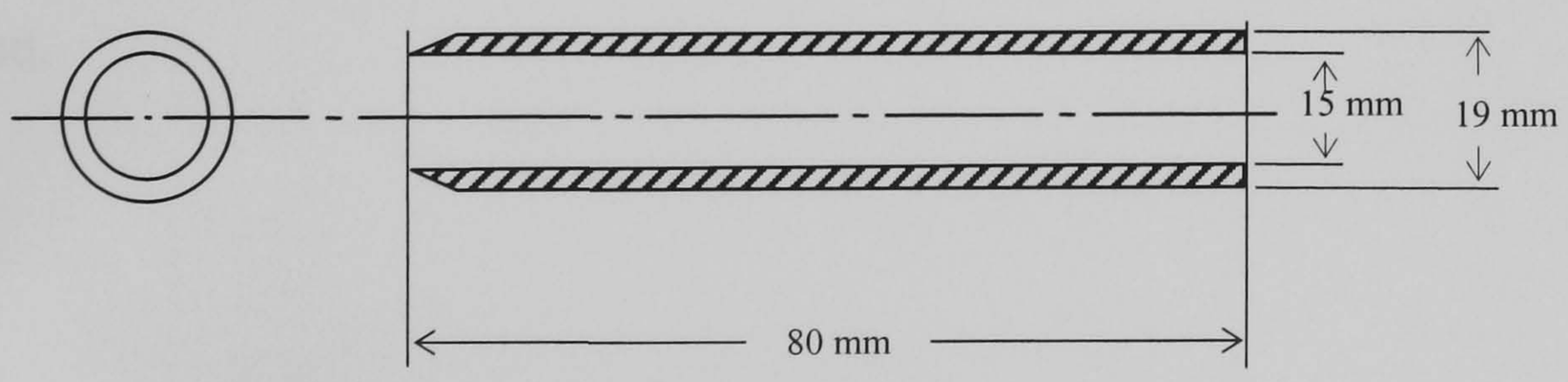

Figure A2: Drawing of the stainless steel cylinder head insert which was press fitted into the hole in the cylinder head

The optical system consisted of three endoscope probes with different observation angles, a pressure sleeve, three pressure windows to be used with the appropriate endoscope probe, an optical linkage and a CCD camera. The endoscope is a long thin stainless steel tube having an outer sheath diameter of 5 mm and containing series of rigid lenses for optical transmission, as shown in Figure A3 (c). The optical components are only allow temperatures of up to 110 ^{0}C. Therefore a cooling system for the supply of filtered and cooled air was provided within the endoscope to prevent it from being damaged during engine firing. Filtered compressed air from the utility facilities was used for this purpose. The endoscope system was provided with three different angles of observation, 0^0, 30^0 and 70^0, each with a field of view of 80^0. These provide flexibility when using different types of injector nozzles in visualising the sprays as well as providing the choice to view the whole combustion chamber. The depth of field of the endoscope was from 1 mm beyond the lens to infinity, which eliminates the requirement to focus. The endoscope was fitted together with a specially designed pressure window mounted to the pressure sleeve and inserted into the cylinder head from the outside. The window was designed to withstand the high temperatures and pressures of the combustion chamber. The pressure sleeve, shown in Figure A3 (b), has an internal nylon sleeve on both ends which act as a guide for the endoscope. The fully assembled cylinder inserts and various sleeves with the endoscope are shown in Figure A4. The images from the endoscope are transmitted to the camera via an optical linkage that housed four rigid rod-like lens relay tubes. The optical linkage assembly was coupled to the endoscope and camera by self-centering quick snap connectors, which provided automatic optical alignment of the endoscope image with the camera. To capture images of a complete combustion event, a photographic system enabling high-speed photography would be required.

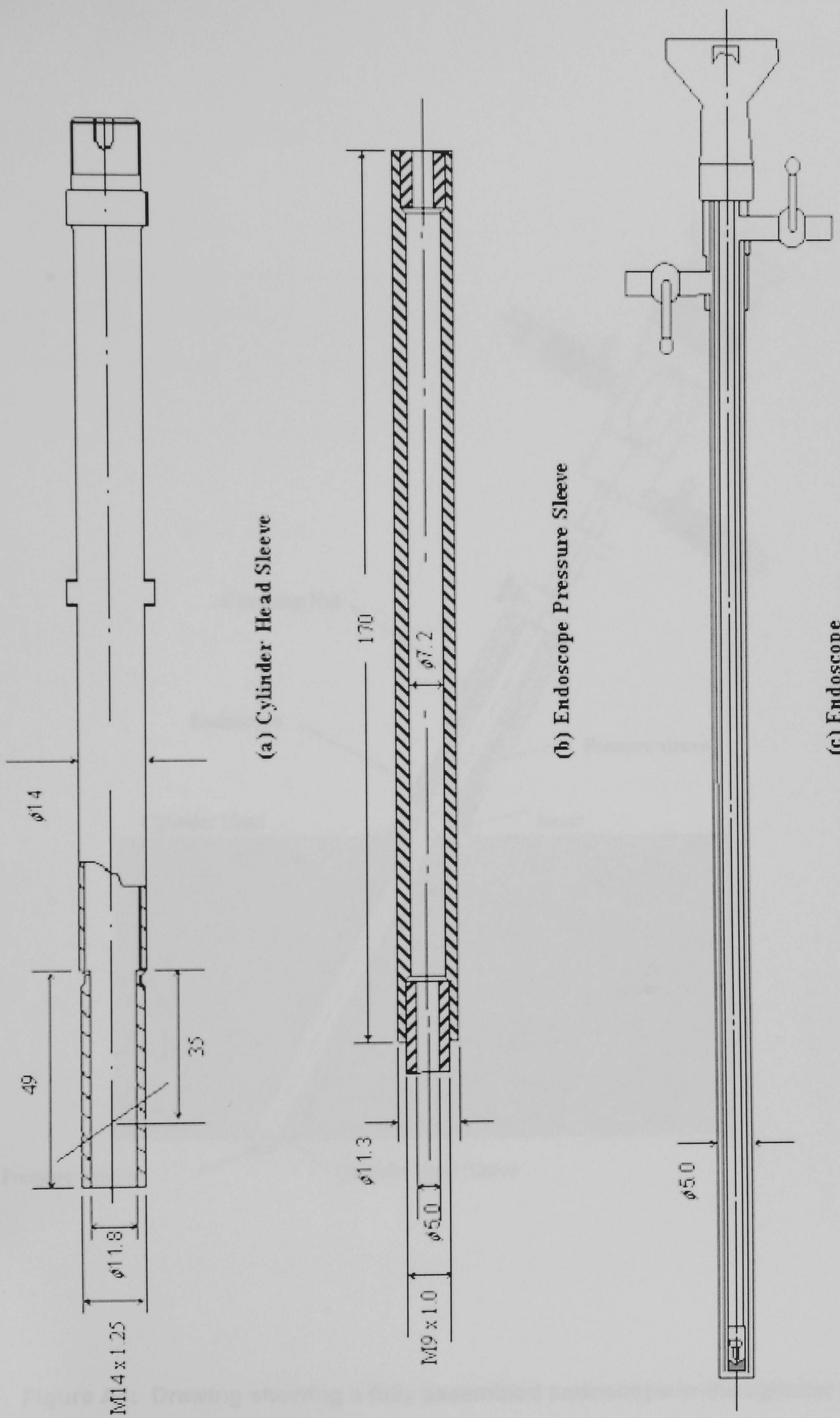

Figure A3: Various components required in assembling the endoscopic system

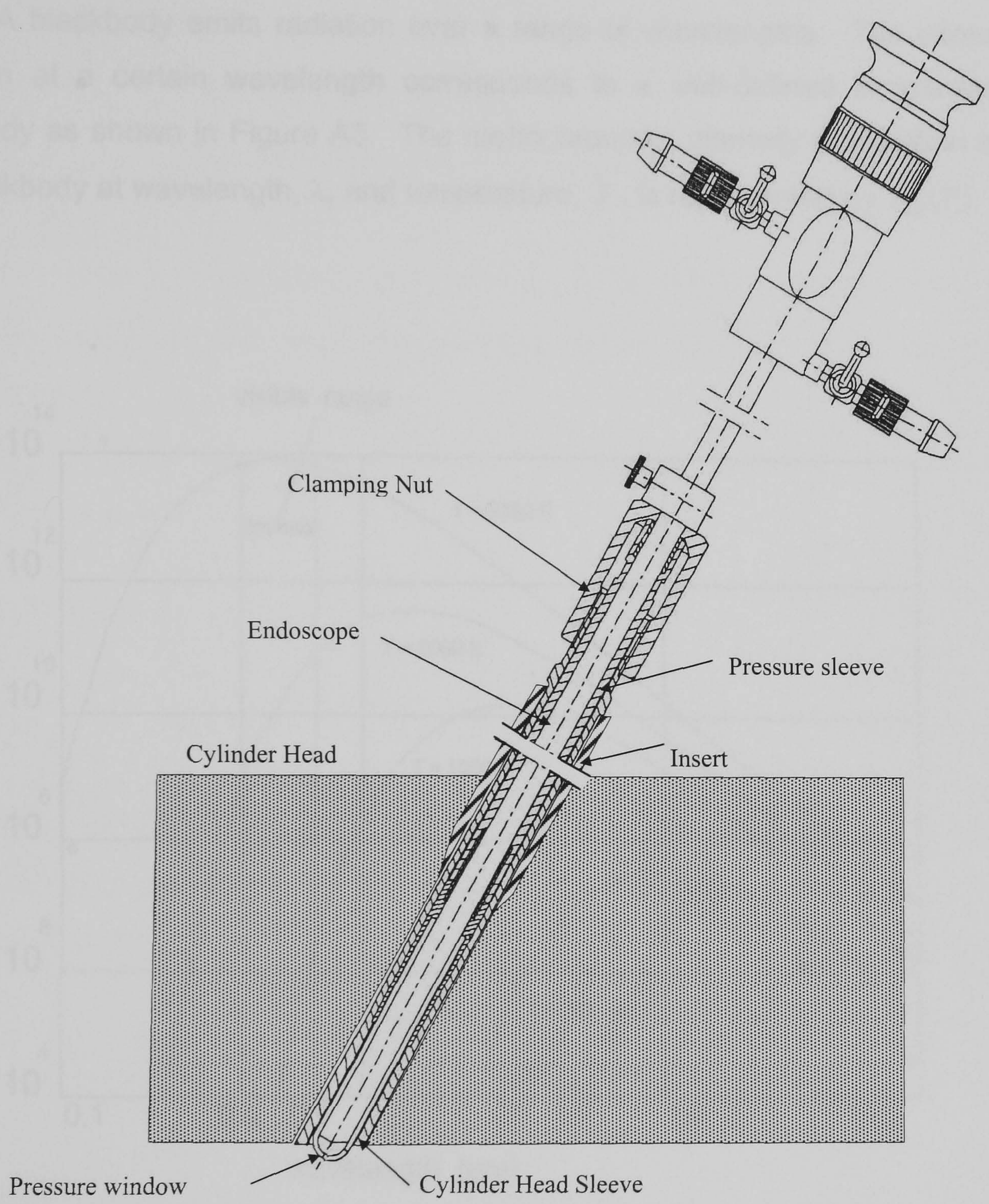

Figure A4: Drawing showing a fully assembled endoscope in the cylinder head

PRINCIPLE OF THE TWO-COLOUR METHOD

A blackbody emits radiation over a range of wavelengths. The intensity of the radiation at a certain wavelength corresponds to a well-defined temperature of the blackbody as shown in Figure A5. The monochromatic intensity of radiation emitted by the blackbody at wavelength, λ, and temperature, T, is represented by $I_{b\lambda}(T)$.

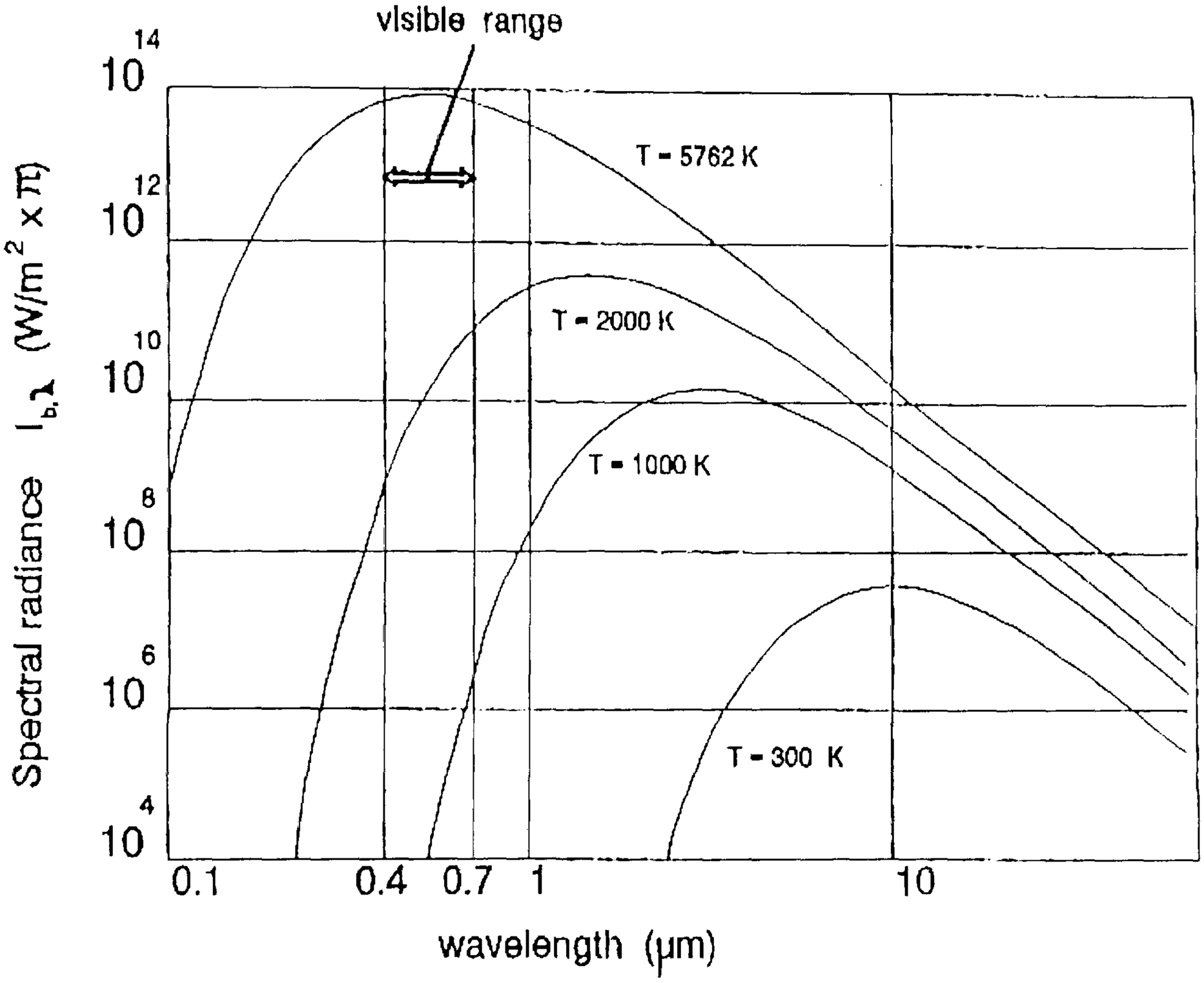

Figure A5: Emission spectra of a black body at different temperatures

A non-blackbody also emits radiation over a range of wavelengths, but the intensity of radiation is less than that of a blackbody by the monochromatic emissivity, ε_λ. The monochromatic intensity of radiation emitted by the non-blackbody at wavelength, λ, and temperature, T, is represented by $I_\lambda(T)$.

By definition, the monochromatic emissivity, ε_λ, of the body at wavelength, λ, is given by;

$$\varepsilon_\lambda = \frac{I_\lambda(T)}{I_{b\lambda}(T)} \tag{A1}$$

where $\varepsilon_\lambda < 1$ for the non blackbody

$\varepsilon_\lambda = 1$ for a blackbody at any wavelength

The blackbody apparent temperature, T_a, is defined as the temperature of a blackbody which will emit the same radiation as a non-blackbody at temperature, *T*. Thus, we have;

$$I_{b\lambda}(T_a) = I_\lambda(T) \tag{A2}$$

Equation (A1) can be written as;

$$\varepsilon_\lambda = \frac{I_{b\lambda}(T_a)}{I_{b\lambda}(T)} \tag{A3}$$

The intensity of radiation from a blackbody is given by Planck's function and Wien's Law as a function of temperature and wavelength as;

$$I_{b\lambda} = \frac{2c_1}{\lambda^5\left[e^{c_2/\lambda T} - 1\right]} \tag{A4}$$

where c_1 is Planck's first radiation constant = 3.7418 x 10^8 Wμm^4/m^2

c_2 is Planck's second radiation constant = 0.014388 x 10^6 μmK.

Substituting equation (A4) into equation (A3) yields;

$$\varepsilon_\lambda = \frac{e^{c_2/\lambda T} - 1}{e^{c_2/\lambda T_a} - 1} \tag{A5}$$

However, the monochromatic emissivity of soot particles produced by diesel flames is neither unity nor independent of wavelength. Thus, the emissivity of the diesel flame has to be estimated by using empirical correlation developed by Hottel and Broughton (Hottel and Broughton, 1932);

$$\varepsilon_\lambda = 1 - e^{-KL/\lambda^\alpha} \tag{A6}$$

Where K is the absorption coefficient per unit flame thickness.

L is the geometric flame thickness along the light axis of the flame detection system (optical path length).

α is the spectral range constant.

Substituting equation (A6) into equation (A5) and simplifying the equation yields;

$$KL = -\lambda^\alpha \ln\left[1 - \frac{e^{c_2/\lambda T} - 1}{e^{c_2/\lambda T_a} - 1}\right] \tag{A7}$$

The two-colour method used in diesel flame temperature and soot concentration calculation is based on measuring the incandescent soot radiation spectrum at two selected wavelengths. Two separate monochromatic intensity measurements are taken simultaneously and represented by, $I_{\lambda 1}$, at the shorter wavelength, λ_1, and $I_{\lambda 2}$, at the longer wavelength, λ_2. By substituting the apparent temperatures of the flame, T_{a1}, and T_{a2}, measured at the two known wavelengths, λ_1 and λ_1, the temperature, T, of the soot particles can be calculated by using equation (A8) below;

$$\left[1 - \frac{e^{c_2/\lambda_1 T} - 1}{e^{c_2/\lambda_1 T_{a1}} - 1}\right]^{\lambda_1^{\alpha_1}} = \left[1 - \frac{e^{c_2/\lambda_2 T} - 1}{e^{c_2/\lambda_2 T_{a2}} - 1}\right]^{\lambda_2^{\alpha_2}} \tag{A8}$$

Substituting the temperature, *T,* calculated from equation (A8) back into equation (A7) will give the estimated value of the soot concentration, *KL*.

COMPUTER CODE FOR THREE-ZONE MODEL, HEAT RELEASE RATE CALCULATION

```
clear all
close all

EngineGeometry;                 %1.0 Call script file containing engine specifications
Constant1;                      %2.0 Call script file containing value of species coefficients
CylinderPressure;               %3.0 In-cylinder pressure data
InjectionRates;                 %4.0 Fuel injection rate data


%1.0    Define species properties

H=26;                           % fuel dodecane
C=12;
mair=3.60e-3;                   % mass of air (kg)
mresidual=0.05*mair;            % mass of residual gases (kg)
phi=1.0;                        % F/A Equivalence ratio
psi=3.773;                      % molar N/O ratio
y=H/C;                          % H/C molar ratio
epsilon=4/(4+y);                % stoichiometric F/A ratio
mtrap=mair+mresidual;           % mass of trapped air in cylinder (kg)
yb=mresidual/mtrap;             % mass fraction of residual gas (kg)
Mf=1.008*H+12.011*C;            % Molecular mass of fuel (kg/kmol)


%2.0    Define moles of burned mixture per mole O2 (CO2, H2O, O2 and N2)
%       (Ref: Heywood,1988 p.104)

nbCO2=epsilon*phi;
nbH2O=2*(1-epsilon)*phi;
nbO2=1-phi;
nbN2=psi;
nb=phi*(1-epsilon)+1+psi;


%3.0    Define moles of unburned mixture per mole O2, in mixture
%       (Fuel, CO2, H2O, O2 and N2)
%       (Ref: Heywood,1988 p.105)

nuCO2=yb*epsilon*phi;
nuH2O=2*yb*(1-epsilon)*phi;
nuO2=1-yb*phi;
nuN2=psi;
nuf=(4*(1-yb)*(1+2*epsilon)*phi)/Mf;
nu=(1-yb)*(4*(1+2*epsilon)*phi/Mf+1+psi)+yb*nb;
mRP=32+4*phi*(1+2*epsilon)+28.16*psi;
alpha=(32*(1+y/4))/(12.011+1.008*y);
yuO2=(nuO2*MO2)/mRP;
```

```
%4.0      Molecular mass of species & gas constants

Mu=mRP/nu;
Mb=mRP/nb;                                  % kg/kmol
Ru=Ro/Mu;                                   % kJ/kgK
Rb=Ro/Mb;
Rf=Ro/Mf;

%5.0      Initial conditions and estimates of Pressure and Temperature;

N=2000;                                     % Engine speed (rpm)
mf=0;                                       % initial fuel mass
Tw=350;                                     % wall surface temperature (K)
vp=2*Ls*N/60;                               % piston speed (m/s)
Pr=0.05+4.2*(n-1)-6.7*(n-1)^2;              % prandtl number (Ref: Heywood, 1988, pp 142)

%6.0      Start Loop

Tu(1)=500;                                  % Initial value of unburned zone temp. @ theta= -180
Tb(1)=900;                                  % Initial value of burned zone temp. @ theta= -180
Tf(1)=400;                                  % Initial value of fuel zone temp. @ theta= -180
mu(1) = mtrap;                              % Initial value of unburned zone mass @ theta= -180
mf(1) = mf;                                 % Initial value of fuel zone mass @ theta= -180
dQudth(1)=0;
Qt(1)=0;
Wt(1)=0;


% Stepsize for theta

h=1;
j=1;
theta = -179;                               % (next time step)
mtrap = mtrap/1.1;
mcyl(1) = mtrap;
mfi(1) = 0;

for jc=-179:h:180;


%7.0      Calculate unburned gas properties (Cpu, dhu, duu) of CO2, H2O, O2, N2, Fuel

%   Specific Heats of unburned species, cpu (kJ/kgK)
cpuCO2(j)=nuCO2/mRP*Ro*(ACO2+BCO2*Tu(j)+CCO2*Tu(j)^2+DCO2*Tu(j)^3+ECO2*Tu(j)^4);
cpuH2O(j)=nuH2O/mRP*Ro*(AH2O+BH2O*Tu(j)+CH2O*Tu(j)^2+DH2O*Tu(j)^3+EH2O*Tu(j)^4);
cpuO2(j)=nuO2/mRP*Ro*(AO2+BO2*Tu(j)+CO2*Tu(j)^2+DO2*Tu(j)^3+EO2*Tu(j)^4);
cpuN2(j)=nuN2/mRP*Ro*(AN2+BN2*Tu(j)+CN2*Tu(j)^2+DN2*Tu(j)^3+EN2*Tu(j)^4);
cpuf(j)=nuf/mRP*(Af+Bf*Tu(j)+Cf*Tu(j)^2+Df*Tu(j)^3+Ef/(Tu(j))^2);

%   Specific Enthalpy of unburned species, hu (kJ/kg)
huCO2(j)=nuCO2/mRP*Ro*(ACO2*Tu(j)+BCO2/2*Tu(j)^2+CCO2/3*Tu(j)^3+DCO2/4*Tu(j)^4+ECO2/5*Tu(j)^5);
huH2O(j)=nuH2O/mRP*Ro*(AH2O*Tu(j)+BH2O/2*Tu(j)^2+CH2O/3*Tu(j)^3+DH2O/4*Tu(j)^4+EH2O/5*Tu(j)^5);
huO2(j)=nuO2/mRP*Ro*(AO2*Tu(j)+BO2/2*Tu(j)^2+CO2/3*Tu(j)^3+DO2/4*Tu(j)^4+EO2/5*Tu(j)^5);
huN2(j)=nuN2/mRP*Ro*(AN2*Tu(j)+BN2/2*Tu(j)^2+CN2/3*Tu(j)^3+DN2/4*Tu(j)^4+EN2/5*Tu(j)^5);
huf(j)=nuf/mRP*(Af*Tu(j)+Bf/2*Tu(j)^2+Cf/3*Tu(j)^3+Df/4*Tu(j)^4-Ef/Tu(j));
```

```
%   Specific Internal Energy of unburned species, uu (kJ/kg)
uuCO2(j)=huCO2(j)-nuCO2/mRP*Ro*Tu(j);
uuH2O(j)=huH2O(j)-nuH2O/mRP*Ro*Tu(j);
uuO2(j)=huO2(j)-nuO2/mRP*Ro*Tu(j);
uuN2(j)=huN2(j)-nuN2/mRP*Ro*Tu(j);
uuf(j)=huf(j)-nuf/mRP*Ro*Tu(j);

 %   Sum of properties
 cpu(j)=cpuCO2(j)+cpuH2O(j)+cpuO2(j)+cpuN2(j)+cpuf(j);
 hu(j)=huCO2(j)+huH2O(j)+huO2(j)+huN2(j)+huf(j);
 uu(j)=uuCO2(j)+uuH2O(j)+uuO2(j)+uuN2(j)+uuf(j);


 %8.0     Calculate unburned heat transfer (dQfdth=0)

 mumix(j)=3.3e-7*(Tu(j)^0.7)/(1+0.027*phi);          % mixture viscosity (kg/ms or N.s/m2)
 Reyn(j)=rho*vp*B/mumix(j);                          % Reynolds number
 k(j)=mumix(j)*cpu(j)/Pr;                            % mixture thermal conductivity (kW/mK)

 % heat transfer rate of unburned zone
 dQudt(j)=Acomb(j)*(a/B*k(j)*(Reyn(j)^b)*(Tu(j)-Tw)+c*(Tu(j)^4-Tw^4));   %(kJ/s)
 dQudth(j)=-dQudt(j)/(6*N);                                              %(kJ/deg)
 Qw(j)=dQudth(j)*(theta+179);                                            %(kJ)
 Qt(j)=-1*Qw(j);

 mcyl(j) = mtrap;                                    % Mass in cylinder at reference point
 mo(j) = mcyl(j);
 Uo(j) = mo(j)*uu(j);                                % internal energy of cyl. at reference point

 Wo(j) = P(j)*(dVdth(j)*(theta+179));
 Wt(j) = Wo(j);

 K = 1+alpha/yuO2;


 %9.0      Fuel Zone  (between SOI to EOI)

 if theta >= -5

   dn=0.194;                                         % nozzle diameter (m)
   An=pi*(dn^2)/4;                                   % Nozzle area (m2)

 if theta <= 2
       mcyl(j) = mfi(j) + mtrap;

   else
       mfi(j) = mfi(j-1);
       mcyl(j) = mcyl(j-1);
   end

   Vn=(6*N*mfi(j))/(rhof*An*5);
   Vinj(j)=Vn;
   cpf(j)=(Af+Bf*Tf(j)+Cf*Tf(j)^2+Df*Tf(j)^3+Ef/(Tf(j))^2)/Mf;
   hf(j)=(Af*Tf(j)+Bf/2*Tf(j)^2+Cf/3*Tf(j)^3+Df/4*Tf(j)^4-Ef/Tf(j))/Mf;
   uf(j)=hf(j)-Ro/Mf*Tf(j);
   Hf(j)=mfi(j)*hf(j);
```

```
%10.0    Solving non-linear equations using Newton-Raphson Method

 total = 0;
       mu_t=mu(j-1);
       mf_t = mf(j-1);
       Tb_t=Tb(j-1);

Xi = [mu_t; mf_t; Tb_t];

  while total == 0

     F11 = 1;
     F12 = 1 - K;
     F13 = 0;
     F21 = Ru.*Tu(j);
     F22 = Rf.*Tf(j) - K.*Rb.*Tb_t;
     F23 = K.*Rb.*mfi(j) - K.*Rb.*mf_t;
     F31 = uu(j);

     %    Calculate burned gas properties
           Specific Enthalpy of burned species, hb (kJ/kg)
    hbCO2=nbCO2/mRP*Ro*(aCO2*Tb_t+bCO2/2*Tb_t^2+cCO2/3*Tb_t^3+dCO2/4*Tb_t^4+eCO2/5*Tb_t^5);
    hbH2O=nbH2O/mRP*Ro*(aH2O*Tb_t+bH2O/2*Tb_t^2+cH2O/3*Tb_t^3+dH2O/4*Tb_t^4+eH2O/5*Tb_t^5);
    hbO2=nbO2/mRP*Ro*(aO2*Tb_t+bO2/2*Tb_t^2+cO2/3*Tb_t^3+dO2/4*Tb_t^4+eO2/5*Tb_t^5);
    hbN2=nbN2/mRP*Ro*(aN2*Tb_t+bN2/2*Tb_t^2+cN2/3*Tb_t^3+dN2/4*Tb_t^4+eN2/5*Tb_t^5);

    %    Specific Internal Energy of burned species, ub (kJ/kg)
    ubCO2=hbCO2-nbCO2/mRP*Ro*Tb_t;
    ubH2O=hbH2O-nbH2O/mRP*Ro*Tb_t;
    ubO2=hbO2-nbO2/mRP*Ro*Tb_t;
    ubN2=hbN2-nbN2/mRP*Ro*Tb_t;

    ub(j)=ubCO2+ubH2O+ubO2+ubN2;

    F32 = uf(j) - K.*ub(j);

    %    Determining dubi/dTb for F33;
    F33CO2 = nbCO2/mRP*Ro*(aCO2+bCO2*Tb_t+cCO2*Tb_t^2+dCO2*Tb_t^3+eCO2*Tb_t^4-1);
    F33H2O = nbH2O/mRP*Ro*(aH2O+bH2O*Tb_t+cH2O*Tb_t^2+dH2O*Tb_t^3+eH2O*Tb_t^4-1);
    F33O2 = nbO2/mRP*Ro*(aO2+bO2*Tb_t+cO2*Tb_t^2+dO2*Tb_t^3+eO2*Tb_t^4-1);
    F33N2 = nbN2/mRP*Ro*(aN2+bN2*Tb_t+cN2*Tb_t^2+dN2*Tb_t^3+eN2*Tb_t^4-1);
    F33 = K.*(mfi(j)-mf_t).*(F33CO2+F33H2O+F33O2+F33N2);
    dFidXi = [F11 F12 F13; F21 F22 F23; F31 F32 F33];
    %pause


%11.0     Solving for mu, mf, Tb;
 u = mu_t + mf_t + (mfi(j)-mf_t).*K - mcyl(j);
 v = mu_t.*Ru.*Tu(j) + mf_t.*Rf.*Tf(j) + (mfi(j)-mf_t).*Rb.*Tb_t.*K - P(j).*V(j);
 w = Wt(j) - Uo - Qt(j) - mfi(j).*hf(j) + mu_t.*uu(j) + mf_t.*uf(j) + (mfi(j)-mf_t).*K.*ub(j);

 Fi = [u; v; w];

 result = Xi - (dFidXi\Fi);

 mu_n = result(1);
 mf_n = result(2);
 Tb_n = result(3);
```

```
%9.0        Calculate burned gas properties
%        Specific Enthalpy of burned species, hb (kJ/kg)

Tb_t = Tb_n;

hbCO2=nbCO2/mRP*Ro*(aCO2*Tb_t+bCO2/2*Tb_t^2+cCO2/3*Tb_t^3+dCO2/4*Tb_t^4+eCO2/5*Tb_t^5);
hbH2O=nbH2O/mRP*Ro*(aH2O*Tb_t+bH2O/2*Tb_t^2+cH2O/3*Tb_t^3+dH2O/4*Tb_t^4+eH2O/5*Tb_t^5);
hbO2=nbO2/mRP*Ro*(aO2*Tb_t+bO2/2*Tb_t^2+cO2/3*Tb_t^3+dO2/4*Tb_t^4+eO2/5*Tb_t^5);
hbN2=nbN2/mRP*Ro*(aN2*Tb_t+bN2/2*Tb_t^2+cN2/3*Tb_t^3+dN2/4*Tb_t^4+eN2/5*Tb_t^5);

%  Specific Internal Energy of burned species, ub (kJ/kg)
ubCO2=hbCO2-nbCO2/mRP*Ro*Tb_t;
ubH2O=hbH2O-nbH2O/mRP*Ro*Tb_t;
ubO2=hbO2-nbO2/mRP*Ro*Tb_t;
ubN2=hbN2-nbN2/mRP*Ro*Tb_t;

ub(j)=ubCO2+ubH2O+ubO2+ubN2;

u = mu_n + mf_n + (mfi(j)-mf_n).*K - mcyl(j);
v = mu_n.*Ru.*Tu(j) + mf_n.*Rf.*Tf(j) + (mfi(j)-mf_n).*Rb.*Tb_t.*K - P(j).*V(j);
w = Wt(j) - Uo - Qt(j) - mfi(j).*hf(j) + mu_n.*uu(j) + mf_n.*uf(j) + (mfi(j)-mf_n).*K.*ub(j);

u_out = abs(0.001 - abs(u));
v_out = abs(0.001 - abs(v));
w_out = abs(1 - abs(w));

%pause

mb(j)=abs((1+alpha/yuO2)*(mfi(j)-mf_n));
%mcyl_t = mb(j) + mu_n + mf_n;

if (u_out < 10) & (v_out < 10) & (w_out < 10) & (mu_n > 0) & (mf_n > 0) & (Tb_n > 0) %& (mb(j) > 0)
   mu(j) = mu_n;
   mf(j) = mf_n;
   Tb(j) = Tb_n;
   mb(j)=(1+alpha/yuO2)*(mfi(j)-mf_n);
   mt(j)=mb(j)+mu(j)+mf(j);
   mb(j)=abs((1+alpha/yuO2)*(mfi(j)-mf_n));

   total = 1;

   if mu_n < mcyl(j);
      mu_t = mu_n;
   end

   if mf_n < mfi;
      mf_t = mf_n;
   end

   Tb_t = Tb_n
   Tb13 = sprintf('Problem on Tb not converge, value %5.4f',Tb_t); disp(Tb13)
   disp('need more iteration ..')

end
      disp('press any key to continue, or Ctrl C to terminate')

end

else
   Tf(j) = 0;
   mfi(j) = 0;
   mcyl(j) = mtrap;
```

```
if j ~= 1
    mu(j) = mu(j-1);
    mf(j) = mf(j-1);
    Tb(j) = Tb(j-1);
else
    mu(j) = mu(1);
    mf(j) = mf(1);
    Tb(j) = Tb(1);
end

  mb(j)=(1+alpha/yuO2)*(mfi(j)-mf(j));
  mt(j)=mb(j)+mu(j)+mf(j);

end


%13.     Solving for temperatute, Tu
%        using fourth-order Runge-Kutta Methods

  dTudth(j)=dPdth(j)*Ru*Tu(j)/(P(j)*cpu(j))+dQudth(j)/(mu(j)*cpu(j));
  k1 = dTudth(j);
  TuR2 = Tu(j) + 0.5*k1*h;
  k2 = dPdth(j)*Ru*TuR2/(P(j)*cpu(j))+dQudth(j)/(mu(j)*cpu(j));
  TuR3 = Tu(j) + 0.5*k2*h;
  k3 = dPdth(j)*Ru*TuR3/(P(j)*cpu(j))+dQudth(j)/(mu(j)*cpu(j));
  TuR4 = Tu(j) + k3*h;
  k4 = dPdth(j)*Ru*TuR4/(P(j)*cpu(j))+dQudth(j)/(mu(j)*cpu(j));
  Tu(j+1) = Tu(j) + 1/6*(k1 + 2*k2 + 2*k3 + k4)*h;

if ((theta >= -5) & (theta <= 2))

  %  Solving  for temperatutes Tf using fourth-order Runge-Kutta Methods

  dTfdth(j)=dPdth(j)*Rf*Tf(j)/(P(j)*cpf(j))+(mfi(j)*0.5*(Vinj(j)^2))/(mf(j)*cpf(j));
  k1f = dTfdth(j);
  TfR2 = Tf(j) + 0.5*k1f*h;
  k2f = dPdth(j)*Rf*TfR2/(P(j)*cpf(j))+(mfi(j)*0.5*(Vinj(j)^2))/(mf(j)*cpf(j));
  TfR3 = Tf(j) + 0.5*k2f*h;
  k3f = dPdth(j)*Rf*TfR3/(P(j)*cpf(j))+(mfi(j)*0.5*(Vinj(j)^2))/(mf(j)*cpf(j));
  TfR4 = Tf(j) + k3f*h;
  k4f = dPdth(j)*Rf*TfR4/(P(j)*cpf(j))+(mfi(j)*0.5*(Vinj(j)^2))/(mf(j)*cpf(j));
  Tf(j+1) = Tf(j) + 1/6*(k1f + 2*k2f + 2*k3f + k4f)*h;

  if theta == -5
     Tf(j+1) = Tf(j);
  end

  %pause
  %elseif (theta>=20)

  % mfin=3e-6*30;
  % mfi(j)=mfin;
  % Vinj(j)=Vn;

else

  if j ~=1
     mcyl(j) = mcyl(j-1);
  end

theta = theta + h;
j=j+1;
end
```

```
%1.0      Engine Geometry

B=90e-3;                        % Cylinder bore (m)
rc=18.5;                        % Compression ratio
lconn=140e-3;                   % Connnecting rod length (m)
Ls=90e-3;                       % Stroke (m)
acrank=Ls/2;                    % Crank radius (m)
R=lconn/acrank;                 % Conn. rod to crank radius ratio
Vc=3.27174e-5;                  % Clearance volume (m3)
Acyl=6.36172e-3;                % Cylinder head area (m2)
Ap=5.02655e-3;                  % Piston top area (m2)
n=1.33;


%2.0    Define Volume, Combustion Area and Pressure at each crank angle

m=1;

for th=-179:1:179;
  thrad=th/180*pi;

V(m)=Vc+Acyl*(lconn+acrank*(1-cos(thrad))-sqrt(lconn^2-acrank^2*(sin(thrad))^2));
Acomb(m)=Acyl+Ap+(pi*B)*(lconn+acrank-acrank*cos(thrad)-sqrt(lconn^2-acrank^2*(sin(thrad))^2));
V(m+1)=V(m);
Acomb(m+1)=Acomb(m);

dVdth(m)=(pi*B^2/4)*(acrank*sin(thrad)+(acrank^2*sin(thrad)*cos(thrad))/(sqrt(lconn^2-
acrank^2*(sin(thrad))^2)));
dVdth(m+1)=dVdth(m);

m=m+1;

end

m=1;



%tht=[-180:1:180];

%figure
%plot(tht,V);grid on;
%title('Combustion Chamber Volume');
%xlabel('Crank angle (deg)');
%ylabel('Volume (m3)');

%figure
%plot(tht,Acomb);grid on;
%title('Combustion Area');
%xlabel('Crank angle (deg)');
%ylabel('Acomb (m2)');

%figure
%plot(tht,dVdth);grid on;
%title('Derivative of Volume with respect to Crank Angle');
%xlabel('Crank angle (deg)');
%ylabel('dVdth');
```

%2.0 Constant1

%Coefficients for CO2, H2O, O2, N2 and Fuel

% Coefficients for unburned CO2
ACO2=2.401;
BCO2=8.735e-3;
CCO2=-6.607e-6;
DCO2=2.002e-9;
ECO2=6.327e-16;

% Coefficients for unburned H2O
AH2O=4.070;
BH2O=-1.108e-3;
CH2O=4.152e-6;
DH2O=-2.964e-9;
EH2O=0.807e-12;

% Coefficients for unburned O2
AO2=3.626;
BO2=-1.878e-3;
CO2=7.055e-6;
DO2=-6.764e-9;
EO2=2.156e-12;

% Coefficients for unburned N2
AN2=3.675;
BN2=-1.208e-3;
CN2=2.324e-6;
DN2=-0.632e-9;
EN2=-0.226e-12;

% Coefficients for Fuel, C8H18-iso-octane [Heywood (1988) and Turns (1996)]
Af=-2.3158;
Bf=760.4066e-3;
Cf=-409.4146e-6;
Df=85.4191e-9;
Ef=-129581.46;

% Coefficients for Fuel, C12H26 dodecane [Reid (1987) p.728]
Af=-9.328;
Bf=1.149;
Cf=-6.347e-4;
Df=1.359e-7;

%Coefficients for species at temperature 1000-5000K (burned mixture)
% Coefficients for burned CO2
aCO2=4.4608;
bCO2=3.0982e-3;
cCO2=-1.2393e-6;
dCO2=0.22741e-9;
eCO2=-0.015526e-12;

% Coefficients for burned H2O
aH2O=2.7168;
bH2O=2.9451e-3;
cH2O=-0.80224e-6;
dH2O=0.10227e-9;
eH2O=-0.0048472e-12;

```
% Coefficients for burned O2
aO2=3.6220;
bO2=0.73618e-3;
cO2=-0.19652e-6;
dO2=0.036202e-9;
eO2=-0.0028946e-12;

% Coefficients for burned N2
aN2=2.8963;
bN2=1.51558e-3;
cN2=-0.57235e-6;
dN2=0.099807e-9;
eN2=-0.0065224e-12;

% Molecular weight of species
MCO2=44.009;
MH2O=18.015;
MO2=31.998;
MN2=28.012;


% Universal Gas Constant
Ro=8.314;                                   % kJ/kmolK

%       Heat transfer coefficients based on Annand's Correlation
%       (Ref: Annand, IMechE., 1963)

a=0.49;                                     % 0.25 < a < 0.8
b=0.7;                                      % constant
c=1.6e-12;                                  % (kW/m2K4)
rho=1.15;                                    % mixture density (kg/m3)
```

```
%     Cylinder Pressure

i=1;

for th=-179:i:179;
   thrad=th/180*pi;


 P=
1e2.*[-5.947
-5.947
-5.947
-5.947
-5.947
-6.043
-6.043
-5.947
-6.043
-6.14
-6.043
-6.14
-6.14
-6.14
-6.14
-5.37
-6.236
-6.14
-6.14
-5.947
-6.14
-6.14
-5.947
-6.14
-6.14
-6.14
-6.14
-6.14
-6.043
-6.043
-6.14
-6.043
-6.043
-6.14
-6.043
-6.043
-6.14
-6.043
-5.37
-6.043
-6.043
-5.947
-5.947
-5.947
-5.947
-5.466
-5.466
-5.947
-5.466
-5.947
-5.466
-5.466
-5.37
-5.466
-5.37
-5.466
-5.37
-5.37
-5.37
-5.37
-5.37
-5.37
-5.274
-5.274
-5.274
-5.178
-5.274
-5.178
-5.274
-5.178
-5.274
-5.178
-5.178
-5.178
-5.466
-5.178
-5.466
-5.37
-5.466
-5.37
-5.274
-5.37
-5.37
-5.274
-5.274
-5.274
-5.178
-5.178
-5.274
-4.697
-4.697
-4.697
-4.601
-4.697
-4.601
-4.505
-4.505
-4.409
-4.409
-4.409
-4.697
-4.409
-4.601
-4.505
-4.505
-4.409
-4.409
-3.928
-3.832
-3.832
-3.735
-3.639
-3.735
-3.928
-3.832
-3.735
-3.639
-3.158
-3.158
-2.966
-2.87
-3.062
-2.966
-2.87
-2.293
-2.197
-2.101
-2.293
-2.101
-1.524
-1.427
-1.524
-1.331
-0.754
-0.85
-0.658
0.015
-0.081
0.207
0.881
0.784
1.554
1.554
2.227
2.227
3.092
3.189
4.054
4.535
4.727
```

5.304	38.386	-0.754
6.266	35.597	-0.85
6.939	34.539	-0.754
7.612	33.097	-0.658
8.382	30.789	-0.754
9.343	29.25	-0.85
10.017	27.807	-1.427
10.882	26.365	-1.427
11.459	24.538	-1.62
12.325	23.191	-1.62
13.863	22.422	-1.331
14.536	20.98	-1.524
16.075	19.922	-1.524
16.844	18.383	-2.197
18.479	17.71	-2.101
19.345	16.364	-2.293
20.691	15.594	-2.293
22.518	14.825	-2.389
23.865	13.767	-2.389
25.403	12.998	-2.101
26.846	12.517	-2.293
27.904	11.748	-2.197
29.442	10.786	-2.293
30.789	10.69	-2.293
32.52	9.343	-2.293
33.866	9.247	-2.87
34.732	8.574	-2.87
36.078	7.612	-2.87
36.847	7.708	-3.062
37.809	6.939	-3.062
38.386	6.17	-3.062
39.348	6.266	-3.062
39.444	5.4	-3.062
39.251	5.304	-3.158
38.482	4.727	-3.158
38.674	4.631	-2.87
38.482	3.958	-2.87
39.925	4.054	-2.966
44.733	3.285	-2.966
51.561	2.996	-3.062
55.311	3.189	-3.062
59.927	2.419	-3.062
60.889	2.227	-3.062
60.024	2.419	-3.158
57.619	1.65	-3.158
57.812	1.458	-3.158
58.677	1.746	-3.735
57.812	1.458	-3.639
55.504	0.881	-3.639
54.831	0.688	-3.639
53.003	0.784	-3.639
51.561	0.784	-3.639
49.926	0.111	-3.735
48.58	0.015	-3.639
45.406	0.207	-3.735
43.29	0.015	-3.735
42.425	-0.081	-3.158
40.694	-0.562	-3.832

```
-3.832
-3.832
-3.928
-4.409
-4.409
-4.409
-4.409
-4.409
-4.409
-4.409
-4.505
-4.505
-4.505
-4.505
-4.601
-4.601
-4.601
-4.697
-4.697
-4.697
-4.697
-4.697
-4.697
-5.178
-5.178
-5.178
-5.178
-5.178
-5.178
-5.178
-5.274
-5.274
-5.274
-5.274
-5.274
-5.274]';

  dPdth(i)=(P(i+1)-P(i))/1;
  dPdth(i+1)=dPdth(i);

   i=i+1;
end

i=1;
```

```
%   Injection Rate  (mm3/msec)

j=1;

for th=-179:j:179;
   thrad=th/180*pi;

mfi =
[58.98   59.03   59.28
59.00    59.01   58.92
59.02    58.99   58.61
59.01    58.96   58.53
58.97    58.93   58.55
58.90    59.01   58.80
58.92    58.90   58.73
58.84    58.79   58.94
58.83    60.60   58.94
58.84    65.80   58.89
58.84    68.04   58.92
58.87    67.12   59.03
58.89    63.12   58.88
58.95    60.62   58.64];
58.98    59.80
59.00    58.26

   j=j+1;
end

j=1;
```